

**FACULTY
OF MATHEMATICS
AND PHYSICS**
Charles University

DOCTORAL THESIS

Tomáš Janda

**Investigation of spin structure and dynamics in
magnetically ordered thin films**

Department of Chemical Physics and Optics

Supervisor of the doctoral thesis: prof. RNDr. Petr Němec, Ph.D.

Study programme: Physics

Study branch: Quantum Optics and Optoelectronics

Prague 2020

I declare that I carried out this doctoral thesis independently, and only with the cited sources, literature and other professional sources.

I understand that my work relates to the rights and obligations under the Act No. 121/2000 Sb., the Copyright Act, as amended, in particular the fact that the Charles University has the right to conclude a license agreement on the use of this work as a school work pursuant to Section 60 subsection 1 of the Copyright Act.

In date signature of the author

Title: Investigation of spin structure and dynamics in magnetically ordered thin films

Author: Tomáš Janda

Department: Department of Chemical Physics and Optics

Supervisor: prof. RNDr. Petr Němec, Ph.D., Department of Chemical Physics and Optics

Abstract: This thesis is devoted to the development of methods for imaging and ultrafast manipulation of magnetic textures, such as magnetic domains and domain walls (DWs), and to the investigation of the corresponding magnetization dynamics. We focused on techniques that are, besides ferromagnets (FMs), applicable also to antiferromagnets (AFs), in particular, AF thin films. The employed excitation techniques were mostly based on direct or indirect effects of ultrashort laser pulses. We studied the DW motion induced by a transfer of angular momentum from circularly polarized femtosecond laser pulses in a FM GaMnAsP and we found that the observed macroscopic DW displacement is only possible due to its inertia. In a distinct experiment, picosecond current pulses were generated by an absorption of the ultrashort laser pulses in a vertical PIN diode-based photoconductive switch and used to excite a magnetic film deposited directly on top of the diode. For imaging of AF domain patterns, we developed a simple table-top laser-scanning technique, which is based on a magnetothermoelectric response of the AF textures in the presence of a local laser-induced heating. We first used the method to image the domain structure in a collinear AF CuMnAs utilizing anisotropic magneto-Seebeck effect and we studied the response of the domain pattern to a current pulse excitation. Subsequently, the laser-scanning technique was applied to a non-collinear AF, Mn₃Sn, where the domain structure was visualized via anomalous Nernst effect and the localized laser heating combined with moderate magnetic fields was used also to write magnetic domains.

Keywords: magnetic domain structure, spin torques, magnetic microscopy, magneto-optics, spin-caloritronics

Acknowledgements

The research activities described in this thesis were conducted in a broad collaboration. At this page I want to thank all people whose contributions, advices, and support enabled me to obtain the results summarized below.

At first place, I would like to thank my supervisor, Petr Němec, for creating a stable and comfortable environment for my Ph.D. study, for his patient guidance towards the scientific independence, and for sharing his knowledge in the field of optics, magnetism, and laser physics. Many thanks are dedicated also to Joerg Wunderlich, who became my unofficial second supervisor, an unlimited source of ideas for experiments, and who shared with me his expertise in magnetotransport measurements and in spin-torque and domain wall physics. I am also grateful to all my colleagues from our optical group at the Charles University and spintronics research group of Tomáš Jungwirth at the Institute of Physics, ASCR, v.v.i., for the countless helpful discussions and advices. Namely I want to thank to João Godinho for his selfless help in the lab, Tomáš Ostatnický for the understanding provided by his numerical simulations, František Trojánek for his help with the development of measurement software, Eva Schmoranzarová, Lukáš Nádvorník, Helena Reichlová, Miloš Surýnek, Vít Saidl, Kamil Olejník, Martin Kozák, and Dagmar Butkovičová.

The presented experiments could not be realized without the supply of samples. I thank the growers – the group of Vít Novák at the Institute of Physics, ASCR, v.v.i. (GaMnAs, CuMnAs), the group of Richard Campion at the University of Nottingham (GaMnAsP, CuMnAs, Fe/GaAs), and Dominik Kriegner and Anastasios Markou from Max Planck Institute for Chemical Physics of Solids in Dresden (Mn₃Sn). Many thanks are dedicated to Zbyněk Šobáň from V. Novák's group for fabrication of most of the investigated devices (GaMnAsP, Fe/GaAs, CuMnAs) and to Helena Reichlová for fabrication of the Mn₃Sn devices.

Finally, I want to thank my family for the unfailing support and in this sense also to our optical group at the Charles University which became literally my second family for more than a decade.

Contents

Introduction	3
i Preface	3
ii Thesis aims and outline	4
iii Main publication outputs and author's contribution	6
1 Spin and magnetic order	7
1.1 Spin and magnetic moment	7
1.2 Magnetic order	10
1.3 Energetics of ferromagnets and antiferromagnets	15
1.4 Emergence of magnetic domains and domain walls	20
2 Manipulation of magnetic order	25
2.1 Landau-Lifshitz-Gilbert equation	25
2.2 Manipulation by magnetic field	27
2.3 Spin transfer torque	30
2.4 Spin-orbit torque	36
2.5 Domain wall motion	42
3 Detection of magnetic order	49
3.1 Magneto-optics	50
3.2 Magnetotransport effects	58
4 Studied materials	63
4.1 (Ga,Mn)As and (Ga,Mn)(As,P)	63
4.2 Fe/GaAs	64
4.3 Mn ₃ Sn	65
4.4 CuMnAs	67
5 Voigt effect-based MO microscope integrated in a pump-probe setup	69
5.1 Description of the experimental setup	70
5.2 Verification of the Voigt effect-related microscope sensitivity	73
5.3 Investigation of a piezo-induced strain inhomogeneity	77
5.4 Conclusion and outlook	80
6 Inertial domain wall motion driven by the optical spin transfer torque	83
6.1 Experimental geometry and elastic DW pinning	84
6.2 Inertial DW motion driven by circularly polarized laser pulses	88
6.3 Exclusion of helicity-dependent heating effects	91
6.4 Conclusion	95
7 Ultrafast current pulses in a vertical (anti)ferromagnet-photodiode heterostructure	97
7.1 The device structure and characterization of the photocurrent pulses	98
7.2 Current pulse-induced dynamics of Fe magnetization	103
7.3 Photocurrent pulses in PIN/CuMnAs structure	108
7.4 Conclusion	110

8 Imaging and writing of magnetic domains in a non-collinear antiferromagnet	113
8.1 Scanning thermal gradient microscopy	114
8.2 Imaging of the AF domain structure of Mn ₃ Sn	116
8.3 Heat-assisted writing of domains	120
8.4 Comparison to magneto-optical imaging	122
8.5 Conclusion	123
9 Imaging and manipulation of domain structure in a compensated collinear antiferromagnet	125
9.1 The magneto-thermoelectric imaging method and its verification	126
9.2 Imaging of a reversible current-induced switching	128
9.3 Magnetic anisotropy evaluation via transverse magneto-Seebeck effect	133
9.4 Conclusion	135
Conclusion	137
Bibliography	141
List of Figures	155
List of Abbreviations	157
List of Symbols	159
List of publications	163
Appendices	165
A From single electron to solid	165
B STT at a normal-metal/ferromagnet interface	166
C Derivation of current-induced STTs on magnetization	167
D Magnetic anisotropy of the studied Fe/GaAs epilayer	168
E The effect of strain on the magnetic energy density of (Ga,Mn)As	170
F Elastic DW expansion, geometrical pinning, and Hall detection of a DW position	171

Introduction

i Preface

Magnetic properties of materials have been exploited for centuries in various applications. These usually relied on the utilization of the macroscopic stray fields emanating from magnetic bodies. At the beginning of the 20th century quantum physics revealed the microscopic origin of magnetism being related to spin, a purely quantum-mechanical property of elementary particles. For a long time, however, this fact didn't play an important role in the applications still dominantly based on manipulation and detection of macroscopic magnetic elements via magnetic fields. The situation has changed with the discovery of phenomena in which the behavior of individual spins plays a crucial role, such as the giant magnetoresistance [1]. Its utilization in hard-disk drives and magnetic random access memories proved the application potential of spin in information technologies and helped to establish a new research field - the spin electronics or *spintronics* [2, 3].

The development of spintronics has been accelerated by the recent enormous expansion of microelectronics. The semiconductor (CMOS) technology has gone through an astonishing improvement benefiting from the development of nanofabrication processes. However, the ultimate speed-up and downscaling of the electronic devices has brought the technology to its physical limits [4]. The operation frequency saturated already more than a decade ago at ≈ 3 GHz limited by the vast amount of heat generated by shifting the charge forth and back in the billions of nano-elements. The increasing number of transistors per chip (increasing density), following the famous Moore's law, thus remained the only way to significantly increase the device performance. However, with the < 10 nm feature-size in the current chips there is very little space for further improvement.

Utilization of electron spin instead of (or together with) its charge is considered as a promising way forward. Spin, unlike charge, is a purely quantum vectorial property which brings in new unprecedented phenomena and functionalities. The focus of spintronics is to utilize these effects to enable a new class of devices for information processing and storage with superior parameters in terms of processing frequency, energy consumption, non-volatility or radiation hardness. Spin has many favorable properties which allow to reach this goal. It can be manipulated without the charge transport thus allowing for much more energy efficient operation and consequently much higher processing frequencies. Spin-based solid-state memories [5] are intrinsically non-volatile and radiation-hard, unlike the current 'on-chip' fast memories. Using the same technology for nonvolatile information storage and processing would allow for their close integration in a single chip thus eliminating the energy- and time-demanding conversion between the electronic and magnetic technology. Moreover, spin as a quantum property can represent not only the digital information but could be also used to realize quantum computing.

Until recently, spintronic research has been carried out mainly in ferromagnetic materials or ferromagnet/non-magnet heterostructures, where spin has been injected from the ferromagnet into the non-magnet. Ferromagnets (FMs) are already used in many applications and they can be relatively easily imaged or manipulated thanks to their non-zero macroscopic magnetization. On the other hand, the net magnetization generates long-range dipolar fields which complicate the high density integration of such devices. Information stored in FM bits can be also destroyed when exposed to relatively weak external magnetic fields. Recently, an increasing attention has been paid to

antiferromagnetic (AF) materials [6–8], in which the direction of spin alternates at the atomic scale such that the net magnetization is zero. This makes the magnetic order invisible on the outside and gives antiferromagnets some very appealing properties for spintronic applications. The absence of magnetic stray fields allows for high integration density of AF memory bits. The stored information is secure against magnetic scanners and robust against external magnetic fields of the order of ~ 10 T. The exchange-field enhanced spin-dynamics [9] allows for ultrafast information manipulation with the theoretical limit in THz range – typically 2-3 orders of magnitude faster than in FMs. The highly reproducible multilevel resistance switching (memristor behavior) observed in some AFs [10,11] is favorable for realization of synaptic elements for artificial neuromorphic networks combining memory and logic functions [7]. Last but not least, AFs are also more abundant in nature than ferromagnetic materials. A broad range of metals and, unlike ferromagnets, also (topological) insulators, semiconductors and semimetals with robust antiferromagnetic order well above room temperature is available. Nevertheless, the same favorable properties which make AFs interesting make them also more difficult to study or control. Many of the imaging techniques require non-zero magnetization or thick samples. Imaging of thin AF films, which are of particular interest for spintronics, is especially challenging. Similarly, the external or locally generated magnetic fields, commonly used to manipulate FMs, are not applicable in case of AFs. In order to efficiently couple to an antiferromagnet the magnetic field would have to alternate its direction at the atomic scale following the staggered Néel spin order. Generating such a field has been regarded unfeasible hindering the research and applications of AFs. This has changed with the understanding that relativistic spintronic effects based on spin-orbit coupling (SOC) can generate an effective magnetic field with the desired locally alternating direction when sending a global electrical current through the antiferromagnet [12]. Such staggered field can manipulate AFs as easily as a uniform magnetic field can manipulate FMs. This idea was proved in a compensated collinear AF CuMnAs [10] together with a purely electrical readout of the AF state via another SOC-based effect – anisotropic magnetoresistance. Altogether this opens a route towards the antiferromagnetic memory and logic devices with the described superior properties operated by the highly scalable electrical means.

ii Thesis aims and outline

For successful utilization of magnetically ordered materials in spintronic applications it is important to study the properties of their domain structure – magnetic domains and domain walls (DWs) – and its response to various excitations. The domain structure can significantly affect the device performance. Moreover, magnetic domains or DWs themselves may become the central functional elements of the technology being used to encode information in memory [13] or logic [14] devices. Imaging and investigation of magnetic domain structure and its dynamics is therefore important to assess the utility of the material for spintronics. **The aim of this thesis is, therefore, to develop methods for ultrafast manipulation of magnetic nanostructures (in particular magnetic domains and domain walls) and for their detection (imaging). Having in mind the high application potential of antiferromagnetic materials we focus on methods which are, apart from ferromagnets, also applicable to antiferromagnets, especially to thin antiferromagnetic films, which are of particular interest for construction of spintronic devices.**

In the first part of the thesis we give a theoretical background related to the research presented in the experimental part of the work. Despite being a bit lengthy, we believe

that the explanation originating from the elementary building blocks of magnetism with minimum necessary inputs from external literature may be beneficial, especially when the thesis is used as an introductory material for students, as usually done in our department. The aim of the theoretical part is to provide a solid background so that the thesis is useful also for readers who are not necessarily experts in the field.

In chapter 1 we first show how spin derives from the relativistic quantum theory and we describe its basic properties and interactions. Subsequently, we introduce different types of magnetic order and explain how it arises from the quantum mechanical exchange interaction between the spins. We continue by introducing the additional interactions that contribute to the total magnetic energy of a FM or AF sample and we show how a magnetic domain structure and domain walls arise from their competition. In chapter 2 we focus on the response of magnetic order to nonequilibrium conditions. We describe the different means of manipulation of magnetic states – via external magnetic fields, current-induced spin transfer and spin-orbit torques and their optical counterparts. Finally, we discuss the particular case of a DW propagation, induced by both the magnetic fields and electric currents. Chapter 3 is devoted to detection methods which can be used to image the magnetic state of a sample. Special attention is paid to techniques which allow for detection of the AF order. Among these, we focus on easily accessible, table-top techniques – magneto-optics and magneto-transport – and we describe the underlying effects on a phenomenological level. In chapter 4 we briefly describe the basic properties of the materials studied in this work – GaMnAs(P), Fe, Mn₃Sn, and CuMnAs.

The obtained experimental results are divided in 5 chapters corresponding to the separate experimental studies performed in different materials. In chapter 5 we aim to develop a versatile optical setup for studying spin textures with simultaneous high spatial and temporal resolutions by combining the wide-field magneto-optical microscopy and the pump-probe optical technique into one instrument. The setup performance is tested on GaMnAs samples utilizing the second-order magneto-optical effects, which allow in principle also to detect an AF order. In chapter 6 we study the optically driven DW motion in a closely related material, GaMnAsP. The ultrashort circularly polarized laser pulses absorbed by a DW transfer their spin angular momentum to the local magnetization thus inducing the wall motion in a direction depending on the light polarization. From our results we conclude that the DW motion has an inertial character allowing the DW to move on macroscopic distances long after the excitation pulse is gone. In chapter 7 we develop and characterize a device based on an optical PIN-diode design which allows for a simple generation of ultrashort (~ 10 ps) electrical pulses exciting a magnetic film grown on top of the diode. Such short pulses are necessary for investigation of the ultrafast THz-scale AF dynamics. The last two chapters focus on developing techniques for imaging and manipulation of AF domain structures. We study both a non-collinear AF (Mn₃Sn, chapter 8) and a collinear AF (CuMnAs, chapter 9) which are very different regarding the material symmetries and, consequently, the relevant phenomena which are sensitive to their AF order. To image the AF domains we scan the sample surface with a localized laser-induced thermal gradient and detect a global thermoelectric response. Despite the experiments in the collinear AF CuMnAs were performed first, the interpretation of the signal due to anisotropic magneto-Seebeck effect (AMSE) has been less intuitive compared to the thermoelectric imaging of Mn₃Sn based on the anomalous Nernst effect (ANE). To introduce our new thermal scanning method we, therefore, present the local ANE measurements on Mn₃Sn films first, followed by the AMSE measurements on CuMnAs which require a more complex data analysis. Besides the imaging, we demonstrate in Mn₃Sn a heat-assisted writing of defined AF domain patterns using moderate magnetic fields. Manipulation of the AF

domains in CuMnAs is achieved by spin-orbit torque pulses and for higher current amplitudes we observe a domain shattering into a nano-fragmented state.

iii Main publication outputs and author's contribution

By the date of the thesis submission, the experimental results presented in this work have been or are about to be published in 5 scientific papers (3 papers already published, 1 accepted, and 1 in preparation), namely

- T. Janda, P. E. Roy, R. M. Otxoa, Z. Šobáň, A. Ramsay, A. C. Irvine, F. Trojánek, M. Surýnek, R. P. Campion, B. L. Gallagher, P. Němec, T. Jungwirth, and J. Wunderlich. Inertial displacement of a domain wall excited by ultra-short circularly polarized laser pulses. *Nature Communications* **8**, 15226 (2017).
- H. Reichlova, T. Janda, J. Godinho, A. Markou, D. Kriegner, R. Schlitz, J. Zelezny, Z. Soban, M. Bejarano, H. Schultheiss, P. Nemeč, T. Jungwirth, C. Felser, J. Wunderlich, and S. T. B. Goennenwein. Imaging and writing magnetic domains in the non-collinear antiferromagnet Mn₃Sn. *Nature Communications* **10**, 5459 (2019).
- T. Janda, L. Nádvorník, J. Kuchařík, D. Butkovičová, E. Schmoranzzerová, F. Trojánek, and P. Němec. Voigt effect-based wide-field magneto-optical microscope integrated in a pump-probe experimental setup. *Review of Scientific Instruments* **89**, 073703 (2018).
- T. Janda, J. Godinho, T. Ostatnický, E. Pfitzner, G. Ulrich, A. Hoehl, S. Reimers, Z. Šobáň, T. Metzger, H. Reichlová, V. Novák, R. P. Campion, J. Heberle, P. Wadley, K. W. Edmonds, O. J. Amin, J. S. Chauhan, S. S. Dhesi, F. Maccherozzi, R. M. Otxoa, P. E. Roy, K. Olejník, P. Němec, T. Jungwirth, B. Kaestner, and J. Wunderlich. Magneto-Seebeck microscopy of domain switching in collinear antiferromagnet CuMnAs. *accepted in Physical Review Materials*.
- T. Janda, T. Ostatnický, P. Němec, R. P. Campion, V. Hills, Z. Šobáň, and J. Wunderlich. Spin-polarized ultrafast current pulses in a vertical ferromagnet-photodiode heterostructure. *in preparation*.

The author of this thesis constructed the wide-field magneto-optical and scanning magneto-thermoelectric imaging setups and performed all far-field optical, magneto-optical, and magneto-thermoelectric measurements presented in these publications. The author processed the measured data, participated in their interpretation, and contributed to preparation of the manuscripts.

Besides the aforementioned papers, these results have been presented by the author at 4 international conferences (one invited talk, 2 contributed talks, and 1 poster presentation). Furthermore, during his Ph.D. study, T. Janda contributed to another 6 experimental studies published in peer-reviewed journals.

1. Spin and magnetic order

Magnetism of solids is closely connected to the angular momentum of elementary particles from which they consist. As the magnetic moment is inversely proportional to the particle mass, we can usually neglect the magnetic moments of atomic nuclei. The main source of magnetic moments are electrons. The angular momentum of electron has two contributions – the orbital motion of electron around nucleus and an intrinsic angular momentum called *spin*. Spin has nothing to do with any mechanical motion. It is an internal degree of freedom of electron (and other elementary particles) which is introduced by quantum mechanics. As spin is the central object of spintronics we will first look how it arises from quantum theory and describe its basic properties including the spin-orbit coupling which is the origin of many of the effects discussed in this thesis. Subsequently, we describe how different types of magnetic ordering arise from the mutual interaction between the individual spins. Besides the exchange coupling, which is responsible for the magnetic order, there are also other effects, arising from the spin-orbit and Zeeman interactions, which may not prefer the uniform spin alignment. As a result of competition of all these interactions, the magnetic configurations of macroscopic samples may become rather complex and difficult to predict. Investigation of these spin textures, which allows to understand the magnetic properties of the studied material and which is of great importance also for practical applications, is the main focus of this thesis.

1.1 Spin and magnetic moment

The existence of spin was indicated by the Stern-Gerlach experiment in 1922 where a ray of silver atoms was split in two when passing through an inhomogeneous magnetic field [15]. The even number of beams was in contradiction with the quantization of orbital angular momentum having always an odd number of possible projections to the field direction that are equal to integer multiples of \hbar , the reduced Planck constant. Later the same result was obtained for hydrogen atoms in the ground state having zero orbital momentum [16] thus proving that electron possesses an additional intrinsic angular momentum with only two possible half-integer projections of $\pm\hbar/2$ corresponding to the “spin-up” and “spin-down” states. A year later Paul Dirac showed that the existence of spin is a natural consequence of incorporating Einstein’s special relativity into quantum mechanics [17].

The Dirac relativistic equation of motion for a particle with an electrical charge q and a rest mass m_0 in an electromagnetic field described by vector and scalar potentials \mathbf{A} and ϕ , respectively, reads [18]

$$i\hbar\frac{\partial\psi(\mathbf{r},t)}{\partial t} = (c\boldsymbol{\alpha} \cdot (\hat{\mathbf{p}} - q\mathbf{A}) + \mathbb{1}q\phi + \beta m_0 c^2)\psi(\mathbf{r},t), \quad (1.1)$$

where $\hat{\mathbf{p}} = -i\hbar\nabla$ is the momentum operator, $\boldsymbol{\alpha} = \begin{pmatrix} \mathbb{0} & \boldsymbol{\sigma} \\ \boldsymbol{\sigma} & \mathbb{0} \end{pmatrix}$, $\beta = \begin{pmatrix} \mathbb{1} & \mathbb{0} \\ \mathbb{0} & -\mathbb{1} \end{pmatrix}$, $\mathbb{0}$ and $\mathbb{1}$ are 2×2 zero and unity matrices, $\boldsymbol{\sigma}$ is the vector of Pauli matrices and c is the speed of light. The state of the particle is represented by a 4-component wavefunction ψ which describes its internal degrees of freedom. The wavefunction can be split into two 2-component parts $\psi = \begin{pmatrix} \psi_+ \\ \psi_- \end{pmatrix}$ where ψ_+ and ψ_- in non-relativistic limit correspond to the solution in form of a particle and an antiparticle, respectively.

The existence of spin can be easily shown in the non-relativistic approximation of

(1.1), called Pauli equation [18], which for electron ($q = -e$, $m_0 = m_e$) reads

$$i\hbar \frac{\partial \psi_+}{\partial t} = \left(\frac{1}{2m_e} (\hat{\mathbf{p}} + e\mathbf{A})^2 + \mu_B \boldsymbol{\sigma} \cdot \mathbf{B} - e\phi + m_e c^2 \right) \psi_+, \quad (1.2)$$

where $\mathbf{B} = \nabla \times \mathbf{A}$ is the magnetic field corresponding to \mathbf{A} and $\mu_B = \frac{e\hbar}{2m_e}$ is Bohr magneton. Let's first examine the first term on the right hand side with $\mathbf{A} = \frac{B}{2}(-y, x, 0)$ describing a constant magnetic field along z -axis. For weak fields we get [18]

$$\frac{1}{2m_e} (-i\hbar \nabla + e\mathbf{A})^2 \approx -\frac{\hbar^2 \Delta}{2m_e} - \frac{ie\hbar \mathbf{A} \nabla}{m_e} = -\frac{\hbar^2 \Delta}{2m_e} + \frac{e}{2m_e} \hat{l}_z B, \quad (1.3)$$

where \hat{l}_z is the z -component of the angular momentum operator $\hat{\mathbf{l}} = \hat{\mathbf{r}} \times \hat{\mathbf{p}}$. We can use Bohr model to calculate the magnetic moment associated with $\hat{\mathbf{l}}$, i.e., with the orbital motion of electron around nucleus [19]

$$\hat{\mathbf{m}}_l = \frac{1}{2} \oint \mathbf{r} \times I d\mathbf{l} = -\frac{1}{2} e \mathbf{r} \times \mathbf{v} = -\frac{e}{2m_e} \hat{\mathbf{l}} = -g \mu_B \frac{\hat{\mathbf{l}}}{\hbar}. \quad (1.4)$$

Here \mathbf{v} is the orbital velocity of electron, I is the corresponding current, and the integral is running along the current loop. Factor g represents the ratio between the magnetic moment in units of μ_B and the angular momentum in units of \hbar (here $g = 1$). The last term in (1.3) now can be rewritten as

$$E_l = \frac{e}{2m_e} \hat{\mathbf{l}} \cdot \mathbf{B} = -\hat{\mathbf{m}}_l \cdot \mathbf{B}. \quad (1.5)$$

and obviously describes the energy of a magnetic dipole generated by the orbital motion of electron in an external magnetic field. This contribution is called *Zeeman energy*.

The second term in Pauli equation, $\mu_B \hat{\boldsymbol{\sigma}} \cdot \mathbf{B}$, has the same Zeeman form, therefore we can interpret it as energy of an additional intrinsic magnetic moment of electron which we express, in analogy to (1.4), as

$$\hat{\mathbf{m}}_s = -\mu_B \hat{\boldsymbol{\sigma}} = -g \mu_B \frac{\hat{\mathbf{s}}}{\hbar}, \quad (1.6)$$

where we introduce the spin operator $\hat{\mathbf{s}}$. The projection of electron magnetic moment to the field direction was measured to be $\pm \mu_B$ [16] which together with the separation of the two angular momentum projections by \hbar gives a g -factor of 2 for electron spin and (1.6) leads to the standard definition of spin operator

$$\hat{\mathbf{s}} = \frac{\hbar}{2} \hat{\boldsymbol{\sigma}}. \quad (1.7)$$

The Pauli matrices

$$\hat{\sigma}_x = \begin{pmatrix} 0 & 1 \\ 1 & 0 \end{pmatrix} \quad \hat{\sigma}_y = \begin{pmatrix} 0 & -i \\ i & 0 \end{pmatrix} \quad \hat{\sigma}_z = \begin{pmatrix} 1 & 0 \\ 0 & -1 \end{pmatrix} \quad (1.8)$$

together with the unity matrix $\mathbb{1}$ form a basis for the vector space of 2×2 Hermitian matrices. Hermitian operators represent physical observables, that's why the matrix formalism based on Pauli matrices is frequently used [18].

The individual components of spin \hat{s}_i do not commute so they can't be simultaneously measured. However, $\hat{\mathbf{s}}^2$ commutes with the component pointing in the quantization direction, which is usually defined by the direction of magnetic field. Therefore, these two operators have common eigenstates and sharp simultaneously measurable values (while the other two components are indeterminate). The eigenstates are in the matrix formalism represented by vectors [18]

$$|\uparrow\rangle = \begin{pmatrix} 1 \\ 0 \end{pmatrix} e^{E_\uparrow t / i\hbar} \quad |\downarrow\rangle = \begin{pmatrix} 0 \\ 1 \end{pmatrix} e^{E_\downarrow t / i\hbar} \quad (1.9)$$

called “spin-up” and “spin-down” with the corresponding values of spin projection $\hbar/2$ and $-\hbar/2$, respectively. $E_{\uparrow} = -E_{\downarrow} = \mu_B B$ is half of the Zeeman splitting. These two orthogonal states form a basis and any spin state can be expressed as their linear combination

$$|\psi\rangle = a|\uparrow\rangle + b|\downarrow\rangle, \quad (1.10)$$

where $|\langle\uparrow|\psi\rangle|^2 = |a|^2$ and $|\langle\downarrow|\psi\rangle|^2 = |b|^2$ are the probabilities of finding electron in $|\uparrow\rangle$ and $|\downarrow\rangle$ state, respectively, provided that $|\psi\rangle$ is normalized.

Spin precession. If an electron appears in a magnetic field which does not point along its magnetic moment there is a torque on the moment due to the Zeeman interaction leading to Larmor precession. This can happen, for instance, when electrons spin-polarized along \mathbf{s} are injected into a ferromagnet with magnetization $\mathbf{M} \nparallel \mathbf{s}$. In the language of quantum mechanics the injected spin state $|\psi\rangle$ is not the eigenstate of Zeeman Hamiltonian $\hat{H}_Z = \mu_B \hat{\boldsymbol{\sigma}} \cdot \mathbf{B}$, i.e., it is not a stationary state and evolves in time. The (stationary) eigenstates are given by (1.9) with spin pointing along and against the magnetic field. In their basis any spin state has the form of (1.10). For magnetic field along z and spin along x $|\psi\rangle = (|\uparrow\rangle + |\downarrow\rangle)/\sqrt{2}$ and the expectation value of magnetic moment along x is

$$\langle\hat{m}_x\rangle = \langle\psi| -\mu_B \hat{\sigma}_x |\psi\rangle = -\frac{\mu_B}{2} (\langle\uparrow|\hat{\sigma}_x|\downarrow\rangle + \langle\downarrow|\hat{\sigma}_x|\uparrow\rangle) = -\mu_B \cos \Omega t, \quad (1.11)$$

where $\Omega = 2\mu_B B/\hbar$ is the Larmor frequency. Analogously we obtain $\langle\hat{m}_y\rangle = \mu_B \sin \Omega t$ and $\langle\hat{m}_z\rangle = 0$ which corresponds to a counterclockwise precession of the magnetic moment around the applied field. This result is in agreement with classical physics where the evolution of the moment is given by the magnetic field-induced torque, $\frac{d\mathbf{m}}{dt} = -\frac{g\mu_B}{\hbar} \mathbf{m} \times \mathbf{B}$ [19]. This result can be generalized also for effective magnetic fields acting on the magnetic moment, such as magnetic anisotropy field, spin-orbit field, etc.

Spin-orbit coupling. Pauli equation (1.2), as the non-relativistic limit of the complete Dirac equation (1.1), ignores some of the most interesting spintronic effects like anisotropic magnetoresistance, spin-orbit torque, anomalous, planar, and spin Hall effects, and their thermal counterparts. These effects arise from the interaction of moving electron spin with an electric field. For a single electron the spin-orbit coupling (SOC) can be derived from (1.1) as one of the corrections to Pauli equation in the order v^2/c^2 . The SOC contribution to Hamiltonian reads [20]

$$\hat{H}_{SO} = -\frac{e}{2m_e c^2} \hat{\mathbf{s}} \cdot (\hat{\mathbf{v}} \times \mathbf{E}). \quad (1.12)$$

This result can be understood in terms of relativistic transformation of the electromagnetic field. If electron moves with velocity \mathbf{v} in electric field \mathbf{E} , this field transforms partially to a magnetic field $\mathbf{B}_{SO} = -\frac{1}{c^2}(\mathbf{v} \times \mathbf{E})$ in the electron’s rest frame. This magnetic field then acts on the spin magnetic moment of electron in order to align it with the field thus minimizing the corresponding Zeeman energy, $\hat{H}_{SO} = -\hat{\mathbf{m}}_s \cdot \mathbf{B}_{SO} = \frac{e}{m_e} \hat{\mathbf{s}} \cdot \mathbf{B}_{SO} = -\frac{e}{2m_e c^2} \hat{\mathbf{s}} \cdot (\hat{\mathbf{v}} \times \mathbf{E})$, where the additional factor of 1/2 in the last expression is due to the Thomas precession of the electron’s rest frame [21].

In radially symmetric electric field (e.g., in atoms) $\mathbf{E} = -\nabla\phi = -\frac{r}{r} \frac{d\phi}{dr}$ and we get [22]

$$\hat{H}_{SO} = -\frac{e}{2m_e c^2} \frac{1}{r} \frac{d\phi}{dr} \hat{\mathbf{s}} \cdot (\hat{\mathbf{r}} \times \hat{\mathbf{v}}) = -\frac{e}{2m_e^2 c^2} \frac{1}{r} \frac{d\phi}{dr} \hat{\mathbf{s}} \cdot \hat{\mathbf{l}}, \quad (1.13)$$

i.e., \hat{H}_{SO} represents the interaction energy of spin and orbital angular momenta of

electron. This explains the term spin-orbit coupling. In the presence of SOC $\hat{\boldsymbol{l}}$ and $\hat{\boldsymbol{s}}$ are not conserved anymore. Instead, the total angular momentum $\hat{\boldsymbol{j}} = \hat{\boldsymbol{l}} + \hat{\boldsymbol{s}}$ becomes the constant of motion. From (1.12) we see that SOC will play the strongest role in heavy elements, especially for the inner electrons, due to the strong electric field of the nucleus.

Until now we restricted ourselves to magnetic properties of a single electron. In appendix A we briefly describe how the situation changes when we move to many-electron atoms which, eventually, form a solid. We explain how the additional interactions lead to an intraatomic coupling of the electronic angular momenta and formation of the total atomic magnetic moments.

1.2 Magnetic order

Materials containing permanent magnetic moments can be divided into several categories. If the interaction between neighboring moments is weak we speak about *paramagnets*. In paramagnetic materials the atomic magnetic moments are disordered by thermal fluctuations but they tend to align in an external magnetic field giving rise to a magnetization pointing along the external field. If the coupling between the magnetic moments is strong enough they can order spontaneously. Depending on the character of the order we distinguish several material classes. In this thesis we investigate two of them – *ferromagnets* (FMs) and *antiferromagnets* (AFs). In FMs all the magnetic moments are parallel. In AFs the moments form several sublattices within which the moments are parallel but the different sublattice magnetizations are either antiparallel or adopt a more complex arrangement, both resulting in zero total magnetization. All FMs and AFs are ordered only below certain critical temperature and become paramagnetic above it.

1.2.1 Paramagnetism

Let's first consider the ground energy level of a *localized* magnetic moment split by the Zeeman interaction ($\Delta E_Z \approx 0.1 \text{ meV}$ for $B = 1 \text{ T}$). The sublevels occupation is governed by the Boltzman statistics [19]. The thermodynamic average of magnetic moment reads

$$\langle m \rangle = \frac{\sum_i m_i \exp(-E_i/k_B T)}{\sum_i \exp(-E_i/k_B T)}, \quad (1.14)$$

where the total atomic magnetic moment $\hat{\boldsymbol{m}} = -g_J \mu_B \hat{\boldsymbol{J}}/\hbar$ takes projections $m_{z_i} = -g_J \mu_B m_J$ with the corresponding energies $E_i = \mu_0 g_J \mu_B m_J H$, $m_J = -J, -J+1, \dots, J$. $H = B/\mu_0$ is the magnetic field strength and g_J is the Landé g-factor given by the L, S , and J values. For small H the sublevels are almost equally occupied and $\langle m \rangle \approx 0$. However, with increasing H (and the corresponding energy splitting) the lowest-energy state is preferentially occupied leading to nonzero magnetization $M = n \langle m \rangle$, where n is the spatial density of magnetic moments. Evaluation of (1.14) gives

$$M_z = n g_J \mu_B J \left(\frac{2J+1}{2J} \coth \frac{2J+1}{2J} x - \frac{1}{2J} \coth \frac{x}{2J} \right) = n m_0 \mathcal{B}_J(x), \quad (1.15)$$

where $m_0 = g_J \mu_B J$ is the saturated magnetic moment, $\mathcal{B}_J(x)$ is the Brillouin function, and $x = \mu_0 g_J \mu_B J H / k_B T$. An important quantity describing the response of a magnetic material to an external magnetic field is the magnetic susceptibility $\chi = M/H$ given by the initial slope of the magnetization curve (1.15)

$$\chi = \frac{M}{H} = \frac{\mu_0 n g_J^2 \mu_B^2 J(J+1)}{3 k_B T} = \frac{C}{T}, \quad (1.16)$$

where μ_0 is the magnetic permeability of vacuum and C is the Curie constant. This is the famous Curie law of paramagnetism [19].

In materials where the electrons responsible for magnetism are *delocalized* the energy levels split to broad bands characterized by the density of states $\mathcal{D}(E) \sim \sqrt{E}$. In an external magnetic field the spin-up and spin-down bands shift by $E_Z = \pm\mu_0\mu_B H$. The surplus of electrons in the lower-lying spin-subband is $n^\uparrow - n^\downarrow \approx \mathcal{D}(E_F)\mu_B\mu_0 H$, where E_F is the Fermi energy. The corresponding magnetization is $M = (n^\uparrow - n^\downarrow)\mu_B$, hence the paramagnetic (Pauli) susceptibility reads [19]

$$\chi_P = \frac{M}{H} = \mu_0\mu_B^2\mathcal{D}(E_F). \quad (1.17)$$

χ_P is temperature independent and about two orders of magnitude smaller than Curie susceptibility (1.16) at room temperature as only the electrons close to E_F respond to the changes of external magnetic field and temperature.

1.2.2 Molecular field theory

Ferromagnets In FMs magnetic moments spontaneously align below a critical temperature even in an absence of any external magnetic field giving rise to a spontaneous magnetization the magnitude of which is, to first approximation, independent of external magnetic field. This spontaneous alignment was originally explained in terms of a huge internal magnetic field which is proportional to the magnetization. This is the central idea of Weiss's molecular field theory [19]. Later it turned out that no such field in reality exists and that the spin alignment arises from quantum mechanical exchange interaction. Nevertheless, Weiss's model remains useful for understanding the basic properties of magnetically ordered materials.

Now we can use the results derived above for paramagnets where the external magnetic field \mathbf{H} has to be replaced by the total internal field $\mathbf{H}^i = \mathbf{H} + \mathbf{H}_W = \mathbf{H} + n_W\mathbf{M}$. Here \mathbf{H}_W is the Weiss's molecular field and the proportionality factor $n_W \approx 10^2 - 10^3$. The magnetization is given by (1.15) where now $x = \mu_0 g_J \mu_B J(H + n_W M)/k_B T$. In zero external magnetic field we get from (1.15) for the spontaneous magnetization M_s

$$\frac{M_s}{M_0} = \mathcal{B}_J(x_0), \quad (1.18)$$

where $M_0 = nm_0$ is the saturation magnetization and $x_0 = \mu_0 m_0 n_W M_s / k_B T$. The expression for x_0 can be rearranged to $M_s/M_0 = (nk_B T / \mu_0 M_0^2 n_W) x_0$ which can be rewritten using the definition of the Curie constant (1.16) as

$$\frac{M_s}{M_0} = \frac{J+1}{3J} \frac{T}{C n_W} x_0. \quad (1.19)$$

The simultaneous solution of equations (1.18) and (1.19) is shown in Fig. 1.1 for different magnitudes of the total angular momentum J [19].

When approaching to the critical temperature T_C , $x_0 \sim M_s \rightarrow 0$ and $\mathcal{B}_J(x_0) \approx x_0(J+1)/3J$. This combined with (1.18) and (1.19) gives $T_C = C n_W$ which is the Curie temperature at which the ferromagnet reversibly loses the spontaneous alignment. Above T_C the magnetic moments are disordered and the material behaves like a paramagnet. From $M/M_0 = \mathcal{B}_J(x)$ in small- x limit we get after a straightforward algebra the paramagnetic susceptibility

$$\chi = \frac{M}{H} = \frac{C}{T - T_C}. \quad (1.20)$$

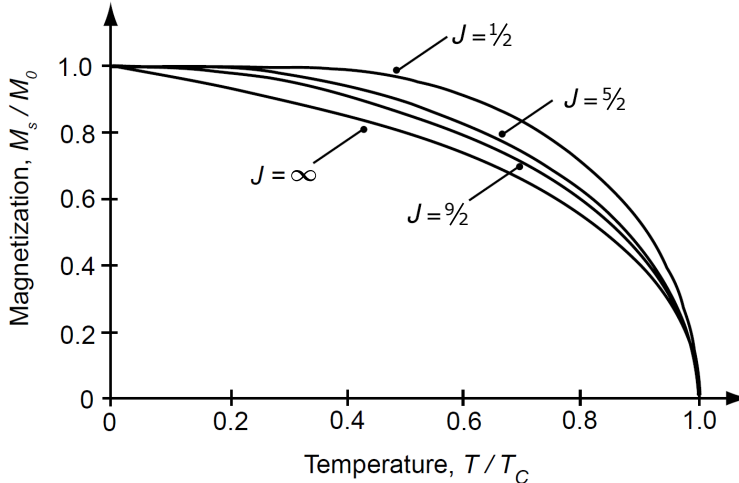


Figure 1.1: Temperature dependence of spontaneous magnetization. Temperature dependence of the spontaneous magnetization M_s in a ferromagnet for different magnitudes of the underlying magnetic moments described by the quantum number J of the total atomic angular momentum. The case of $J = \infty$ corresponds to classical macroscopic moments, e.g., ferromagnetic nanoparticles. [19]

The idea of molecular field can be applied also to delocalized electrons [19]. The internal field can be again expressed as $\mathbf{H}^i = \mathbf{H} + n_S \mathbf{M}$. The Pauli susceptibility in the internal field is $\chi_P = M/(H + n_S M)$ and, therefore, the response to the external field gives

$$\chi = \frac{M}{H} = \frac{\chi_P}{1 - n_S \chi_P}. \quad (1.21)$$

The susceptibility is enhanced by n_S and diverges for $n_S \chi_P \rightarrow 1$ when the spontaneous order is established. This condition can be rephrased in form of Stoner criterion

$$\mathcal{I} \mathcal{N}_{\uparrow, \downarrow}(E_F) > 1, \quad (1.22)$$

where $\mathcal{N}_{\uparrow, \downarrow}(E) = \mathcal{D}(E)/2n$ is the density of states per atom for one spin state and $\mathcal{I} \approx 1$ eV for 3d metals. The metals which meet (1.22) become spontaneously ferromagnetic. Among 3d elements this is the case only for Fe, Co, and Ni.

Antiferromagnets The molecular field theory can be also applied to AFs. For two antiparallel sublattices A and B ($\mathbf{M}_A = -\mathbf{M}_B$) the internal fields $\mathbf{H}_{A,B}^i = \mathbf{H} - n_W \mathbf{M}_{B,A}$, where $n_W > 0$ stands for the antiferromagnetic intersublattice coupling (we neglect the FM intrasublattice coupling) [19]. The spontaneous magnetization of each sublattice follows the Brillouin curve $|\mathbf{M}_{A,B}|(T)$ shown in Fig. 1.1 with T_C replaced by Néel temperature T_N .

Above T_N , in the paramagnetic state we can use the Curie law with the internal fields

$$\mathbf{M}_{A,B} = \chi \mathbf{H}_{A,B}^i = (C/2T)(\mathbf{H} - n_W \mathbf{M}_{B,A}). \quad (1.23)$$

The condition for appearance of a spontaneous AF order at T_N is a non-zero magnetization $\mathbf{M}_{A,B} = -\mathbf{M}_{B,A}$ in zero external field H which inserted in (1.23) yields the Néel temperature

$$T_N = C n_W / 2 \quad (1.24)$$

and adding of equations (1.23) gives the susceptibility

$$\chi = \frac{M_A + M_B}{H} = \frac{C}{T + T_N} \quad (1.25)$$

which does not diverge because the effect of external field is always opposed by the AF coupling.

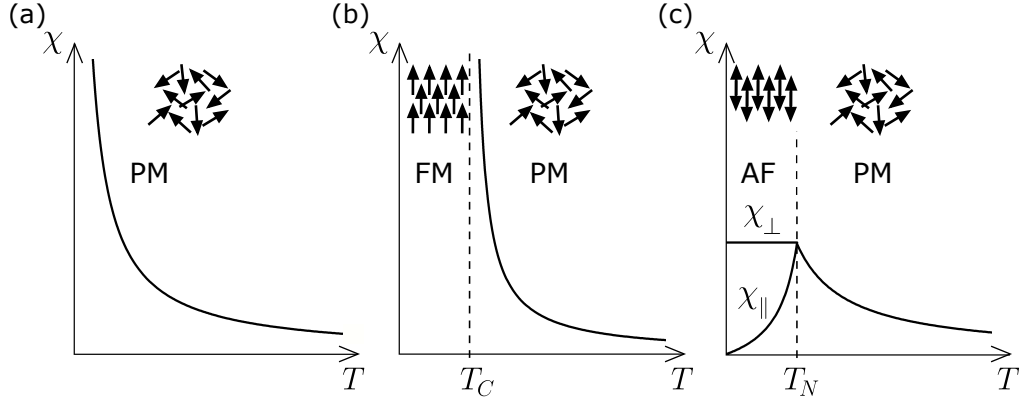


Figure 1.2: Magnetic susceptibilities of different magnetic materials. Response of different magnetic materials to external magnetic field illustrated by the magnetic susceptibility χ : (a) paramagnet (PM), (b) ferromagnet (FM), (c) antiferromagnet (AF). Both FM and AF become PM above critical temperature T_C (T_N).

Below T_N we have to distinguish whether the field is applied along or perpendicular to the antiferromagnetic vector $\mathbf{L} = \mathbf{M}_A - \mathbf{M}_B$ [19]. In the former case the susceptibility can be expressed in the same form as the paramagnetic one, $\chi_{\parallel} = C_{\parallel}/(T + n_W C_{\parallel}/2)$, where $C_{\parallel} = C[3J/(J+1)]\partial\mathcal{B}_J/\partial x|_{x_0}$. The response of the saturated sublattices is zero ($\chi_{\parallel} \rightarrow 0$ for $T \rightarrow 0$). With increasing temperature the alignment is disturbed by thermal fluctuations and χ_{\parallel} increases, finally reaching the paramagnetic value $1/n_W$ at T_N . When \mathbf{H} is applied perpendicularly to \mathbf{L} the sublattices tilt towards the field direction. The susceptibility $\chi_{\perp} = 1/n_W$ is temperature independent. The response of paramagnets, FMs, and AFs to the external magnetic field is illustrated in Fig. 1.2.

Since $\chi_{\perp} > \chi_{\parallel}$, \mathbf{L} should always rotate perpendicular to the applied field. If the field is applied along a direction which is preferred by the magnetic moments (e.g., due to magnetic anisotropy) the competition between these two preferences leads at certain field strength to *spin-flop*, a transition to 90° rotated canted configuration.

1.2.3 Exchange interaction

Despite being able to explain the basic properties of magnetically ordered materials, the idea of global molecular field of ≈ 100 T strength aligning the magnetic moments is not correct. Instead, the long-range magnetic order is caused by a local electrostatic interaction between nearby electrons in conjunction with the Pauli exclusion principle [19]. The Pauli principle, which applies to all fermions (particles with half-integer spin), says that two electrons can't be simultaneously in the same quantum state. In other words, two electrons in the same position in space have to have opposite spin, or, electrons with the same spin avoid each other. Since the electrostatic potential energy decreases with increasing distance between the electrons, the configuration with parallel spins is energetically more favorable. Within an electron shell of an atom this leads to the first Hund's rule, i.e., filling first all the different orbitals with one particular spin ('maximize S ') which minimizes the spatial overlap of the electronic charge and the corresponding energy.

Let's consider two electrons with the same spin in states $\phi_1(\mathbf{r}_1)$ and $\phi_2(\mathbf{r}_2)$ where the total wavefunction of the system is $\Phi(\mathbf{r}_1, \mathbf{r}_2) \sim \phi_1(\mathbf{r}_1)\phi_2(\mathbf{r}_2)$. Since the electrons are indistinguishable, the charge density $-e|\Phi|^2$ must not change when we exchange their position, i.e., $|\Phi(\mathbf{r}_1, \mathbf{r}_2)| = |\Phi(\mathbf{r}_2, \mathbf{r}_1)|$. Because of the Pauli principle the probability of finding the electrons in the same place has to be zero $|\Phi(\mathbf{r}_1, \mathbf{r}_1)| = 0$. These two conditions are satisfied by an antisymmetric function Φ_A . The spin part of the wavefunction is symmetric spin triplet $|1\rangle$ ($S = 1$) so the total wavefunction $\Psi_I = \Phi_A|1\rangle$ is antisymmetric. Another totally antisymmetric solution we get for electrons with opposite spins described by antisymmetric spin singlet $|0\rangle$ ($S = 0$) and symmetric spatial wavefunction, $\Psi_{II} = \Phi_S|0\rangle$. The spatial parts of the two solutions are [23]

$$\Phi_{A,S} = (1/\sqrt{2})[\phi_1(\mathbf{r}_1)\phi_2(\mathbf{r}_2) \mp \phi_1(\mathbf{r}_2)\phi_2(\mathbf{r}_1)]. \quad (1.26)$$

As already mentioned, the Coulomb interaction energy is smaller in the case of aligned spins, $E_I < E_{II}$, where

$$E_{I,II} = \langle \Psi_{I,II} | \hat{H} | \Psi_{I,II} \rangle = \int \Phi_{A,S}^* \frac{e^2}{4\pi\epsilon_0|\mathbf{r}_1 - \mathbf{r}_2|} \Phi_{A,S} d\mathbf{r}_1 d\mathbf{r}_2 = \Delta \mp \mathcal{J} \quad (1.27)$$

$$\mathcal{J} = \int \phi_1^*(\mathbf{r}_1)\phi_2^*(\mathbf{r}_2) \frac{e^2}{4\pi\epsilon_0|\mathbf{r}_1 - \mathbf{r}_2|} \phi_1(\mathbf{r}_2)\phi_2(\mathbf{r}_1) d\mathbf{r}_1 d\mathbf{r}_2. \quad (1.28)$$

Here Δ is a constant energy offset and \mathcal{J} is called *exchange integral* as it contains two states with exchanged positions of the electrons. It can be easily shown that replacing the Coulomb Hamiltonian by $\hat{H} = (1/4)(E_{II} + 3E_I) - (E_{II} - E_I)\hat{\mathbf{S}}_1 \cdot \hat{\mathbf{S}}_2$, where $\hat{\mathbf{S}}_1$ and $\hat{\mathbf{S}}_2$ are dimensionless spin operators of the individual electrons, gives the correct expectation values $E_{I,II}$ in states $\Psi_{I,II}$ [23]. We can omit the first term and keep only the spin-dependent part which, using (1.27), gives the exchange Hamiltonian

$$\hat{H}_{ex} = -2\mathcal{J}\hat{\mathbf{S}}_1 \cdot \hat{\mathbf{S}}_2. \quad (1.29)$$

For $\mathcal{J} > 0$ the spins tend to align parallel which is the case of the mentioned intraatomic interaction inside the electron shell. For the interaction of two electrons on neighboring atoms the opposite ($\mathcal{J} < 0$) is often true. Electrons with opposite spins can spread their wavefunctions further towards the neighbor. The reduced localization leads, thanks to the uncertainty principle for position and momentum $\Delta x \Delta p \geq \hbar/2$, to reduced kinetic energy [18].

The direct exchange interaction between two magnetic atoms requires extended electron orbitals which is the case of $3d$ metals. For a roughly half-filled d-shell the AF coupling is preferred since the spin-up electron from one atom can only spread its wavefunction if the neighboring atom has empty spin-up orbitals, i.e., if the neighboring atom has spin-down. On the other hand, for almost empty or almost filled d-shell the electrons can extend to empty orbitals with the same spin on the neighboring atom which results in FM coupling. This roughly explains why Cr and Mn are AFs, while Fe, Co, and Ni are FMs [19].

In systems where the electrons responsible for magnetism are more localized or in diluted magnetic systems the magnetic order is explained by some kind of mediated exchange interaction [19]. In metals the exchange between localized spins is mediated via delocalized conduction (usually s-) electrons which is described by *s-d* model. The isolated magnetic moment polarizes the nearby conduction electrons (parallel or antiparallel to it), which in turn polarize other isolated moments leading to long-range FM order. A similar effect is considered in systems where the magnetic atoms are far from each other, diluted in nonmagnetic host lattice. The magnetic impurity polarizes

the delocalized electrons (or holes) which transmit the interaction to the other magnetic atoms. This leads to effective coupling between the localized moments, which can have both FM or AF character. This kind of indirect coupling is known as the Zener's *kinetic-exchange* or the RKKY interaction [24] and takes place for instance in the case of the diluted FM semiconductors (Ga,Mn)As and (Ga,Mn)(As,P) which will be studied in chapters 5 and 6, respectively.

Up to now we only considered parallel FM or antiparallel AF order as a result of the exchange coupling. If the magnetic moments are arranged in triangles where each of them experiences the same AF exchange coupling to the other two, they will not create a collinear spin texture. If two moments in the triangle are antiparallel the third one will be frustrated as both possible orientations it can choose will make one couple unsatisfied (parallel). Instead, the spins will prefer a noncollinear arrangement where the frustration is equally distributed among all three moments and the net magnetization is zero. In chapter 8 we investigate a representative of these noncollinear AFs, Mn_3Sn .

1.3 Energetics of ferromagnets and antiferromagnets

The energy associated with a magnetic order has two main sources – the short-range electrostatic and long-range magnetostatic interactions. The former include exchange and crystal-field effects. The latter are associated with an energy of the net magnetization in a magnetic field and, therefore, are not present in AFs. The variety of different energy contributions in combination with the general principle of energy minimization is the root of many interesting magnetic phenomena including the existence of complex magnetic microstructures like magnetic domains, domain walls, or skyrmions.

1.3.1 Magnetization and magnetic fields

We have shown that FMs and AFs contain one or more magnetic sublattices with a parallel alignment of magnetic moments. We can ascribe each sublattice α the magnetization \mathbf{M}_α which is the magnetic moment density in a volume V , $\mathbf{M}_\alpha = \sum_V \mathbf{m}_\alpha / V$ and the net magnetization $\mathbf{M} = \sum_\alpha \mathbf{M}_\alpha$. Since we want to describe magnetic microstructures, V is a nanometer-scale volume and \mathbf{M}_α are averaged over a microsecond time-scale to average out the fluctuations of the microscopic moments. The distribution of individual magnetic moments is replaced by the magnetization $\mathbf{M}(\mathbf{r})$, smoothly varying on a mesoscopic scale, which is called the *continuous medium approximation* [19].

Magnetic field can be generated either by electrical currents or by magnetized ($\mathbf{M} \neq 0$) bodies. In the former case the field is obtained using the Biot-Savart law. The latter case can be transformed to the former one. According to Ampère, magnetized body can be replaced in the calculation by an equivalent distribution of currents generating the same magnetic field. In particular, magnetic field \mathbf{B} of a single magnetic moment \mathbf{m} is the same as that of a tiny current loop, which expressed in polar coordinates reads [19]

$$B_r = 2 \frac{\mu_0 m}{4\pi r^3} \cos \theta; \quad B_\theta = \frac{\mu_0 m}{4\pi r^3} \sin \theta; \quad B_\phi = 0. \quad (1.30)$$

where the relation between the moment size and the corresponding current is $m = IA$, with A being the loop area, as follows from (1.4). The field (1.30) shown in Fig. 1.3(a) has the same form as that of an electric dipole $\mathbf{p} = q\delta\mathbf{l}$. That's why, magnetic moment is also called *magnetic dipole*. An electric dipole consists of two individual charges $\pm q$ separated by δl . In analogy, magnetic charges (monopoles) can be also introduced. The total magnetic field generated by a given distribution $\mathbf{M}(\mathbf{r})$ can be calculated by a

direct integration over the dipolar fields (1.30) of the mesoscopic elements $\mathbf{M}(\mathbf{r})dV$ or, sometimes much easier, as the field generated by the equivalent distribution of virtual currents or charges. These, however, do not exist in reality and the magnetic moments arising from quantum mechanics are the real building blocks of magnetism in materials.

The non-existence of magnetic charges is expressed by one of the Maxwell's equations, $\nabla \cdot \mathbf{B} = 0$, which says that \mathbf{B} is divergenceless, i.e., it has no sources or sinks and the field lines are closed loops. The relation between a magnetic field and its cause, a current density \mathbf{j} , is expressed by another Maxwell's equation $\nabla \times \mathbf{B} = \mu_0 \mathbf{j}$.

In the presence of magnetized material we have to take into account that \mathbf{j} consists of the real charge currents \mathbf{j}_c and the virtual Ampère's currents \mathbf{j}_m associated with the magnetization \mathbf{M} of the medium. However, \mathbf{j}_m is not a measurable quantity. It can be shown that $\mathbf{j}_m = \nabla \times \mathbf{M}$ [19]. Therefore, it is useful to introduce an auxiliary magnetic field

$$\mathbf{H} = \mathbf{B}/\mu_0 - \mathbf{M} \quad (1.31)$$

for which the relation $\nabla \times \mathbf{H} = \mathbf{j}_c$ contains only the real conduction currents.

The \mathbf{H} -field is not anymore divergenceless, $\nabla \cdot \mathbf{H} = -\nabla \cdot \mathbf{M}$. In general case when both conduction currents and magnetized bodies are present we can split the \mathbf{H} -field to two separate contributions: \mathbf{H}_c generated by the currents and \mathbf{H}_m generated by the magnetization. These two fields have very different properties. \mathbf{H}_c behaves like \mathbf{B} ($\nabla \cdot \mathbf{H}_c = 0$, $\nabla \times \mathbf{H}_c = \mathbf{j}_c$) and is called *solenoidal* field because of the closed-loop field lines. \mathbf{H}_m behaves like electric field \mathbf{E} ($\nabla \cdot \mathbf{H}_m = -\nabla \cdot \mathbf{M}$, $\nabla \times \mathbf{H}_m = 0$) and is called *conservative* field [19]. In analogy to electric field ($\nabla \cdot \mathbf{E} = \rho/\epsilon_0$) we can define the fictitious magnetic charge-density $\rho_m = -\nabla \cdot \mathbf{M}$ which is the virtual source (sink) of \mathbf{H}_m . In other words, the \mathbf{H}_m -field emanates from places with nonuniform magnetization. This is shown in Fig. 1.3 where we compare the distribution of \mathbf{H}_m , \mathbf{M} , and \mathbf{B} in a uniformly magnetized block of material in the absence of any external magnetic field. \mathbf{B} is continuous whereas the discontinuity of \mathbf{H}_m is caused by the surface magnetic charges of density $\pm M$ resulting from the discontinuity of \mathbf{M} . The magnetic charges are associated with a large energy and thus unwanted which is referred to as the *charge avoidance principle*. This leads to a breakup of the uniform magnetization to magnetic domains as will be discussed later.

Demagnetizing field Outside the magnet \mathbf{H}_m and \mathbf{B} have the same distribution ($\mathbf{B} = \mu_0 \mathbf{H}_m$). This outer field is called *stray field*. Inside the magnet \mathbf{H}_m has the opposite direction to \mathbf{M} which generates it. That's why within the volume of the magnet \mathbf{H}_m is called *demagnetizing field*, \mathbf{H}_d .

It turns out that in a uniformly magnetized body having the shape of an ellipsoid \mathbf{H}_d is also uniform and given by [19]

$$\mathbf{H}_d = -\mathcal{N}\mathbf{M}, \quad (1.32)$$

where \mathcal{N} is the demagnetizing tensor represented by a symmetric 3×3 matrix. For \mathbf{M} pointing along one of the principal axes of the ellipsoid, \mathcal{N} has a diagonal form $(\mathcal{N}_x, \mathcal{N}_y, \mathcal{N}_z)$ and $\mathbf{H}_d \parallel \mathbf{M}$. Moreover, only two of the diagonal elements are independent as $\sum_i \mathcal{N}_i = 1$. In this thesis we only investigate thin magnetic films which represent a limit of an ellipsoid with one finite and two infinite dimensions. In such case we can find \mathcal{N}_i just by the symmetry. For a film in the xy -plane, $\mathcal{N} = (0, 0, 1)$.

1.3.2 Demagnetizing and Zeeman energy

The magnetization $\mathbf{M}(\mathbf{r})$ responds to the local magnetic field $\mathbf{H}(\mathbf{r})$ inside the magnet which consists of the external applied field and the demagnetizing field created by the

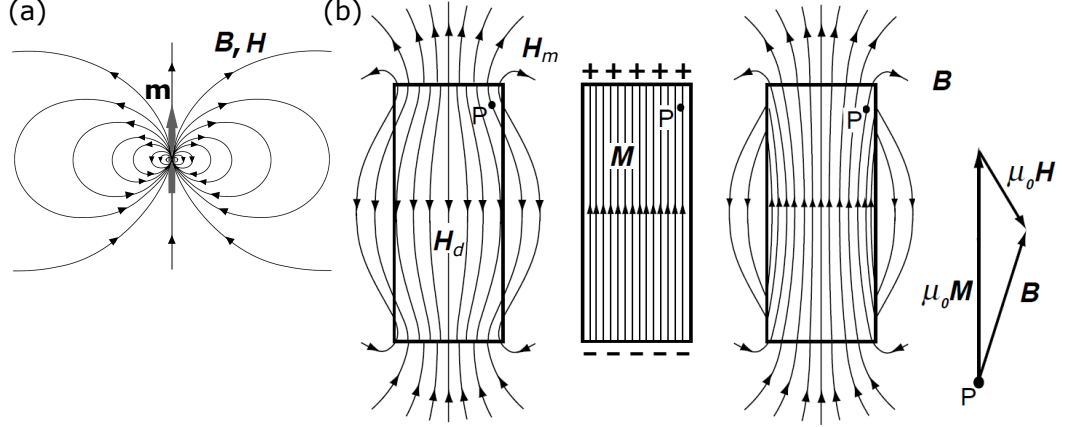


Figure 1.3: Relations between magnetization and magnetic fields. (a) Dipolar magnetic field generated by a single magnetic moment m . (b) Distribution of magnetic fields generated by a uniformly magnetized body. Field lines of B are closed loops whereas H_m emanates from the fictitious charges associated with the discontinuous magnetization at the top and bottom surface. The relation between the three vectors is shown in point P inside the magnet where H_m pointing against M and B is called demagnetizing field H_d [19].

magnetization itself, $H = H_{ext} + H_d$. We will evaluate the interaction energy of the magnet with the external and the demagnetizing field separately.

Demagnetizing energy To calculate the self-energy of the magnetized body in its own demagnetizing field let's consider a spherical mesoscopic spatial element having the moment $M(\mathbf{r})dV$ inside the magnet. According to (1.5), its energy in the local field H_{loc} is $E_{loc} = -\mu_0 M \cdot H_{loc} dV$. The local field can be expressed as $H_{loc} = H_d + M/3$, where the demagnetizing field of the whole body is reduced by the demagnetizing field of the spherical cavity in which the element dV resides [19]. The integration over the whole magnet yields the total interaction energy

$$E = -\frac{\mu_0}{2} \int_V M \cdot H_d dV - \frac{\mu_0}{6} \int_V M^2 dV, \quad (1.33)$$

where the factor $1/2$ is to prevent the double counting as each element $M(\mathbf{r})dV$ contributes both as a magnetic moment and as a source of the demagnetizing field. The second integral removes the self-interaction of the element with itself which would act to reduce the local magnetization, but is much weaker than the exchange interaction which acts to align the moments (increase M). In other words, we expect M only to change direction within the magnet, but the size is constant and equal to the spontaneous magnetization M_s , thanks to exchange. Then the second term is independent of the distribution $M(\mathbf{r})$ and we omit it in the following. The local demagnetizing energy density then reads

$$\epsilon_d = -\frac{1}{2} \mu_0 M \cdot H_d. \quad (1.34)$$

Zeeman energy The energy of a magnetized body in an external magnetic field H_{ext} is obtained as a sum of all the elementary contributions (1.5) from the mesoscopic moments $M(\mathbf{r})dV$. The total Zeeman energy E_Z and the local energy density ϵ_Z read

$$E_Z = -\mu_0 \int_V M \cdot H_{ext} dV, \quad \epsilon_Z = -\mu_0 M \cdot H_{ext}. \quad (1.35)$$

1.3.3 Magnetic anisotropy energy

Magnetic anisotropy means the tendency of the magnetic moments to lie along certain directions in the material, so-called easy axes (EAs). This preference arises from the particular arrangement of atoms in the crystal lattice and its symmetry and as such is present both in FMs and AFs. We distinguish the intrinsic *magnetocrystalline* anisotropy which reflects the symmetry of the ideal crystal lattice and the extrinsic anisotropies induced by the applied stress or surface effects. The effect of the demagnetizing field in FMs, described in the previous section, is sometimes also called the *shape* anisotropy as it prefers certain magnetization axis depending on the sample shape. Magnetic anisotropy is temperature-dependent and has to vanish at the magnetic ordering temperature (T_C or T_N) [19]. The different contributions to the total magnetic anisotropy usually have different temperature dependencies which can be utilized to control the EAs' positions or to excite magnetization dynamics [25].

The crystal symmetry is imprinted in the magnetocrystalline anisotropy by the interaction of the magnetic atom with the surrounding crystal-field (single-ion anisotropy) and by the long-range interaction with the dipolar fields of the other magnetic atoms in the lattice (two-ion anisotropy) [19].

Single-ion anisotropy The essence of the crystal-field effect is that the electrons in the magnetic atom tend to occupy certain orbitals with an appropriate symmetry to minimize the interaction energy with the crystal-field. The spin-orbit coupling then leads to the magnetic moment orientation in certain crystallographic direction.

The energy of the electrostatic interaction between the charge density $\rho_0(\mathbf{r})$ of the electrons responsible for magnetism and the surrounding charge represented by the crystal-field potential $\varphi_{CF}(\mathbf{r})$ is $E_a = \int \rho_0(\mathbf{r})\varphi_{CF}(\mathbf{r})d^3r$. Both ρ_0 and φ_{CF} have certain angular symmetries and can be expanded to series in terms of spherical harmonics Y_l^m . This is called the multipole expansion. The interaction energy becomes a series [19]

$$E_a = \sum_{l=0,2,4,\dots} \sum_{m=-n,\dots,n} \kappa_l^m A_l^m Y_l^m(\theta, \phi), \quad (1.36)$$

where κ_l^m and A_l^m are constants associated with the charge density distribution of the magnetic atom and with the symmetry of the crystal environment, respectively. Usually it is enough to keep only the first few terms in the series which describe the major symmetry features of the charge distributions.

Two-ion anisotropy Another contribution to the magnetocrystalline anisotropy arises from the anisotropic nature of the dipole-dipole interaction. The interaction energy of two parallel magnetic dipoles is $E_{dip} = -\mathbf{m}_1 \cdot \mathbf{B}_{21}$, where \mathbf{B}_{21} is the dipolar field (1.30) generated by the dipole \mathbf{m}_2 at the position of the dipole \mathbf{m}_1 . The energy is minimized when the two dipoles point along the line connecting them (head to tail configuration). The total dipolar field acting on a single magnetic moment in a magnetic crystal is given by the sum of the dipolar fields from all the other dipoles and can be expressed as $\mathbf{H}_{dip} = f_{dip}\mathbf{M}$ [19]. In general, f_{dip} is a tensor which depends on the structure of the crystal lattice. Consequently, the interaction energy of \mathbf{M} with \mathbf{H}_{dip} depends on the orientation of \mathbf{M} with respect to the crystal axes. In cubic crystals $f_{dip} = 0$ from symmetry but in other structures the dipole-dipole interaction may be a significant source of magnetic anisotropy.

We will discuss the particular magnetic anisotropies of the materials studied in this thesis in the respective chapters. Here we only give the leading terms of the anisotropy

energy density for the most relevant cubic (ϵ_c) and uniaxial (ϵ_u) anisotropies [26]

$$\epsilon_c = \frac{K_c}{4}(\sin^2 2\phi \sin^4 \theta + \sin^2 2\theta) \quad (1.37)$$

$$\epsilon_u = K_u \sin^2 \vartheta, \quad (1.38)$$

where θ and ϕ are the polar and azimuthal angles of magnetization measured from the [001] and [100] crystallographic directions of the cubic crystal lattice, respectively, and ϑ is the deviation of \mathbf{M} from the EA of the uniaxial system. K_c and K_u are the lowest-order cubic and uniaxial anisotropy constants. For $K_c > 0$ the EAs coincide with the $\langle 100 \rangle$ axes of the cubic lattice, whereas for $K_c < 0$ they become the hard axes (energy maxima) and $\langle 111 \rangle$ become the EAs. It is useful to express the anisotropy energy in terms of an effective anisotropy field H_a which is defined as the external magnetic field necessary to saturate the magnetization along the hard direction and is given as $H_a = 2K_a/\mu_0 M_s$, where $a = c, u$ and M_s is the spontaneous magnetization.

Induced anisotropies Thin magnetic films, which are studied in this thesis, have to be grown on some substrate. This leads to additional contributions to the magnetic anisotropy given by the lattice constant mismatch between the film and substrate [27] or by the symmetry-breaking effects on the surface of the magnetic layer [27,28]. Moreover, magnetic anisotropy can be modified by an intentional application of mechanical stress via a piezo-electric transducer [29], as we do in chapter 5, by patterning, etc.

The strain-induced modification of magnetic anisotropy can be qualitatively understood (in the case of the single-ion anisotropy) as a consequence of the crystal-field modification caused by the lattice distortion. The change of the interatomic distance has also effect on the two-ion anisotropy. The surface anisotropies arise from the fact that the crystal environment in which the surface magnetic atoms reside is very different from that inside the magnetic crystal. The surface anisotropies play a crucial role in very thin (few nm) layers [28].

1.3.4 Exchange energy

The exchange interaction forces the magnetic moments to be parallel (in FMs) or to keep some other alignment, e.g., antiparallel (in collinear AFs) or more complex one. Any deviation from this arrangement will impose an energy penalty expressed in terms of a gradient of the respective order parameter. The local exchange energy density is derived by a Taylor expansion of the Heisenberg exchange Hamiltonian (1.29) which yields for a FM [23]

$$\epsilon_x = (A/M_s^2)[(\nabla M_x)^2 + (\nabla M_y)^2 + (\nabla M_z)^2], \quad (1.39)$$

where A is the exchange stiffness constant, which relates to the exchange integral (1.28) as $A \approx 2\mathcal{J}S^2z/a_0$. Here, S is the atomic spin, z is the number of atoms per unit cell, and a_0 is the lattice parameter. The total exchange energy is obtained simply by an integration over the sample volume. Expressed in polar coordinates where $M_x = M_s \sin \theta \cos \phi$, $M_y = M_s \sin \theta \sin \phi$, and $M_z = M_s \cos \theta$, (1.39) becomes

$$\epsilon_x = A[(\nabla \theta)^2 + \sin^2 \theta (\nabla \phi)^2]. \quad (1.40)$$

In an equilibrium single-domain case the exchange energy can be ignored. It becomes important whenever the spin alignment is violated, for instance, by the existence of magnetic domain walls or by excitation of the magnetic order, e.g., via a spin-torque. The exchange energy plays an important role especially in the dynamics of AFs where it is responsible for the THz resonant frequencies.

1.4 Emergence of magnetic domains and domain walls

The domain idea was a consequence of the observation that some materials showing zero net magnetization in zero magnetic field can achieve the saturation magnetization ($\mu_0 M \approx 1 \text{ T}$) by applying only a tiny field (as low as 10^{-6} T). Such field would have negligible effect on a paramagnet. The explanation is that it is a FM which consists of regions, so-called *domains*, within which the magnetic moments are parallel but the magnetizations of the different domains can point in different directions, thus averaging out in a macroscopic sample. The strong response to the external magnetic field is given by the fact that the field does not have to order the individual moments but only to align the domains which can be done by an energy-efficient domain-wall motion.

The reason for the emergence of magnetic domains is basically the large demagnetizing energy (1.34) associated with a uniformly magnetized body. The general tendency to minimize the total free energy of the magnet usually leads to the breakup of the uniform magnetization into domains. This may lead to an increase of other energy contributions, like exchange or anisotropy. The equilibrium domain structure is, therefore, a result of the competition of the different energy terms and depends on the intrinsic material properties (exchange and anisotropy constants), extrinsic factors (sample shape, size, applied magnetic field), as well as on the history of the sample.

When looking for the magnetic configuration which minimizes or eliminates the demagnetizing energy it is useful to use the concept of magnetic charges as a sources of the H -field [19]. The charge density is $\rho_m = -\nabla \cdot \mathbf{M}$ which becomes $\mathbf{M} \cdot \mathbf{n}$ at a surface of the body (\mathbf{n} being the unit surface normal), i.e., any point at a surface of a magnet where \mathbf{M} is not parallel to the surface is a source of external stray field and internal demagnetizing field \mathbf{H}_d . In the bulk \mathbf{H}_d may emanate from the boundaries between the domains, so-called *domain walls* (DWs). The procedure to reduce the magnetic charges and eventually eliminate them is shown in Fig. 1.4. The large demagnetizing energy is first reduced by splitting to smaller domains and completely removed by the 90° rotated *closure* domains. In the final configuration there are no magnetic charges as $\mathbf{M} \perp \mathbf{n}$ at the surface and $-\nabla \cdot \mathbf{M} = 0$ in each DW and, therefore, $\mathbf{H}(\mathbf{r}) = 0$ everywhere.

So far we didn't take into account the magnetic anisotropy. The domain structure in Fig. 1.4 (c) with 90° DWs would be compatible with a cubic anisotropy having EAs along $\langle 100 \rangle$ directions. In any case, the very existence of domain walls violates both the exchange and magnetic anisotropy. The energy cost associated with creating DWs prevents the sample from breaking into too small domains.

1.4.1 Magnetic domain walls

The exchange penalty associated with a domain wall can be easily evaluated using (1.29) [23]. Two spins making a small angle θ have their exchange interaction energy higher by $\Delta E_x \approx \mathcal{J}S^2\theta^2$ compared to the parallel configuration. For a DW between two antiparallel domains the spin rotates by 180° over N atomic sites. Hence, $\theta = \pi/N$ and the energy cost for such chain of spins is $E_x = \mathcal{J}S^2\pi^2/N$. A planar wall contains $1/a_0^2$ such chains per unit area and the energy density associated with the domain wall is $\sigma_x = \mathcal{J}S^2\pi^2/Na_0^2$.

The exchange penalty obviously vanish for $N \rightarrow \infty$. The reason why the DW does not unwind itself to minimize the exchange energy is the opposing magnetic anisotropy. The magnetization has to rotate out of the easy direction inside a DW which costs an additional energy. For the uniaxial anisotropy (1.38) the anisotropy energy penalty for one chain of spins is $E_a = a_0^3 \sum_{i=1}^N K_u \sin^2 \theta_i \approx (Na_0^3/\pi) \int_0^\pi K_u \sin^2 \theta d\theta = NK_u a_0^3/2$ which, unlike exchange, prefers thin DWs [23]. The total areal energy density associated

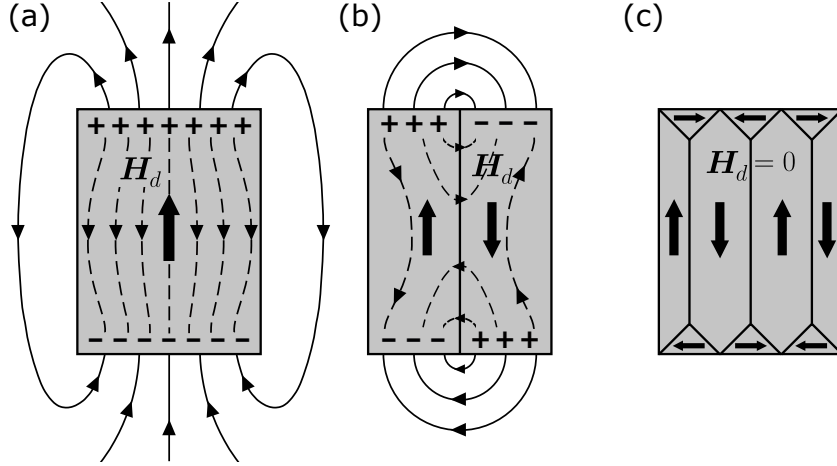


Figure 1.4: Formation of magnetic domain structure. The uniform magnetization configuration is associated with a large demagnetizing energy (a). The magnetic field emanates from the fictitious magnetic charges. The charges of the same sign tend to avoid each other. Splitting to smaller domains reduces the demagnetizing field (b). Closure domains with 90° rotated magnetization completely eliminate all charges and the associated demagnetizing energy (c).

with a DW reads

$$\sigma_{DW} = \frac{\mathcal{J}S^2\pi^2}{Na_0^2} + \frac{NK_u a_0}{2}. \quad (1.41)$$

The fact that we can associate a surface energy density with a DW means that the DW behaves like a soap membrane trying always to minimize its surface under given circumstances. This elastic behavior, which is discussed in more detail in appendix F, is the key property which enabled us to observe the effects of a DW inertia in the experiments of chapter 6.

The equilibrium DW width is given by minimizing the total DW energy density, i.e., by solving equation $d\sigma_{DW}/dN = 0$ which yields the DW width δ_{DW} and the corresponding energy density σ_{DW}

$$\delta_{DW} = a_0 N_{eq} = \pi S \sqrt{2\mathcal{J}/K_u a_0} = \pi \sqrt{A/K_u}; \quad \sigma_{DW} = \pi \sqrt{AK_u}. \quad (1.42)$$

We distinguish two basic types of DWs - the *Bloch* wall in which the magnetization rotates in a plane parallel to the plane of the wall and the *Néel* wall in which the magnetization rotates in a plane perpendicular to the plane of the wall [19, 26], as shown in Fig. 1.5. The remarkable property of the Bloch wall is that the rotation of \mathbf{M} inside the wall does not produce any magnetic charges. Indeed, for a DW in the yz -plane $\rho_m = -\nabla \cdot \mathbf{M} = -\partial M_x / \partial x = 0$ as $M_x = 0$ everywhere. On the other hand, for the Néel wall $M_x = M_s \sin(\pi x / \delta_{DW})$ and the resulting charge density is $\rho_m = -(\pi M_s / \delta_{DW}) \cos(\pi x / \delta_{DW})$. Therefore, in the bulk the Bloch wall is usually preferred. On the other hand, in thin films, where \mathbf{M} usually lies in the film plane in order to reduce the demagnetizing energy (as in Fig. 1.5), the out-of-plane rotation of \mathbf{M} in a Bloch wall is energy costly and the Néel wall is preferred.

As explained above, the domain structure and properties of DWs depend mainly on three energy terms: demagnetizing, exchange, and anisotropy energy. Since the exchange usually does not differ so much among different materials, the key properties are the magnetic anisotropy and the sample shape and size.

The uniaxial anisotropy constant in different materials spans over many orders of magnitude. The low-anisotropy materials are usually called magnetically *soft* and

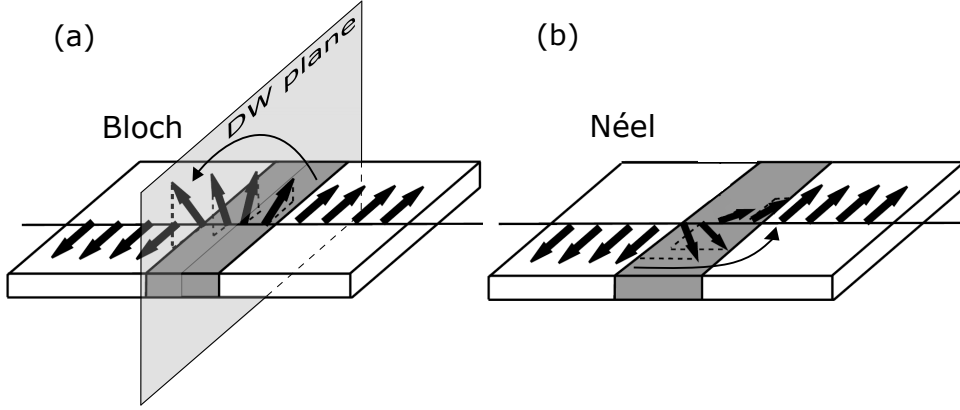


Figure 1.5: Internal structure of magnetic domain walls. The two basic types of DWs - (a) the Bloch wall where the magnetization rotates in the DW plane and (b) the Néel wall where the magnetization rotates in the plane perpendicular to the DW plane [19].

have large magnetic susceptibility (are easy to magnetize), wide DWs, and in zero external magnetic field are in multidomain demagnetized state [23]. An example of such material is permalloy ($\text{Ni}_{80}\text{Fe}_{20}$) with $K_u = 0.15 \text{ kJ m}^{-3}$, $\delta_{DW} = 2 \mu\text{m}$, and $\sigma_{DW} = 10 \mu\text{J m}^{-2}$ [19]. The opposite extreme are the magnetically *hard* materials with large magnetic anisotropy and thin DWs such as $\text{Nd}_2\text{Fe}_{14}\text{B}$ or SmCo_5 ($K_u = 17.2 \text{ MJ m}^{-3}$, $\delta_{DW} = 2.6 \text{ nm}$, and $\sigma_{DW} = 57.5 \text{ mJ m}^{-2}$) [19]. These materials are hard to magnetize or demagnetize, i.e., they tend to stay in a uniformly magnetized state even in zero external magnetic field and, therefore, are used as permanent magnets.

The energy penalty associated with the existence of DWs prevents their formation in very small FM particles where the demagnetizing energy associated with a uniform magnetization state is lower than the energy of a multidomain state. The critical size below which the particle remains single-domain is $r_{SD} \approx 9\sigma_{DW}/\mu_0 M_s^2$ which gives, e.g., for CoPt: $r_{SD} \approx 300 \text{ nm}$ [23].

In this thesis we are interested in thin film samples. In an infinite film with an in-plane magnetic anisotropy there is no demagnetizing field and, therefore, no energy gain from splitting into domains. If the film has an out-of-plane magnetic anisotropy the magnetization stays in a single-domain state provided that the anisotropy field is larger than the demagnetizing field, i.e., $K_u > \mu_0 M_s^2/2$, when any small deviation of \mathbf{M} from the out-of-plane direction increases energy. This condition is fulfilled for materials with strong magnetic anisotropy or small magnetization which is the case of the diluted magnetic semiconductor GaMnAsP studied in chapter 6. In reality the thin-film samples are not infinite and contain defects which can be understood as local perturbations of the free energy density. These imperfections play the key role in the process of magnetization switching because they serve as nucleation centers for magnetic domains. Therefore, the switching of real thin films usually proceeds through multidomain states.

1.4.2 Domain structure in antiferromagnets

As we have just shown, the existence of a domain structure in ferromagnets is promoted by the demagnetizing field. The extra energy associated with DWs is balanced by the decrease of the demagnetizing energy in a multidomain state. In antiferromagnets the situation is very different. In zero external magnetic field, compensated AFs have zero net magnetization and, therefore, no demagnetizing fields. Despite this, in many AFs the existence of a domain structure was confirmed. Its origin is, however, more

complicated and less understood.

The domain walls in AFs are governed by the same physical principles as in FMs. The rotation of antiferromagnetically ordered spins in the boundary between two domains violates the exchange which tends to unwind the wall but is opposed by the magnetic anisotropy. The DW width and internal structure are established in order to minimize its energy cost which is, nevertheless, nonzero.

There are different mechanisms believed to be responsible for a stable domain structure in AFs in the absence of a demagnetizing field. The presence of DWs may be thermodynamically favored thanks to the increased entropy [30,31]. As the DWs are not stabilized by the demagnetizing fields they can wander a bit around their equilibrium positions driven by the thermal fluctuations. This increases the entropy S associated with the wall which decreases the free energy F . The change of the free energy by introducing a DW is $\Delta F = A\sigma_{DW} - T\Delta S$, where A is the DW area. This mechanism can stabilize the multidomain state ($\Delta F < 0$) provided that the DW energy is low enough, i.e., in the case of a weak magnetic anisotropy ($\sigma_{DW} \sim \sqrt{K_a}$).

It turns out that in AFs magneto-elastic interactions play an important role. The difference between the bulk and surface magneto-elastic strains produced at T_N during the phase transition into the AF state generates virtual “incompatibility elastic charges” [32] which have an analogous effect to the magnetic charges producing the demagnetizing field in FMs. The minimization of the corresponding energy leads to the formation of AF domains. Moreover, in real AFs containing lattice defects the domain structure established at T_N is also stabilized by these imperfections which pin the DWs down.

Apart from compensated AFs there also exist AF materials where the magnetic moments are slightly canted because of additional interactions, having a small ferromagnetic moment ($M \neq 0$). These AFs are known as *weak ferromagnets* [30] and their domain structure is usually governed, as in FMs, by the demagnetizing field, although it’s weak.

2. Manipulation of magnetic order

In the previous chapter we discussed the basic properties of materials where a spontaneous magnetic order appears as a consequence of the quantum-mechanical exchange interaction. The uniform magnetic state preferred by the exchange is, on the other hand, disfavored by the long-range magnetostatic or magnetoelastic interactions. The *equilibrium* magnetic configuration, which balances the different counteracting interactions, corresponds to a local or the absolute minimum of the total free energy of the magnetic body.

In this chapter we describe the response of the magnetic order to *non-equilibrium* conditions when a nonzero torque acts on the magnetization exerted either by a classical magnetic field or by effective fields originating from spin transport between different parts of the sample or from spin-orbit interaction. The main effects resulting from these excitations include the magnetization precession, switching, and DW motion.

We start with the Landau-Lifshitz-Gilbert equation which describes the magnetization dynamics in general, irrespective of the nature of the excitation source - magnetic field, electrical current, or electromagnetic radiation. We follow with a description of the magnetic field-induced magnetization switching employing the simple Stoner-Wolfarth model which is useful in thin-film samples and we also mention how this simple view is affected by sample imperfections. Subsequently, we introduce the physics of the current-induced spin transfer torque and spin-orbit torque and their optical counterparts. The common feature of these phenomena is that a non-equilibrium spin density is created within a magnetically ordered material, either by injection from an external source or directly in the magnet via the spin-orbit coupling, which is misaligned with the local magnetization and exerts a torque on it via the exchange coupling. Finally, we show how the magnetic field and the spin-torque effects can induce a DW motion and we describe the basic properties of the DW dynamics.

2.1 Landau-Lifshitz-Gilbert equation

Dynamics of ferromagnets The total free energy of a sample consists of several contributions described in section 1.3. A static magnetization configuration corresponds to a local free energy minimum in the configuration space. When the conditions change, e.g., when the magnitude or direction of the external magnetic field changes, the energy landscape in the configuration space changes as well and the magnetization changes direction in order to find the new energy minimum. The new equilibrium is a result of a new balance found between the various energy contributions in the changed conditions. This complicated behaviour can be described in terms of a local effective magnetic field \mathbf{H}_{eff} acting on the magnetization in every point of the sample. The total free energy density can be written simply as $\epsilon_{tot} = \epsilon_d + \epsilon_Z + \epsilon_a + \epsilon_x = -\mu_0 \mathbf{M} \cdot \mathbf{H}_{eff}$. If the magnetization makes an angle ϑ with \mathbf{H}_{eff} the equilibrium condition $\partial\epsilon_{tot}/\partial\vartheta = 0$ gives $MH_{eff} \sin\vartheta = 0$. The last expression corresponds to the cross-product of the two vectors, i.e., we conclude that the torque exerted on the magnetization by the effective field has to vanish in every point of the sample in equilibrium

$$\mathbf{M} \times \mathbf{H}_{eff} = 0 \tag{2.1}$$

and the effective field $\mathbf{H}_{eff} = -(1/\mu_0 M_s) \delta \epsilon_{tot} / \delta \mathbf{e}_M$ reads¹ [19]

$$\mathbf{H}_{eff} = \frac{2A}{\mu_0 M_s} \nabla^2 \mathbf{e}_M - \frac{1}{\mu_0 M_s} \frac{\partial \epsilon_a}{\partial \mathbf{e}_M} + \mathbf{H}_d + \mathbf{H}_{ext}, \quad (2.2)$$

where \mathbf{e}_M is the unit vector in the direction of magnetization. The first contribution arises from exchange interaction and the second from magnetic anisotropy. In the case of uniaxial anisotropy the second term corresponds to the anisotropy field, $H_u = 2K_u/\mu_0 M_s$, pointing along the EA. The same is true also in the case of cubic anisotropy for small deviations from the EAs. Equations (2.1) and (2.2) together with given boundary conditions allow to find the equilibrium magnetic configuration, which is the approach used by micromagnetic simulations.

Out of the equilibrium there is a nonzero torque on magnetization which equals to the time variation of the magnetization

$$\frac{d\mathbf{M}}{dt} = -\frac{gL\mu_B\mu_0}{\hbar} \mathbf{M} \times \mathbf{H}_{eff}, \quad (2.3)$$

which is known as the Landau-Lifshitz equation [19]. Once the magnetization is out of equilibrium this equation describes its precession around the effective field which would last forever. In reality there are processes which dissipate the energy of the precessional motion resulting in a damped precession with \mathbf{M} inclining towards the direction of \mathbf{H}_{eff} . These dissipative processes were taken into account via a phenomenological damping term by Gilbert leading to the *Landau-Lifshitz-Gilbert* (LLG) equation [19]

$$\frac{d\mathbf{M}}{dt} = -\frac{gL\mu_B\mu_0}{\hbar} \mathbf{M} \times \mathbf{H}_{eff} + \frac{\alpha}{M_s} \mathbf{M} \times \frac{d\mathbf{M}}{dt}, \quad (2.4)$$

where α is the Gilbert damping constant.

Any abrupt change in \mathbf{H}_{eff} will lead to the magnetization precession. This can be a magnetic field-pulse induced, e.g., by an ultrashort electrical current pulse [33] or an ultrafast modification of magnetic anisotropy induced by ultrashort optical pulses [34]. In the last two decades new excitation mechanisms were discovered which are based on spin-polarized itinerant electrons exerting a torque on the magnetization. The spin polarization \mathbf{s} is either delivered from an external polarizer like, e.g., a FM element [35, 36] or a circularly polarized light beam [37, 38], or created locally via relativistic SOC [39, 40]. These effects are described by additional terms in LLG of the form $\mathbf{M} \times (\mathbf{M} \times \mathbf{s})$ (antidamping-like torque) or $\mathbf{M} \times \mathbf{s}$ (field-like torque) and will be discussed later in this chapter.

Solving the LLG equation (2.4) for a given magnetic anisotropy, sample shape (demagnetizing field), and applied magnetic field yields the ferromagnetic resonance (FMR) frequency ω_{FMR} of the spatially uniform magnetization precession. This frequency can be determined experimentally by measuring the absorption of a microwave radiation which is resonantly enhanced at the frequency of the Larmor precession of the magnetic moments (FMR technique) [19]. Alternatively, the precession can be triggered by the absorption of an ultrashort laser pulse and the precessional frequency is determined from the temporal variation of the measured magneto-optical response (optical FMR) [41, 42]. The measured resonant frequency in turn allows to determine the anisotropy constants K_a , the Landé g-factor g_L , and the spontaneous magnetization M_s , which represent the fingerprints of the magnetic material.

¹Here $\frac{\delta \epsilon_{tot}}{\delta \mathbf{e}_M} = \left(\frac{\delta \epsilon_{tot}}{\delta e_{Mx}}, \frac{\delta \epsilon_{tot}}{\delta e_{My}}, \frac{\delta \epsilon_{tot}}{\delta e_{Mz}} \right)$ and δ stands for the functional derivative defined as $\frac{\delta \epsilon_{tot}}{\delta e_{Mi}} = \frac{\partial \epsilon_{tot}}{\partial e_{Mi}} - \nabla \cdot \frac{\partial \epsilon_{tot}}{\partial \nabla e_{Mi}}$, $i = x, y, z$.

The FMR frequency basically corresponds to the maximum frequency at which the magnetization can be efficiently manipulated. For the case of uniaxial anisotropy (1.38) of $\mu_0 H_u = 50$ mT, $g_L = 2$, and for zero external magnetic field, $\omega_{FMR} = g_L \mu_B \mu_0 H_u / \hbar \approx 10$ GHz. This puts an upper limit on the writing-speed of memories based on ferromagnets.

Dynamics of antiferromagnets The fundamental difference between the dynamics of FMs and AFs is that the uniform precession of AF moments naturally involves the exchange interaction between the sublattices which results in a substantial increase in the resonant frequency compared to FMs [9]. In FMs the exchange plays a role only in the case of spatially nonuniform dynamics (spin-wave resonances) [41, 43].

The dynamics of the AF moments can be described by equations having the form of (2.4) for the individual sublattice magnetizations which are coupled via the exchange interaction [44, 45]. The AF exchange is taken into account by adding the exchange field \mathbf{H}_{ex} , which has the meaning of the molecular field described in section 1.2.2, into the effective field \mathbf{H}_{eff} (2.2). For a collinear AF with two oppositely oriented sublattice magnetizations $\mathbf{M}_A = -\mathbf{M}_B$, the exchange field acting on the sublattice A (B) is $\mathbf{H}_{ex}^A = -n_W \mathbf{M}_B$ ($\mathbf{H}_{ex}^B = -n_W \mathbf{M}_A$). Any deviation of the magnetic moments from the antiparallel configuration induces a strong exchange torque which makes the AF dynamics generally more complex and faster compared to FMs. The antiferromagnetic resonance (AFMR) frequency for a simple case of a collinear AF with uniaxial magnetic anisotropy was derived in [44], $\omega_{AFMR} = (g_L \mu_B \mu_0 / \hbar) \sqrt{H_u (H_u + 2H_{ex})}$. For the exchange field of 100 T (and keeping $\mu_0 H_u = 50$ mT) the AF resonant frequency $\omega_{AFMR} \approx 1$ THz. The exchange enhancement factor $\omega_{AFMR} / \omega_{FMR} \approx \sqrt{2H_{ex} / H_u}$ makes the dynamics of AFs roughly two orders of magnitude faster compared to the anisotropy-field-driven dynamics of FMs.

The effect of moderate magnetic fields on AFs is negligible. In order to efficiently couple to the staggered magnetic order of collinear AFs the acting field has to be staggered as well, i.e., it has to alternate its direction on atomic scale following the antiparallel spin texture. The difference between the effects of staggered and non-staggered fields on AF order is explained in more detail at the end of section 2.3.1 and in Fig. 2.4. The staggered magnetic field cannot be created by external means but an effective field of these properties can be generated by spin polarized electrons exerting a torque on the AF moments [46]. The spin polarization responsible for the torque is again either delivered from an external polarizer [47] or induced locally by various SOC-related effects [12, 46, 48]. These effects will be discussed in more detail further in this chapter. The AF order can be manipulated also by ultrashort optical pulses as reviewed in [49] or utilizing the exchange-spring effect in FM-AF multilayers [50].

2.2 Manipulation by magnetic field

Magnetic fields have been used for the manipulation of magnets for centuries and still remain the most widely employed control mechanism in the technological applications based on FMs. In the previous section we described the GHz-scale dynamics of magnetization induced by changes in \mathbf{H}_{eff} , e.g., by applying an external magnetic field. In this section we discuss how the magnetization switching proceeds based on the energy considerations. We first use a simple model of magnetization reversal via coherent rotation to introduce the magnetic hysteresis. After that we follow by considering a more realistic switching process involving the effects of domain nucleation and DW motion and pinning.

2.2.1 Stoner-Wolfarth model

Very small magnetic particles as well as thin films stay in a single-domain state even in the absence of external magnetic field. The critical size below which the presence of even a single DW is energetically unfavorable is of the order of 100 nm for hard uniaxial FMs. The magnetization reversal of such particles proceeds via coherent rotation of magnetic moments which is described by the *Stoner-Wolfarth* model [19, 23, 26]. It is the simplest analytical model which exhibits hysteresis.

The total free energy density of a uniformly magnetized ellipsoid of revolution with a uniaxial anisotropy and EA along the symmetry axis is

$$\epsilon_{tot} = K_u \sin^2 \vartheta + \frac{\mu_0}{2} (\mathcal{N}\mathbf{M}) \cdot \mathbf{M} - \mu_0 \mathbf{H}_{ext} \cdot \mathbf{M}, \quad (2.5)$$

where ϑ is the deviation of \mathbf{M} from the EA. The demagnetizing tensor has a diagonal form of $\mathcal{N} = \{(1 - N)/2, (1 - N)/2, N\}$, $N \in \langle 0, 1 \rangle$, and the demagnetizing energy can be expressed in the same form (apart from a constant term) as the uniaxial magnetocrystalline anisotropy, $\epsilon_d = K_d \sin^2 \vartheta$, where $K_d = (1/4)\mu_0 M_s^2 (1 - 3N)$. When the external magnetic field is applied at an angle $\vartheta_H > 90^\circ$ and increased (slowly compared to ω_{FMR}) the magnetization will rotate following the shift of the minimum of $\epsilon_{tot}(\vartheta)$ and eventually switch (irreversibly jump to a lower energy minimum) as shown in Fig. 2.1. The energy minima are given by $d\epsilon_{tot}/d\vartheta = 0$ and $d^2\epsilon_{tot}/d\vartheta^2 > 0$ conditions and the switching occurs when $d^2\epsilon_{tot}/d\vartheta^2 = 0$.

When the magnetic field is applied along the EA ($\vartheta_H = 180^\circ$) the switching occurs when the field magnitude reaches the effective anisotropy field

$$H_c = 2 \frac{K_u + K_d}{\mu_0 M_s}. \quad (2.6)$$

H_c is known as the *coercive field* [19]. In the general case of multi-domain switching H_c is defined as the field needed to reduce the net magnetization or its projection to the field direction to zero. When applying the opposite field the switching occurs for $-H_c$ resulting in a rectangular M-H loop, so-called hysteresis loop [see Fig. 2.1(b)]. For field applied at an increasing angle with respect to the EA the coercive field decreases and the hysteresis loop becomes narrower. When the field is applied along the hard axis ($\vartheta_H = 90^\circ$) there is no hysteresis and the magnetization smoothly rotates towards the field direction.

The hysteresis loop appears in the field range where two minima of $\epsilon_{tot}(\vartheta)$ exist which are separated by an energy barrier. The existence of the barrier, i.e., the fact that the system may become stuck in an energy state which is not the global energy minimum, is the reason for the irreversible magnetic behavior [see Fig. 2.1(a)]. If the system could ‘tunnel’ through the barrier to occupy always the global minimum, the hysteresis would never exist. In larger samples, processes such as domain nucleation and DW motion allow such ‘tunneling’ at high enough fields which leads to lower coercive fields than those calculated within the Stoner-Wolfarth model [19].

The magnetization switching of perfect thin films can be also described by the Stoner-Wolfarth model. A thin film with a perpendicular magnetic anisotropy represents the $N \rightarrow 1$ limit of Eq. (2.5). In soft magnetic materials the magnetization usually lies in the film plane and the demagnetizing field is zero. The magnetization switching then proceeds via coherent rotation which is confined to the sample plane [19].

2.2.2 Effects of sample imperfections

Domain nucleation In real large enough samples the coercive field is never as large as (2.6). The reason is the presence of defects (including the sample edges) which serve

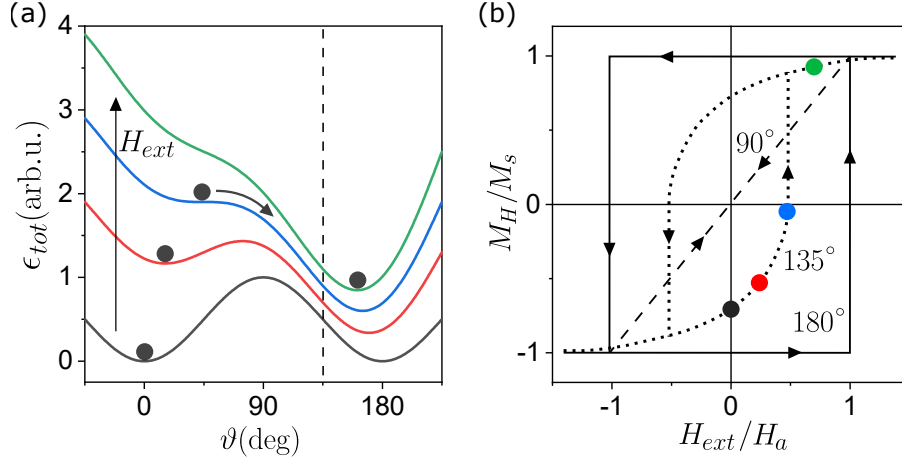


Figure 2.1: Stoner-Wolfarth model of magnetization switching. (a) The total free energy density of a magnetic particle or a thin film in an increasing external field H_{ext} applied at an angle $\vartheta_H = 135^\circ$ (dashed line). The magnetization direction (black dots) follows the local energy minimum and eventually switches to the global minimum. The curves are vertically shifted for clarity. (b) Magnetic hysteresis loops for $\vartheta_H = 90^\circ$ (hard axis), 135° , and 180° (EA). Magnetization states from (a) are indicated by dots of corresponding color. M_H is the magnetization projection to the direction of H_{ext} , $H_a = 2(K_u + K_d)/\mu_0 M_s$.

as nucleation centers for domains. In an inhomogeneous sample the energy density (2.5) becomes a function of position. The magnetic anisotropy may vary due to local strains or strain relaxation in the proximity of the defects (edges), inhomogeneities in material composition, surface properties, etc. The demagnetizing energy is also perturbed by surface asperities, e.g., by the edge roughness of thin films. If the surface variations are sharp enough the magnetization cannot accommodate by pointing always parallel to the surface and the corresponding magnetic charges are sources of strong local demagnetizing fields [19]. These local fields are oriented against the magnetization, thus making the external field needed to switch the magnetization lower [see Fig. 2.2(a)].

Instead of constant height of the energy barrier throughout the sample as in the Stoner-Wolfarth model there is a distribution of barrier heights and corresponding switching fields due to the inhomogeneity of the real sample. When a magnetic field is applied against the magnetization of a single-domain sample (e.g. a thin film) the switching first occurs in the places with lowest switching field where reverse domains are nucleated. Note, that the magnetization in such places is still exchange-coupled to the surrounding material which hinders the switching, i.e. the exchange interaction tends to smooth the magnetic inhomogeneities [19]. Once the reverse domain exceeds a critical size which is of the order of the domain wall width δ_{DW} in the material (1.42) it can grow by a DW motion driven by the Zeeman energy gain.

The nucleation process is also influenced by temperature. Thermal fluctuations allow the system to overcome energy barriers of some maximum height which scales with its thermal energy $k_B T$, thus effectively smearing out small variations of $\epsilon_{tot}(\vartheta)$. The anisotropy constants and spontaneous magnetization also decrease with increasing temperature which makes the system magnetically softer with smaller coercive field.

Domain wall pinning Once a domain is nucleated, the magnetization switching can continue via a DW motion. Since the DW energy depends on the magnetic anisotropy and exchange stiffness, $\sigma_{DW} \sim \sqrt{AK_a}$, the DW may become pinned at the sample inhomogeneities where A and K_a differ from the bulk values. Depending on whether σ_{DW} is smaller or larger in the defect it serves either as a trap or a barrier to the DW

motion. The pinning is most efficient when the defect diameter is comparable to the DW width δ_{DW} and especially for planar defects since the whole DW can lower its energy [19].

In a simple 1D case (magnetic nanowire) with one DW the energy of the magnet depends only on the position of the DW along the wire. It can be expressed as $E_{tot} = f(x) - 2\mu_0 M_s H x$, where $f(x)$ represents the varying DW energy along the inhomogeneous wire and the second term is the Zeeman energy of the two domains in the applied field [19]. For $T = 0$ the moving DW always stops in places where $dE_{tot}/dx = 0$, i.e. where $f(x)$ has a particular slope, $f'(x) = 2\mu_0 M_s H$. Increasing H shifts a bit the DW until it reaches the inflection point of E_{tot} , $f''(x) = 0$, when it gets depinned and jumps to the next pinning center with large enough slope of f . This discontinuous DW motion, known as the *Barkhausen jumps*, is illustrated in Fig. 2.2(b). Hysteresis loops of real macroscopic samples consist of many such jumps.

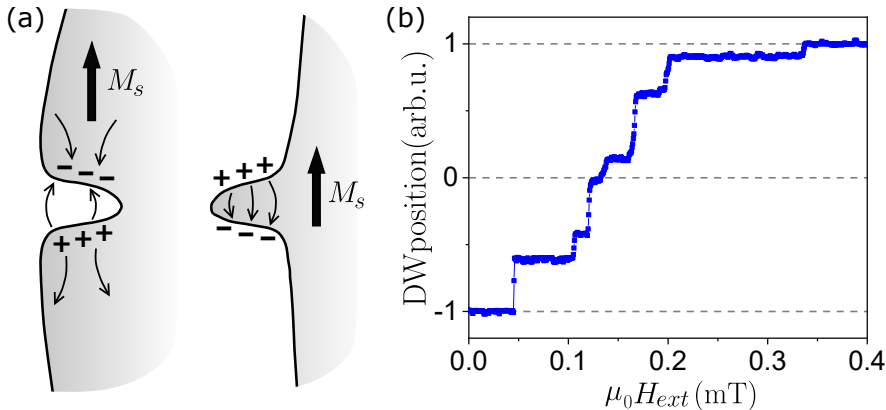


Figure 2.2: Effect of defects on magnetization switching. (a) Local demagnetizing fields (thin arrows) in the proximity of edge asperities which help nucleation of reverse domains. (b) Discontinuous DW motion (Barkhausen jumps) measured in a FM nanowire [51].

The effect of nonzero temperature is that the DW can overcome the energy barriers with certain probability which decreases with increasing barrier height. At a given applied field it takes some time to depin from the defect. Consequently, the hysteresis loop is not a rigid object. It depends on how fast the field is changed – a slower sweep gives a smaller coercive field.

2.3 Spin transfer torque

In nonmagnetic materials the electron spins are randomly oriented and don't play any role in the electron transport.² On the other hand, in FMs the exchange splitting results in a partial electron-spin polarization. In devices containing FM elements with different magnetization orientation or in DWs, where the magnetization rotates continuously, the spin polarization can be transferred between different parts of the device leading to a torque on magnetization, so-called spin transfer torque (STT).

This effect was first considered by Berger as being responsible for a DW motion in a magnetic wire excited by current pulses [52, 53]. Later the focus moved to magnetic nanostructures consisting of FM layers separated by a nonmagnetic spacer which was motivated by the discovery of the interlayer exchange coupling [54] and the giant magnetoresistance (GMR) effect [1, 55]. It turned out that the interlayer coupling may be

²In this moment we don't take into account relativistic effects like, for instance, spin Hall effect which lead to spin polarization even in nonmagnetic materials.

understood as an exchange interaction mediated by the spin-polarized electrons traveling across the spacer layer. In 1996 Slonczewski [35] and Berger [56] independently predicted that electrical current run across a FM/nonmagnetic metal (NM)/FM multilayer can produce a STT strong enough to switch the magnetization in one of the layers. The experimental confirmation came soon after [36, 57] utilizing the GMR effect as a probe of the mutual orientation of magnetization in the FM layers. Later a substantial tunneling magnetoresistance (TMR) effect was also observed in FM/insulator(I)/FM multilayers [58, 59].

2.3.1 Physics of STT

When a spin-polarized current flows through an environment with magnetization \mathbf{M} which is not collinear with the current polarization \mathbf{s} , the magnetization exerts a torque on the itinerant spins aligning them along the local magnetization direction. The spin current in turn exerts a torque on the magnetization which we call the STT. The strength of STT can be calculated directly by considering the mutual precession of the itinerant spin and magnetization in their exchange fields [60]. Alternatively, in systems where the total spin is conserved, STT can be evaluated by determining the change in the spin current upon interaction with the magnetization. We will use this theoretical picture, described in [35, 61, 62], as it quite instructively shows the effects taking place during the spin transfer.

The spin conservation means that the changes in \mathbf{M} and \mathbf{s} have to compensate each other. In other words, the change in the spin current upon interaction with the magnetization corresponds to the change in \mathbf{M} , i.e. to the torque \mathbf{T} acting on \mathbf{M} . When a spin current density \mathbf{Q} flows along x -axis perpendicular to a NM/FM interface the torque on a unit area of the interfacial magnetization is

$$\mathbf{T}_{ST} = \mathbf{e}_x \cdot (\mathbf{Q}^i + \mathbf{Q}^r - \mathbf{Q}^t), \quad (2.7)$$

where the superscripts i, r , and t label the incident, reflected, and transmitted spin current density which is defined as

$$\mathbf{Q} = (\hbar^2/2m_e) \text{Im}(\psi^* \boldsymbol{\sigma} \otimes \nabla \psi). \quad (2.8)$$

The outer product \otimes of the spin and momentum operators makes \mathbf{Q} a tensor having a direction in the spin space and a direction of propagation in the real space. The spin currents in (2.7) can be obtained directly from the definition (2.8) by inserting an appropriate wavefunction. In appendix B we perform the calculation for the free-electron wavefunction which is expressed as a linear combination of the FM eigenstates $|\uparrow\rangle$ and $|\downarrow\rangle$. The important result is that there is no torque associated with the spin-component parallel to \mathbf{M} (chosen $\parallel \mathbf{e}_z$). The torque from the transverse ($\mathbf{Q}_x \perp \mathbf{M}$) spin-component is generally nonzero. There are three distinct effects that contribute to the net spin transfer, as illustrated in Fig. 2.3(a). [61] In the following, θ is the polar and ϕ the azimuthal angle of the incident spin, k_x is the wavevector component along the current flow in the NM and similarly $k_x^\uparrow, k_x^\downarrow$ for the majority and minority spin channel in the FM.

First is the *spin filtering* effect. The two spin components of the incident wavefunction get reflected (transmitted) with different probabilities at the NM/FM interface due to the exchange splitting ΔE_x in the FM [different height of the energy step for the \uparrow -/ \downarrow -components in the bottom panel of Fig. 2.3(a)]. Consequently, the ratio of the \uparrow -/ \downarrow -components (i.e. the transverse spin component) differs for the spatially separated reflected and transmitted states which results in the discontinuity of the transverse spin current at the interface and the corresponding torque on \mathbf{M} .

The second contribution arises from a *spin rotation* of the reflected electrons. This is due to the generally complex reflection amplitudes R_\uparrow, R_\downarrow for the \uparrow, \downarrow -components of ψ . The transverse component of the reflected spin current \mathbf{Q}_x^r is proportional to the factor $R_\uparrow^* R_\downarrow = |R_\uparrow^* R_\downarrow| e^{i\Delta\phi}$ (see Eq. B.4), whose complex phase $\Delta\phi$ has a meaning of the azimuthal angle by which the electron spin rotates upon reflection. Importantly, since the reflection amplitudes depend on the wavevector component parallel to the NM/FM interface, electrons approaching the interface from different angles have their spins rotated differently. Summing over the electron ensemble efficiently averages the reflected transverse spin component to zero.

The last effect is the *spin precession* of the transmitted electrons. This is caused by the difference in kinetic energies of the majority and minority spins in the FM because of the exchange band-splitting. This results in a phase factor of $e^{i(k_x^\downarrow - k_x^\uparrow)x}$ in the transverse component of the transmitted spin current \mathbf{Q}_x^t , which describes a precession of the transmitted spin around the z -axis as the electron propagates through the FM. It can be understood as a spin precession in the exchange field of the magnetization $\mathbf{M} \parallel \mathbf{e}_z$. Electrons incident under different angles again acquire different precession angles which leads to efficient dephasing of the transverse spin component at a distance of few lattice constants.

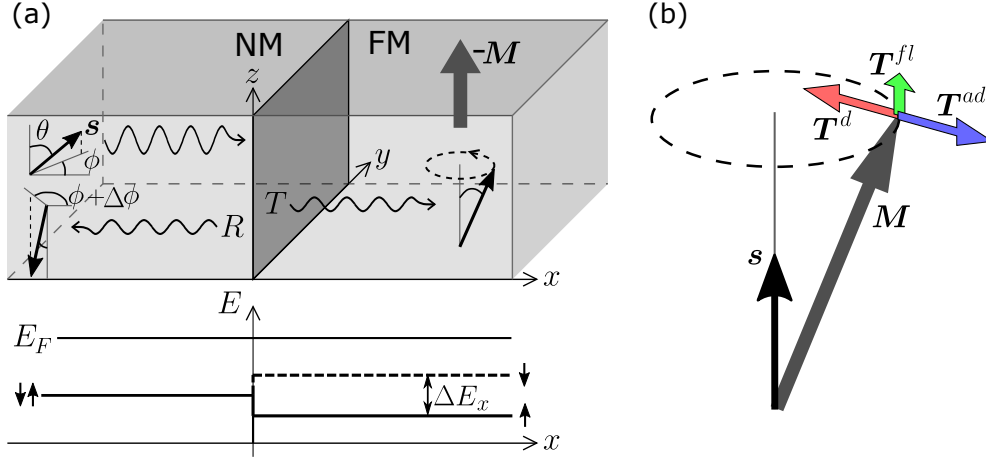


Figure 2.3: Physics of the spin transfer torque. (a) Spin-dependent scattering at the NM/FM interface due to the exchange band-splitting ΔE_x . Spin-filtering changes the \uparrow/\downarrow -ratio in the electron wavefunction by predominantly transmitting majority and reflecting minority spins. Spin rotation upon reflection and spin precession upon transmission averages out the transverse spin. (b) Different torques acting on magnetization: antidamping-like torque $\mathbf{T}^{ad} \sim \mathbf{M} \times (\mathbf{M} \times \mathbf{s})$, field-like torque $\mathbf{T}^{fl} \sim \mathbf{M} \times \mathbf{s}$, and damping $\mathbf{T}^d \sim \mathbf{M} \times (d\mathbf{M}/dt)$.

Since there is almost no transverse spin current leaving the NM/FM interface, we can conclude that it was completely absorbed by the interfacial FM layer and transformed to the torque on the magnetization, \mathbf{T}_{ST} . From Eq. (B.4) we get $\mathbf{T}_{ST} = Q_{xx}^i \mathbf{e}_x + Q_{yx}^i \mathbf{e}_y = (\hbar^2 k_x / 2m_e) \sin \theta (\cos \phi \mathbf{e}_x + \sin \phi \mathbf{e}_y)$. Thus, the torque acts always in the direction which is given by the cross-section of the plane perpendicular to \mathbf{M} and the plane containing both \mathbf{M} and \mathbf{s} , i.e., it can be written as $\mathbf{T}_{ST}^{ad} \sim \mathbf{M} \times (\mathbf{M} \times \mathbf{s})$. This is known as the *antidamping-like* (or *adiabatic*) STT as it points against (or along) the damping term in the LLG equation (2.4), as shown in Fig. 2.3(b). To be precise, the transverse components of the outgoing spin current are not completely zero and there is also a perpendicular torque, $\mathbf{T}_{ST}^{fl} \sim \mathbf{M} \times \mathbf{s}$, known as the *field-like* (or *non-adiabatic*) torque since the spin polarization acts as an effective field forcing \mathbf{M} to precess around it. The field-like torque is usually much weaker than the antidamping-

like one. However, in FM/I/FM structures they may become comparable in strength [62].

STT in antiferromagnets It has been shown in [47] that the antidamping-like STT from a FM layer to an adjacent AF layer can efficiently manipulate the AF moments. For example, in a two-sublattice collinear AF the effective field $\mathbf{H}_{ST,j} \sim \mathbf{M}_j \times \mathbf{s}$ acting on the sublattice magnetizations \mathbf{M}_j has the desired staggered character. The corresponding torques $\mathbf{T}_{ST,j} \sim \mathbf{M}_j \times \mathbf{H}_{ST,j}$ tilt the sublattice magnetizations away from the exactly antiparallel alignment thus inducing a strong exchange torques on \mathbf{M}_j which lead to the precession of the AF moments in the plane perpendicular to \mathbf{s} [9,47], as shown in Fig. 2.4(a). An ultrafast switching of the AF order via this STT-induced precession has been predicted recently [63]. Since the STT strength is proportional to the AF order parameter, $\mathbf{L} = \mathbf{M}_A - \mathbf{M}_B$, it is expected to be the same order of magnitude as the STT in FMs [47]. The STT is also expected to behave similarly in more complex AFs with non-collinear spin textures [47].

A uniform (non-staggered) magnetic field (a real field or a uniform spin polarization acting via a field-like torque) does not trigger a magnetic dynamics in AFs, unless they have a negligible anisotropy. This case is depicted in Fig. 2.4(b). The out-of-plane uniform field rotates the sublattice magnetizations in the plane which does not violate the exchange but it costs anisotropy energy. The anisotropy field \mathbf{H}_a (along the EA) exerts torques \mathbf{T}_a which tilt the magnetizations out-of-plane inducing the exchange torques \mathbf{T}_{ex} . These, however, point against the torques exerted by the external magnetic field thus hampering the magnetization dynamics.

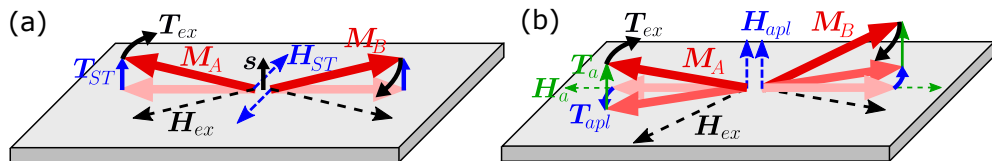


Figure 2.4: Staggered and non-staggered fields in AFs. Comparison of the effect of a staggered STT-induced effective field \mathbf{H}_{ST} (a) and a uniform (non-staggered) external field \mathbf{H}_{apl} (b) on an AF. The staggered field tilts (torque \mathbf{T}_{ST}) the moments out of the antiparallel arrangement, thus inducing a strong exchange fields \mathbf{H}_{ex} and torques \mathbf{T}_{ex} which eventually rotate the moments within the sample plane. In (b) the uniform field rotates the moments in the plane (torque \mathbf{T}_{apl}). The deviation from the EA (anisotropy field \mathbf{H}_a) induces torques \mathbf{T}_a which tilt the moments out of the plane and induce the exchange torques \mathbf{T}_{ex} which, however, point against the \mathbf{T}_{apl} hampering the magnetic dynamics.

2.3.2 Optical STT

Besides the current-induced STT there exists also its optical counterpart (OSTT) where the spin polarization is delivered by photons. Absorption of circularly polarized light creates a population of partially spin-polarized carriers which exert STT on the magnetization. This effect was predicted [37] and recently observed [38] in a ferromagnetic semiconductor GaMnAs. In this material, a high density of spin-polarized photo-carriers can be created due to the direct band gap and optical selection rules. This process, known as the *optical orientation* [64], is based on the conservation of the total angular momentum in the electron-photon system during the optical transition. The circularly polarized light can be viewed as consisting of photons with angular momentum projection of $\pm\hbar$ (for σ^\pm helicity) along the light propagation direction which is transferred to the photo-excited electron-hole pair when the photon is absorbed [64]. The band structure of the GaAs host is depicted in Fig. 2.5(a) showing the heavy

hole (HH), light hole (LH), and spin-orbit split-off (SO) bands and the conduction band (CB). The optical transitions from HH, LH, and SO bands to CB have different relative probabilities, as indicated by the numbers in Fig. 2.5(b). The transition probabilities are given by the matrix elements of the dipole operator D between the involved initial (i) and final (f) Bloch states [65], $p = |\langle J^f, m_J^f | D_{\pm} | J^i, m_J^i \rangle|^2$, where J and m_J are the quantum numbers indicating respectively the magnitude and projection of the angular momentum of the electron states and the index \pm denotes the spin ($\pm\hbar$) of the absorbed photon. For a photon energy $E_g < \hbar\omega < E_g + \Delta_{SO}$ only the transitions from HH ($m_J = \pm 3/2$) and LH ($m_J = \pm 1/2$) bands are involved. Consequently, for a given light helicity, the density of the photo-carriers of one spin orientation is 3-times larger than the density of the photo-carriers with the opposite spin orientation resulting in the spin polarization of $P_s = |n_{\uparrow} - n_{\downarrow}| / (n_{\uparrow} + n_{\downarrow}) = 0.5$ in an ideal case [65]. In reality, due to experimental imperfections, a polarization of $P_s \approx 0.4$ can be achieved [64, 65]. The optically injected spin polarization decreases and eventually drops to zero [65] as the photon energy approaches and surpasses the SO-CB energy splitting ($\hbar\omega = E_g + \Delta_{SO} = 1.86$ eV at $T = 10$ K, corresponding to a vacuum wavelength of $\lambda_0 \approx 670$ nm) when transitions from the SO band to CB are involved.

The spin-polarized photo-carriers (spin density \mathbf{s}) and the localized Mn moments (magnetization \mathbf{M}) are coupled via exchange interaction and their coupled precessional dynamics is described by the following equations [37, 38]

$$\frac{d\mathbf{M}}{dt} = \frac{\mathcal{J}}{\hbar} \mathbf{M} \times \mathbf{s}, \quad (2.9a)$$

$$\frac{d\mathbf{s}}{dt} = \frac{\mathcal{J} S_{Mn} c_{Mn}}{\hbar M_s} \mathbf{s} \times \mathbf{M} + \mathcal{P} \mathbf{n} - \frac{\mathbf{s}}{\tau}, \quad (2.9b)$$

where \mathcal{J} is the carrier-Mn moment exchange coupling constant, $S_{Mn} = 5/2$ is the Mn moment magnitude, c_{Mn} is the Mn moment density, \mathcal{P} is the rate per unit volume of the optical injection of carrier spins with initial orientation given by the unit vector \mathbf{n} , and τ is the photo-carrier spin lifetime.

The precession period of photo-electron spin in the exchange field of the magnetization is $\sim 2\pi\hbar/\mathcal{J}S_{Mn}c_{Mn} \sim 100$ fs [38]. During the precession the spin density decays mainly from two reasons - it dephases due to the exchange interaction with the fluctuating Mn moments and the carriers themselves decay by recombination. The timescales of both these processes are on the order of tens of picoseconds in GaMnAs [37, 38]. Consequently, the photo-electron spins with initial spin orientation \mathbf{n} experience many precessions before they decay with a random spin orientation. By averaging over the whole photo-electron population there is zero net loss of the angular momentum to the environment, i.e., the angular momentum is completely transferred to the magnetization [37]. In the corresponding limit of $\tau\mathcal{J}S_{Mn}c_{Mn}/\hbar \gg 1$, we can neglect the last term in Eq. (2.9b) which results in a steady-state spin density of $\mathbf{s}_0 \approx (\hbar\mathcal{P}/\mathcal{J}S_{Mn}c_{Mn}M_s)(\mathbf{n} \times \mathbf{M})$ which inserted into Eq. (2.9a) yields [38]

$$\frac{d\mathbf{M}}{dt} \approx \frac{\mathcal{P}}{S_{Mn}c_{Mn}M_s} \mathbf{M} \times (\mathbf{n} \times \mathbf{M}). \quad (2.10)$$

The geometry of the experiment [38] is shown in Fig. 2.5(c). The laser pulse incident along the sample normal injects photo-electrons spin-polarized along \mathbf{n} whose precession around the in-plane magnetization results in an in-plane steady-state spin density which in turn exerts a torque on \mathbf{M} tilting it out of the sample plane. This kind of spin torque corresponds to the antidamping-like (or adiabatic) current-induced STT, see Fig. 2.3(b) and the adjacent discussion.

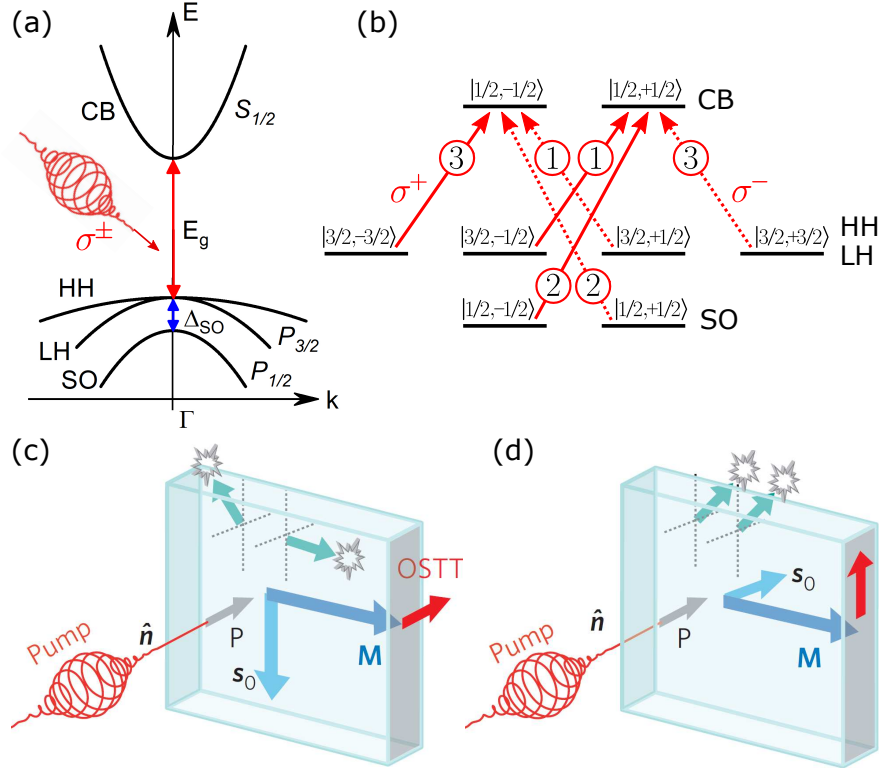


Figure 2.5: Optical orientation and OSTT in GaMnAs. (a) Sketch of the GaAs band structure close to the Γ -point showing the heavy hole (HH), light hole (LH), and spin-orbit split-off (SO) valence sub-bands and conduction band (CB). The band gap $E_g = 1.52\text{eV}$ and SO band splitting $\Delta_{SO} = 0.34\text{eV}$ at a temperature of 10 K. (b) Schematic of the optical orientation process for circularly left (σ^+) and right (σ^-) polarized light. The ket-vectors $|J, m_J\rangle$ indicate the electron angular momentum in different states and the numbers in circles are the relative probabilities of the optical transitions. (c) OSTT induced in GaMnAs by photo-electrons optically injected with a rate \mathcal{P} and spin-polarization along the sample normal \hat{n} . After many precessions around the magnetization the electron spins decay with random spin orientation (cyan arrows) and the entire angular momentum is transferred via the steady-state spin density s_0 to the magnetization M . (d) The same process for photo-holes. Due to their ultrashort spin lifetime τ the hole spins rotate only small angle and decay with a well defined spin orientation transferring most of the angular momentum to the environment. The in-plane OSTT $\sim \tau$ is much weaker than the effect of photo-electrons. (c) and (d) taken from [38].

The situation is very different in the case of the photo-injected holes which experience a strong SOC. This limits the photo-hole spin lifetime to $\tau \sim 1 - 10\text{fs}$ [37] which is considerably shorter than the hole precession period (tens of femtoseconds). Consequently, the photo-hole spin rotates only a small angle before it decays to the environment with still a well defined orientation. In other words most of the photo-injected angular momentum is transferred to the environment, not to the magnetization. This behavior is well described by the opposite limit, $\tau \mathcal{J} S_{Mn} c_{Mn} / \hbar \ll 1$, in which we can neglect the cross product in Eq. (2.9b) and we get the steady-state spin density $s_0 \approx \tau \mathcal{P} \hat{n}$ and the torque on magnetization [38]

$$\frac{dM}{dt} \approx \frac{\tau \mathcal{J} \mathcal{P}}{\hbar} M \times \hat{n}. \quad (2.11)$$

This situation is illustrated in Fig. 2.5(d). The optical STT acting in the sample plane is proportional to the ultrashort photo-hole spin lifetime and, therefore, the contribution

of photo-holes to the OSTT can be neglected in GaMnAs. The spin torque of the form (2.11) corresponds to the field-like (or non-adiabatic) STT discussed previously, see Fig. 2.3(b) and the adjacent discussion.

The OSTT allows for an ultrafast manipulation of magnetic order, as demonstrated in a single-domain case in [38]. When applied to inhomogeneous spin textures, this could be useful for magnetic storage and processing [13,14]. In chapter 6 we utilized this effect in a closely related ferromagnetic semiconductor GaMnAsP with a perpendicular magnetic anisotropy to excite an inertial DW motion with a direction controlled by the light helicity.

2.4 Spin-orbit torque

Recently a distinct type of spin torque has been proposed [39,66] and experimentally observed [40,67,68] which does not need any external source of the spin polarization. It is based on the spin-orbit interaction, which couples the orbital and spin degrees of freedom of an electron. Sending an electrical current through the material with a strong SOC leads to a generation of non-equilibrium spin polarization which exerts a torque on magnetization via the exchange interaction. This torque is known as the *spin-orbit torque* (SOT).

2.4.1 Spin-orbit coupling in solids

As described in section 1.1, SOC arises when electron moves in an electric field giving rise to an energy contribution of the form $\hat{H}_{SO} \sim \hat{\mathbf{S}} \cdot (\hat{\mathbf{v}} \times \mathbf{E})$. Therefore, the strongest SOC is observed in heavy elements such as platinum where the electron orbital velocities are largest. In the central potential of an atom the electron motion corresponds to a certain orbital angular momentum and the SOC Hamiltonian can be rewritten as $\hat{H}_{SO} \sim \hat{\mathbf{S}} \cdot \hat{\mathbf{L}}$. In the case of conduction electrons which often occupy the central-symmetric s-orbitals ($L = 0$) the spin-orbit energy splitting arises from a specific symmetry breaking of the crystal structure [20,69,70].

In a crystal the electron energies form bands with energy parametrized by the electron spin and wavevector, $E^\sigma(\mathbf{k})$ ($\sigma = \uparrow$ or \downarrow), and the SOC Hamiltonian becomes $\hat{H}_{SO} \sim \hat{\mathbf{S}} \cdot (\hat{\mathbf{k}} \times \mathbf{E})$. The SOC is obviously symmetric under time reversal, $E_{SO}^\uparrow(\mathbf{k}) = E_{SO}^\downarrow(-\mathbf{k})$. In a material with spatial inversion symmetry $E_{SO}^\sigma(\mathbf{k}) = E_{SO}^\sigma(-\mathbf{k})$ also applies. The two symmetries together imply $E_{SO}^\uparrow(\mathbf{k}) = E_{SO}^\downarrow(\mathbf{k})$, i.e., zero spin-orbit band splitting [20,69,70]. In other words, the SOC requires the inversion symmetry to be broken in order to spin-split the energy bands.

The inversion symmetry may be broken in the bulk by the crystal structure itself (bulk inversion asymmetry, BIA) as, for instance, in the zinc-blende structure of III-V and II-VI semiconductors [71]. In addition, the inversion symmetry is broken in heterostructures by interfaces, asymmetric doping, internal or external electric fields, which is known as the structural inverse asymmetry (SIA) [72]. Finally, the crystal symmetry is also broken by defects such as impurity atoms. While BIA and SIA are present in the whole volume or within a plane in the sample and can be described by effective spin-orbit fields, the randomly distributed impurities act locally and manifest themselves in spin-dependent scattering and spin-decay mechanisms.

In thin-film structures, taking into account only the in-plane electron motion, there are two main contributions to the SOC – the Rashba [72] and Dresselhaus [71] coupling arising from SIA and BIA, respectively. For example in (001)-grown GaAs the respective Hamiltonians are [69,70]

$$\hat{H}_R = \alpha_R(-k_x\sigma_y + k_y\sigma_x) \quad \hat{H}_D = \beta_D(k_x\sigma_x - k_y\sigma_y), \quad (2.12)$$

where α_R and β_D are the Rashba and Dresselhaus coupling constants that scale with the strength of the SOC and x , y , and z are chosen along [100], [010], and [001] crystallographic directions, respectively. If we express the SOC Hamiltonian in a form analogical to the Zeeman interaction, $\hat{H}_{SO} = \mu_B \hat{\boldsymbol{\sigma}} \cdot \mathbf{B}_{SO}$, we obtain the effective spin-orbit fields

$$\mathbf{B}_R(\mathbf{k}) = \frac{\alpha_R}{\mu_B} \begin{pmatrix} k_y \\ -k_x \end{pmatrix} \quad \mathbf{B}_D(\mathbf{k}) = \frac{\beta_D}{\mu_B} \begin{pmatrix} k_x \\ -k_y \end{pmatrix}. \quad (2.13)$$

The directions of these effective spin-orbit fields with respect to the electron k -vector are shown in Fig. 2.6(a,b). The circle represents the electron states at the Fermi level which take part in the transport. Generally, the SO-fields depend on the material, growth direction, strain, or the parameters of the heterostructure leading to a rich variety of possible field textures [69].

The effective spin-orbit fields and the spin-dependent scattering on impurities can induce a non-equilibrium spin polarization – in the bulk of a FM or AF layer or at an interface in a heterostructure – which will exert the spin-orbit torque on the magnetic moments. The two underlying phenomena currently discussed as being the sources of the spin-polarization are the *inverse spin galvanic effect* (ISGE) and the *spin Hall effect* (SHE).

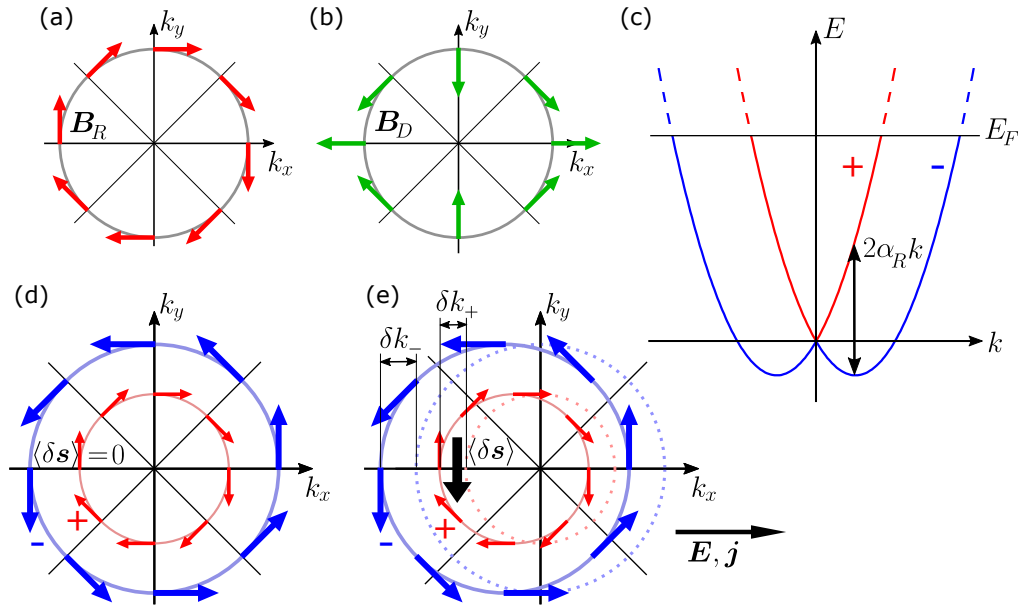


Figure 2.6: Effective SO-fields and current-induced spin polarization. The Rashba (a) and linear Dresselhaus (b) spin-orbit fields associated with SIA and BIA, respectively. (c) Conduction band splitting by the Rashba SOC. (d) k -dependent spin polarization induced by the Rashba SO-field. Symmetric equilibrium electron distribution gives zero net spin polarization. (e) Non-equilibrium electron distribution under external electrical field \mathbf{E} . Net spin polarization $\langle \delta \mathbf{s} \rangle$ is generated perpendicular to the current (\mathbf{j}) direction and the SIA axis (z).

2.4.2 SOT induced by the inverse spin galvanic effect

To explain the basic physics of the ISGE let's consider a simplified model in a form of a free-electron energy dispersion. Adding the Rashba SOC \hat{H}_R (2.12) to the free-electron Hamiltonian gives the eigenenergies [69, 70]

$$E_{\pm}(\mathbf{k}) = \frac{\hbar^2 k^2}{2m_e^*} \pm \alpha_R |\mathbf{k}|, \quad (2.14)$$

where m_e^* is the effective electron mass. The k -dependent SO-splitting of the conduction band is shown in Fig. 2.6(c). The orientation of spin induced by the SO-field for all electronic states at the Fermi level E_F is obtained by rotation of the dispersion curves around the energy axis and is shown in Fig. 2.6(d). The two circles correspond to the (+) and (-) branch of the dispersion and have opposite spin textures. In equilibrium the correlation between the electron k -vector and spin does not show on the outside since the electrons are distributed symmetrically in the k -space, i.e., they are moving in all directions with the same probability. When an external electric field is applied, the electron distribution in k -space becomes asymmetric, as shown in 2.6(e), since the electrons drift against the field. The asymmetry leads to a net spatially uniform non-equilibrium spin polarization in each branch which is known as the inverse spin galvanic effect. As shown in [69], the contributions from the two branches have different magnitudes and do not cancel out. The total non-equilibrium ISGE-induced spin density reads [69]

$$\langle \delta \mathbf{s} \rangle \approx \frac{m_e^* \alpha_R}{e \hbar E_F} \mathbf{j} \times \mathbf{e}_z, \quad (2.15)$$

where \mathbf{j} is the current density injected in the xy -plane. For the Rashba SOC the induced spin polarization points always perpendicular to the current and to the SIA axis. In more general case, taking into account also the BIA-induced SOC, the spin polarization direction depends on the orientation of the current with respect to the crystallographic axes [69].

It has been realized that the ISGE mechanism in nonmagnetic material can exert a torque on the magnetization of an adjacent FM layer via absorption of the SO-induced spin component perpendicular to the magnetization at the interface between the two materials [73]. In this case the SO-induced spin is transferred via the same mechanisms as those discussed in the case of the STT in section 2.3.1, i.e., by the spin-filter, spin-rotation, and spin-precession effects. Moreover, it turned out that the ISGE can induce the spin polarization and the corresponding SOT also directly in a *single* FM layer [39, 40, 66, 74] and even in AFs with an appropriate crystal symmetry [10, 12].

The total Hamiltonian in the presence of both the SOC and the s - d exchange coupling between the conduction electron spins and the localized magnetic moments of the FM reads [39, 69]

$$\hat{H} = \frac{\hbar^2 k^2}{2m_e^*} + \hat{H}_R - \mathcal{J}_{sd} \frac{\hat{\mathbf{M}}}{M_s} \cdot \hat{\boldsymbol{\sigma}}, \quad (2.16)$$

where \mathcal{J}_{sd} is the s - d exchange coupling constant. The effect of the SOC in a FM is that the equilibrium spin polarization of conduction electrons, which is parallel or antiparallel to the in-plane oriented magnetization, gets a non-equilibrium contribution $\langle \delta \mathbf{s} \rangle$ non-collinear with \mathbf{M} when a current flows through the FM. This SO-induced spin density exerts a field-like torque on \mathbf{M} via the s - d exchange interaction [39, 69]

$$\mathbf{T}_{SO}^{fl} \equiv \mu_0 \mathbf{M} \times \mathbf{H}_{SO} = -\mathcal{J}_{sd} \langle \delta \mathbf{s} \rangle \times \frac{\mathbf{M}}{M_s}, \quad (2.17)$$

where the effective SO-field reads

$$\mathbf{H}_{SO} = \frac{\mathcal{J}_{sd} \langle \delta \mathbf{s} \rangle}{\mu_0 M_s} = \frac{\mathcal{J}_{sd} m_e^* \alpha_R}{\mu_0 e \hbar E_F M_s} \mathbf{j} \times \mathbf{e}_z. \quad (2.18)$$

This result is obtained from (2.15) in the limit of a weak exchange ($\mathcal{J}_{sd} \ll \alpha_R k_F$) but

the thorough calculation in [39] gives the same result also for a more realistic case of a strong exchange ($\mathcal{J}_{sd} \gg \alpha_R k_F$).

Apart from the field-like SOT there exists also another torque with the antidamping-like symmetry associated with a non-equilibrium spin polarization induced along the z -axis. The origin of this spin component is explained in terms of the intrinsic Berry curvature [75], the same effect considered as being the origin of the intrinsic SHE [76]. In this picture the non-equilibrium spin density does not arise from the scattering-induced redistribution of carriers in the k -space described above. Instead, the itinerant spins acquire a z -component during their acceleration in between the scattering events [75]. The itinerant spins initially polarized in the sample plane by the exchange interaction with \mathbf{M} feel a time-dependent effective field $\Delta B_{eff} \sim \alpha_R E t$ along the y -axis when accelerated by $\mathbf{E} \parallel \mathbf{e}_x$ which turns them towards the z -axis. Thus induced non-equilibrium spin density then exerts via the exchange interaction a torque on the magnetization which for the Rashba SOC has the following antidamping-like symmetry [75]

$$\mathbf{T}_{SO}^{ad} \sim \mathbf{M} \times [(\mathbf{j} \times \mathbf{e}_z) \times \mathbf{M}]. \quad (2.19)$$

The antidamping-like SOT is of particular importance for the magnetic-memory applications as it acts against the equilibrium-restoring Gilbert damping during the switching process. Since the SOTs change sign with reversing the electrical current they allow for the reversible magnetization switching.

Optical SOT An optical counterpart of the current-induced SOT has recently been observed in the ferromagnetic semiconductor GaMnAs [25]. Here, an absorption of a laser pulse creates an excess population of electrons and holes. Since the torque relies on the SOC the holes which are, unlike the conduction electrons, strongly SO-coupled play the key role in the OSOT mechanism. The photogenerated holes relax within ~ 100 fs to the Fermi level creating a non-equilibrium excess hole density. The increased total number of occupied hole states in the SO-coupled exchange-split valence band can result in a non-equilibrium hole spin polarization that is misaligned with the Mn moments. The non-equilibrium spin density exerts a torque on \mathbf{M} until the excess holes recombine (~ 10 ps). A large-angle magnetization reorientation within ~ 1 ps and a subsequent precession was reported in [25]. In contrast to the OSTT [38], which arises from the light-magnetization angular momentum transfer, the light polarization does not play any role in the OSOT.

Néel SOT in antiferromagnets Recently, a new kind of current-induced SOT has been predicted to act in AFs with an appropriate symmetry which is referred to as the Néel spin-orbit torque (NSOT) [12]. It is a bulk effect which does not require interfacing with other magnetic or nonmagnetic layers.

The recent understanding that the SOC can generate a spin-polarization locally in certain parts of the crystal unit cell even in a material which does possess the bulk space inversion symmetry [77] opened a way to manipulate single-layer AF samples by an electrical current [12]. The authors of [77] consider non-magnetic materials and argue that it is not primarily the global symmetry of the crystal lattice which determines the ability of the material to produce the spin polarization but rather the local symmetries of the individual lattice sites. The global symmetry decides whether the individual contributions from the different sites average out or not.

There are three possible combinations of the global and local symmetries which differ regarding the nature of the resulting spin polarization [77]. (i) All atomic sites in the unit cell possess the inversion symmetry and, consequently, the lattice is also globally inversion-symmetric. In this case neither local nor global net spin polarization

is induced by an electrical current. In the remaining two cases at least one atomic site lacks the inversion symmetry. At these sites a local spin polarization is induced by current and the net spin polarization is given as the vector sum over the local contributions. (ii) If the lattice still has a global inversion symmetry the individual contributions from different inverse-asymmetric sites average to zero and no net spin polarization is present. (iii) If the lattice is globally inversion-asymmetric too the local spin polarizations will not average out and the net spin polarization appears as discussed for the cases of BIA and SIA in the previous paragraphs.

The case (ii) is particularly interesting as it allows for a generation of staggered effective magnetic fields in the bulk [12]. Because of the global inversion symmetry the energy bands are doubly degenerate but the two components of the bands may have opposite spin polarizations, each spatially localized in one of the two separate real-space sectors which form the inversion partners. In antiferromagnets where the spin sublattices coincide with the two inversion-partner sublattices the staggered spin polarization acts as a staggered effective field exerting a field-like SOT on the sublattice magnetizations, as shown in Fig. 2.7(a). Among the AF materials, this kind of symmetry has so far been confirmed for Mn_2Au (for which the NSOT was initially predicted in [12]) and CuMnAs . In the latter material, the effect was experimentally observed for the first time to induce a reversible switching of the AF moments [10, 78, 79] and later the same was confirmed also in Mn_2Au [11].

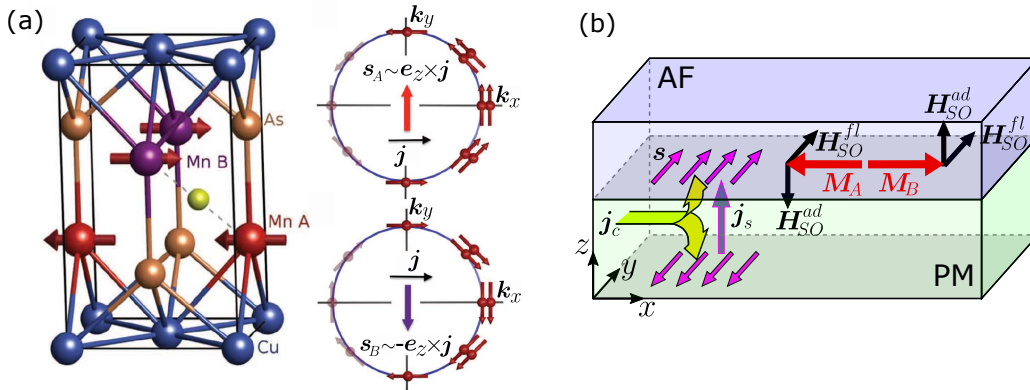


Figure 2.7: Spin-orbit torques in antiferromagnets. (a) The unit cell of AF CuMnAs with the two magnetic sublattices being the inversion partners. Locally broken inversion symmetry induces spatially separated staggered spin polarizations $s \sim \pm e_z \times j$ located at the two magnetic sublattices which exert the field-like Néel SOT. (b) The SHE in a PM generating a spin current j_s incident on a PM/AF interface. The effective field associated with the antidamping-like component of the SHE-induced SOT has the desired staggered character and can manipulate the interfacial magnetic moments just like the STT in a FM/AF structures. (a) reprinted from [10].

2.4.3 SOT induced by the spin Hall effect

In heterostructures containing PM/FM(AF) bilayers there exists an additional SO-induced mechanism resulting in a net spin current and the corresponding SOT, known as the *spin Hall effect* [80–83]. In analogy to the ordinary Hall effect (OHE), which induces a charge current perpendicular to the driving electrical current and the applied magnetic field, the SHE induces in the PM layer a pure spin current j_s (without a net charge current) perpendicular to the driving charge current j_c in zero external magnetic field. The relation between the direction e_s of the spin angular momentum s forming the spin current and the directions of j_s and j_c is [84]

$$\mathbf{j}_s = \alpha_{SH}(\mathbf{e}_s \times \mathbf{j}_c), \quad (2.20)$$

where the ratio between the spin and charge current, α_{SH} , is the spin-Hall angle which describes the sign and strength of the SHE and is related to the SO-coupling constant.

As depicted in Fig. 2.7(b), the transverse spin current is caused by a preferential deflection of the electrons with opposite spins to opposite directions. Consequently, there is a zero net spin density in the bulk but the opposite spin accumulations appear at the opposite edges of the PM layer. The spin accumulation is opposed by a spin diffusion back to the bulk of the PM resulting in a steady state spin density in the vicinity of the sample edges [82]. If the PM is interfaced with a FM(AF) layer³ the SHE-induced spin current incident from the PM on the interface is transformed to the torque on the magnetic moments in the FM(AF) layer via the same mechanisms as in the case of the STT. Recently, switching of the magnetic order via the SHE-induced SOT has been observed in FMs [68,85] and AFs [86]. The difference between STT and SHE-SOT is in the origin of the spin current – a separate FM layer (external polarizer) in the case of STT and the SOC in the adjacent PM layer in the case of SHE-SOT.

The spin-dependent deflection of electrons leading to the spin accumulation is caused by both extrinsic and intrinsic mechanisms [81]. The extrinsic ones are associated with a spin-dependent scattering from charged impurities [80]. The so-called *skew scattering* [81] can be understood in a classical picture where the electric field \mathbf{E} produced by the impurity atom transforms partially to a magnetic field $\mathbf{B} \sim \mathbf{v} \times \mathbf{E}$ in the electron's rest frame. The direction of the field depends on whether the electron deflects to the right or to the left and, therefore, the corresponding Zeeman energy is (for a given direction of the electron spin) different in both cases. That's why the electrons with one spin preferentially scatter to the right and that with the opposite spin deflect to the left in order to save the energy. Another scattering process called *side-jump* [81] leads to a transverse shift of the electron's position without the change of its propagation direction. The electrons with opposite spins again experience transverse shifts in opposite directions. After many of these jumps the electrons with opposite spins end at the opposite edges of the sample.

The intrinsic contribution to the SHE has been theoretically studied in [76,87] and recently reviewed in [81]. The physical picture given in [76] for a 2D electron model system with Rashba SOC is similar to the case of the antidamping-like ISGE-induced SOT [75]. It arises from a time dependent effective SO-field felt by the electrons accelerated in an external electric field (applied along x -axis). Since the SO-field is k -dependent, it changes in time as the electron moves in the k -space under the action of the electric field. As the electron accommodates to the changing SO-field it acquires an out-of-plane spin component with opposite directions ($\pm z$) for electrons moving in the opposite directions ($\pm y$) perpendicular to the driving charge current [76,81].

As discussed in [88], the SHE-induced SOT has both the field-like component, $\mathbf{T}_{SHE}^{fl} \sim \mathbf{M} \times (\mathbf{j}_c \times \mathbf{e}_z)$, and the antidamping-like component, $\mathbf{T}_{SHE}^{ad} \sim \mathbf{M} \times [(\mathbf{j}_c \times \mathbf{e}_z) \times \mathbf{M}]$, as in the case of ISGE-induced SOT. Since both effects, SHE and ISGE, can simultaneously appear in the HM/FM(AF) structures their separation is challenging.

³The magnetic film has to be sandwiched between two different PM layers otherwise the SHE-induced torques acting at the two interfaces cancel out. The same holds also for the ISGE-induced torques at the two interfaces. Therefore, the SOT structures usually contain asymmetric stack – heavy metal(HM)/FM(AF)/normal metal(NM) – with the HM providing a strong SOC.

2.5 Domain wall motion

As already mentioned, the magnetization switching in real magnetic samples proceeds via a DW motion. Moreover, devices based on a DW motion in nanowires represent a promising concept of a memory with the potential of combining non-volatility, high capacity, and ultra-fast response [13]. DWs can be driven by various means, including magnetic fields, light, and electrical currents. In the following, we focus on 180° DWs in systems with perpendicular-to-plane uniaxial magnetic anisotropy where the DWs have the simple Bloch or Néel character. DWs in in-plane magnetized systems have more complex internal structure, like transverse or vortex walls, which require 2D micromagnetic simulations. Nevertheless, most of the results obtained below still remain valid for transverse walls treated in a 1D approximation [89,90].

2.5.1 Field-induced DW motion

The magnetization dynamics in a DW driven by an external magnetic field is described by the LLG equation (2.4). Since we expect the magnetization to change only its direction, while $|\mathbf{M}| = M_s$ is constant, it is favorable to express (2.4) in spherical coordinates [26,91]

$$\sin \theta \frac{d\theta}{dt} = -\frac{g_L \mu_B}{\hbar M_s} \frac{\delta \epsilon_{tot}}{\delta \phi} - \alpha \sin^2 \theta \frac{d\phi}{dt}, \quad (2.21a)$$

$$\sin \theta \frac{d\phi}{dt} = \frac{g_L \mu_B}{\hbar M_s} \frac{\delta \epsilon_{tot}}{\delta \theta} + \alpha \frac{d\theta}{dt}, \quad (2.21b)$$

where θ is the polar angle and ϕ the azimuthal angle of the magnetization, as depicted in Fig. 2.8(a). The functional derivatives of the total free energy density represent the effective field \mathbf{H}_{eff} containing the contributions from the external magnetic field, magnetic anisotropy, demagnetizing field, and exchange stiffness.

For 180° DWs in materials with uniaxial magnetic anisotropy the equations (2.21) can be solved rigorously (below a critical DW velocity), as was shown by Walker [92]. In the following, we examine the motion of a pure Bloch wall driven by an external magnetic field applied along the EA [26]. We choose the EA along the z -axis and the DW lying in the xz -plane moves along the y -axis, as shown in Fig. 2.8(a). In spherical coordinates a pure Bloch wall is described by a constant azimuthal angle $\phi = 0^\circ$ and a transition $\theta = 0^\circ \rightarrow 180^\circ$. The free energy density associated with the DW is

$$\epsilon_{tot} = A(\theta'^2 + \sin^2 \theta \phi'^2) + \sin^2 \theta (K_u + K_d \sin^2 \phi) - \mu_0 M_s H_{ext} \cos \theta, \quad (2.22)$$

where $K_d = \mu_0 M_s^2 / 2$ and θ' and ϕ' are spatial derivatives of the angles along the direction of the DW motion ($' = d/dy$). The time derivatives in (2.21) can be expressed via the spatial derivatives and the DW velocity, $d/dt = -v d/dy$. The equations of motion (2.21) then become [26]

$$-v \sin \theta \theta' = \frac{2g_L \mu_B}{\hbar M_s} [A(\sin^2 \theta \phi')' - K_d \sin^2 \theta \sin \phi \cos \phi] + \alpha \sin^2 \theta v \phi', \quad (2.23a)$$

$$\begin{aligned} -v \sin \theta \phi' &= \frac{2g_L \mu_B}{\hbar M_s} [-A\theta'' + \sin \theta \cos \theta (A\phi'^2 + K_u + K_d \sin^2 \phi)] \\ &+ \frac{g_L \mu_B \mu_0}{\hbar} H_{ext} \sin \theta - \alpha v \theta'. \end{aligned} \quad (2.23b)$$

For low enough magnetic fields there exists a solution with constant ϕ throughout the wall ($\phi' = 0$), which describes a steady DW motion with a constant velocity. This means that the driving and dissipation forces, represented by the last two terms in

(2.23b), have to cancel each other. Consequently, the expression in the square brackets equals zero and an integration gives

$$\theta' = \sin \theta \sqrt{(K_u + K_d \sin^2 \phi)/A}. \quad (2.24)$$

Using this result, Eq. (2.23a) yields the relation between the DW velocity and the constant angle ϕ describing the distortion of the Bloch wall during its motion. From Eq. (2.23b) we then obtain the driving field H_{ext} corresponding to this DW velocity

$$v = \frac{gL\mu_B\mu_0}{\hbar} M_s \sin \phi \cos \phi \sqrt{\frac{A}{K_u + K_d \sin^2 \phi}}, \quad (2.25)$$

$$H_{ext} = \alpha M_s \sin \phi \cos \phi. \quad (2.26)$$

The Walker's analytical solution gives a valuable insight into the mechanism of the field-driven DW motion [26, 92]. As depicted in Fig. 2.8(a), the applied magnetic field induces the DW motion indirectly. The static Bloch DW produces no stray field ($\phi = 0$). The torque associated with the external magnetic field rotates the magnetization inside the DW out of the wall plane ($\phi > 0$) inducing a demagnetizing field. It is this demagnetizing field which exerts the torque on the wall magnetization in the right direction, i.e. within the xz -plane, thus causing the whole DW to move along the y -axis. It is also directly visible from the equation of motion (2.23a) that for the Walker's solution ($\phi' = 0$) the only term causing θ to change is the demagnetizing one.

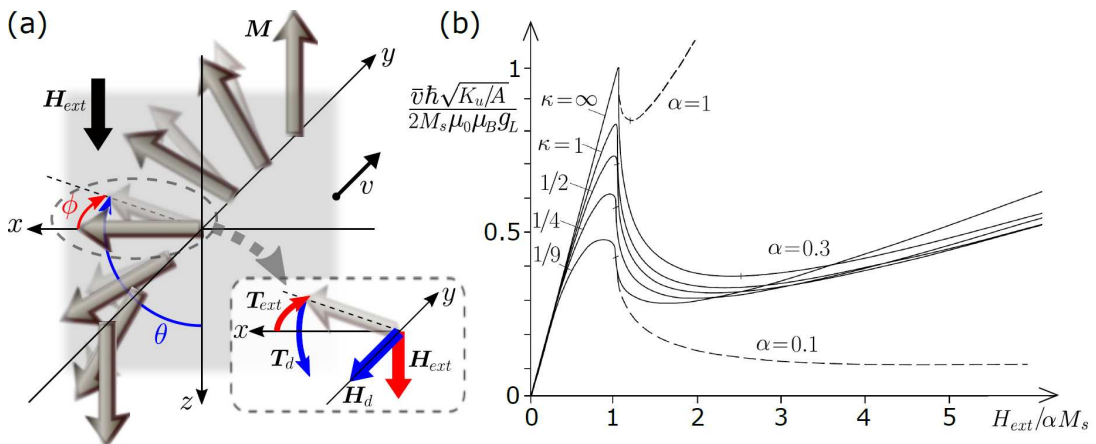


Figure 2.8: Field-induced DW motion. (a) Sketch of a static (dark arrows) and a moving (light arrows) 180° Bloch DW in a uniaxial material with the angles θ and ϕ describing the magnetization direction. Inset: The external magnetic field \mathbf{H}_{ext} applied along the EA turns the magnetization out of the wall plane (torque \mathbf{T}_{ext}) inducing a demagnetizing field \mathbf{H}_d . The corresponding torque \mathbf{T}_d rotates the magnetization in the xz -plane causing the whole DW to move with a constant (below the WB) velocity v along the y -direction. (b) The average DW velocity for different values of κ and α showing two linear regimes - a steady motion below the WB and a precessional motion far above the WB - and a complex transient regime with a negative DW mobility just above the WB. (b) taken from [26].

The steady motion, characterized by a constant ϕ and the DW velocity (2.25), is only possible as long as the induced demagnetizing field balances, via the damping term in (2.23b), the driving torque of the external magnetic field. However, the demagnetizing field cannot exceed the saturation magnetization M_s and for high enough external fields this balance is no more possible. The critical field at which the driving torque surpasses the counteracting demagnetizing torque is called *Walker (breakdown) field*.

At this point the DW internal structure breaks down and the magnetization within the wall starts to precess around the external magnetic field, switching periodically between the Bloch and Néel configurations.

The peak velocity in the steady regime reaches [26]

$$v_p = \frac{gL\mu_B\mu_0}{\hbar} \sqrt{\frac{2A\kappa}{\mu_0}} f(\kappa), \quad (2.27)$$

where $\kappa = K_u/K_d$ and $f(\kappa) = \sqrt{1+1/\kappa} - 1$. No constant-velocity solution of (2.23) exists beyond this point. The corresponding values of the azimuthal magnetization angle in the DW and the driving field are [26]

$$\sin \phi_p = \sqrt{\kappa f(\kappa)}, \quad H_p = \frac{2\alpha K_u}{\mu_0 M_s} f(\kappa) \sqrt[4]{1 + \frac{1}{\kappa}}. \quad (2.28)$$

Above the Walker breakdown (WB) the DW motion becomes irregular and is treated numerically. The precessing magnetization causes the DW to move forth and back following the changing direction of the demagnetizing field. Nevertheless, one can still define an average DW velocity by averaging over the cycle of the magnetization precession. For zero damping, the forward and backward motion of the DW would cancel out, however, for realistic values of α the forward motion takes over. The precessing magnetization within the DW gives rise to a net damping torque $\alpha \mathbf{M} \times d\mathbf{M}/dt$ which increases with the precession rate (i.e. with increasing H_{ext}) and turns the magnetization towards the EA, thus driving the DW motion [93]. The average velocity \bar{v} calculated numerically in [26] is shown in Fig. 2.8(b) for different values of κ and α . The initial linear increase of the velocity with H_{ext} in the steady regime is followed by a complex transient regime with negative DW mobility $\mu = dv/dH_{ext}$ just above the WB and by further linear increase of the average velocity in the precessional regime far above the WB.

In the derivation above, we considered an infinite 180° Bloch DW in a thick sample. In such a case the only nonzero component of the demagnetizing field is the one perpendicular to the DW plane ($N_x = N_z = 0, N_y = 1, \mathbf{H}_d = -\mathbf{M}_y$). For a finite DW, e.g. for a DW in a nanowire patterned from a thin magnetic film, N_x and N_z become nonzero and $N_y = 1 - N_x - N_z$ is reduced. The corresponding demagnetizing field, which is responsible for the actual DW motion, is reduced as well. Consequently, the point of the instability of the DW internal structure, i.e. the Walker breakdown, is reached at lower values of the driving magnetic field. As derived in [89], the Walker field is reduced by the factor of $|N_y - N_x|$.

The DW motion discussed so far is known as the *viscous-flow* motion. According to equation (2.25) the DW moves with a nonzero velocity for any nonzero applied magnetic field. However, in real samples one has to take into account the DW pinning at defects. For zero temperature the DW motion would be blocked until the field reaches a critical value H_{crit} necessary to overcome the disorder-related energy barriers. For finite temperatures and low H_{ext} the DW motion is thermally activated and proceeds via the discrete Barkhausen jumps from one pinned configuration to the next, the so-called *creep* motion. The creep regime is characterized by a strongly nonlinear $v(H_{ext})$ dependence [94, 95]

$$v = v_0 \exp \left[-\frac{U_C}{k_B T} \left(\frac{H_{crit}}{H_{ext}} \right)^\mu \right] \quad (2.29)$$

which describes the DW motion sufficiently below H_{crit} . In the equation, v_0 is a proportionality constant, U_C is related to the height of the disorder-induced pinning energy barrier, and μ is a universal dynamic exponent, the value of which is given by the dimensionality of the system. With increasing magnetic field the creep motion smoothly

turns into the viscous-flow motion with the linear $v(H_{ext})$ dependency.

DW mass and inertia. The energy associated with a DW, given by Eq. (1.42), changes when the DW moves. On the example of a Bloch wall driven by an external magnetic field, which was discussed above, we see that the tilt of the wall magnetization out of the DW-plane stores an additional demagnetizing energy, i.e., K_u is replaced by $K_u + K_d \sin^2 \phi$ [see e.g. Eq. (2.22)] and the DW energy reads [26]

$$\sigma_{DW} = \pi \sqrt{A(K_u + K_d \sin^2 \phi)} \approx \sigma_{DW}^0 + \frac{\pi^2 A K_d}{2\sigma_{DW}^0} \phi^2, \quad (2.30)$$

where the last expression is obtained by a Taylor expansion of the square root and $\sigma_{DW}^0 = \pi \sqrt{A K_u}$ is the DW energy at rest. For a weak excitation ($\phi \ll 1$) the DW velocity (2.25) increases linearly with the magnetization tilt angle

$$v \approx \frac{g_L \mu_B \mu_0}{\hbar} M_s \phi \sqrt{\frac{A}{K_u}}, \quad (2.31)$$

i.e., the DW energy increases as a square of the DW velocity, $\sigma_{DW} = m^* v^2 / 2$. Here we introduce, based on the analogy to the kinetic energy of a mass, the effective DW mass m^* [96], which follows from Eqs. (2.30) and (2.31)

$$m^* = \left(\frac{\hbar}{g_L \mu_B \mu_0} \right)^2 \frac{K_d}{A M_s^2} \sigma_{DW}^0. \quad (2.32)$$

As in the case of massive objects, the DW mass manifests itself in inertial effects. In particular, the torque on the DW does not result in an immediate DW motion - there is a certain lag - and, conversely, the DW can move after the driving force is turned off [97]. These effects are observed also when the DW motion is induced by an electrical current [98–100]. The duration of the transient inertial motion is given by a characteristic relaxation time of the deformed magnetization texture [101]. The concept of the DW mass is more general and applies also to more complex spin textures than the Bloch wall considered above. One can always define [101] the angle ϕ which is a measure of the DW deformation during its motion and there exists a relation between this DW deformation and the DW displacement or velocity [100–102]. The DW mass is a measure of the DW energy increase associated with a certain deformation of the DW internal structure.

2.5.2 Current-induced DW motion

The DWs in magnetic nanowires can be moved, besides the magnetic field, also by an electrical current via the STT as first considered by Berger [52, 53] already a few decades ago. However, only relatively recently the current-induced DW motion has gained a lot of attention thanks to its applicability in spintronic memories [13] and logic devices [14] where the STT, unlike the external magnetic field, offers a scalable control mechanism.

In order to include the STT-related terms in the LLG equation (2.4) one can proceed by considering the s - d model of ferromagnetism [103], where the spin current density \mathbf{Q} carried by the mobile s -electrons and the magnetization due to the more localized d -electrons can be distinguished. The derivation is performed in appendix C and the complete LLG equation amended by the STT-induced torques reads [90, 103]

$$\frac{\partial \mathbf{M}}{\partial t} = -\gamma^* \mu_0 \mathbf{M} \times \mathbf{H}_{eff} + \frac{\alpha^*}{M_s} \mathbf{M} \times \frac{\partial \mathbf{M}}{\partial t} + b_j (\mathbf{e}_j \cdot \nabla) \mathbf{M} - \frac{c_j}{M_s} \mathbf{M} \times (\mathbf{e}_j \cdot \nabla) \mathbf{M}, \quad (2.33)$$

where \mathbf{e}_j is the unit vector in the direction of the electrical current flow and γ^* and α^* are the renormalized gyromagnetic ratio and Gilbert damping constant, respectively (see appendix C). The amplitudes $c_j = \beta b_j$ and $b_j \sim jP$ of the two current-induced torques have the units of velocity and scale with the current density j and with the degree of the current spin polarization P . The relative strength of the two STTs is given by $\beta \equiv \tau_{ex}/\tau_{sf}$, where τ_{ex} is the precession time of the itinerant spin in the exchange field of the magnetization and τ_{sf} is the spin-flip relaxation time.

The physical origin of the “ b_j ” term is well understood. As the electron spin crosses the DW, it experiences the continuously rotating exchange field of the wall magnetization. In the first approximation, the electron spin follows adiabatically the magnetization direction, that’s why the “ b_j ” term is called “adiabatic” torque [52, 90, 104]. The divergence of the spin current induced by the inhomogeneous magnetization in turn acts as a torque on the magnetization, as discussed in section 2.3.1. In the picture of the spin conservation one can say that the itinerant electron spin flipped upon crossing the DW is compensated by rotating the localized spins within the DW in the opposite sense which leads to a shift of the whole DW in the direction of the electron flow [62].

Several different microscopic mechanisms were proposed to explain the origin of the “ c_j ” term such as linear momentum transfer [104] or spin-flip scattering [103, 105]. This term is known as the “non-adiabatic” torque as it derives from the inability of the electron spin to instantaneously follow the spatially varying magnetization in the DW that leads to a certain lag [105]. Therefore, it is relevant especially for thin DWs⁴ and in layered structures (like spin valves and magnetic tunnel junctions) where the magnetization changes abruptly along the current flow.

Interestingly, as pointed out in [105], when the spin-flip processes are neglected (a pure adiabatic torque) the entire spin carried by the electrical current is transferred to the magnetization, however, the torque corresponds to an effective field pointing perpendicular to the EA leading only to a deformation of the DW but not to a steady motion. On the other hand, when the spin-flip processes which do not conserve the total angular momentum are taken into account the resulting non-adiabatic torque component acts analogously to a standard magnetic field pointing along the EA, thus moving the whole DW, as discussed in chapter 2.5.1.

Let’s assume a perfect Bloch wall in a defect-free nanowire oriented along the y -direction, as shown in Fig. 2.9(a). In the adiabatic approximation ($\beta = 0$) the only nonzero current-induced spin torque, $\mathbf{T}_{AD} \sim \partial\mathbf{M}/\partial y$, points perpendicular to both the local magnetization and the current direction and tends to rotate the wall magnetization around the wire axis, i.e. to move the DW along the wire. While doing so, the torque also deforms the originally stray-field-free Bloch wall and the wall magnetization is tilted out of the wall plane [52, 102]. Consequently, the induced demagnetizing field compensates the STT and stops the motion on a nanosecond timescale. After switching the current off the DW restores its original profile while moving back to the original position [102]. No steady DW motion is expected in this case until the current magnitude reaches a threshold value [see Fig. 2.9(b)]. Similarly to the Walker field in the previous chapter also the Walker-like threshold current corresponds to the situation when the demagnetizing field reaches maximum and is not able to compensate the driving torque anymore [90]. Above the threshold, the wall magnetization precesses switching between the Bloch and Néel configurations and the DW moves along the electron flow with an average velocity $b_j/(1 + \alpha^2)$ (far above the threshold) [89].

The intrinsic threshold current for the adiabatic DW motion turned out to be much larger than the threshold currents observed in experiments. This discrepancy was re-

⁴Depending on the microscopic model the relevant length to which the DW width has to be compared is the Fermi wavelength [104], Larmor precession length [105], or spin diffusion length [103].

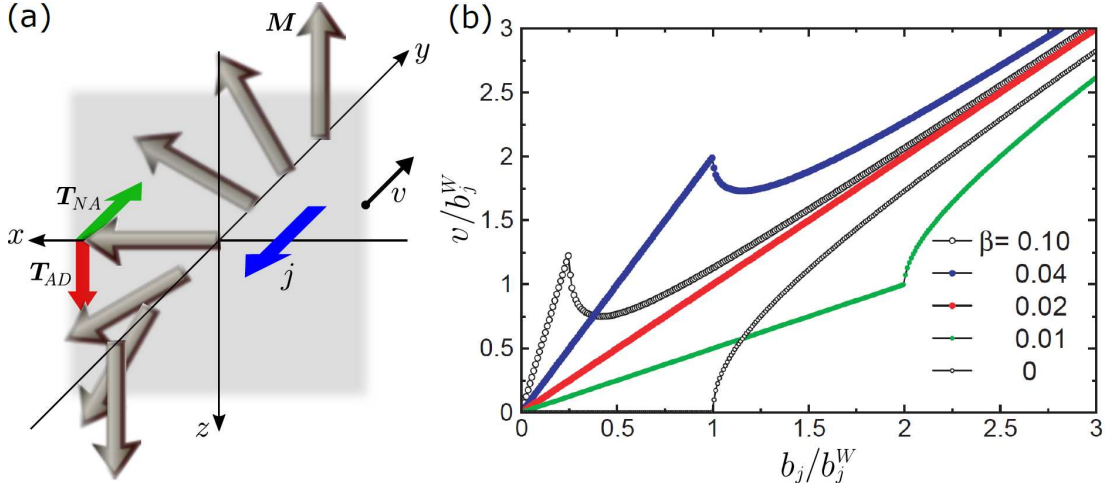


Figure 2.9: Current-induced DW motion. (a) Sketch of a 180° Bloch DW in a uniaxial material driven by the STT. The directions of the adiabatic (\mathbf{T}_{AD}) and the non-adiabatic (\mathbf{T}_{NA}) torque components generated by the electrical current density \mathbf{j} are indicated by arrows. (b) The average DW velocity for $\alpha = 0.02$ and different values of β in a perfect nanowire. The cusp corresponds to the Walker threshold separating the steady and the precessional regimes of the DW motion. b_j^W corresponds to the critical current density. The data are taken from [90] where it was calculated for an in-plane magnetized system, however, the same behavior is observed for perpendicular-to-plane magnetized materials [106].

solved by introducing the non-adiabatic STT, [103]. This torque, $\mathbf{T}_{NA} \sim \mathbf{M} \times \partial \mathbf{M} / \partial y$, acts along the wire axis tilting the wall magnetization out of the wall plane in exact analogy to the action of an external magnetic field (see section 2.5.1). The STT-induced demagnetizing field then exerts a torque which turns the magnetization around the wire axis thus driving the DW along the wire. In contrast to the adiabatic torque, for non-adiabatic STT there is no intrinsic threshold for the DW motion, however, in real nanowires the defect-induced pinning cause an extrinsic threshold which is observed in the experiments [93].⁵ For strong enough current density the tilt of the wall magnetization passes a critical point ($\phi \approx \pi/4$) beyond which the wall magnetization starts to precess leading to an irregular DW motion accompanied by a change in the DW mobility as shown in Fig. 2.9(b). Depending on the Gilbert damping α and on the relative strengths of the adiabatic and non-adiabatic torque components, given by the value of β , the mobility increases ($\beta < \alpha$) or decreases ($\beta > \alpha$) above the threshold.

The Walker-like critical current density reads [89]

$$j_W = \frac{eM_s^2 \gamma \delta_{DW}}{g_L \mu_B P} \frac{\alpha}{|\beta - \alpha|} |N_y - N_x|, \quad (2.34)$$

where δ_{DW} is the width of the moving wall which is slightly reduced compared to the static DW width.⁶⁷ When taking into account both the external magnetic field and electrical current the DW velocity below and above the threshold can be in the 1D model expressed as [89]

$$v_1 = \frac{\gamma \delta_{DW}}{\alpha} \left(H_{ext} + \frac{c_j}{\gamma \delta_{DW}} \right) \quad \text{and} \quad v_2 = \frac{\gamma \delta_{DW} \alpha}{1 + \alpha^2} \left(H_{ext} + \frac{c_j}{\gamma \delta_{DW}} \right) + \frac{b_j}{1 + \alpha^2} \quad (2.35)$$

⁵We note that for weak electrical currents a pinning-dominated creep DW motion is observed, as in the previously discussed case of the field-driven DW motion.

⁶We take here for simplicity $K_u \gg K_d$ which is a good approximation for the perpendicular-to-plane magnetized GaMnAsP studied in this thesis.

⁷We omit the asterisk which marks the renormalized parameters γ and α .

respectively. The expressions illustrate what was already mentioned above, i.e., that the non-adiabatic STT acts as an additional magnetic field with a magnitude of $c_j/\gamma\delta_{DW}$. The adiabatic STT can only move the DW above the Walker threshold where it becomes the dominant driving mechanism for $\alpha \ll 1$ with a velocity $v_2 \approx b_j$.

3. Detection of magnetic order

Since the magnetic state of magnetically ordered systems results from a complex interplay of different interactions between the magnetic moments, depends on history and sample imperfections, it is difficult to predict the domain structure. Both for research and application purposes it is important to be able to detect or image the magnetic state of the sample which may result from the action of one of the driving mechanisms described in chapter 2.

Various methods have been developed to detect magnetic order. In this thesis we focus on imaging, i.e., on methods with a spatial resolution. The basic distinction lies in what they are sensitive to - magnetic stray fields, magnetization, lattice distortions, etc. The first class of methods, which can detect by various means the stray fields (or their gradients) stemming from magnetic domains (or domain walls), is represented by the *Bitter technique* [26], *magnetic force microscopy* [26,107], or the recently developed *nitrogen-vacancy(NV)-center microscopy* [108,109]. More convenient are methods which can directly sense magnetization, such as electron polarization methods [26,110] and *magneto-optical (MO) microscopy* [26,111] which is probably the most commonly used magnetic imaging technique. *Transmission electron microscopy* [26] is in most cases sensitive to the total magnetic flux density, $\mathbf{B} \sim \mathbf{M} + \mathbf{H}$, which deflects the imaging electrons via the Lorentz force. Finally, there are methods sensitive to the tiny lattice distortions caused by magnetic order, such as *X-ray* and *neutron diffraction* techniques [23,26]. The main disadvantage of these methods is that they require large-scale experimental facilities such as a synchrotron or a nuclear reactor.

Besides the actual interaction mechanism which leads to a visualization of magnetic textures, the various methods also differ in the information depth, achievable spatial and temporal resolutions, or the acquisition scheme, i.e., whether they are parallel or scanning. Another important point is the sensitivity to AF order, since AFs have recently gained a considerable attention due to their great application potential in spintronics [6,8]. From the methods mentioned above, neutron diffraction has been traditionally used to study AF ordering. However, this technique requires quite large sample volume and is, therefore, not suited for investigation of thin films or imaging. Another option is to utilize the coupling between an electromagnetic radiation and magnetic moments - the so-called magneto-optical effects [49]. In order to image collinear compensated antiferromagnets, only the second-order MO effects, such as the *Voigt effect* (or *magnetic linear dichroism (MLD)*), are applicable. These effects are usually very weak in the visible or near infrared (NIR) range. On the other hand, for certain X-ray energies the MO response is resonantly enhanced for 3d transition metals or 4f rare earth elements [112]. This also allows for element-specific signal detection. X-ray magnetic linear dichroism in combination with *photoemission electron microscopy* (XMLD-PEEM) [113] has become a well established technique capable of high-resolution imaging of compensated collinear AFs [10,11]. For completeness, we also mention other imaging methods applicable to AFs - *second harmonic generation* [49,114], *spin-polarized scanning tunneling microscopy* [115,116], and *NV-center microscopy* [108,109].

Apart from imaging, various spatially unresolved techniques are commonly used to characterize magnetic samples. Among these, *magnetotransport* measurements represent a big class of methods which utilize the influence of magnetic state on the charge and heat transport. These methods give an integrated information about the area which is defined by the device contact geometry. However, even the magnetotransport effects can be used to obtain a spatially resolved information if the driving force (e.g.

the heat gradient) is applied locally. In chapters 8 and 9 we develop such experimental techniques to image AF domain structures and we, therefore, introduce the underlying magnetotransport effects in the following.

3.1 Magneto-optics

Magneto-optical imaging is based on small alterations of the polarization state of light transmitted through or reflected from a magnetic material. These polarization changes are directly linked to the magnetization orientation in the sample which allows for visualization of the magnetic domain structure in a polarizing microscope [26]. Despite being one of the oldest magnetic imaging techniques, magneto-optics still belongs among the most prominent ones. The main advantage of MO microscopy, when compared to the more sophisticated electron, X-ray, or magnetic force microscopies, is its simplicity and low cost while offering still good (sub-micron) spatial and excellent temporal resolution [111]. These properties make MO microscopy suitable for most domain characterization studies.

3.1.1 Magneto-optical effects

The microscopic origin of MO effects lies in the interplay between the magnetization-induced exchange band-splitting and the spin-orbit coupling [117]. The Zeeman splitting may be induced also by an external magnetic field in a paramagnetic material, as was the case of the originally observed Faraday, Kerr, or Voigt MO effects in the 19th century [118]. MO signal may be induced also by a spin-polarized carrier population in an otherwise nonmagnetic material. In this thesis we focus on the imaging of magnetically ordered materials and in the following we introduce the basic terminology and physics of the magnetization-induced MO effects.

It is easier to understand the MO effects which appear during transmission through a magnetic sample. The presence of magnetization breaks the material's symmetry and makes it optically anisotropic, i.e., the index of refraction depends on the direction of light propagation through that material and on the light polarization. Let's consider the light incidence (described by the wavevector \mathbf{k}) along the sample normal \mathbf{n} ($\mathbf{k} \parallel \mathbf{n}$). We distinguish two MO geometries [118] - the *Faraday geometry* with magnetization pointing along the light propagation ($\mathbf{M} \parallel \mathbf{k}$) and the *Voigt geometry* with $\mathbf{M} \perp \mathbf{k}$. In both geometries there exist two proper light modes which are conserved during their propagation through the magnetic medium. These two proper modes have different complex indices of refraction, n . Consequently, in a general case, an arbitrary incoming polarization state is changed upon transmission through the magnetic medium since any general polarization state can be expressed as a linear combination of the two differently transmitted proper modes.

In the Faraday geometry the two proper modes are the left- (σ^+) and right-handed (σ^-) circular-polarized modes [118]. In a magneto-optical measurement the sample is illuminated by a linearly polarized (σ^0) light which can be expressed as a linear combination of the proper modes, $\sigma^0 = (\sigma^+ + \sigma^-)/2$. The difference in the real part of the refractive indices, $\text{Re}\{n_+\} \neq \text{Re}\{n_-\}$, leads to a phase shift between the two circularly polarized components - the *magnetic circular birefringence* (or *Faraday effect*) - which results in the rotation of the polarization plane of the linearly polarized wave upon transmission through the sample. The difference in the imaginary part of the refractive indices, $\text{Im}\{n_+\} \neq \text{Im}\{n_-\}$, causes an unequal absorption of the two circular modes - the *magnetic circular dichroism* - and the incident linear polarization becomes elliptic upon transmission through the sample.

In the Voigt geometry the two proper modes are the linearly polarized modes parallel (σ^{\parallel}) and perpendicular (σ^{\perp}) to the magnetization [118]. Here, the difference in the imaginary parts of the refractive indices, $\text{Im}\{n_{\parallel}\} \neq \text{Im}\{n_{\perp}\}$ (the *magnetic linear dichroism*), leads to the polarization plane rotation, whereas the difference in the real parts of the refractive indices, $\text{Re}\{n_{\parallel}\} \neq \text{Re}\{n_{\perp}\}$ (the *magnetic linear birefringence*), induces an ellipticity in the originally linear polarization. Both effects are also known as the *Voigt effect*.

Analogous MO effects are observed also upon reflection of a linearly polarized light from a magnetic sample [118]. However, in this case one cannot directly associate the observed polarization rotation (or the induced ellipticity) with either a birefringence or a dichroism of the circularly or linearly polarized proper modes. Both birefringence and dichroism in general take part in the polarization rotation and both contribute to the induced ellipticity. This is because in reflection instead of the refractive index an amplitude reflection coefficient becomes the relevant parameter whose relation to the refractive index is nonlinear. For perpendicular incidence of the linearly polarized wave and $\mathbf{M} \parallel \mathbf{k}$ the difference in magnitudes of the complex reflection coefficients for the circular proper modes, $|r_{+}| \neq |r_{-}|$, induces an ellipticity in the reflected wave while the difference in complex phases of the reflection coefficients, $\arg\{r_{+}\} \neq \arg\{r_{-}\}$, leads to the polarization plane rotation. This effect is known as the *polar Kerr effect*. For $\mathbf{M} \perp \mathbf{k}$, in analogy to the Voigt effect in transmission, $|r_{\parallel}| \neq |r_{\perp}|$ induces a polarization rotation and $\arg\{r_{\parallel}\} \neq \arg\{r_{\perp}\}$ induces an ellipticity. Both the polar Kerr effect (PKE) and the Voigt effect (VE) in reflection were utilized to visualize magnetic domains in this thesis and will be described in more detail in the following. For completeness we note that for inclined light incidence to the sample another two types of Kerr effect are observed which are sensitive to the in-plane magnetization [118] - the *longitudinal Kerr effect* sensitive to the magnetization component parallel to the plane of incidence and the *transverse Kerr effect* sensitive to the magnetization component perpendicular to the plane of incidence.

The crucial difference between the effects observed in the Faraday and the Voigt geometry is that the former are linear in magnetization M whereas the latter are quadratic in M . Therefore, the Kerr effects change sign when \mathbf{M} is reversed while the Voigt effect remains unchanged, unable to distinguish the two antiparallel magnetic states. On the other hand, the odd-in- \mathbf{M} nature of the Kerr effect excludes its existence in compensated collinear AFs while the Voigt effect should be still present since the contributions from the two antiparallel sublattices do not average out.

The MO effects described above directly follow from the bulk properties of a magnetic material by solving the Maxwell's equations supplemented by the material relations connecting all electric and magnetic fields in a given material. Combining these equations we obtain the wave equation [119]

$$\nabla^2 \mathbf{E} - \nabla(\nabla \cdot \mathbf{E}) = \mu \varepsilon \frac{\partial^2 \mathbf{E}}{\partial t^2} + \mu \sigma \frac{\partial \mathbf{E}}{\partial t}, \quad (3.1)$$

where ε and σ are the ac permittivity and conductivity tensors, respectively, containing information about the magnetic properties of the sample. Both ε and σ are spectrally dependent and we take for simplicity μ as a scalar quantity equal to the vacuum permeability μ_0 .¹ Inserting the solution in form of a plane electromagnetic wave, $\mathbf{E}(\mathbf{r}, t) = \mathbf{E}_0 e^{-i(\omega t - \mathbf{k} \cdot \mathbf{r})}$, into the wave equation we obtain

$$k^2 \mathbf{E}_0 - \mathbf{k}(\mathbf{k} \cdot \mathbf{E}_0) - \omega^2 \mu_0 \varepsilon_{ef} \mathbf{E}_0 = 0, \quad (3.2)$$

¹The effect of magnetization on optical constants through the magnetic permeability is about two orders of magnitude smaller than its effect through the permittivity tensor at optical frequencies and can be neglected [26].

where we introduced the effective permittivity $\varepsilon_{eff} = \varepsilon_0 + i\sigma/\omega$ with ε_0 being the vacuum permittivity and σ containing the response of the whole system to perturbing electric field [119]. The origin of the MO effects lies, on the phenomenological level, in the particular dependence of σ on the magnetization which can be calculated for a given material from its electronic band structure [119].

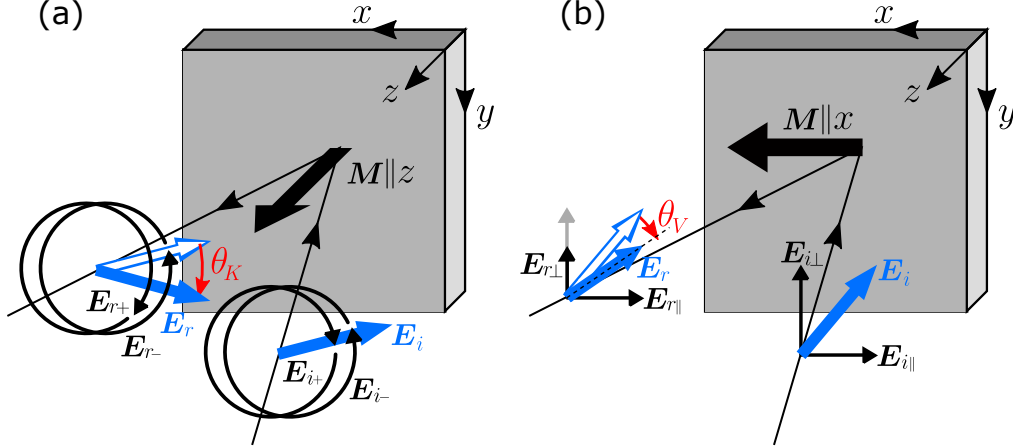


Figure 3.1: Magneto-optical effects in reflection geometry. (a) The polar Kerr effect is proportional to the perpendicular-to-plane magnetization component. The PKE-induced polarization rotation is caused by a difference in the phase-shift between the right-handed (\mathbf{E}_-) and left-handed (\mathbf{E}_+) circularly polarized proper modes upon reflection from the sample. (b) The Voigt effect is proportional to the square of the in-plane magnetization component. The corresponding polarization rotation is caused by a difference in the real amplitude reflection coefficients of the two proper modes linearly polarized parallel (\mathbf{E}_\parallel) and perpendicular (\mathbf{E}_\perp) to the magnetization. In the sketches the light propagates under a non-zero angle of incidence just for clarity.

Polar Kerr effect. For an otherwise isotropic medium, which would be described by a scalar permittivity, the magnetization-induced symmetry-breaking makes ε a tensor quantity which for $\mathbf{M} \parallel \mathbf{k} \parallel \mathbf{n}$ (the geometry of the PKE) being chosen along the z -axis reads [118, 119]

$$\varepsilon_{eff} = \varepsilon_0 \begin{pmatrix} \varepsilon_{xx} & \varepsilon_{xy} & 0 \\ -\varepsilon_{xy} & \varepsilon_{xx} & 0 \\ 0 & 0 & \varepsilon_{zz} \end{pmatrix}, \quad (3.3)$$

where $\varepsilon_{xy} \sim M$. Inserting (3.3) into the wave equation (3.2) and using the relation $k = \omega n \sqrt{\varepsilon_0 \mu_0}$ we get for the electric field components

$$(n^2 - \varepsilon_{xx})E_{0x} - \varepsilon_{xy}E_{0y} = 0 \quad (3.4a)$$

$$\varepsilon_{xy}E_{0x} + (n^2 - \varepsilon_{xx})E_{0y} = 0 \quad (3.4b)$$

$$\varepsilon_{zz}E_{0z} = 0. \quad (3.4c)$$

The last equation gives $E_{0z} = 0$, i.e., the solution is a transverse wave. A nontrivial solution of the first two equations corresponds to a zero determinant which gives the refractive indices of the two proper modes

$$n_{\pm}^2 = \varepsilon_{xx} \pm i\varepsilon_{xy}. \quad (3.5)$$

Inserting this result back to (3.4) yields the relation between the electric field components, $E_{0y} = \pm iE_{0x}$, which corresponds to the left- and right-handed circularly

polarized waves. The Faraday effect in transmission geometry follows directly from the difference in the refractive indices (3.5) [118], as already explained. In reflection we calculate the amplitude reflection coefficients for the circular proper modes via the Fresnel relations, $r_{\pm} = (1 - n_{\pm})/(1 + n_{\pm})$. These complex coefficients can be expressed in an exponential form, $r_{\pm} = r_{0\pm} \exp(i\alpha_{\pm})$.

To obtain the Kerr rotation θ_K and ellipticity ψ_K let's assume a linearly polarized incident wave whose polarization plane makes an angle β_i with the x -axis. Using the Jones matrix formalism [120] we can express the incident wave as

$$\mathbf{E}_{0i} = \begin{pmatrix} E_{0x} \\ E_{0y} \end{pmatrix} \sim \begin{pmatrix} \cos \beta_i \\ \sin \beta_i \end{pmatrix} = \frac{1}{2} \left[e^{-i\beta_i} \begin{pmatrix} 1 \\ i \end{pmatrix} + e^{i\beta_i} \begin{pmatrix} 1 \\ -i \end{pmatrix} \right]. \quad (3.6)$$

By multiplying the two circular proper modes by the respective reflection coefficients we get the reflected wave

$$\mathbf{E}_{0r} \sim \frac{1}{2} \begin{pmatrix} r_{0+} e^{i(\alpha_+ - \beta_i)} + r_{0-} e^{i(\alpha_- + \beta_i)} \\ i r_{0+} e^{i(\alpha_+ - \beta_i)} - i r_{0-} e^{i(\alpha_- + \beta_i)} \end{pmatrix}, \quad (3.7)$$

which is in general an elliptically polarized wave. The orientation of its semi-major axis β_r and its ellipticity ψ_r ² can be obtained using the following relations [118]

$$\chi \equiv \frac{E_{0y}}{E_{0x}} \quad \tan 2\beta = \frac{2\text{Re}\chi}{1 - |\chi|^2} \quad \sin 2\psi = \frac{2\text{Im}\chi}{1 + |\chi|^2}. \quad (3.8)$$

Applied to (3.7) we get after straightforward manipulations simple results for the polar Kerr rotation and ellipticity, respectively

$$\theta_K \equiv \beta_r - \beta_i = \frac{1}{2}(\alpha_- - \alpha_+) \quad \psi_K \equiv \psi_r = \frac{1}{2} \arcsin \left(\frac{r_{0+}^2 - r_{0-}^2}{r_{0+}^2 + r_{0-}^2} \right) \approx \frac{1}{2} \left(\frac{r_{0+}}{r_{0-}} - 1 \right). \quad (3.9)$$

Importantly, the obtained polar Kerr rotation and ellipticity are independent of the polarization plane orientation β_i of the incident wave which is the consequence of the axial symmetry of the system. The approximate relation for ψ_K holds if the magnetization-induced polarization changes are small, i.e. for $|\varepsilon_{xy}| \ll |\varepsilon_{xx}|$. In the same approximation one can rewrite the refractive indices (3.5) as $n_{\pm} \approx \sqrt{\varepsilon_{xx}} [1 \pm (i/2)(\varepsilon_{xy}/\varepsilon_{xx})]$ and express the polar Kerr rotation and ellipticity in a unified way by a complex Kerr angle [118]

$$\tilde{\theta}_K \equiv \theta_K + i\psi_K = \frac{\varepsilon_{xy}}{\sqrt{\varepsilon_{xx}}(1 - \varepsilon_{xx})}. \quad (3.10)$$

Since $\varepsilon_{xy} \sim M$ the Kerr effect is linear in M and switches sign when the magnetization is reversed. The proportionality of the Kerr effect to the off-diagonal component of the permittivity (or conductivity) tensor points to the correspondence between this effect and the anomalous Hall effect (AHE) which arises from the odd-in- \mathbf{M} transverse conductivity in transport measurements [119].

Voigt effect. In the Voigt geometry, $\mathbf{M} \perp \mathbf{k} \parallel \mathbf{n}$, and choosing the in-plane magnetization along the x -axis the permittivity tensor is obtained from (3.3) by a permutation of indices [119]

$$\varepsilon_{eff} = \varepsilon_0 \begin{pmatrix} \varepsilon_{xx} & 0 & 0 \\ 0 & \varepsilon_{yy} & \varepsilon_{yz} \\ 0 & -\varepsilon_{yz} & \varepsilon_{yy} \end{pmatrix}. \quad (3.11)$$

²Ellipticity is defined as $\tan \psi \equiv a_{min}/a_{maj}$, where a_{maj} and a_{min} are the semi-major and semi-minor axes of the polarization ellipse, respectively.

After inserting the permittivity tensor into (3.2) the condition of a zero determinant gives the refractive indices for the two proper modes

$$n_{\parallel}^2 = \varepsilon_{xx} \quad (3.12a)$$

$$n_{\perp}^2 = \varepsilon_{yy}(1 + \varepsilon_{yz}^2/\varepsilon_{yy}^2). \quad (3.12b)$$

Solving the wave equation (3.2) with the refractive indices (3.12a) and (3.12b) gives the electric fields $E_{0\parallel} = E_{0x}(1, 0, 0)$ and $E_{0\perp} = E_{0y}(0, 1, \varepsilon_{yz}/\varepsilon_{yy})$, respectively. Since the MO effects are weak, $\varepsilon_{yz}/\varepsilon_{yy} \ll 1$, we can conclude that the proper modes in the Voigt geometry are transverse waves linearly polarized parallel and perpendicular to the magnetization.

The Voigt-effect-induced polarization rotation and ellipticity upon transmission through the sample follow directly from the differences in imaginary and real parts of the refractive indices (3.12) [118], respectively. In a reflection geometry we again obtain the amplitude reflection coefficients using the Fresnel relations, $r_{\parallel} = (1 - n_{\parallel})/(1 + n_{\parallel})$, where $r_{\parallel} = r_{0\parallel} \exp(i\alpha_{\parallel})$, and analogically for r_{\perp} . Assuming again the incident wave with a linear polarization of arbitrary orientation β_i , the reflected wave $\mathbf{E}_r = \begin{pmatrix} \cos \beta_i r_{\parallel} \\ \sin \beta_i r_{\perp} \end{pmatrix}$ and $\chi = \tan \beta_i (r_{0\perp}/r_{0\parallel}) e^{i(\alpha_{\perp} - \alpha_{\parallel})}$. Using the formulae (3.8) and under the assumption of weak MO-induced polarization changes we obtain the Voigt rotation and ellipticity

$$\theta_V \equiv \beta_r - \beta_i = \sin 2\beta_i \frac{1}{2} \left(\frac{r_{0\perp}}{r_{0\parallel}} - 1 \right) \quad \psi_V \equiv \psi_r = \sin 2\beta_i \frac{1}{2} (\alpha_{\perp} - \alpha_{\parallel}). \quad (3.13)$$

Unlike in the case of the polar Kerr effect, the Voigt effect depends on the incident polarization since the in-plane magnetization breaks the axial symmetry. Let's consider only the rotation for simplicity, i.e., r_{\perp}/r_{\parallel} is real. Then θ_V can be expressed as [119]

$$\theta_V \approx \frac{n_0 \sin 2\beta_i}{2(n_0^2 - 1)} \left(\varepsilon_{xx} - \varepsilon_{yy} - \frac{\varepsilon_{yz}^2}{\varepsilon_{yy}} \right), \quad (3.14)$$

where $n_0 = \sqrt{\varepsilon_{eff}/\varepsilon_0}$ is the isotropic refractive index of the medium in the absence of magnetization. Since $\varepsilon_{xx} - \varepsilon_{yy}$ is even in magnetization due to the Onsager relations [119] and ε_{yz} is odd in \mathbf{M} , the Voigt effect is quadratic in M in the leading order. Usually it is satisfied that $\varepsilon_{yz}/\varepsilon_{yy} \ll 1$ and the Voigt effect is generated purely by the difference in the diagonal components of the permittivity (or conductivity) tensor and is, therefore, intimately linked to the anisotropic magnetoresistance (AMR) effect observed in transport measurements [119].

3.1.2 Magneto-optical microscopy

The magnetization-dependent changes in polarization of light transmitted through or reflected from a magnetic sample are used to visualize the magnetic domain structure in polarizing (magneto-optical) microscopes [26, 111, 121]. As discussed above, the MO effects cause a rotation of the incident linear polarization and make it slightly elliptic. An elliptically polarized light can be converted to a linearly polarized light by a phase compensator, e.g., a quarter-wave plate. Therefore, we will omit ellipticity and consider only the MO-induced polarization rotation θ .

The basic idea of a polarizing microscope is to convert the light polarization changes to light intensity changes via a polarizer (see the inset of Fig. 3.2). We distinguish two main microscope schemes - a *laser-scanning* microscope [121] and a *wide-field* microscope [26, 111]. In the former case, the polarization rotation is measured locally

using a focused laser spot and the sample image is assembled from such individual measurements performed in each point of a grid while scanning the laser spot over the sample surface. This “serial” technique has an obvious disadvantage of a long acquisition time. On the other hand, it is perfectly suited for using lasers benefiting from their stability and it allows for using highly sensitive “lock-in” detection schemes based on, e.g., an optical bridge or a photoelastic modulator.

In this thesis, we utilized the wide-field MO microscopy in which the information from the whole viewfield is acquired in parallel. To put it simply, it is an ordinary optical microscope equipped by a couple of polarizers, as shown in Fig. 3.2. To suppress or visualize the ellipticity additional components such as a phase compensator are needed. To reach a high image contrast it is also important to minimize unwanted (other than MO-induced) polarization changes in the setup caused, e.g., by a strain in the optical components or by light scattering.

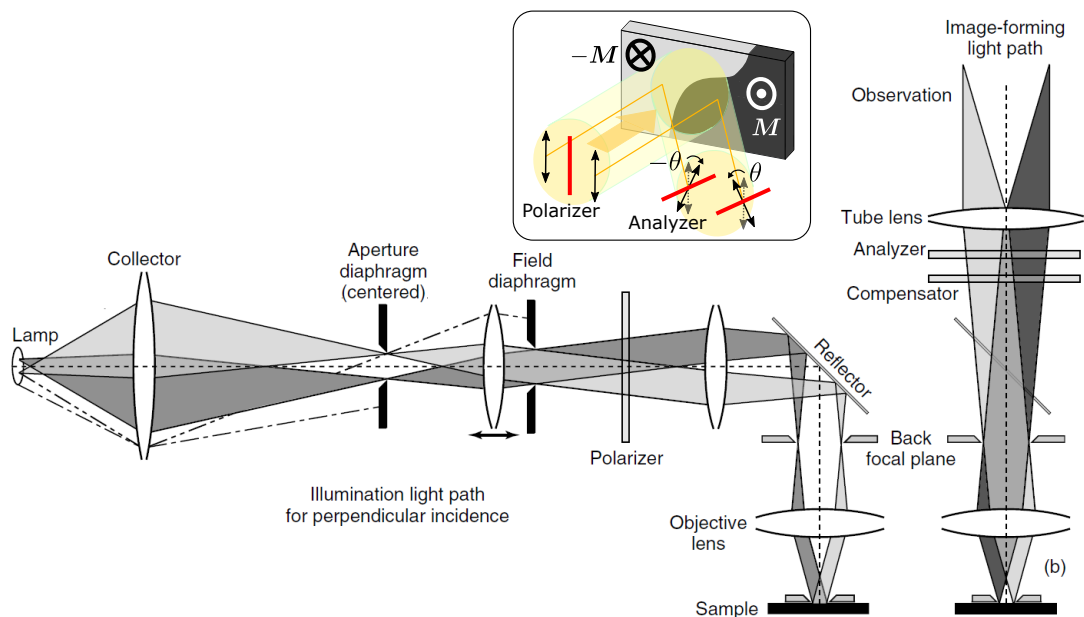


Figure 3.2: Wide-field MO microscope. Sketch of the Köhler setup for homogeneous illumination [121]. The aperture diaphragm sets the range of the angles of incidence of the light illuminating the sample. The field diaphragm sets the illuminated area on the sample surface. The imaging path is shown separately for clarity. Inset: The working principle of a MO microscope. The difference in polarization plane orientation upon reflection of a linearly polarized light from oppositely magnetized domains is converted by an analyzer into the difference in intensity which can be detected by a CCD camera.

The wide-field MO microscopes usually employ the Köhler illumination technique [121] depicted in Fig. 3.2. The light source (typically an arc discharge lamp or an LED) is first projected by the collector lens onto the aperture diaphragm whose lateral position sets the angle of incidence of the light on the sample surface. Here it is centered creating a symmetric light cone illuminating the sample. Under such conditions from the Kerr effects only the polar one gives a net contribution to the polarization rotation. To be sensitive to the in-plane magnetization via the longitudinal or transverse Kerr effects the aperture diaphragm has to be shifted off-axis choosing the corresponding angle of incidence of the light on the sample. Behind the second lens there is a plane conjugated to the sample surface plane where the field diaphragm is placed selecting which part of the sample is illuminated. After setting the linear polarization by a polarizer, the third lens images the light source into the back focal plane of the objective lens which then converts each point of this image into a bunch of parallel rays illumi-

nating the sample. This ensures a homogeneous illumination of the sample. The light reflected from each point of the sample is then converted to a bunch of parallel rays by the infinity-corrected objective lens, passes the compensator and analyzer and is focused by the tube lens creating a primary image. This image may be detected by a CCD chip or observed via an eyepiece.

The mechanism which creates an observable contrast in the MO microscope is sketched in the inset of Fig. 3.2. The polarization plane of a linearly polarized light reflected from the two oppositely magnetized domains gets rotated via PKE by the same angle θ but in opposite sense. With an analyzer set perpendicular to the polarizer no contrast would be observable since the light from the two domains would be quenched by the same amount. However, by rotating the analyzer by θ from that symmetric position the light from one of the domains is totally blocked while the light from the other domain is still partially transmitted giving the maximum contrast. In reality, due to imperfect polarizers and depolarization effects on the optical surfaces in the microscope [122], for any orientation of the analyzer there is always light coming through it that is creating a non-magnetic background in the image. This leads to a decrease of the visual contrast and to an increase of the optimal analyzer opening angle, as shown below. The undesirable background intensity can be removed by a subtraction of a reference image taken in a state with a fixed magnetization orientation, e.g., in the magnetically saturated state. This subtraction procedure highlights the changes in magnetization orientation with respect to the reference state and, consequently, it allows to detect magnetization-induced polarization rotations of the order of 100 μrad .

To evaluate the visual contrast between differently oriented magnetic domains observed in a MO microscope we choose the polarization basis given by the incident linear polarization and the orthogonal one and we consider a small magnetization-induced polarization rotation $\theta \ll 1$ upon reflection from the sample. The electric field of the reflected wave has a component \mathbf{E}_N along the incident electric field, which corresponds to a regular reflection (for $M = 0$), and a MO-induced component $\mathbf{E}_{MO} \sim M$ or M^2 along the perpendicular direction. Let's consider two magnetic domains with opposite out-of-plane magnetizations observed via the PKE in the Faraday geometry or two domains with mutually orthogonal in-plane magnetizations observed via the VE in the Voigt geometry. In both cases the polarization plane of light reflected from the two domains is rotated by the same angle but in opposite sense, i.e., the electric field reflected from the two domains is $\mathbf{E}_r = \mathbf{E}_N \pm \mathbf{E}_{MO}$ and $\theta \approx \pm E_{MO}/E_N$. The light intensity detected after reflection from the two domains and passing through an analyzer rotated by an angle of $\pi/2 + \alpha$ from the incident polarization direction reads

$$I_{1,2} = E_N^2 \sin^2(\alpha \pm \theta) + I_0 \approx (E_N \sin \alpha \pm E_{MO} \cos \alpha)^2 + I_0, \quad (3.15)$$

where I_0 is the background intensity 'leaking' through the setup because of the imperfect polarizers and the depolarization effects [122]. The visual contrast between the domains is defined as [26]

$$C_{MO} = \frac{I_1 - I_2}{I_1 + I_2}. \quad (3.16)$$

The optimal orientation of the analyzer to reach the maximum contrast is given by the condition $dC_{MO}/d\alpha = 0$ which yields [26]

$$\tan \alpha_C^{opt} = \sqrt{\frac{E_{MO}^2 + I_0}{E_N^2 + I_0}} \quad (3.17a)$$

$$C_{MO}^{opt} = \frac{E_{MO}E_N}{\sqrt{(E_{MO}^2 + I_0)(E_N^2 + I_0)}} \approx \frac{E_{MO}}{\sqrt{E_{MO}^2 + I_0}}, \quad (3.17b)$$

where the second expression in (3.17b) holds for weak depolarization $I_0 \ll E_N^2$.

C_{MO} is not the only important parameter. In addition, the visibility of domains is strongly affected by a signal-to-noise ratio r_{SN} . The main noise sources are the *shot noise* resulting from the quantized nature of light, the *electronic noise* given by the detection apparatus, and the noise caused by fluctuations of the light source, the optical setup and the sample. The latter is proportional to the incident light intensity I_i . In modern MO microscopes the image is usually captured by a CCD camera for which the electronic noise is mainly given by the *dark current* and the *readout noise* which are independent of I_i . In modern cameras the electronic noise is significantly suppressed and in an ideal case the main issue is the shot noise which is proportional to the square root of the reflected light intensity, $N_{shot} = \sqrt{(I_1 + I_2)/2}$. The relevant signal is $S_{MO} = I_1 - I_2$ and therefore, $r_{SN} = (I_1 - I_2)/\sqrt{(I_1 + I_2)/2}$. The condition $dr_{SN}/d\alpha = 0$ gives the optimal angle of the analyzer to maximize r_{SN} [26]

$$\tan \alpha_{SN}^{opt} = \sqrt[4]{\frac{E_{MO}^2 + I_0}{E_N^2 + I_0}} = \sqrt{\tan \alpha_C^{opt}} \quad (3.18a)$$

$$r_{SN}^{opt} = \frac{4E_{MO}E_N}{\sqrt{(E_{MO}^2 + I_0)} + \sqrt{(E_N^2 + I_0)}} \approx 4E_{MO}, \quad (3.18b)$$

where the last expression is again valid for $I_0 \ll E_N^2$. Since $\alpha \ll 1$, $\alpha_{SN}^{opt} > \alpha_C^{opt}$ and the best domain visibility is obtained when turning the analyzer slightly beyond α_C^{opt} . It is also worth noting that for $I_0 \ll E_N^2$ the crucial parameter (the figure of merit) for the domain visibility is only the MO-induced field amplitude E_{MO} and the background intensity I_0 , not the MO rotation angle θ [26]. Since E_{MO} increases with the incident light intensity, MO microscopy requires powerful light sources. After setting the optimal analyzer angle, the image r_{SN} can be further enhanced by long exposure times and image averaging, provided that the domain pattern is static.

3.1.3 Dynamic magneto-optical measurements

Combination of MO effects with ultrashort laser pulses allows to study an evolution of a magnetization state with a sub-picosecond resolution directly in the time domain [123]. In the so-called *pump-probe* experiment the sample is first excited by a strong (pump) laser pulse which temporarily modifies its properties - both magnetic (magnetization magnitude and direction) and optical (nonmagnetic refractive index). With a certain time delay a weaker (probe) laser pulse interacts with the excited material whose modified properties imprint into the probe pulse properties - intensity and polarization. This process is repeated at a MHz repetition rate of the pulsed laser for a given time-delay and the probe pulses are averaged by a detector to build up a sufficiently strong signal. By an analysis of the detected probe light the state of the sample at the particular time-delay after the excitation can be inferred and by changing the time-delay a temporal evolution the sample state is straightforwardly obtained.

During the measurement, the pump beam is periodically modulated (e.g. by an optical chopper). Consequently, the probe signal measured at the modulation frequency corresponds to the pump-induced changes in the probe pulses, which are mediated by the perturbed sample state. In other words, the relative change of the probe properties with respect to the reference sample state (without excitation) is measured. The pump-probe method is inherently immune against certain experimental artifacts present in a single-beam (static) experiment since the signal arises only from the area where the pump- and probe-beam foci overlap, i.e., only from the excited sample.

The pump-probe technique has become particularly successful in semiconductors [124]. The relative change in intensity of the probe pulses is caused by the changes in occupation of the electronic bands induced by an absorption of the pump pulse and gives information about the photo-excited carrier dynamics [125, 126]. The relative change in polarization of the probe pulses is linked via the MO effects to the pump-induced magnetization (or carrier spin) dynamics [127, 128]. Since the different MO effects, which are sensitive to different magnetization spatial components, have different properties the measured MO signal can be decomposed to the individual contributions and the pump-induced magnetization-vector motion can be traced in 3D at a sub-ps timescale [129].

3.2 Magnetotransport effects

The presence of an external magnetic field (or magnetization) in a material modifies its transport properties and we speak about ordinary (or anomalous) magnetotransport effects [19, 130]. Depending on the nature of the driving force, we distinguish the *spin-electronic effects*, where the carrier transport is induced by an electric field, and the *spin-caloritronic effects* [130], where the carriers are driven by a thermal gradient. The magnetotransport effects may be also classified based on the experimental geometry (let's restrict ourselves only to thin magnetic films). In the *Hall geometry*, the magnetization \mathbf{M} is perpendicular to the film plane in which the driving force is applied and the resulting anomalous transport is induced in the film plane in a direction perpendicular to the driving force. This is the case of, e.g., anomalous Hall [131, 132] and Nernst [130] effects. If magnetization lies in the sample plane, it induces a difference between the transport in the direction parallel and perpendicular to \mathbf{M} . This results in the anisotropic magnetoresistance [19] and anisotropic magneto-thermopower [130].

3.2.1 Spin-electronic effects

When an electric field \mathbf{E} is applied in a conductive material, the resulting current density \mathbf{j} is given by the Ohm's law

$$\mathbf{j} = \hat{\sigma} \mathbf{E}, \quad (3.19)$$

where the electrical conductivity tensor $\hat{\sigma}$ is the inverse of the resistivity tensor, $\hat{\rho} \equiv \hat{\sigma}^{-1}$. In an otherwise isotropic material, which would be described by scalar ρ and σ , the presence of magnetic induction \mathbf{B} (and/or magnetization \mathbf{M}) and the spin-orbit coupling breaks the symmetry [132]. This results in non-zero off-diagonal elements of $\hat{\rho}$ and $\hat{\sigma}$, which manifests itself as the *Hall effect*, and in the inequivalence of the diagonal elements, which is the cause of the *anisotropic magnetoresistance*.

Anomalous Hall effect (AHE). For a cubic lattice system and $\mathbf{B} \parallel \mathbf{M}$ pointing along z -axis the resistivity tensor reads [132]

$$\hat{\rho} = \begin{pmatrix} \rho_{xx} & -\rho_H & 0 \\ \rho_H & \rho_{xx} & 0 \\ 0 & 0 & \rho_{zz} \end{pmatrix}. \quad (3.20)$$

Here, ρ_H is the transverse (or Hall) resistivity comprising the magnetic field-induced (ordinary) part ρ_H^O and the magnetization-induced (extraordinary or anomalous) part ρ_H^A . In a magnetically saturated state, $M = M_s$, the total Hall resistivity can be expressed as [132]

$$\rho_H = \rho_H^O + \rho_H^A = R_0 B + R_A \mu_0 M_s, \quad (3.21)$$

where R_0 and R_A are the ordinary and anomalous Hall coefficients, respectively, and $\mathbf{B} = \mu_0 \mathbf{H}_{ext}$ for a thin film.³ The ordinary and anomalous contributions to the Hall resistivity can be distinguished by measuring its dependence on magnetic field. For high enough fields, in a magnetically saturated state, only the OHE contributes to the resistivity change with a slope proportional to R_0 . Extrapolation of this linear dependence to $B = 0$ gives the anomalous resistivity, as shown in Fig. 3.3(d).

The OHE is caused by the Lorentz force which deflects the itinerant carriers in a direction that is perpendicular to the applied electric and magnetic fields [19]. The carriers accumulate at the sample edge resulting in a transverse (Hall) voltage, as depicted in Fig. 3.3(a). In section 2.4.3 we already introduced the spin Hall effect [81] which arises from the SOC-induced deflection of carriers with opposite spins to the opposite transverse directions. In a non-magnetic material, where the carriers are not spin-polarized, this effect results in opposite spin accumulations on the opposite sample edges which is not accompanied by any charge imbalance [see Fig. 3.3(b)]. The anomalous Hall effect arises in FMs from the very same physical processes as those leading to the SHE in PMs, namely the skew scattering, the side-jump, and the intrinsic effects [76, 80, 81] [see section 2.4.3]. In a FM, the carriers which form the electrical current have their spins preferentially oriented in one direction and the spin-dependent carrier deflection thus results in both the spin and charge accumulation on the sample

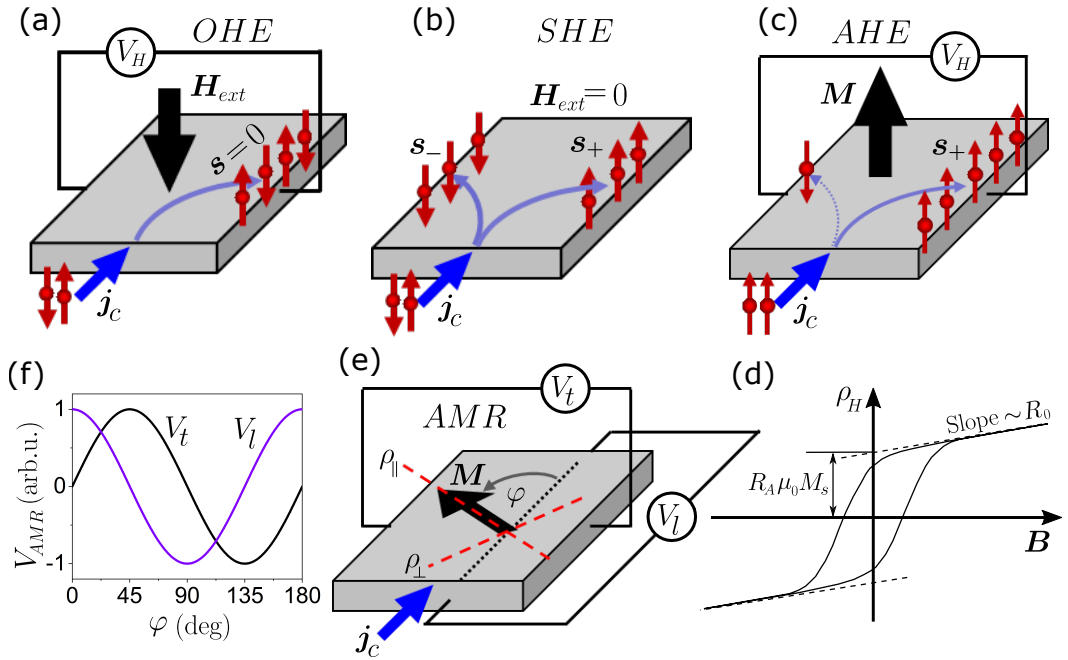


Figure 3.3: The Hall effects and anisotropic magnetoresistance. (a) Ordinary Hall effect, caused by the Lorentz force, induces a transverse voltage but no spin accumulation. (b) Spin Hall effect in a PM, induced by a spin-dependent deflection of charge carriers, results in a transverse spin accumulation but no voltage. (c) Anomalous Hall effect in a FM, induced by the same mechanisms as SHE, results in both transverse spin and charge accumulations. (d) Hysteretic dependence of the total resistivity on magnetic field allows to separate the (always present) linear OHE contribution from AHE in FMs. (e) Longitudinal (V_l) and transverse (V_t) anisotropic magnetoresistance caused by the difference in the material's resistivity along and perpendicular to magnetization. (f) Dependence of V_l and V_t on the magnetization orientation relative to the current direction.

³The experimentally relevant (applied) field is the magnetic intensity \mathbf{H}_{ext} . On the other hand, for OHE, the magnetic flux density $\mathbf{B} = \mu_0(\mathbf{H}_{ext} + \mathbf{H}_d + \mathbf{M})$ is relevant. However, for a perpendicularly magnetized thin film the demagnetizing field $\mathbf{H}_d = -\mathbf{M}$, i.e., $\mathbf{B} = \mu_0 \mathbf{H}_{ext}$.

edges, as depicted in Fig. 3.3(c).

The AHE, generated by the off-diagonal resistivity (conductivity) tensor elements, share the same origin with the MO polar Kerr effect described in section 3.1.1. In this correspondence, the electrical current direction in AHE plays the role of the light linear polarization direction in PKE. Both effects are directly proportional to the perpendicular-to-plane component of magnetization [cf. Eqs. (3.10) and (3.21)]. In the case of PKE this allows for an imaging of magnetic domains with a light wavelength-limited spatial resolution [see section 3.1.2]. AHE lacks the spatial resolution but can be utilized to determine the position of a single DW in a cross-shaped device (Hall cross) with a nanometer-scale precision, as demonstrated in [132] and summarized in appendix F.

Anisotropic magnetoresistance (AMR). In the case of an in-plane magnetized material (e.g., for \mathbf{M} along the x -axis), the resistivity tensor is obtained from Eq. (3.20) by a permutation of indices (as was done with permittivity to derive the Voigt effect, see section 3.1.1). The resistivity becomes anisotropic within the sample plane due to the inequivalence $\rho_{xx} \neq \rho_{yy}$. In the following we adopt, in analogy to the VE, the notation ρ_{\parallel} and ρ_{\perp} instead of ρ_{xx} and ρ_{yy} for the resistivities in the directions parallel and perpendicular to \mathbf{M} , respectively. When the magnetization is rotated within the sample plane, the resistivity measured in the direction of the current flow follows a harmonic dependence on the angle φ between the direction of \mathbf{M} and the current [19]

$$\rho_l = \rho_0 + \frac{\Delta\rho}{2} \cos 2\varphi, \quad (3.22)$$

which is known as the *longitudinal AMR* [see Figs. 3.3(e, f)]. Here, $\rho_0 = (\rho_{\parallel} + \rho_{\perp})/2$ is the average resistivity and $\Delta\rho = \rho_{\parallel} - \rho_{\perp}$ is the resistivity anisotropy.

In a Hall-cross geometry AMR also gives rise to a φ -dependent voltage measured on the transverse contacts. The transverse resistivity follows the same dependence, which is just shifted in φ by $\pi/4$ [19]

$$\rho_t = \frac{\Delta\rho}{2} \sin 2\varphi. \quad (3.23)$$

This effect is known as the *transverse AMR* or the *planar Hall effect* [see Figs. 3.3(e, f)].

As already mentioned, AMR is related to the MO Voigt effect. There, the difference in reflection of the optical wave components polarized parallel and perpendicular to \mathbf{M} leads to the polarization rotation, i.e., to induction of a wave component that is polarized perpendicular to the incident wave. This is analogous to the transverse AMR where an electric field component (voltage) transverse to the current flow is induced. Both effects share the same angular dependence with maximum magnitude and opposite signs for $\varphi = \beta_i = \pm\pi/4$ [cf. Eqs. (3.23) and (3.13)]. The longitudinal AMR corresponds directly to the definition of the VE, i.e., to the difference in the reflection for the parallel and perpendicular polarization, if we exchange the reflection coefficients with the resistivities for the parallel and perpendicular current. The VE could be in principle also measured as the difference of the reflected intensities of light polarized parallel and perpendicular to \mathbf{M} , however, this technique is less sensitive than the detection of the polarization rotation.

The disadvantage of AMR for determination of the magnetization direction is that this effect is, like the VE, even in \mathbf{M} , i.e., it cannot distinguish antiparallel magnetic states in a FM. This, however, becomes an advantage when it comes to AFs. Unlike AHE, AMR is present in compensated collinear AFs, such as CuMnAs [10]. Moreover,

it has been demonstrated recently that a second-order AMR effect allows to distinguish the AF states with antiparallel Néel vectors [133].

3.2.2 Spin-caloritronic effects

Besides the electric field, carrier transport can be induced also by a temperature gradient. In a conductor, the temperature broadening of the Fermi-Dirac distribution function in the hot region is accompanied by a diffusion of the hot electrons and holes towards the cold region (see Fig. B1 in Ref. [130]). Since the conductivity is energy-dependent in the vicinity of the Fermi level (e.g., larger for electrons than for holes) the heat current is accompanied also by a nonzero charge current. This is the essence of the Seebeck effect.

Generally, the relationship between the local driving forces - the electric field $\mathbf{E} = -\nabla\phi$ (electrical potential gradient) and the temperature gradient ∇T - and the induced heat (\mathbf{j}_Q) and charge (\mathbf{j}_c) currents can be expressed as [130]

$$\begin{pmatrix} \mathbf{E} \\ \mathbf{j}_Q \end{pmatrix} = \begin{pmatrix} 1/\sigma & S \\ \Pi & \kappa \end{pmatrix} \begin{pmatrix} \mathbf{j}_c \\ -\nabla T \end{pmatrix}, \quad (3.24)$$

where σ and κ are the electrical and thermal conductivities and S and Π are the Seebeck and Peltier coefficients, respectively. Provided that the conductivity variation in the vicinity of the Fermi energy E_F is linear on the scale of the thermal energy $k_B T$, i.e. $(k_B T)^2 |(\partial^2 \sigma(E)/\partial E^2)|_{E_F} \ll \sigma(E_F)/(\pi^2/3e^2)$, the Seebeck coefficient is obtained as [130]

$$S = -\frac{\pi^2 k_B^2 T}{3e} \frac{\partial}{\partial E} \ln \sigma(E)|_{E_F}. \quad (3.25)$$

In the presence of magnetization and SOC, the conductivity and, consequently, the Seebeck coefficient become anisotropic due to the broken symmetry, i.e., the Seebeck coefficient can be expressed in the form of a matrix analogous to (3.20) [134]. For magnetic moments along in-plane x -axis we have [cf. Eq. (3.11)]

$$\hat{S} = \begin{pmatrix} S_{\parallel} & 0 & 0 \\ 0 & S_{\perp} & -S_N \\ 0 & S_N & S_{\perp} \end{pmatrix}. \quad (3.26)$$

The off-diagonal matrix elements (S_N) induce the *anomalous Nernst effect* (ANE) - the thermal equivalent to AHE - and the unequal diagonal matrix elements ($S_{\parallel} \neq S_{\perp}$) lead to the anisotropic magneto-Seebeck effect (AMSE) - the thermal equivalent to AMR [134].

Anomalous Nernst effect (ANE). The Nernst voltage can be expressed in a form analogous to Eq. (3.21) comprising the ordinary (magnetic field-dependent, ONE) and anomalous (magnetization-dependent, ANE) contribution. The description and geometries of ONE and ANE are identical to those depicted in Figs. 3.3(a) and (c), respectively, with the electrical current density \mathbf{j}_c replaced by temperature gradient ∇T . The linear dependence of ANE on the magnetization component perpendicular to ∇T and the voltage measurement direction ($V_{ANE} \sim M_s |\nabla T| \sin \varphi$) can be utilized to determine the magnetization direction or a DW position in a FM sample [51, 135, 136]. Here, ANE has a major advantage, compared to AHE, that the thermal gradient can be applied also perpendicular to a simple magnetic bar, i.e., it is not limited to cross-bar structures. Such ANE measurement using side heaters along a magnetic bar with perpendicular-to-plane magnetic anisotropy allowed us to determine the position of a

single DW in the bar with $\lesssim 20$ nm precision [51]. Moreover, one can even apply the temperature gradient in the direction perpendicular to the sample plane, which allows to detect in-plane magnetization [137]. We utilized this geometry in the experiments on imaging of the domain structure in a non-collinear AF Mn_3Sn which are presented in chapter 8. In this material the linear-in-M effects, such as PKE, AHE, and ANE, are present due to the non-collinear spin arrangement [138].

Anisotropic magneto-Seebeck effect (AMSE). The magnetization-induced anisotropy manifests itself also as a difference between the Seebeck coefficients in cases of magnetization pointing parallel and perpendicular to the heat gradient [134]. In analogy to AMR, the electromotive forces generated in longitudinal (parallel to ∇T) and transverse (perpendicular to ∇T) directions when magnetization is rotated in the sample plane follow the same harmonic dependencies [cf. Eqs. (3.22) and (3.23)]

$$E_l = -(S_0 + \frac{\Delta S}{2} \cos 2\varphi)|\nabla T| \quad E_t = -\frac{\Delta S}{2} \sin 2\varphi|\nabla T|, \quad (3.27)$$

where $S_0 = (S_{\parallel} + S_{\perp})/2$ and $\Delta S = S_{\parallel} - S_{\perp}$ and φ describes the angle between \mathbf{M} and ∇T . This effect is called the anisotropic magneto-Seebeck effect (AMSE) or, alternatively, anisotropic magneto-thermopower [134, 139]. The transverse AMSE is also known as the *planar Nernst effect* [140]. As a thermal analogue to the VE and AMR, AMSE should be also present in compensated collinear AFs, such as CuMnAs. This, and the possibility to apply easily local thermal gradients via focussed electromagnetic radiation [136], motivated us to the development of an AMSE-based imaging method which allowed us to visualize the domain structure of CuMnAs in a table-top experiment. The imaging method and its application to CuMnAs is presented in chapter 9.

4. Studied materials

4.1 (Ga,Mn)As and (Ga,Mn)(As,P)

Standard ferromagnets are usually metals, such as transition metal FMs (Fe, Co, Ni, and their compounds), reaching often high T_C . In these materials the exchange interaction couples the magnetic atoms directly. The metallic behaviour is useful for data storage but problematic for utilization in logic applications. From this point of view, diluted magnetic semiconductors (DMSs) represent an attractive material class since they show ferromagnetic properties which are tunable by doping, external electric fields [141], or illumination [142] thanks to their semiconducting nature. (Ga,Mn)As [143, 144] is the most prominent and best explored representative of the DMS class.

Despite being limited by the low ordering temperature ($T_C \lesssim 190$ K), (Ga,Mn)As has become a test-bed material for new spintronic effects [25, 38] as well as for developing proof-of-principle spintronic devices [145]. This is due to the unique combination of robust and tunable ferromagnetism, direct band gap, and strong spin-orbit interaction. In the experiments described in this thesis, we utilized mainly two properties of (Ga,Mn)As and (Ga,Mn)(As,P) - the extraordinarily strong second-order MO response [146] (chapter 5) and, conversely, the strong response of the magnetism to a circularly polarized light observed as the optical STT [38] (chapter 6). In the following, most of the information about (Ga,Mn)As is true also for (Ga,Mn)(As,P) [147], which differs mainly in the magnetic anisotropy (MA), as discussed at the end of this section.

$\text{Ga}_{1-x}\text{Mn}_x\text{As}$ is derived from the well-understood semiconductor GaAs with a zincblende crystal structure in which a small fraction ($\approx 1\text{--}10\%$) of the gallium atoms is replaced by manganese, as illustrated in Fig. 4.1(a). The Mn atoms deliver permanent magnetic moments (spin $S = 5/2$) due to the half-filled d -shell and, at the same time, they serve as acceptors providing one free hole per atom due to the missing p -electron. The nature of the ferromagnetic coupling in (Ga,Mn)As [24, 144] is illustrated in Fig. 4.1(b-d). Pure manganese itself would be antiferromagnetic, however, when diluted in (Ga,Mn)As the individual Mn atoms are too far from each other and the short-range direct exchange is not strong enough to align the moments (b). The holes introduced into the material are antiferromagnetically exchange-coupled to the localized Mn spins. The holes in close proximity to a given Mn atom align their spin antiparallel to that Mn $5/2$ -spin. Conversely, the Mn spins that overlap with the spatially extended hole wavefunction tend to align antiparallel to its spin, i.e., parallel to each other (c). For large enough hole density the parallel alignment of the Mn moments spreads to the whole crystal (d). This kind of indirect carrier-mediated exchange is known as the Zener's kinetic-exchange interaction [24].

In order to prevent formation of the thermodynamically more stable MnAs inclusions, (Ga,Mn)As is prepared by a molecular beam epitaxy at a relatively low temperature ($\approx 250^\circ\text{C}$) [148]. Consequently, the epitaxial layers contain a significant density of point defects [144]. The most common ones are the manganese interstitials (Mn_I) and the anti-site defects (As_{Ga}) shown in Fig. 4.1(a). Both defects serve as double donors compensating two free holes per atom. Since the strength of the FM coupling in (Ga,Mn)As scales with the hole density these defects are highly undesired. Moreover, the magnetic moments of Mn_I align antiparallel to the moments of the Mn atoms at the cation lattice-sites reducing the total magnetization.

It turned out that the carrier density and T_C of the material can be significantly increased by a proper post-growth thermal treatment [144]. Annealing at relatively low temperatures causes Mn_I diffusion towards the free surface of the (Ga,Mn)As layer

where it gets passivated by oxidation. By careful optimization of the synthesis and annealing procedures for layers with different Mn content, as performed in [148], the hole compensation by defects can be completely suppressed. Consequently, clear dependencies of transport and magnetic parameters, such as the hole density, the saturation magnetization, T_C , or the MA on the Mn content were observed for this high-quality sample series [41].

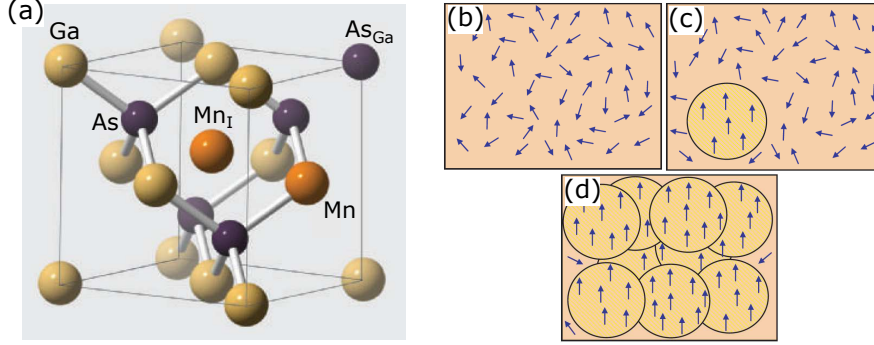


Figure 4.1: Crystal structure and ferromagnetism of (Ga,Mn)As and (Ga,Mn)(As,P). (a) Zinc-blende crystal structure of (Ga,Mn)As derived from the GaAs host lattice by replacing part of the Ga atoms with manganese. The most frequent defects, Mn interstitials (Mn_I) and anti-site defects (As_{Ga}), are shown. In (Ga,Mn)(As,P) additionally part of the As atoms is replaced with phosphorus. (b) - (d) Onset of the carrier mediated ferromagnetism with increasing density of the free holes. The direct exchange between the localized Mn spins (arrows) is not enough to polarize the material (b). The Mn spins in a proximity of a partially delocalized hole (circle) tend to polarize antiparallel to its spin, i.e. parallel to each other (c). If the hole density is high enough the polarized clusters overlap and the FM order spreads to the entire crystal (d). (a) - (d) reproduced from [144].

The magnetic anisotropies of (Ga,Mn)As [27,41] and (Ga,Mn)(As,P) [42] have been extensively studied both theoretically and experimentally. Three main intrinsic contributions have been identified. First, it is the cubic MA reflecting the symmetry of the host zinc-blende crystal structure and given by (1.37) with the EAs along [100], [010], and [001] directions. The second contribution arises due to the strain induced in the magnetic epilayer by the lattice-mismatched GaAs substrate. Incorporation of a substantial amount of manganese leads to a slight increase of the in-plane lattice constant compared to the pure GaAs whereas adding phosphorus has the opposite effect. The resulting compressive strain [in (Ga,Mn)As] / tensile strain [in (Ga,Mn)(As,P)] adds an energy contribution of $\epsilon_{out} = -K_{out} \cos^2 \theta$, where $K_{out} < 0$ ([001] hard axis) for (Ga,Mn)As and $K_{out} > 0$ ([001] EA) for (Ga,Mn)(As,P). Finally the third contribution, known as the *effective shear strain*, introduces an inequivalency between the in-plane [110] and $[\bar{1}10]$ directions giving a contribution of $\epsilon_{sh} = (K_{sh}/2) \sin^2 \theta (\sin 2\phi - 1)$. In a typical case $K_{sh} > 0$, i.e., $[\bar{1}10]$ is preferred. Furthermore, as has been shown in [41], the in-plane MA of the $Ga_{1-x}Mn_xAs$ epilayers can be smoothly tuned by the sample composition since the cubic MA decreases with increasing x while the uniaxial contribution K_{sh} remains constant.

4.2 Fe/GaAs [28]

A combination of ferromagnetic and semiconducting material properties represents one of the possible ways to new functionalities of electronic devices. The realisation of this goal in form of DMSs, such as GaMnAs, is hindered by the low Curie temperature of these materials. Another option is to utilize hybride structures where the ferromagnetic

and semiconducting properties are spatially separated. Here, Fe/GaAs heterostructure represents the ‘obvious’ choice. Iron is one of the best explored ferromagnets with a robust spin order ($T_C = 770^\circ\text{C}$ in bulk), high spin polarization and large magnetization ($\mu_0 M_s = 2.15\text{ T}$ at room temperature in bulk). On the other hand, GaAs is the most widely used and best explored III-V semiconducting substrate, which is well lattice-matched to Fe. Below T_C , Fe adopts a *bcc* crystal structure with lattice constant almost precisely matching half of the zinc-blende GaAs lattice parameter. This allows for good epitaxial growth of Fe on GaAs with four Fe *bcc* cells growing on top of one GaAs unit cell.

In this work we study ultrathin ($\approx 2\text{ nm}$) Fe epitaxial films grown on (001)-oriented GaAs multilayer with varying doping in order to form a PIN diode below the ferromagnet. The Fe growth on GaAs(001) is known to be accompanied by many surface-related effects that can result in significantly altered properties of the Fe thin film compared to the bulk crystal. Processes such as substrate surface reconstruction, substrate atoms segregation and outdiffusion, and intermixed interface compound formation take place, which can affect the Fe magnetic moment magnitude, the lattice constant (and the related strain), the magnetic anisotropy, etc. In bulk, the iron MA is dominated by the first-order cubic contribution with the corresponding easy, intermediate, and hard axes along $\langle 100 \rangle$, $\langle 110 \rangle$, and $\langle 111 \rangle$ directions, respectively. In thin Fe films the strong demagnetizing field ($\sim 2\text{ T}$) makes the MA easy-plane with a weaker in-plane anisotropy of the order of $\sim 10\text{ mT}$. The cubic energy minima along $[100]$ and $[010]$ are preserved with an additional energy contribution of uniaxial form (EA $\parallel [110]$) induced by the surface effects. This kind of uniaxial MA preferring either $[110]$ or $[1\bar{1}0]$ moment orientation is quite common in magnetic films grown on zinc-blende substrates such as GaAs or GaP (e.g., in GaMnAs/GaAs EA $\parallel [1\bar{1}0]$ [41], in CuMnAs/GaP EA $\parallel [110]$ of GaP [149]). In Fe/GaAs(001) the uniaxial anisotropy constant is inversely proportional to the film thickness [for films thicker than ~ 8 monolayers (ML)] which points to the surface origin of this anisotropy component. Among the effects discussed as the possible origins of the magnetic inequivalency between $[110]$ and $[1\bar{1}0]$ directions are the particular orientation of the Fe-As bonds, which dominate the Fe/GaAs interface formation, or the anisotropic strain or strain relaxation along these two directions.

Since the uniaxial MA, which dominates in the ultrathin Fe films, weakens with increasing thickness of the film, there is a crossover from uniaxial to biaxial anisotropy that eventually converges to pure cubic MA for thick Fe films. This is accompanied by splitting of the ‘uniaxial’ EA to two EAs which turn from $[110]$ towards $[100]$ and $[010]$ directions with increasing film thickness. According to the published results, the splitting point occurs for thickness of $\sim 25\text{ ML}$. Our $\approx 2\text{ nm}$ (14 ML) thin films should, therefore, have a single EA along $[110]$ direction. This is, however, not the case and our films exhibit a biaxial MA, as we discuss in detail in Appendix D.

4.3 Mn_3Sn

Antiferromagnetic semimetal Mn_3Sn is a prominent representative of non-collinear AFs with a triangular spin arrangement. The non-trivial spin texture gives these AF materials some very appealing properties that are usually considered as being limited only to ferromagnets. In FMs, the net magnetization gives rise to the linear MO effects (Faraday and Kerr effects), anomalous Hall and Nernst effects and to the spin-polarized charge currents. These effects are crucial for investigation of FMs and their practical applications. On the other hand, the typical AFs with a collinear compensated spin structure possess a high symmetry which not only leads to the zero magnetization but also prohibits the aforementioned phenomena. This makes the investigation and control

of these AF materials particularly difficult.

The recent understanding that the anomalous electron velocity, which is responsible for AHE, ANE, MO Kerr effect (MOKE), etc., arises from non-vanishing Berry curvature in the k -space [131, 150] has led to predictions [151–153] that these phenomena could be present also in fully compensated AFs, provided that certain symmetries are broken in these materials. The non-collinear triangular spin lattice of Mn_3Sn meets these symmetry criteria and large anomalous transport and MO effects were indeed observed in this material in zero magnetic field: AHE [154], ANE [138], MOKE [155]. Mn_3Sn has been also intensively studied with regard to its unusual band structure containing so-called Weyl points [138, 152, 156–159]. These singular topological features in principle allow for significant enhancement of the magnetotransport response.

The unit cell of Mn_3Sn is depicted in Fig. 4.2(a). It crystallizes in a hexagonal structure with $P6_3/mmc$ space group [160]. The Mn atoms are arranged in layers (two in each unit cell) parallel to the basal plane. In each Mn layer the atoms are arranged in a kagome-type lattice which can be seen as composed of Mn hexagons surrounding the Sn atoms or triangles filling the space between the Sn atoms.

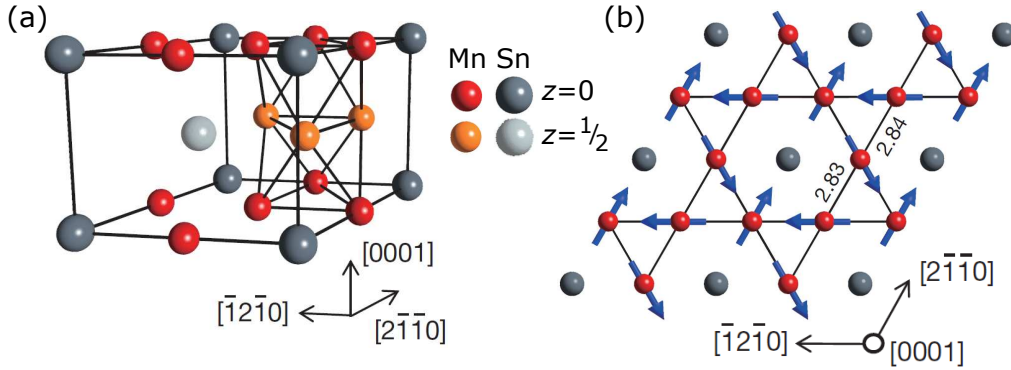


Figure 4.2: Crystal and magnetic structures of Mn_3Sn . (a) The crystallographic unit cell of Mn_3Sn . Atoms in different basal planes ($z=0, 1/2$) are distinguished by different colours. (b) Kagome-type Mn lattice in the Mn_3Sn film plane with magnetic moments indicated by arrows – the neighboring moments make an angle of 120° . Each Mn moment has its local EA parallel to the in-plane direction towards its nearest-neighbor Sn sites. Moments on the corresponding Mn atoms in the neighboring kagome planes are parallel to each other. Reproduced from [154].

The non-collinear spin texture within each Mn kagome plane, which is shown in Fig. 4.2(b), is a result of a geometrical frustration [19]. The triangular lattice doesn't allow the antiferromagnetically coupled spins to simultaneously minimize energies of all the mutual exchange interactions. In the case of collinear arrangement, two from the three spins forming the triangle can align antiparallel, however, the third one is frustrated as it would be always parallel to one of the two neighbors. As a result, the three spins align within the kagome plane at 120° with respect to each other, which is the energetically most favourable solution. The spin configuration shown in Fig. 4.2(b) was experimentally confirmed in bulk crystals [161], however, several alternative spin arrangements in the basal plane have been discussed as candidates for the ground state [162–165]. The anisotropy of the three magnetic sublattices partly cancels out [161] which allows for the experimental manipulation of the antiferromagnetic order. In the spin configuration shown in Fig. 4.2(b), only one of the spins points along its local EA, which is given by the direction towards its in-plane nearest-neighbor Sn atoms [166]. The tendency of the other two spins to align with their local EAs distorts the perfect 120° angles between the spins in the triangle and gives rise to a small uncompensated magnetic moment of $\sim 0.002 \mu_B$ per Mn atom [161, 166]. This moment allows for

manipulation of the AF spin texture by moderate magnetic fields but is not the origin of the anomalous electron velocity and the consequent effects.

The Mn_3Sn epitaxial thin films for our experiments were grown by ultra-high vacuum magnetron sputtering on $\text{MgO}(111)$ single crystal substrates with a 5 nm Ru buffer layer [160]. The 50 nm thick Mn_3Sn layer was grown by cosputtering at room temperature and subsequently the stack was annealed at 300°C in situ for 10 minutes and capped with 3 nm of Al to prevent oxidation (see the Methods section in [167] for details). The normal of the Mn_3Sn thin film coincides with the $[0001]$ crystallographic direction, i.e., the Mn kagome planes and triangular spin texture are parallel to the film plane. The film Néel temperature is 420 K, the same as reported for bulk crystals [161]. We, therefore, assume for our films the same spin texture as shown in Fig. 4.2(b).

4.4 CuMnAs

CuMnAs is a fully compensated collinear antiferromagnet which was first prepared by direct synthesis from the constituent elements [168, 169]. These bulk crystals had orthorhombic structure and the AF ordering survived up to $\sim 350\text{K}$. Later, CuMnAs was grown also by molecular beam epitaxy in form of thin films on various substrates including GaAs, GaP, and Si [78, 170]. These films have a tetragonal crystal structure which is shown in Fig. 4.3(a). Mn atoms are arranged in layers parallel to the film plane with spins ferromagnetically coupled within each layer and with two adjacent Mn planes coupled antiferromagnetically [171]. The two adjacent Mn planes belong to opposite magnetic sublattices A and B. In zero external magnetic field, the two sublattices exactly compensate each other, $\mathbf{M}_A = -\mathbf{M}_B$, i.e., CuMnAs has no net magnetic moment. Most explored are films grown on GaP, which exhibit in-plane magnetic anisotropy that is either uniaxial (EA $\parallel [010]$, typically in thinner layers with a thickness of $\sim 10\text{ nm}$) or biaxial (EAs $\parallel [110]$ and $[1\bar{1}0]$, in thicker layers with a typical thickness of $\sim 50\text{ nm}$) [149, 172, 173].¹ However, a recent comprehensive MO study [174] has shown that the magnetic anisotropy of CuMnAs may not be governed exclusively by the film thickness. In addition, the anisotropy may be affected by device patterning. The Néel temperature of a 500 nm thick CuMnAs layer was determined by a neutron diffraction as $(480 \pm 5)\text{ K}$ [172], however, as shown by MO experiments [149, 174], T_N may be lower for very thin ($\sim 10\text{ nm}$) films.

The tetragonal CuMnAs lattice possesses a combined PT symmetry, i.e., it is invariant under time reversal combined with another spatial transformation, such as inversion [the inversion center is indicated by the yellow ball in Fig. 4.3(a)]. Consequently, phenomena that are odd under time reversal, such as AHE and its thermoelectric and optical counterparts, ANE and MOKE, have to vanish [153]. This significantly narrows the spectrum of available techniques sensitive to the AF order in CuMnAs thin films. From the transport and optical methods, only the effects originating from the symmetric part of conductivity tensor remain. This includes AMR which is again accompanied by thermoelectric and optical counterparts – anisotropic magneto-Seebeck effect, Voigt effect (VE), and X-ray magnetic linear dichroism (XMLD).

The crystal symmetry restricts also excitation (control) mechanisms. In particular, electrical currents in CuMnAs are not globally spin polarized and, consequently, an antiferromagnetic version of metallic or tunneling junctions [AF/NM(I)/AF] showing GMR (TMR) and STT switching analogous to that in FM-based structures is not possible [153]. Furthermore, since CuMnAs is fully compensated, it is also insensitive to moderate magnetic fields. This can be circumvented by utilizing an exchange bias

¹These are CuMnAs crystal directions. Note that the CuMnAs unit cell is 45° rotated with respect to that of the GaP substrate, i.e., $[100]_{\text{CuMnAs}} \parallel [110]_{\text{GaP}}$ [170].

from an adjacent FM film. In [175], the AF order in CuMnAs/Fe stack could be manipulated with magnetic fields as weak as ~ 0.1 T. However, this was only possible due to the very small thickness of the CuMnAs film (~ 5 nm).

The specific symmetry of CuMnAs crystal lattice has also positive consequences. The full lattice is centrosymmetric, however, it can be divided into two sublattices, which, individually, have broken inversion symmetry and form inversion partners. These two sublattices coincide with the two magnetic sublattices. As a consequence, when an electric current flows along the Mn planes, it becomes spin polarized locally with opposite polarization on the two sublattices, so that the net spin polarization is zero [12]. The staggered spin polarization acts as an effective magnetic field that alternates between the Mn planes and, therefore, allows for a highly efficient manipulation of the Néel spin order of CuMnAs (see Fig. 2.4 and the Néel SOT in section 2.4.2).

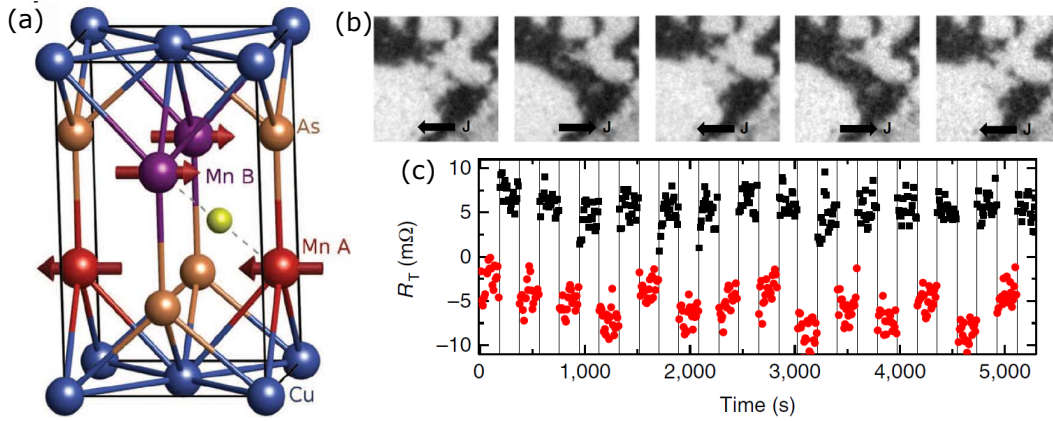


Figure 4.3: Crystal structure and electrical switching of CuMnAs. (a) CuMnAs crystal structure and AF ordering. The full crystal is centrosymmetric (the inversion center is marked by yellow ball), however, the individual magnetic sublattices have broken inversion symmetry and form inversion partners. (b) XMLD-PEEM images and (c) AMR detection of a reversible 90° reorientation of CuMnAs AF order by NSOT pulses of alternating polarity. Reproduced from [10, 173].

The current pulse-induced NSOT-based switching of the Néel vector predicted in [12] was confirmed by experiments in CuMnAs films [10, 173], where a 90° reorientation of magnetic moments was detected via AMR. The latter is even in magnetization, hence it cannot distinguish magnetic states with opposite Néel vectors. However, the second-order AMR allows to detect also a 180° Néel vector reversal upon reversing the polarity of the writing current [133]. Néel vector switching by electrical pulses of lengths in the range from ms down to sub-ns and even by pulses of THz radiation (~ 1 ps duration) was achieved [79] and a prototype memory device with NSOT writing and AMR readout was demonstrated [78]. The domain structure of CuMnAs and its modification by the current pulses was visualized by a combination of XMLD and photoelectron emission microscopy (XMLD-PEEM) [10, 173]. This technique is powerful but requires an expensive experimental infrastructure – a synchrotron. A more available probe of the AF order is provided by the MO effects in the optical wavelength range. The linear MO effects, such as MOKE, vanish in CuMnAs [153], however, the second-order Voigt effect proved to be very useful as it allows to determine the Néel temperature and the magnetic anisotropy of the thin films [149] in a table-top experiment. So far, imaging of the CuMnAs domains via the VE has not been successful. In chapter 9 we focus on the thermoelectric counterpart of AMR and VE (XMLD), which is the anisotropic magneto-Seebeck effect. We demonstrate that this effect combined with a locally generated heat gradient can be used to image the CuMnAs domain structure.

5. Voigt effect-based MO microscope integrated in a pump-probe setup

MO phenomena represent a perfect tool for an investigation of magnetization patterns and their dynamics thanks to the ability to create ultrashort photon pulses and focus them into a small volume. The temporal resolution, given mainly by the laser pulse duration, is essentially limited by the oscillation period of the optical field (≈ 2 fs in visible range) and the achievable spatial resolution is given by the light wavelength in far-field applications and can even reach tens of nanometers in near-field measurements. High spatial resolution is necessary for an investigation of the nano-scale magnetic textures, such as magnetic domains, DWs, and spin waves, which represent the functional elements of spintronic devices [13, 14], which themselves have typically micrometer-scale dimensions. The picosecond-scale temporal resolution is needed to understand the behavior of these micro-magnetic objects and their response to various excitation mechanisms.

Simultaneous high temporal and spatial resolutions can be achieved in a pump-probe experiment if the laser pulses are focused on a sample surface using an objective lens with a high numerical aperture. The time- and spatially-resolved maps of the MO response are assembled from the individual local pump-probe measurements by changing the pump-probe delay and the laser spots positions on the sample surface. The latter is accomplished either by moving the sample with a piezo-positioner [127] or by tilting the incoming laser beams with respect to the objective optical axis [128]. In any case, this is an extremely time-consuming measurement. Another option is a stroboscopic wide-field imaging where the probe pulses are used to image the sample surface for a given time-delay which is then continuously varied. However, this technique is much more complicated to implement [176].

In many cases, however, the high temporal and spatial resolutions do not have to be really simultaneous. The approach, we decided to follow, is to use a wide-field MO microscope to quickly assess the sample magnetic properties and their (in)homogeneity over a large area and identify the regions of interest which can be subsequently investigated by the local MO pump-probe technique integrated in the MO microscope. This solution allows to obtain both the spatially- and time-resolved information at reasonable measurement times.

In the following, we first describe in detail the optical setup integrating the wide-field MO microscope with the spatially-resolved pump-probe functionality. Subsequently, a sensitivity of the MO microscope to in-plane magnetized domains through the Voigt effect is verified. Finally, we demonstrate the utility of the combined spatial and temporal resolutions in our setup by investigation of a (Ga,Mn)As sample attached to a piezoelectric transducer, which allows to apply a voltage-controlled strain. The strain-induced modification of magnetic anisotropy [27, 29] proved to be a promising feature for spintronic applications since it allows for, e.g., an electrical control of a DW mobility [106] or magnetization precession [38]. However, samples glued to a piezoelectric transducer usually show rather inhomogeneous properties due to an inhomogeneous transfer of strain between the piezo-stack and the sample [177]. We show that the MO microscope can easily distinguish sample regions with a different effect of the piezo-stressor on the magnetic anisotropy and the pump-probe measurements performed in these preselected areas show also significant differences in the local magnetization dynamics.

The results presented in this chapter were published in [178]. The spatially-resolved pump-probe MO setup was constructed by L. Nádvořník [179] while the author of this thesis assembled the Voigt effect-based wide-field MO microscope, integrated both setups together, and performed all the presented experiments.

5.1 Description of the experimental setup

Our experimental setup is sketched in Fig. 5.1. It consists of two parts - the wide-field MO microscope and the spatially-resolved pump-probe setup - which can be used independently as well as in conjunction benefiting from the specific advantages of these two distinct methods.

Pump-probe setup with a high spatial resolution. As a source of the ultrashort laser pulses we used a Ti:sapphire laser (Spectra Physics, Mai Tai HP) generating linearly polarized pulses of ≈ 100 fs duration and ≈ 10 nm spectral width at a repetition rate of 80 MHz. The central wavelength of the laser pulses is continuously tunable in the range of 690–1040 nm. Each laser pulse is split by a polarizing beamsplitter (PBS) into a strong pump pulse and a weaker probe pulse. The division of the laser power between the pump and probe arm of the setup is controlled by a half-wave plate (HWP) placed in front of the beamsplitter. An additional HWP is used in each arm that in a combination with a polarizer (Pol.), which is used to define the linear polarization of the beams, allows to set the required intensities of the pump and probe beams independently.¹ The pump beam is periodically interrupted by an optical chopper at a frequency of ≈ 2 kHz and is guided through an optical delay line, which allows to set the time-delay of the probe pulses with respect to the pump pulses in the range of -0.5–3.5 ns.

Since the pump and probe beams spatially overlap in the detection part of the setup they have to be spectrally separated. This is accomplished by two different dielectric edge filters F1 and F2 placed in the pump and probe arms, respectively. The F1 filter transmits only the short-wavelength and F2 only the long-wavelength part of the original pulse spectrum. To match the maximum of the MO response of our samples [see Fig. 5.2(d)] we tuned the laser to a central wavelength of 774 nm and used F1 (Thorlabs, NF785-33) and F2 (Thorlabs, FBH780-10) leading to a spectral separation of ≈ 9 nm between the pump and probe pulses.² The additional filters F2 placed in front of the detectors block the scattered pump photons, which improves significantly the signal-to-noise ratio of the measured pump-probe traces. More details about the spectral filtering technique may be found in [180].

After spectral filtering, the pump beam is reflected towards the sample by a piezo-controlled mirror (Newport, AGM100D) which sets precisely the direction of the beam propagation with respect to the objective optical axis and, consequently, the pump laser spot position on the sample surface. Both laser beams pass a series of polarization components [polarizer, half-, and quarter-wave plate (QWP)] which set the desired polarization state - linear polarization in the case of the probe beam and linear or circular polarization in the case of the pump beam.³ Subsequently, the pump and probe beams are merged by a beamsplitter (BS) and focused by an objective lens [Mitutoyo

¹Instead of the HWP, a gradient neutral density filter could be alternatively used in each arm to set the beams intensities.

²Other combinations of central laser wavelength and filters can be used to cover different spectral regions.

³We usually measure two pump-probe traces with opposite handedness of the circular polarization of the pump pulses and calculate their average (difference) to identify the helicity-independent (dependent) parts of the signal which may correspond to different excitation mechanisms [38].

Plan Apo 20, with a numerical aperture of 0.42] on the sample surface where they form spots of $\approx 1.6 \mu\text{m}$ diameter. The objective lens is attached to a 3D piezo-positioner (Newport, non-magnetic version of NPXYZ100SG-D) which allows for a precise focusing and the laser spots positioning. The pump-probe separation on the sample surface, which is achieved by the pump beam tilting, is limited by the objective input aperture and in our case can exceed $20 \mu\text{m}$. However, for separations larger than $10 \mu\text{m}$ the optical aberrations in the objective lens cause the laser spot distortion [179].

The sample is placed in an optical cryostat (Advanced Research Systems, temper-

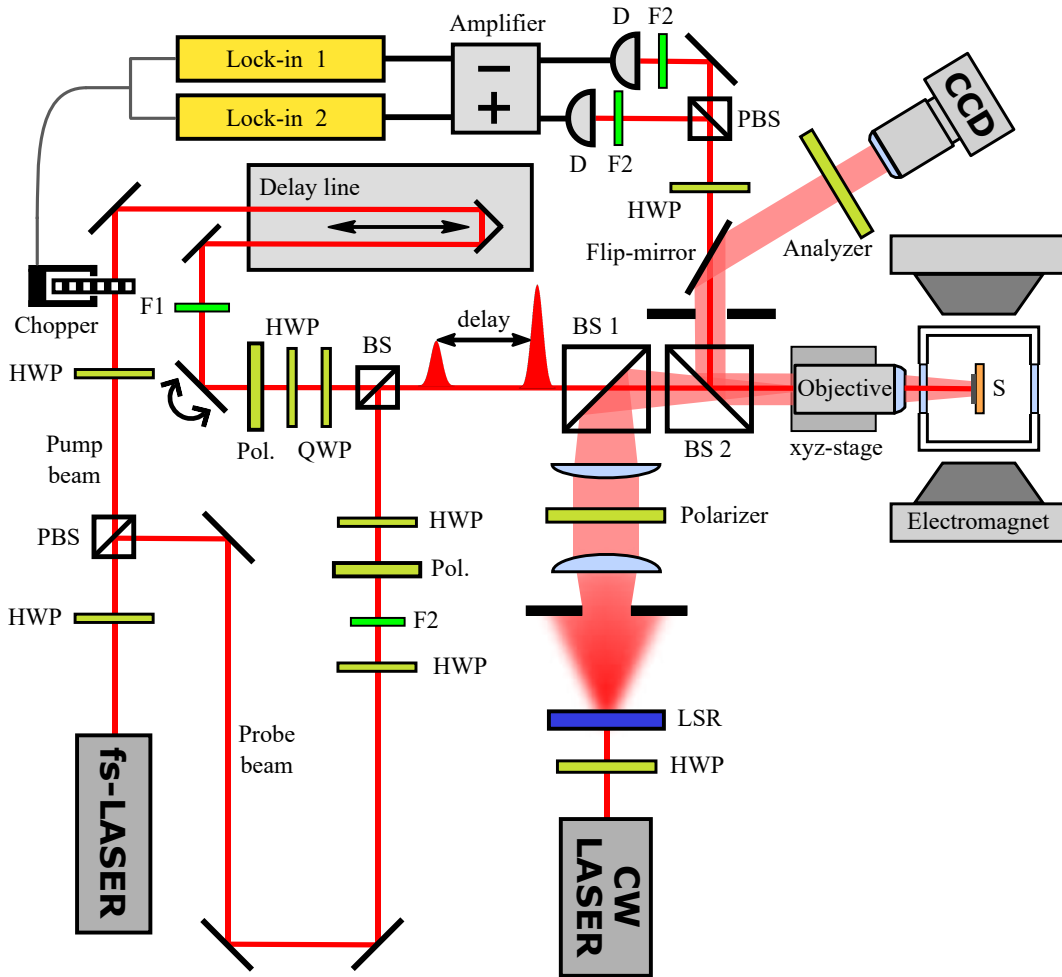


Figure 5.1: Pump-probe experimental setup with a high spatial resolution combined with a wide-field MO microscope. *Pump-probe experiment:* Each pulse emitted by a femtosecond (fs) laser is divided into pump and probe pulses by a polarizing beam splitter (PBS) with an intensity ratio set by a half-wave plate (HWP). Another pair of HWP and polarizer (Pol.) is used to set the intensity in each beam. Filters F1 and F2 are used to spectrally separate the pump and probe beams. Sets of polarizer, half-, and quarter-wave plate (QWP) define the polarization of pump and probe pulses which are then merged by a beam splitter (BS), with a variable mutual time delay set by a delay line, and focused on the sample (S) by an objective lens. The sample is placed in an optical cryostat between the poles of an electromagnet. Beams reflected from the sample are directed by BS 2 towards an optical-bridge detection system where the pump pulses are suppressed by filters F2. *MO microscope:* HWP and polarizer are used to set intensity and vertical (s) polarization of light emitted by a continuous-wave (CW) laser. A laser speckle reducer (LSR) suppresses interference effects due to the laser coherence. The optical system creates a symmetric light cone illuminating the sample, and the reflected light is guided by an optional flip-mirror through an analyzer to a CCD camera.

ature range of 10–800 K) between the poles of an electromagnet (Walker Scientific, model HV-4H) which allows to apply up to 600 mT field. The probe pulses reflected from the sample are collimated by the objective lens and propagate, with the flip-mirror lowered, towards the so-called *optical bridge* [181] which allows for a sensitive detection of the pump-induced polarization rotation. Here, the probe beam is split by a polarizing beamsplitter in two beams detected separately by a couple of photodiodes (D). The electronic signals from the two detectors are added (for a transient reflectivity measurement) and subtracted (for a transient polarization rotation measurement), amplified, and processed by lock-in amplifiers, which extract the signal modulated at the chopper frequency. Prior to the actual measurement, with the pump beam blocked, the difference signal is set to zero by rotating the HWP placed in front of the PBS in the optical bridge. This represents the reference state without the sample excitation. When the pump beam is unblocked, the sample magnetic state changes which causes (via the MO effects) a rotation of the polarization plane of the probe pulses reflected from the sample. The resulting non-zero difference signal is directly proportional to the pump-induced polarization rotation angle θ [181].

Voigt effect-based wide-field MO microscope. The usual construction and general working principle of a MO microscope were described in section 3.1.2. In our setup we made a few modifications: we used a coherent imaging light source, a simpler illumination path, and, most importantly, we utilized a second-order MO effect - the Voigt effect (VE). The second-order MO effects are only rarely used to investigate FMs, since they are usually weaker and more difficult to separate from magnetization-independent optical signals than the linear effects, such as the Kerr effects. The situation is very different in collinear AFs where the linear MO effects vanish and the Voigt effect remains the only applicable MO probe.

The MO microscope setup integrated in the previously described pump-probe setup is depicted in Fig. 5.1. As an illumination source we used a Ti:sapphire continuous-wave (CW) laser (Spectra Physics, model 3900S) which can be tuned in the range of 700–1000 nm. The continuous spectral tunability of the illumination source is very useful to optimize the microscope MO sensitivity for a given sample, as we show in section 5.2, and allows to use the microscope for an investigation of various material systems with MO response located in different spectral regions. Additional advantages of a laser compared to the traditional incoherent light sources are a high illumination intensity and a high stability, both desired in MO microscopy. The downside of coherent light sources when used for illumination purposes is the presence of interference effects and, consequently, an inhomogeneous illumination - the so-called speckles. To suppress the interference effects we used a laser speckle reducer (Optotune, model LSR-3005-24D-VIS) which disrupts the laser light coherence. It consists of a diffuser moving at a high frequency relative to another static diffuser which, in combination with a sufficiently long integration time of the image detector, effectively averages out the speckle pattern.

The divergent light beam from the despeckler is first collimated and the desired linear polarization is set by a polarizer (Thorlabs, LPNIR 100-MP). The light intensity can be continuously tuned by rotating the HWP placed in front of the polarizer. The beam is then reflected by a 50:50 beamsplitter towards the objective lens while being focused to its back focal plane. The light reflected from the sample is collimated by the objective lens, passes through an analyzer (the same as the polarizer), and is focused onto the sensor of a high-speed CCD camera (Allied Vision Tech, model Prosilica GX 1050).

Since we are interested in imaging of magnetic domains via the Voigt effect which is strongest at normal light incidence, all the optical components are centered to the

common optical axis and, consequently, the objective lens creates a symmetric light cone illuminating the sample. Moreover, in this geometry the contributions from the longitudinal and transverse Kerr effects, which are also sensitive to in-plane magnetization, average to zero, which helps to prove the pure Voigt effect sensitivity of the MO microscope in case of the in-plane magnetized samples. The axial geometry also allows us to simplify a bit the Köhler illumination scheme (see Fig. 3.2) by omitting one of the lenses since we don't need the aperture diaphragm to set an oblique light incidence. Another advantage of the setup with a perpendicular light incidence on the sample is that we don't need an objective lens with a large numerical aperture. Such lenses have very short working distances and small input apertures which limits considerably the maximum achievable pump-probe spatial separation on the sample surface, as explained above. Finally, since the polar Kerr effect (PKE) also gives maximum response for perpendicular light incidence, our MO microscope can be used for imaging both the in-plane magnetized materials (via the VE) and the perpendicular-to-plane magnetized materials (via the PKE) without any change in its settings when switching between these two cases.

In our setup, the linear polarization of light illuminating the sample is set by the polarizer to be either horizontal (p-polarization) or vertical (s-polarization). For other orientations of the incident linear polarization, the beamsplitters cause a significant phase shift between the s- and p-component of the wave resulting in a strong light ellipticity and substantially lower visual contrast between the magnetic domains.

As explained in section 3.1.2, the optimal orientation of the analyzer to reach the maximum visual contrast and signal-to-noise ratio is strongly affected by the depolarization effects in the microscope. In our setup, the optimal setting is $3\text{--}5^\circ$ off the crossed position (with respect to the polarizer). Using the differential method, subtracting a reference image taken in the magnetically saturated state, our MO microscope is able to register polarization rotations as small as $100\ \mu\text{rad}$.

Modification of the setup for other experiments in this thesis. The basic experimental scheme described above, which combines focused laser beams and wide-field (MO) imaging, was used, with certain modifications, throughout this thesis in all presented experiments. In chapter 6 we used the MO microscope to monitor the DW position in the perpendicular-to-plane magnetized GaMnAsP (via the PKE) and one femtosecond laser beam was used to excite the DW motion. In chapter 7 we used the spatially resolved pump-probe setup to characterize the laser-induced picosecond electrical current pulses and the microscope was used to image the sample topography (without the MO sensitivity) and to set the laser spots positions in the investigated device. In chapters 8 and 9 the femtosecond laser beam was replaced by a CW laser beam focused on the sample surface where it generated a localized thermal gradient and the magneto-thermoelectric response was registered on the voltage contacts of the device. The microscope was again used to image the device topography and align it with the scanning laser beam.

5.2 Verification of the Voigt effect-related microscope sensitivity

In this section, we demonstrate that our MO microscope is indeed sensitive to in-plane magnetization textures via the Voigt effect. As a test material we used the diluted ferromagnetic semiconductor (Ga,Mn)As which shows an extraordinarily strong second-order MO response [146, 182]. In this material, the competing in-plane biaxial and uniaxial magnetic anisotropy components (described in section 4.1) result in two

EAs making an angle ξ , see Fig. 5.2(a) and appendix E. In a multidomain state, with magnetizations pointing, e.g., in the easy directions 1 and 2 [see Fig. 5.2(a)], the visual contrast between such domains is proportional to the difference in the VE-induced polarization plane rotation of the light reflected from those two domains [182]

$$\Delta\beta(\text{EA1}) - \Delta\beta(\text{EA2}) = 2P^{VE} \cos 2(\gamma - \beta_i) \sin \xi. \quad (5.1)$$

Here $P^{VE} = \theta_V\{\beta_i = \pi/4\}$ (see the left formula in 3.13) is the spectrally dependent MO coefficient describing the strength of the VE. The angles β_i and γ , both measured from the [100] crystallographic direction, denote the polarization plane orientation of the illuminating linearly polarized light and the easy axes bisector orientation, respectively [see Fig. 5.2(a)]. From equation 5.1 it is clear that the maximum contrast between the domains magnetized along different EAs is observed when the incident light is linearly polarized along the EAs' bisector or perpendicular to it, as illustrated in Fig. 5.2(a). Moreover, the MO contrast is maximized in samples with mutually perpendicular EAs, i.e., with $\xi = 90^\circ$. In our test 20 nm thick $\text{Ga}_{1-x}\text{Mn}_x\text{As}$ epilayer grown on GaAs with $x \approx 0.03$ the EAs are tilted by $\approx 15^\circ$ towards the $[\bar{1}10]$ axis due to the uniaxial anisotropy contribution [41], resulting in $\xi \approx 60^\circ$ [see Fig. 5.2(a)]. All the presented experiments were performed at a temperature of 15 K far below the sample Curie temperature of 77 K [41]. The external magnetic field H_{EXT} was applied in the sample plane along either [110] or $[\bar{1}\bar{1}0]$ direction which correspond to positive and negative fields, respectively, as depicted in Fig. 5.2(a).

To verify that the MO contrast observed in our microscope originates from the VE, we performed in-plane magnetic field sweeps and extracted MO hysteresis loops from the images captured by the microscope. For this measurement we selected a region on the sample surface where no domain structure was visible at zero magnetic field, i.e., which was in a single-domain state. During the measurement the magnetic field was changed in small steps from negative to positive fields and back with the microscope taking an image of the sample in each step (without any subtraction of the reference image). Each image was processed in the following way. A sufficiently large homogeneously bright area in the image was chosen (the same for all images) and the pixel gray-scale intensities were averaged within this area giving a single intensity value for each image. As a result we obtain the dependence of the image intensity on H_{EXT} , i.e., a hysteresis loop. The field sweep was repeated 6 times and the measured loops were averaged and shifted vertically to zero (to remove the non-magnetic background in the images).

In Fig. 5.2(b) we show the hysteresis loop measured in a large range of fields - the so-called *major* hysteresis loop. The measured hysteresis loop is even in magnetic field which implies that the underlying MO effect is even in magnetization, as expected in the case of VE. Moreover, the hysteresis loop is quite similar to those measured previously via this MO effect in an analogous sample (see Fig. 1 in Ref. [183]). From the measured hysteresis loop we can infer how the magnetization direction changes during the field sweep [183]. The four step-like changes in the MO signal correspond to switching events when the magnetization reorients abruptly, via a DW running quickly over the imaged area. Between the switching events magnetization points in a direction which corresponds to a local magnetic energy minimum (see appendix E). Provided that the applied field is much weaker than the magnetic anisotropy fields ($H_{EXT} \ll H_c, H_u$), these energy minima correspond to the easy directions 1–4 depicted in Fig. 5.2(a). On the other hand, for $H_{EXT} > H_c, H_u$ the magnetization points close to the external field direction. Therefore, during the field sweep from negative to positive saturation and back the magnetization goes through the sequence $[\bar{1}\bar{1}0] \rightarrow 1 \rightrightarrows 2 \rightrightarrows 3_{EXT} \rightarrow [110] \rightarrow 3 \rightrightarrows 4 \rightrightarrows 1_{EXT} \rightarrow [\bar{1}\bar{1}0]$ [see Fig. 5.2(a)], where \rightarrow denotes a gradual \mathbf{M} reorientation

and \Rightarrow an abrupt switching and the index EXT denotes the easy direction strongly modified by H_{EXT} . The smaller change of the MO signal when switching in larger field compared to the switching in lower field confirms that the magnetization does not switch to EA during the switching event in the higher field. The slope in the major hysteresis curve is partially caused by the gradual \mathbf{M} reorientation in large fields. However, most of the slope is an experimental artifact caused by a magnetic field-induced drag on the objective lens along the focusing direction, which results in a small variation of the light intensity reaching the CCD camera. Since the lens motion is reproducible, once characterized, it can be compensated by the piezo-positioner.

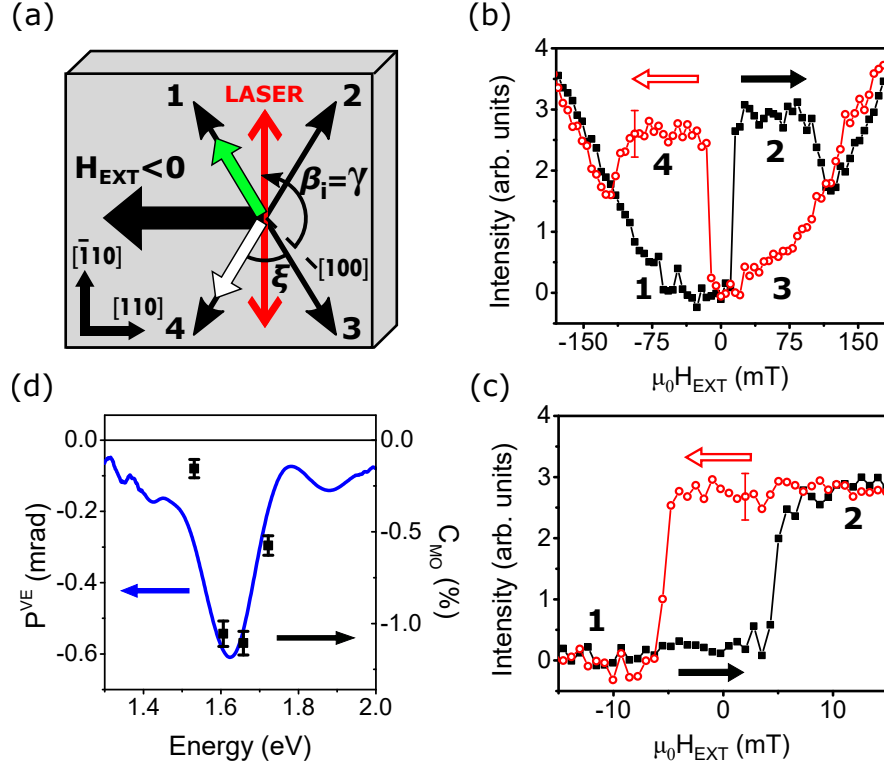


Figure 5.2: Magneto-optical properties of the test (Ga,Mn)As sample. (a) The implemented experimental geometry. The thin black arrows (numbered 1–4) indicate the magnetization easy directions in the sample. The orientations of the laser light polarization plane and the EAs’ bisector are described by angles β_i and γ , respectively. Here, we choose $\beta_i = \gamma$ to maximize the MO contrast. Before the hysteresis loop measurements, the sample was saturated by $\mu_0 H_{EXT} = -600$ mT along the $[\bar{1}\bar{1}0]$ direction. The green arrow along the direction “1” represents the magnetization state in the majority of the sample when H_{EXT} is reduced to zero. In certain parts of the sample, however, the magnetization is oriented along the direction “4”, as indicated by the white arrow (see text for details). (b) and (c) Major and minor hysteresis loops, respectively, measured by the MO microscope via the Voigt effect. Numbers represent the magnetization states depicted in (a), and arrows indicate the direction of the magnetic field change. (d) Independently measured spectral dependence of the Voigt effect magnitude (line) and MO contrast C_{MO}^{O} (points) calculated from images taken by the MO microscope using Eq. 3.16.

In principle, states with \mathbf{M} along the easy directions 1 and 3 (or 2 and 4) are indistinguishable by the VE, however, they can be identified based on the magnetic field direction and history. Since we apply the magnetic field at the same angle with respect to both EAs [see Fig. 5.2(a)], both states $\mathbf{M} \parallel 1$ and $\mathbf{M} \parallel 4$ could be populated when reducing H_{EXT} from the negative saturation to zero. However, we only observed

a single-domain state $\mathbf{M} \parallel 1$,⁴ probably because of a slight misalignment of H_{EXT} from the $[\bar{1}\bar{1}0]$ direction towards the $[\bar{1}10]$ direction.

In Fig. 5.2(c) we show the *minor* hysteresis loop measured in a smaller field-range which corresponds to the magnetization addressing only two of the easy directions $[183]$ in the sequence $1 \Rightarrow 2 \Rightarrow 1$.

In order to further evidence that the source of the MO contrast is the VE we performed the domain imaging at different photon energies. In Fig. 5.2(d) we compare the obtained spectral dependence of C_{MO} , calculated from the domain images captured by the MO microscope using equation 3.16 (points), and the spectrum of the VE-induced polarization rotation measured previously in this sample $[119, 182]$ (line). As immediately apparent, both quantities show very similar spectral dependence.⁵ Since the MO contrast is largest around 1.60 eV, we keep this photon energy for the rest of the experiments performed on this sample.

In a majority of the studied (Ga,Mn)As sample the domain imaging was complicated by a fast switching between the different single-domain states (1–4). Therefore, it was easier to perform the imaging close to the sample edges where a high density of structural defects acting as DW-pinning centers slows down the magnetization switching and the multi-domain magnetic pattern is stabilized in certain field-range. Fig. 5.3(a) shows a topography image of a sample region where there are several scratches present on the sample surface and Fig. 5.3(b) shows a MO image of the same area, where the VE-induced light polarization changes are highlighted. The MO image was obtained by a differential technique. First, a reference image was taken with $H_{EXT} = 25$ mT applied, then the field was switched to -25 mT and a second image was captured from which the reference image was finally subtracted. The result of the subtraction, shown in Fig. 5.3(b), highlights the changes in \mathbf{M} direction in different parts of the sample when switching H_{EXT} from 25 mT to -25 mT. The magnetic domain pattern clearly follows the distribution of the structural defects on the sample surface.

We observe three different intensity levels, marked I, II, and X in Fig. 5.3(b). This might be confusing at first sight, since there are only two EAs corresponding to two different VE-induced polarization rotations. However, this observation can be easily explained. In Figs. 5.3(c)–(e) we plot the minor hysteresis loops extracted from the image regions I, II, and X, respectively. Far away from the scratches - in the dark regions labeled I in Fig. 5.3(b) - the material behaves the same as in the sample parts without visible defects [cf. Figs. 5.2(c) and 5.3(c)], i.e., the magnetization is switching between the easy directions 1 and 2 with the coercive field of $\mu_0 H_{12} = -\mu_0 H_{21} = 4.6 \pm 0.2$ mT. On the other hand, closer to the scratches - in the bright regions labeled II in Fig. 5.3(b) - the hysteresis loop is inverted which implies that the magnetization is switching between the easy directions 4 and 3 (with a slightly higher coercive field of $\mu_0 H_{43} = -\mu_0 H_{34} = 5.4 \pm 0.2$ mT). The most probable explanation of why the magnetization points in the easy direction 4 (instead of 1) in the vicinity of the structural defects when H_{EXT} is reduced from the negative saturation to zero is the defect-induced strain which modifies locally the (Ga,Mn)As magnetic anisotropy. As discussed in detail in appendix E the strain contributes a uniaxial term to the magnetic anisotropy [27] which results in a spatially-dependent reorientation of the EAs by a few degrees. This could be sufficient for the magnetization to choose the easy direction 4 in our case, when H_{EXT} is applied very close to the highly symmetrical direction $[\bar{1}\bar{1}0]$ [see Fig. 5.2(a)]. Finally, in the regions labeled X in Fig. 5.3(b),

⁴The zero-field state of $\mathbf{M} \parallel 1$ was confirmed by an additional experiment, which is not shown here, where H_{EXT} was applied $\approx 6^\circ$ off the direction $[\bar{1}\bar{1}0]$ towards the direction $[\bar{1}10]$, which favors $\mathbf{M} \parallel 4$ state instead.

⁵The deviation at the lowest energy is probably caused by a decreased quantum efficiency of the CCD sensor in this spectral range, which was affecting the observed MO contrast.

which are directly adjacent to the scratches, no change in the detected MO signal is observed in the studied field-range. Most probably, the 20 nm thick (Ga,Mn)As film is missing in these areas because of the mechanical damage. Alternatively, the film could be still present but its magnetic anisotropy is so severely changed by the strain that the magnetization doesn't switch in the field-range of ± 25 mT (see appendix E).

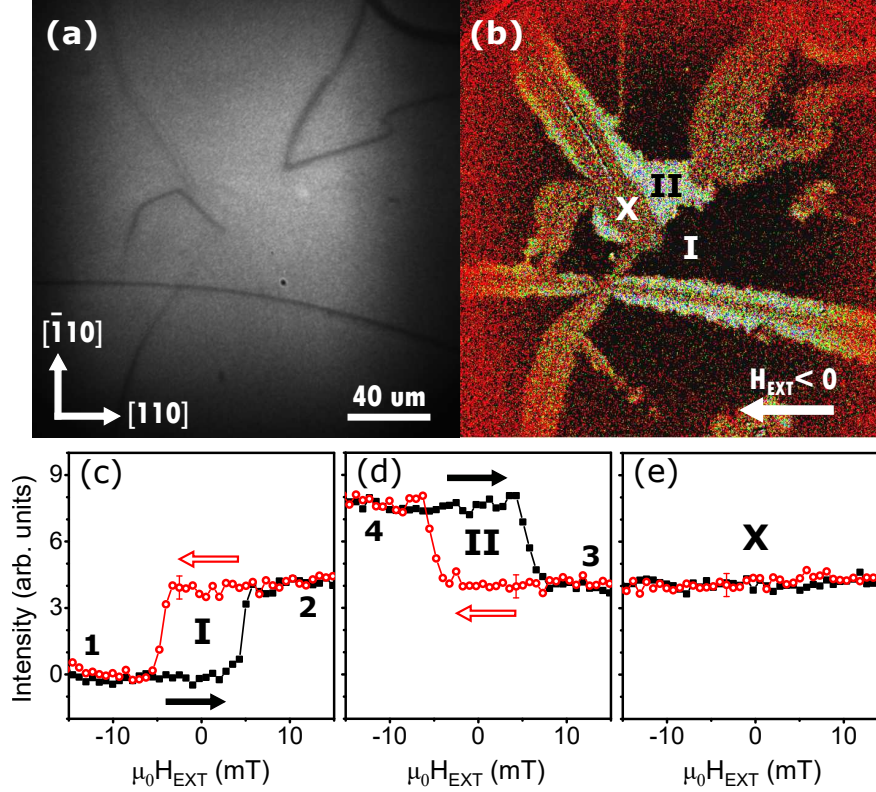


Figure 5.3: Imaging of the sample around surface imperfections. (a) An image showing the position of several defects on the sample surface. (b) A MO image of the same area at -25 mT (with a reference image taken at 25 mT). (c)–(e) Minor hysteresis loops extracted from regions marked as I, II, and X in (b). Numbers represent the magnetization states depicted in Fig. 5.2(a).

5.3 Investigation of a piezo-induced strain inhomogeneity

The manipulation of magnetic anisotropy [29, 106, 184] or spin polarized carriers [185, 186] via a controlled strain application is a promising concept which could find an application in spintronic devices. An elegant way to induce the strain is to attach the investigated sample to a piezoelectric transducer (PZT), which allows for a voltage-control of the strain magnitude in a wide temperature range [177, 187]. This technique has been successfully utilized in (Ga,Mn)As for an *in situ* electrical control of magnetic anisotropy [29], DW mobility [106], and led to the discovery of the optical STT [38]. On the other hand, there are several experimental difficulties. Besides the voltage-tunable strain (typically of $5 \cdot 10^{-4}$ for 150 V applied [177, 187]) there is also a strain induced by the difference in a thermal contraction of the sample and stressor during the sample cooling, which can be even larger. Moreover, the samples attached to a PZT are known to have rather inhomogeneous magnetic properties due to the inhomogeneous transfer of the strain from the piezo-stack through the glue to the investigated sample [177].

In the previous section we observed domain patterns that tightly followed the surface imperfections, which was ascribed to the defect-related spatial variation of the magnetic

anisotropy in the film. This correspondence between the strain and magnetic patterns could be utilized in the hybrid magnetic/PZT structures mentioned above to assess the (in)homogeneity of the strain transfer to the magnetic film.

To demonstrate this, we used a 20 nm thick $\text{Ga}_{1-x}\text{Mn}_x\text{As}$ film with $x \approx 0.038$ ($\xi \approx 53^\circ$, $T_C = 96\text{ K}$) grown on a GaAs substrate that was polished down to $200\ \mu\text{m}$ and attached by the Epotek glue to an uniaxial PZT (Piezomechanik GmbH, part no. PSt 150/2 \times 3/7). [177] All measurements were performed at a temperature of 15 K and with a voltage of -150 V applied to the piezo-stressor (unless stated differently). Both the fs-laser (for pump-probe measurements) and the CW laser (for the MO imaging) were tuned to 774 nm to maximize the MO signal due to the VE in this epilayer [119]. The pump and probe fluences were set to $200\ \mu\text{J cm}^{-2}$ and $40\ \mu\text{J cm}^{-2}$, respectively.

In Fig. 5.4(a) we show an optical image of a selected region on the sample surface with depicted crystallographic directions, EAs (of a bare epilayer without the piezo-stressor attached), and the directions of the voltage-controlled strain and the magnetic field H_{EXT} . Apart from a crack, there is no structure visible on the sample surface.

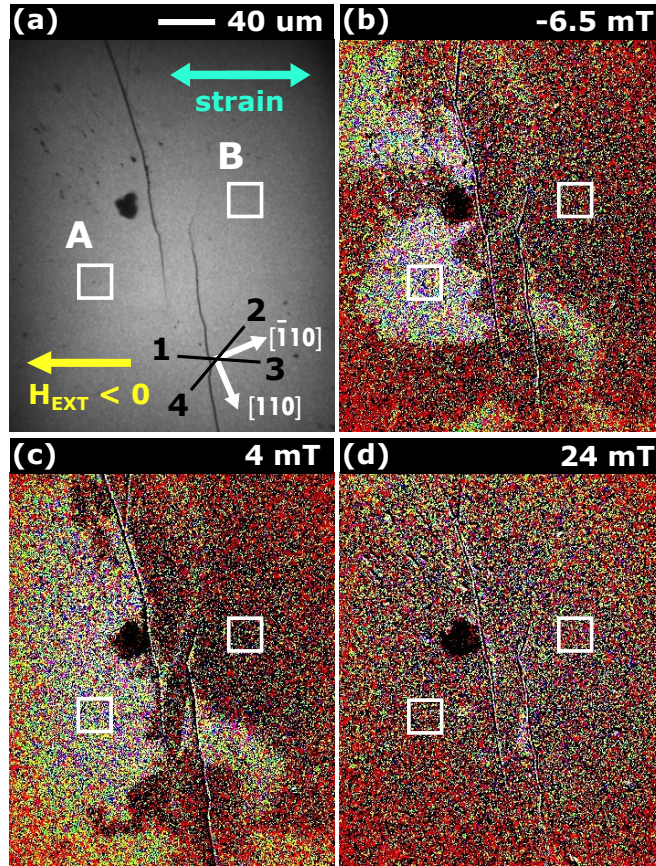


Figure 5.4: Visualization of magnetic inhomogeneity of the (Ga,Mn)As sample attached to a piezoelectric transducer. (a) An optical image of the sample surface with the EAs of the bare unstrained (Ga,Mn)As epilayer depicted by the black lines labeled “1” to “4”. The directions of the applied magnetic field H_{EXT} and the bias-dependent PZT-induced strain are indicated by arrows. The squares labeled A and B border the regions chosen for subsequent hysteresis and pump-probe measurements presented in Fig. 5.5. (b)–(d) Images captured by the MO microscope at different applied magnetic fields (with a reference image taken at -30 mT) showing differences in the magnetization switching process in the regions located right and left from the crack. The imaging was performed with a voltage of -150 V applied to the PZT, however, no significant effect of the voltage was observed.

However, MO imaging during a magnetic field sweep reveals two regions - located right and left from the crack - with a very distinct behavior, as shown in Figs. 5.4(b)–(d). While on the right side we do not register any changes in the MO signal during the field sweep, on the left side we observe a changing pattern which reflects the process of magnetization switching between different EAs via a DW motion.

We take a closer look at the differences between the two studied regions in Fig. 5.5. In panel (a) we show two hysteresis loops extracted from the MO microscope images taken during the field sweep by averaging the signal within the two square-shaped areas labeled A and B in Fig. 5.4(a). In case of a zero strain one of the EAs is close to the applied magnetic field direction [see Fig. 5.4(a)] and a magnetization switching by 180° directly between the easy directions 1 and 3 is expected (see appendix E for details). Since the two antiparallel magnetization states cannot be distinguished by the even-in-M Voigt effect we do not register this switching in region B. Consequently, the observation of the MO signal variation, which reflects the magnetization switching to the other EA, and, in particular, the fact that the magnetization switching appears before the direction of H_{EXT} is reversed, is a clear signature of a significant strain-induced modification of the magnetic anisotropy in region A [see Figs. E.1(c) and (d) and the adjacent discussion in appendix E]. Therefore, the MO microscope allows us to distinguish, via imaging the differences in the magnetization switching process, the sample parts where the epilayer magnetic anisotropy was significantly altered by the attached PZT (part A) and where it was not (part B). The strain mainly originates in

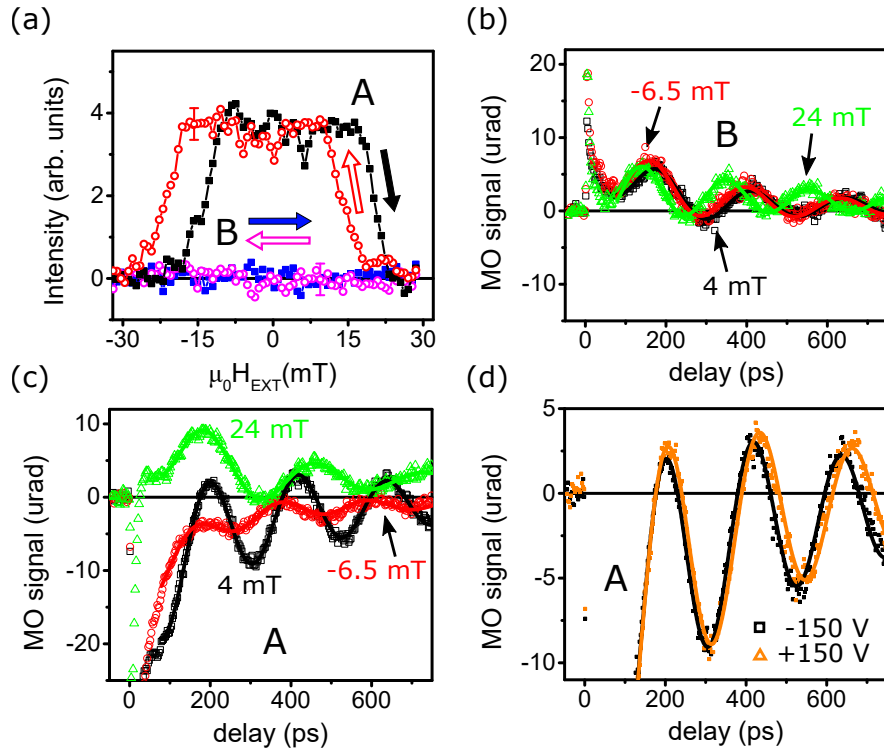


Figure 5.5: Comparison of the magnetization switching and dynamics observed in regions A and B depicted in Fig. 5.4(a). (a) Magnetic hysteresis loops measured by the MO microscope in regions A and B. (b) and (c) MO pump-probe traces, which reflect the magnetization precession triggered by the pump-induced transient modification of magnetic anisotropy, measured for three different values of H_{EXT} in regions B and A, respectively (points). Lines are fits by a damped harmonic function. (d) The change of the precessional signal observed in region A with the voltage applied to the PZT for $H_{EXT} = 4$ mT. No effect of the PZT-voltage was observed in region B.

our case from the thermal contraction mismatch since we do not observe any effect of the applied piezo-voltage on the MO images.

Besides the differences in the magnetization switching, regions A and B show also significantly different laser-induced ultrafast magnetization dynamics, as illustrated by the pump-probe traces in Figs. 5.5(b) and (c). In this experiment, absorption of the pump laser pulse heats the material up which temporarily modifies the magnetic anisotropy (EAs' positions) and, subsequently, the reoriented anisotropy field exerts a torque on the magnetization and induces its precession [25]. The precessional frequency is directly connected with the sample magnetic anisotropy [41]. On a longer timescale the heat dissipation leads to a return of the EA to its equilibrium direction and the magnetization precession is suppressed by the Gilbert damping. The presented pump-probe traces show the helicity-independent part of the MO signal obtained as an average of the curves measured with circularly right and left polarized pump pulses. In region B [see Fig. 5.5(b)] the magnetization precession is almost independent of H_{EXT} apart from a slight increase of the precessional frequency. This observation is in accord with the expected minor modification of the magnetic energy density minimum width by H_{EXT} applied close to the easy direction [see Fig. E.1(b) in appendix E]. Moreover, we have not observed any changes in the pump-probe traces when varying the voltage applied to the PZT which further confirms that the strain is not transferred properly from the PZT to the sample in region B. On the other hand, in region A [see Fig. 5.5(c)] we observe quite significant dependence of the magnetization precession on H_{EXT} . This is consistent with the more pronounced variation of the energy density minimum profile with H_{EXT} expected in the case of the strain-modified magnetic anisotropy [see Fig. E.1(d) in appendix E]. Moreover, the magnetization precession in region A is affected by the voltage applied to the PZT [see Fig. 5.5(d)]. The voltage effect is, however, rather small confirming the dominant influence of the sample/stressor thermal contraction mismatch in our sample.

5.4 Conclusion and outlook

We implemented an experimental scheme combining a pump-probe setup with subpicosecond temporal and micrometer spatial resolutions and a wide-field MO microscope sensitive to both in-plane and perpendicular-to-plane magnetized materials via the Voigt effect and polar Kerr effect, respectively. This combined setup proved to be able to obtain both spatially and time-resolved information about the sample in a reasonable measurement time. The wide-field MO microscope is ideally suited for a rapid inspection of spatially inhomogeneous samples which can be followed by dynamical pump-probe MO experiments in the pre-selected sample parts. The optical setup is very flexible and, with only minor modifications, can be used to a broad variety of experiments - it was utilized in most of the measurements presented in this thesis including imaging of a magnetic domain structure in FMs, non-collinear, and collinear AFs.

The VE-related sensitivity of our MO microscope was verified using a sample of in-plane magnetized diluted ferromagnetic semiconductor (Ga,Mn)As. Here we observed a correspondence between the observed magnetic pattern and the distribution of structural defects which was attributed to the local defect-related strain-induced modification of magnetic anisotropy. The sensitivity of the MO microscope to the strain distribution in the sample was utilized to investigate the (in)homogeneity of magnetic properties of a (Ga,Mn)As sample attached to a piezo-electric transducer. The MO imaging allowed us to identify the sample parts where the magnetic anisotropy of the epilayer was significantly modified by the applied strain and where it was not.

The manipulation of magnetic properties via a controlled strain application is especially appealing for antiferromagnetic spintronics [6, 184] due to the strong effect of magneto-elastic coupling in AFs [32, 188] and the insensitivity of AFs to conventional control mechanisms, such as an external magnetic field [6]. Besides the limited means of control, AFs are also notoriously difficult to detect. The established methods, such as XMLD-PEEM or neutron diffraction, require large-scale experimental facilities. Therefore, table-top MO detection techniques that allow for both high temporal and spatial resolutions attract significant attention nowadays [49]. The quadratic MO effects have been mostly overlooked in FMs since they are usually considerably weaker compared to linear-in-M effects, and it is more difficult to separate them from magnetization-independent optical signals [119]. In AFs, however, the situation is markedly different. In compensated collinear AFs the linear-in-M MO response from the two antiparallel magnetic sublattices averages to zero and the Voigt effect gives the lowest-order nonzero MO response [49].

An example of a fully compensated collinear AF that have been intensively studied recently is CuMnAs (see section 4.4). In this material, the electric control of its magnetic state via the Néel SOT (see section 2.4.2) and a proof-of-principle magnetic memory based on this mechanism have been demonstrated [10, 78]. The pump-probe MO experiments have shown that VE can be utilized to investigate the ultrafast magnetic dynamics and to determine the EAs' positions in thin CuMnAs films [149]. This suggests that VE could be, in principle, also used to image the antiferromagnetic domain structure of CuMnAs. However, the preliminary experiments on MO imaging of CuMnAs films have not been successful yet. The main problem seems to be a combination of a weak MO signal and the presence of additional sources of the light polarization changes, such as structural imperfections. Separation of the MO signal from these non-magnetic signals - an easy task in FMs where the magnetization can be simply reversed by a magnetic field - is much more complicated in AFs. Eventually, this separation might be accomplished by using the temperature and/or spectral dependence of the Voigt effect, which is markedly different from that of, e.g., structural defect-induced polarization changes. This is an open space for future studies.

6. Inertial domain wall motion driven by the optical spin transfer torque

Recently, the physics of magnetic domain wall motion has become a subject of a renewed interest due to the possible utilization of DWs as information carriers in nonvolatile information storage and processing devices [13,14]. There, an external magnetic field or electrical spin transfer torque pulses are used to drive the DWs, as introduced in sections 2.5.1 and 2.5.2. The external torque acts immediately on the DW, however, it is the torque-induced deformation of the wall spin texture that leads to the DW displacement. The timescale, at which the DW structure is modified, depends on the material parameters and the DW type and it lies typically in a nanosecond range [101]. The same timescale governs the DW structure relaxation (accompanied by a transient wall motion) after the excitation torque is switched off [98]. These inertial effects might negatively affect the ability of precise positioning of the DWs in the memory or logic devices and pose a limit on their operation frequency. Therefore, a massless DW motion with the DW following immediately and precisely the driving force is highly desired in case of the ns-range field and current pulses [189].

Recently, it has been shown that, besides the magnetic field and electrical current pulses, also circularly polarized light pulses can be used to manipulate magnetic order [37,38]. The underlying effect, known as the *optical spin transfer torque*, consists in a transfer of the spin angular momentum of the absorbed photons to the magnetization (see section 2.3.2). As such, this effect acts on an ultrashort timescale, as observed in [38]. That experiment was performed in an in-plane magnetized ferromagnetic semiconductor GaMnAs where the OSTT from a 300-fs-long laser pulse induced a coherent precession of the uniform magnetization with a picosecond-scale onset. Subsequently, we demonstrated in a closely related material with perpendicular-to-plane EA, GaMnAsP, that OSTT can also induce a DW motion with a direction controlled by the helicity of the circularly polarized light [190].

The principal idea of the OSTT-driven DW motion is schematically shown in Fig. 6.1(a). The OSTT induced by photo-electrons in the *in-plane* magnetized GaMnAs tilts the magnetization out of the sample plane [see Eq. (2.10), Fig. 2.5(c), and the adjacent discussion]. The torque is obviously zero within a domain of the *perpendicular-to-plane* magnetized GaMnAsP at a normal light incidence since $\mathbf{n} \parallel \mathbf{M}$. Inside a domain wall, however, the magnetization rotates between the two antiparallel states, i.e., it has a non-zero in-plane component and, therefore, the torque on the wall magnetization is non-zero. The OSTT-induced out-of-plane tilt of the wall magnetization as well as the direction of the resulting DW motion is opposite for opposite light helicities [190]. Since the OSTT is acting only inside the DW the optical excitation process is naturally self-aligned.

In [190] we proved the basic idea of the OSTT-induced DW motion by MO imaging of the final position of a DW excited by a train of ultrashort σ^\pm -polarized laser pulses in a simple magnetic bar device. This experiment did not give any information about the temporal characteristics of the excited DW dynamics. In the case of current-induced DW motion it was observed that for very short (~ 1 ns) current pulses, that are shorter than the DW relaxation time, the inertial effects start to dominate over the direct STT-driven motion [100]. In our case of the optical spin injection, the torque is restricted even to much shorter timescale, limited by the picosecond-scale spin-lifetime of the

photo-carriers. In such case, the direct STT-induced DW motion is expected to be negligible and the DW inertia becomes vital for a macroscopic DW displacement in the regime of ultrashort optical excitation.

In order to explore the dynamics of the OSTT-induced DW motion we fabricated more sophisticated devices where the optically excited DW moves in an artificial geometrical pinning potential. These experiments combined with micromagnetic simulations have shown that the DW excited by an ultrashort OSTT pulse indeed moves at timescales orders of magnitude longer than is the duration of the pulse itself proving the crucial role of a DW inertia in the light-helicity-controlled DW motion.

The experiments presented in this chapter were published in [191].

6.1 Experimental geometry and elastic DW pinning

Our experiments were performed in a ferromagnetic semiconductor GaMnAsP with perpendicular-to-plane magnetic easy axis [147]. This material has favourable properties for observing the optical spin-transfer effects. The direct bandgap of the GaAs host allows for optical generation of a high density of photo-carriers, which are spin-polarized due to the optical selection rules [see Figs. 2.5(a,b)] and exert a torque on the magnetization via a strong exchange interaction. At the same time, a strong spin-orbit coupling results in a significant contribution of the non-adiabatic STT to the DW motion in GaMnAsP [106, 192]. The non-adiabatic STT plays a crucial role in the DW motion since it allows for a non-zero DW mobility at low current densities (see section 2.5.2). The low density of magnetic moments in GaMnAsP, when compared to the conventional dense-moment metal ferromagnets, results also in comparatively low excitation densities required for the manipulation of its magnetic order [106, 193]. Last but not least, the field-, current-, or light-controlled magnetic state of the GaMnAsP devices can be easily monitored optically thanks to a strong MO response [42, 129, 146].

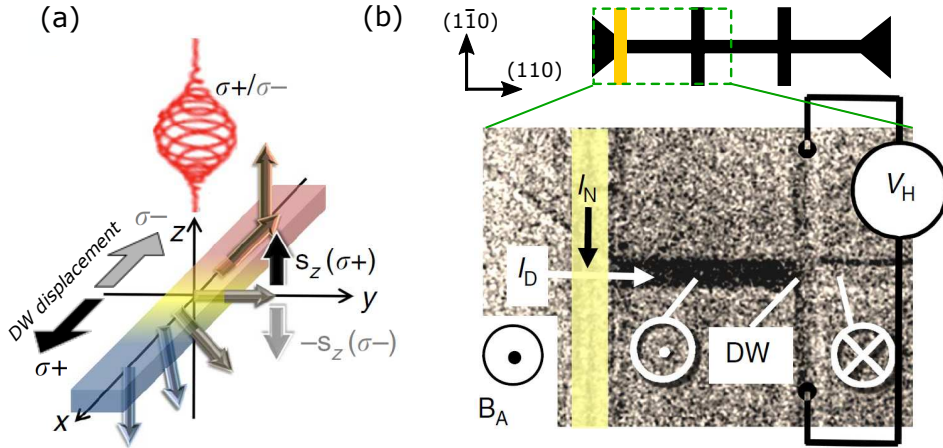


Figure 6.1: OSTT-driven domain wall motion - basic idea and device geometry.

(a) Photo-electron spin density s_z injected by normally incident circularly polarized laser pulses exerts a torque on the in-plane magnetization inside a Bloch wall. The OSTT-induced out-of-plane magnetization tilt and the resulting DW displacement are opposite for the opposite light helicities σ^\pm . (b) Sketch of the device geometry and a differential MO image of the selected area. The DWs are generated by an Oersted field of a current pulse I_N sent through a golden wire (yellow). Magnetic field B_A applied along the EA moves the DW to the cross where it gets pinned at the entrance corners. The DW position within the cross can be monitored by sending a current I_D through the main channel and measuring the Hall voltage V_H .

The experimental devices were fabricated by electron-beam lithography from a 25-nm-thick $\text{Ga}_{0.94}\text{Mn}_{0.06}\text{As}_{0.91}\text{P}_{0.09}$ epilayer grown by low-temperature molecular beam epitaxy on GaAs substrate. The Curie temperature of the annealed ferromagnetic film is 115 K. The device geometry together with a MO micrograph of a selected region is shown in Fig. 6.1(b). The 4 μm -wide horizontal GaMnAsP channel contains two symmetric Hall crosses and widens towards the external electrical contacts. The yellow-highlighted golden wire above the GaMnAsP bar, from which it is electrically isolated, serves for DW nucleation. A current pulse I_N sent through the nucleation wire creates the Oersted magnetic field which reverses the magnetization below the wire, thus creating two DWs. When an external out-of-plane magnetic field B_A is applied, which is stronger than the propagation field B_{PR} (~ 0.1 mT in our film), the right DW propagates towards the cross. At the cross-entrance corners the DW gets pinned due to geometrical reasons and its position can be monitored by sending the current I_D along the magnetic bar and measuring the Hall voltage V_H on the transverse contacts. (For details on the geometrical pinning and Hall detection of the DW position see the appendix F.) The nucleated domain, extending from the nucleation wire to the first cross, appears as a dark region in the MO micrograph in Fig. 6.1(b).

The DW nucleated in the GaMnAsP bar patterned along (110) crystallographic direction has the simple Bloch structure [106]. Magnetic field-driven propagation of such DWs in crossbar structures patterned from perpendicular-to-plane magnetized FM thin films was studied in [132]. The DW shape and propagation through the structure is a result of a competition between the DW-related energy and Zeeman energy of the nucleated domain. The former is proportional to the DW length and the latter to the area of the nucleated domain. In an infinite film, the energetically most favourable solution is a circular domain since in such case DW of minimum length borders domain of maximum area. In a straight bar, the DW is straight and perpendicular to the bar axis and can propagate freely¹ in either direction along the bar depending on the applied field polarity since any DW displacement conserves the DW length.

When the DW reaches the cross entrance it has to increase its length in order to propagate further, as illustrated in Fig. 6.2(a). The energetically optimal shape of the DW is again part of a circle. The DW stays pinned at the cross-entrance corners and its curvature increases, due to the increasing magnetic field B_A , until the DW center reaches center of the cross (half-circle DW). This magnetic field-driven DW expansion is analogous to the inflation of a two-dimensional soap bubble. The DW stretching costs more energy than is the Zeeman gain which results in a *virtual* restoring field B_R that opposes the applied magnetic field B_A . The restoring field strength depends on the position of the expanding DW [see Fig. 6.3(d)] and reaches its maximum $B_R^{max} = 2\sigma_{DW}/M_s w$ when the DW reaches the cross center being a half-circle with diameter equal to the bar width w . Here, M_s is the saturation magnetization and $\sigma_{DW} = \pi\sqrt{AK_u}$ is the DW energy per unit area with A being the exchange stiffness and K_u the effective out-of-plane magnetic anisotropy constant. The DW is released from the cross-entrance corners as soon as the applied field exceeds $B_R^{max} + B_{PR}$, and expands further as in an infinite film. (For details see appendix F.)

In our experiments, we employed the combined MO-microscope & pump-probe optical setup, introduced in chapter 5, supplemented by an electrical detection via anomalous Hall effect. As a light source in the MO microscope we used a green ($\lambda = 525$ nm) LED instead of the near-IR CW laser and we utilized the polar Kerr effect to monitor the DW position in the device. Applicability of this technique is independent of

¹Here we only assume a ‘friction’ from evenly distributed defects whose effect on the DW propagation is described by a coercive intrinsic propagation field B_{PR} , which is considered to be everywhere the same. We don’t take into account the pinning effects due to the device boundary roughness.

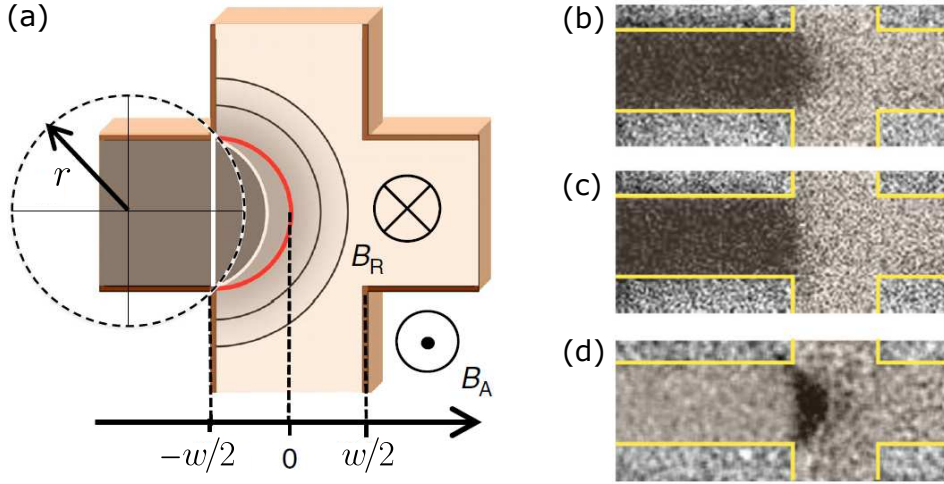


Figure 6.2: Soap-bubble-like domain wall expansion. (a) Schematic illustration of a magnetic field-driven soap-bubble-like expansion of an elastic DW in a symmetric cross structure. The DW stays connected to the cross-entrance corners until it reaches the cross center (red half-circle) when it gets depinned (see appendix F for details). (b) Polar Kerr image of a DW geometrically pinned in a $6\ \mu\text{m}$ -wide crossbar device at $B_A = 0.25\ \text{mT}$ and (c) image of the same DW after B_A has been switched off. (d) Image obtained as the difference of (b) and (c) highlighting the change in the DW shape and position upon removing the magnetic field - the originally round DW bent inside the cross shrinks elastically back into a straight line.

the DW position, however, its resolution is rather low ($\approx 1\ \mu\text{m}$). On the other hand, sensitivity of the electrical detection is restricted only to the cross area where it, however, offers nanometer-scale resolution [132]. Therefore, we used MO microscopy in the OSTT-driven DW motion experiments to detect the DW depinning from the cross entrance, after which the DW is usually displaced by μm -scale distances. The electrical AHE-based method was used to prove the elastic behavior of a DW pinned at the cross entrance. Due to the energy minimization the propagation of the DW in our 2-dimensional cross structure is well defined and can be described by a single position variable (position of the DW center) and there exists unambiguous relation between this coordinate and the measured Hall voltage (see appendix F).

First, we prove the elastic response of a DW geometrically pinned at the cross entrance and verify the applicability of the bubble-like DW propagation model by investigating magnetic field-driven DW motion, without optical excitation. In Fig. 6.2(b) we show a differential Kerr image of a DW pinned at the entrance corners of a $6\ \mu\text{m}$ -wide crossbar device with a field $B_A = 0.25\ \text{mT}$ applied. As one can see, the DW has a round shape bending inside the cross due to the applied magnetic field. Fig. 6.2(c) shows the same DW after the field has been switched off. Without the applied field pressure the DW is pushed back to the cross entrance by the restoring field. To highlight the change in the DW position and shape between (b) and (c), we show in Fig. 6.2(d) the difference of the two Kerr images. The observed behavior is in accordance with the soap-bubble-like model of DW propagation through a cross structure, as described above and in appendix F. Moreover, the symmetric arc shape of the DW, which becomes almost straight after the external field is removed, indicates that the DW pinning due to local defects, expressed in terms of the propagation field B_{PR} , is considerably weaker than the geometrical pinning, given by the maximum restoring field B_R^{max} .

To evidence further the elastic nature of the geometrically pinned DWs in our devices, we applied a unidirectional periodic magnetic field $B_A = B_0|\sin(\omega t)|$ in a

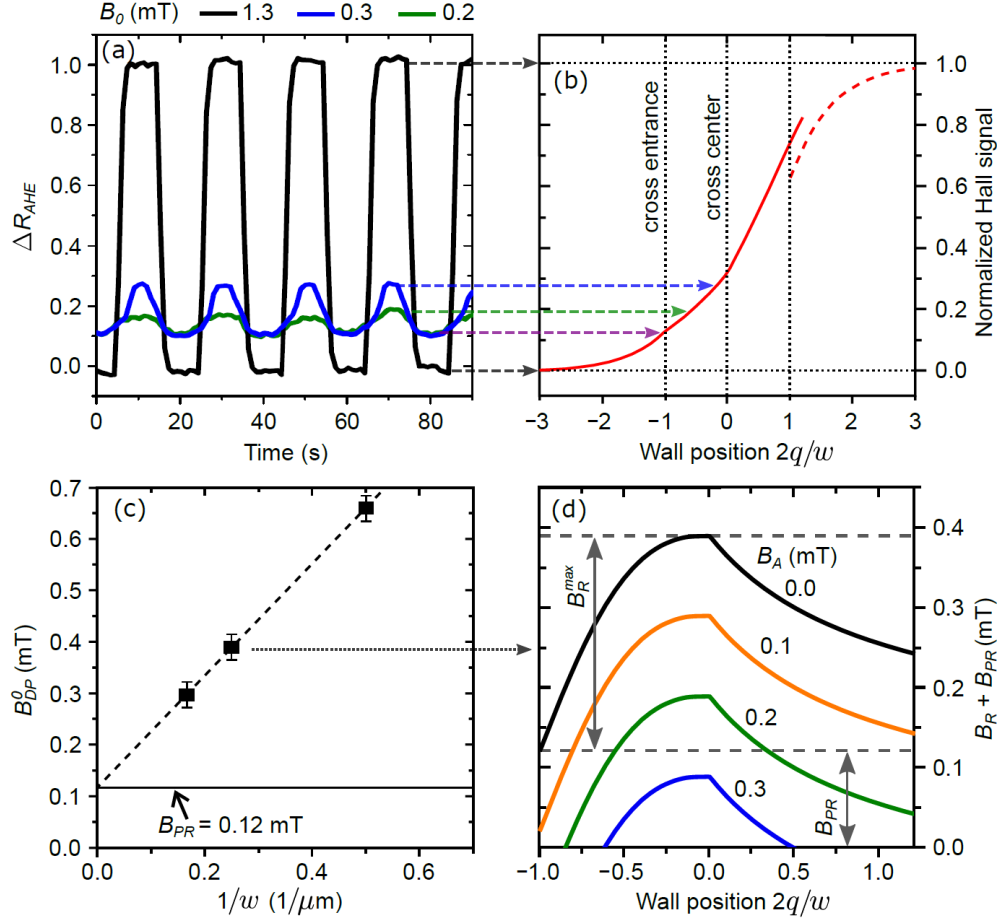


Figure 6.3: Elastic response of a geometrically pinned DW. (a) Change of the Hall resistance measured in a $4\ \mu\text{m}$ -wide cross during excitation with a unidirectional periodic field $B_A = B_0|\sin(\omega t)|$ with $B_0 = 0.2\ \text{mT}$ (green) and $0.3\ \text{mT}$ (blue) plotted relative to the maximum Hall signal due to the saturating field $B_A = 1.3\ \text{mT} \cdot \sin(\omega t)$ (black). (b) Normalized Hall signal as a function of the DW position within the cross predicted by the bubble-model (see appendix F). The DW positions corresponding to different Hall signal levels in (a) are indicated by arrows. (c) DW depinning fields $B_{DP}^0 = B_R^{max} + B_{PR}$ measured in crossbars of different widths showing the inverse proportionality $B_R^{max} \sim 1/w$ predicted by the bubble-model. The error bars correspond to the s.d. derived from 10 individual measurements and the dashed line is a linear fit. (d) Dependence of the effective field opposing the DW propagation in a $4\ \mu\text{m}$ -wide cross based on the B_R^{max} and B_{PR} values obtained from (c). The pinning barrier is lowered by the applied field B_A .

$4\ \mu\text{m}$ -wide cross and monitored the DW position via the Hall voltage measurement. Change of the Hall resistance for a period of $T = 2\pi/\omega = 20\ \text{s}$ and field amplitudes of $B_0 = 0.2\ \text{mT}$ (green) and $0.3\ \text{mT}$ (blue) is shown in Fig. 6.3(a) together with the Hall response to an alternating field $B_A = 1.3\ \text{mT} \cdot \sin(\omega t)$ (black). The latter field is strong enough to switch completely magnetization in the whole cross device between the two antiparallel states, i.e., it corresponds to the maximum achievable Hall signal variation. Normalization of the data to this reference allows us to directly relate the Hall signal to the DW displacement [see Fig. 6.3(b) and appendix F]. The DW positions inferred from the Hall measurement are in good agreement with the prediction of the bubble-model. The DW displacement approximately doubles when the field amplitude B_0 is increased from $0.2\ \text{mT}$ to $0.3\ \text{mT}$. In both cases, the DW elastically shrinks back when the field reduces to zero, as documented by the residual Hall signal of ≈ 0.1 which corresponds to a straight DW at the cross entrance. These results are consistent with the previous MO observations in Figs. 6.2(b)-(d), of a DW approaching the cross center and shrinking

back to a flat line in similar field range. Moreover, the continuous periodic Hall signal indicates a smooth DW motion which is not significantly affected by pinning at local material imperfections.

The DW propagation in the cross structure is opposed by both the propagation field B_{PR} (local pinning at defects) and the restoring field B_R (geometrical pinning at cross-entrance corners). In order to depin from the cross entrance the DW has to pass the cross center, i.e., it has to overcome the full height of the repulsive barrier due to the geometrical pinning, B_R^{max} [see Fig. 6.3(d)]. The depinning field B_{DP}^0 , which is defined as the minimum external magnetic field necessary to release the DW from the cross entrance, is, therefore, given as $B_{DP}^0 = B_R^{max} + B_{PR}$. According to the bubble-model, $B_R^{max} = 2\pi\sqrt{AK_u}/M_s w$ and B_{DP}^0 should be, therefore, also proportional to the inverse bar width with an offset given by B_{PR} . In Fig. 6.3(c) we show the depinning fields measured in crossbar devices with $w = 2, 4, \text{ and } 6 \mu\text{m}$. We get a perfect agreement with the theory, which confirms the applicability of the bubble-like DW propagation model in our structures. From a linear fit of the data and from the independently measured [106] effective perpendicular anisotropy, $K_u = 1.2 \text{ kJ m}^{-3}$, and saturation magnetization, $M_s = 18 \text{ kA m}^{-1}$, we obtain the exchange stiffness of $A = 50 \text{ fJ m}^{-1}$, which is a reasonable value for our GaMnAsP film. In agreement with the previous observations, the pinning on local imperfections is weak, $B_{PR} = 0.12 \text{ mT}$, compared to the geometrical pinning, $B_R^{max} = 0.18\text{--}0.54 \text{ mT}$.

6.2 Inertial DW motion driven by circularly polarized laser pulses

In the following, we exploit the above described elastic behavior of a DW geometrically pinned in the cross structure to prove the significant contribution of inertial effects in the OSTT-induced DW motion. Moreover, since the DW can be depinned from the cross either by external magnetic field $B_A > B_{DP}^0$ or by the OSTT from the circularly polarized laser pulses (LPs), we can calibrate the strength of the OSTT by combining the laser excitation with a field $B_A \leq B_{DP}^0$. The principal idea of our experiment is to utilize the elastic restoring force that acts *continuously* within the entire cross area against the DW propagation driven by the individual *ultrashort* ($\sim 100 \text{ fs}$) LPs. The photo-generated electrons can transfer their spin to the wall magnetization only during their short recombination-limited lifetime of $\sim 10 \text{ ps}$, which is three orders of magnitude shorter than the temporal separation between the consecutive LPs (12.5 ns).

The experiments were performed at a sample temperature of 90 K and using LPs with a wavelength of 750 nm, which excite the electrons slightly above the bottom of the GaAs conduction band. When circularly polarized LPs are used, the photo-electrons become spin-polarized with the degree of polarization approaching the maximum achievable value of 50% [64]. The excited area, given by the Gaussian laser spot of $\approx 1.5 \mu\text{m}$ FWHM, is much larger than the DW width of $\delta_{DW} = \pi\sqrt{A/K_u} \approx 20 \text{ nm}$ in our GaMnAsP film. During the low-temperature measurement, the direct aligning of the laser spot on top of the DW with a nanometer precision is impossible due to the vibrations induced by the operation of the closed-cycle cryostat and by the temperature-related sample drift (both reaching amplitudes of 0.1–1 μm). To circumvent this difficulty, we employed the following measurement procedure, which is sketched in Fig. 6.4(a). First, a straight DW is positioned at the cross entrance. Then, the laser spot is placed in the input bar (between the nucleation area and the cross), 10 μm away from the pinned DW and an external out-of-plane magnetic field B_A such that $B_{DP}^0 (\approx +0.4 \text{ mT}) > B_A > -B_{PR} (\approx -0.1 \text{ mT})$ is applied. In this field range the DW remains pinned at the cross entrance without the laser irradiation - it cannot

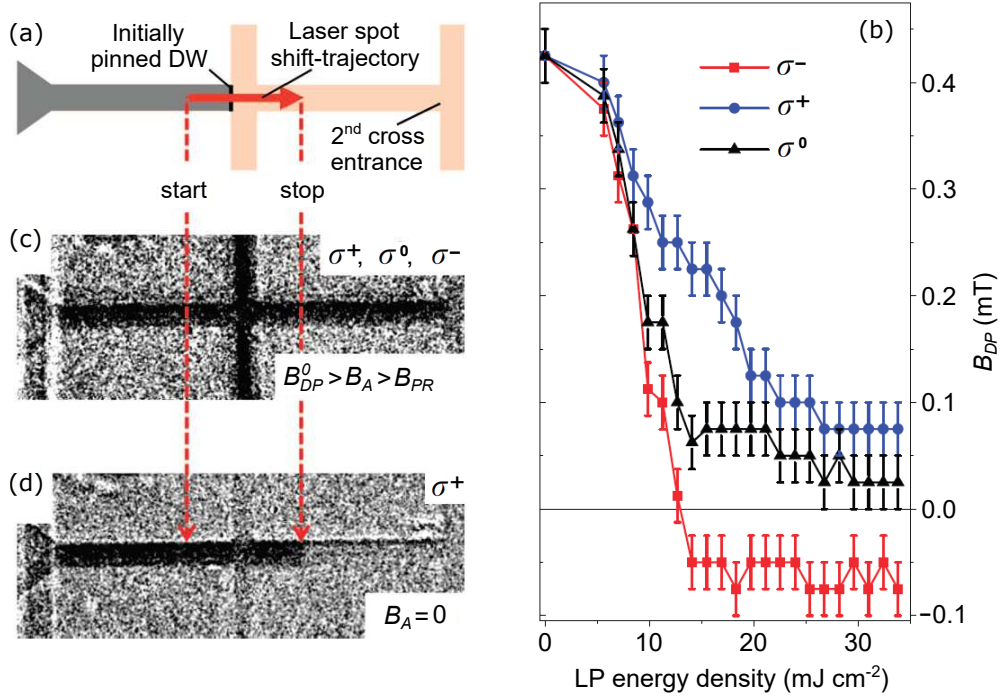


Figure 6.4: Laser-induced helicity-dependent DW depinning. (a) Sketch of the experimental procedure. The DW geometrically pinned at the cross entrance is excited by a focused laser spot that is swept at a rate of $\sim 2 \mu\text{m/ms}$ along the bar from the ‘start’ to the ‘stop’ position located $\approx 10 \mu\text{m}$ left and right from the initial DW position. During the sweep, a constant magnetic field B_A ($B_{DP}^0 > B_A > -B_{PR}$) is applied to adjust the pinning barrier height. After the sweep, the DW position is inferred from AHE measurement and MO imaging. If the DW is still pinned at the cross entrance, the pinning barrier is lowered by increasing B_A by $+0.025 \text{ mT}$ and the sweep is repeated. By stepwise increasing B_A , the depinning field B_{DP} is identified as the lowest B_A required to depin optically the DW. (b) Depinning fields measured for circular left (σ^+), right (σ^-), and linear (σ^0) LP polarizations as a function of the LP energy density. Each datapoint is obtained as an average from 5 independent B_{DP} measurements and the error bars correspond to the maximum scatter of the measured B_{DP} values around the corresponding mean values. (c) Differential MO image of the final domain configuration after the DW was optically depinned from the cross with an additional field $B_{DP}^0 > B_A > B_{PR}$ applied - the DW gets pinned at the second cross entrance, which was not irradiated. (d) The final domain configuration after the DW was depinned by σ^+ -polarized LPs in zero magnetic field - the DW stops at the final irradiated spot.

traverse the cross due to the geometrical pinning barrier and it also cannot move back into the input bar due to B_{PR} . The laser spot is then linearly swept for $20 \mu\text{m}$ along the bar crossing the DW at a velocity of $\sim 2 \mu\text{m/ms}$. During the sweep, $\sim 10,000$ ultrashort LPs separated by 12.5 ns expose the DW. Since the sample drift and most of the vibrations of higher spatial amplitude are slower than the sweep rate, we can consider the sample as being static during the spatial overlap of the DW with the laser spot. The applied procedure therefore allows for a reproducible optical excitation of the DW with always roughly the same number of pulses with a Gaussian profile of the local intensity at the DW location from the consecutive LPs. After the laser sweep, we check the DW position with the MO microscope and, if the DW was not depinned, we repeat the sweep with a slightly higher magnetic field B_A . The external field serves here to adjust the height of the effective energy barrier due to the geometrical pinning [see Fig. 6.3(d)]. The lowest magnetic field B_A , at which the laser beam depins the DW from the cross entrance, is called the *depinning field* B_{DP} (with B_{DP}^0 being the

depinning field without the laser irradiation).

The depinning fields, obtained by the above described measurement procedure, are shown in Fig. 6.4(b) for LPs with circular left (σ^+), right (σ^-), and linear (σ^0) polarization as a function of the laser-pulse energy density. First, we recognize a reduction of B_{DP} with increasing LP energy density for all three light polarizations. In the case of linear polarization, that is, in the absence of the OSTT, we ascribe the reduction of $B_{DP}(\sigma^0)$ fully to the LP-induced sample heating. Since the DW energy $\sigma_{DW} \sim \sqrt{AK_u}$ decreases with increasing temperature, the DW is attracted to the laser-induced hot spot. Importantly, this effect alone is not strong enough to drive the DW through the cross, since we do not observe DW depinning without applying the additional magnetic field $B_A > 0$ up to the highest LP energy densities used in our experiments of more than $\sim 30 \text{ mJ cm}^{-2}$. The saturation of $B_{DP}(\sigma^0)$ observed for LP energy densities larger than $\sim 20 \text{ mJ cm}^{-2}$ indicates that the laser-induced sample heating does not increase anymore. We ascribe this behavior to the saturation of the photo-generated carrier density at very high light intensities.

In the case of circularly polarized LPs, an additional driving force acts on the DW due to the OSTT, whose direction should depend on the light helicity. Indeed, in the entire range of LP energy densities - from zero to saturation - we observe that $B_{DP}(\sigma^+) < B_{DP}(\sigma^0) < B_{DP}(\sigma^-)$ for the positive magnetization orientation of the nucleated domain [such as in Fig. 6.1(b)]. In the case of σ^+ -polarized LPs with large enough energy density (above 12 mJ cm^{-2}) we observe a DW depinning without the help of the external magnetic field B_A , and even with a small negative B_A applied that opposes the DW expansion. For the σ^- -polarized LPs and the same initial domain configuration, we do not observe the DW depinning at zero applied magnetic field up to the highest LP energy densities. Instead, $B_{DP}(\sigma^-)$ saturates again above $\sim 20 \text{ mJ cm}^{-2}$. The difference between the saturation values of $B_{DP}(\sigma^-)$ and $B_{DP}(\sigma^0)$ is attributed to the effect of the OSTT acting against the DW expansion for σ^- laser polarization.

The differential MO image in Fig. 6.4(c) shows the final magnetic configuration after the DW was released from the cross entrance by the laser pulses in conjunction with a positive magnetic field B_A applied, such that $B_{DP}^0 > B_A > B_{PR}$. In such case, the DW after depinning from the irradiated cross continues in propagation along the bar, driven by $B_A > B_{PR}$, until it gets pinned at the entrance of the second cross, which was not irradiated during the laser sweep. In Fig. 6.4(d) we show the final domain configuration after the DW was depinned by σ^+ -polarized LPs at zero applied magnetic field. In this case, the DW is depinned and driven by the laser beam, due to the combined action of heating and OSTT, and stops at the end-point of the laser sweep.

From the results presented in Fig. 6.4, we can conclude that for the given initial domain configuration, the OSTT from σ^+ (σ^-)-polarized laser pulses assists (opposes) the DW depinning. The experiments confirm, that only the σ^+ -polarized LPs can drive the DW over the maximum of the geometrical pinning barrier in the cross center. Considering the ultrashort $\sim 100 \text{ fs}$ LPs time-separated by $\sim 10 \text{ ns}$, the OSTT can drive the DW across the $w/2 = 2 \mu\text{m}$ distance to the top of the pinning barrier only if the DW moves also during substantial part of the dark period in between two successive LPs, i.e., only if the DW is driven by its inertia. The DW depinning without inertia would require unrealistically high DW velocity of more than $\sim 1 \text{ km s}^{-1}$ that is even higher than the maximum magnon velocity in our GaMnAsP film. In the absence of inertia and taking into account the observed and calculated Walker breakdown velocities of $\sim 10 \text{ m s}^{-1}$ [106], the DW displacement during the short $\sim 100 \text{ fs}$ illumination or $\sim 10 \text{ ps}$ photo-electron spin lifetime would be too small and the wall would be driven back to the cross entrance by the repulsive restoring field B_R before arrival of the next optical

pulse and the DW would never depin from the cross.

This conclusion was confirmed by micromagnetic simulations using the Landau-Lifshitz-Bloch formalism performed by our colleagues, which can be found in our publication [191]. The simulations show that during the photo-electron spin lifetime the DW internal structure is severely deformed by the OSTT from the spin-polarized photoelectrons. After they recombine (~ 10 ps), the DW propagates forward for most of the dark period between the successive LPs, self-propelled by the processes of return of the DW structure to the unperturbed one. These processes stand behind of what we call the DW inertia, in agreement with what was observed in the case of current-driven inertial DW motion [100].

To verify our interpretation, we repeated the experiments with the inverted initial domain configuration, i.e., with the negative magnetization orientation ($-M_z^N$) of the nucleated domain. In this case, the OSTT should act in the opposite direction. Indeed, as shown in Fig. 6.5, we observe the opposite helicity dependency of the depinning field for the opposite initial magnetic configurations. The consistency found between $B_{DP}(\sigma^{+(-)}, +M_z^N) \approx -B_{DP}(\sigma^{-(+)}, -M_z^N)$ and $B_{DP}(\sigma^0, +M_z^N) \approx -B_{DP}(\sigma^0, -M_z^N)$ confirms the OSTT mechanism and the high reproducibility of our measurements.

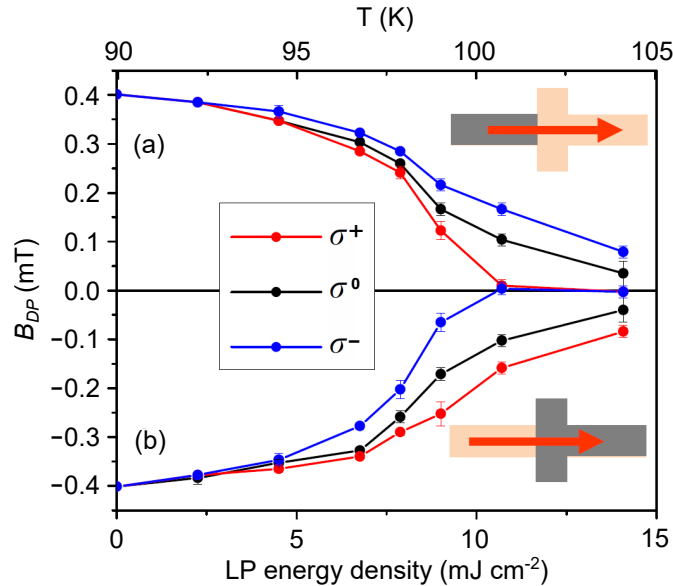


Figure 6.5: Helicity-dependent DW depinning at inverted domain configuration. Depinning field B_{DP} as a function of the LP energy density in a $4\mu\text{m}$ -wide cross for circularly left (σ^+), right (σ^-), and linearly (σ^0) polarized LPs for positive (a) and negative (b) magnetization orientation of the nucleated domain. The laser-induced temperature increase is estimated from the comparison between $B_{DP}(\sigma^0, T = 90\text{ K})$ and $B_{DP}(0, T)$ dependencies and plotted at the top of the graph.

6.3 Exclusion of helicity-dependent heating effects

As mentioned above, the helicity-dependent OSTT-induced driving force on the DW is unavoidably combined with the helicity-*independent* effect of the laser heating. The latter always attracts the DW to the center of the laser-induced hot spot. In order to estimate the laser-induced temperature increase, we compared two complementary measurements - the dependence of B_{DP} on the energy density of σ^0 -polarized LPs at a constant base temperature of 90 K and the dependence of B_{DP} on the base temperature without the laser irradiation. We found that up to the highest LP energy density of 35 mJ cm^{-2} used in our measurements, the temperature at the irradiated spot does not exceed the Curie temperature of our GaMnAsP film of 115 K.

An ordinary absorption of the laser light leads to a central-symmetric temperature profile that results from the Gaussian intensity distribution of the laser beam and the DW is attracted to the center of the hot spot. In a ferromagnet, we have to, however, take into account also the magnetization-dependent absorption of circularly polarized light due to the magnetic circular dichroism (MCD, see section 3.1.1) that leads to a helicity-*dependent* heating effect. If a DW is illuminated, the unequal absorption of the two domains results in a temperature gradient across the DW, which acts as an effective magnetic field pushing the DW towards the hotter domain. The direction of the temperature gradient, and the corresponding force on the DW, is opposite for the opposite initial magnetic configurations [(a) and (b) in Fig. 6.5] and also for opposite LP helicities. In the following, we discuss the contribution of this MCD-induced force to the observed helicity-dependent DW depinning in our cross-devices.

First of all, at the wavelength of 750 nm used in our experiments only $\sim 4\%$ of the incident light is absorbed in the 25 nm thin magnetic film. The rest is absorbed in the GaAs substrate with no dependence on the helicity. Moreover, MCD is a very weak MO effect leading to typical ellipticity magnitudes of $\sim 10^{-3}$, i.e., the difference in absorption between the two oppositely magnetized domains is of the same order of magnitude.

Another argument supporting the OSTT as the dominant mechanism responsible for the helicity-dependent DW depinning is the spectral dependence of B_{DP} presented in Fig. 6.6. The measurement was performed in a $4\ \mu\text{m}$ -wide cross at a base temperature of 75 K. We show separately the helicity-independent (a, c) and helicity-dependent (b, d) part of the measured data obtained as $[B_{DP}(\sigma^-) + B_{DP}(\sigma^+)]/2$ and $B_{DP}(\sigma^-) - B_{DP}(\sigma^+)$, respectively. The dependencies of B_{DP} on the LP energy density at different excitation wavelengths show qualitatively the same behavior - a rapid decrease of B_{DP} due to the helicity-independent heating [Fig. 6.6(a)] accompanied by an increase of the helicity-dependent B_{DP} component [Fig. 6.6(b)]. In Fig. 6.6(c) and (d) we show the spectral dependence of the helicity-independent and helicity-dependent B_{DP} components, respectively, measured at a fixed LP energy density of $7\ \text{mJ cm}^{-2}$. The heating effect in (c) increases (decreasing B_{DP}) with the decreasing wavelength, which is consistent with the increasing absorption coefficient. The wavelength dependence of $B_{DP}(\sigma^-) - B_{DP}(\sigma^+)$ in (d) is consistent with the expected spectral dependence of the OSTT strength, since the maximum spin polarization of the photo-carriers is achieved at the wavelength corresponding to the band-gap energy ($\approx 825\ \text{nm}$). For shorter wavelengths, the spin polarization (and consequently the OSTT) is strongly reduced by the transitions from the spin-orbit split-off band, while MCD is still present. For longer wavelengths, the spin density (and the OSTT) decreases due to the reduced absorption, in agreement with our observations.

The decisive argument against the MCD was given by the following experiment, which allowed us to identify the direction and estimate the magnitude of the MCD-induced temperature gradient across the DW. In the experiment, we monitor the four-point resistance of a uniformly magnetized $18\ \mu\text{m}$ -long bar section between the two crosses of a $6\ \mu\text{m}$ -wide crossbar device while illuminating the bar center by circularly polarized LPs with a certain helicity. We employ a simple resistor network model to relate the total resistance R_T of the entire bar with the local resistance R_{sq} of the illuminated area, which gives us information about the local temperature due to the known $R(T)$ dependence of our GaMnAsP film. By comparing the temperature increase due to the σ^+ and σ^- -polarized LPs we obtain directly the measure of the MCD-induced laser heating.

The resistor network model is sketched in Fig. 6.7(a). The $18 \times 6\ \mu\text{m}$ bar is divided into $9 \times 3 = 27$ squares of $2 \times 2\ \mu\text{m}$ size. Only the central square is illuminated having a

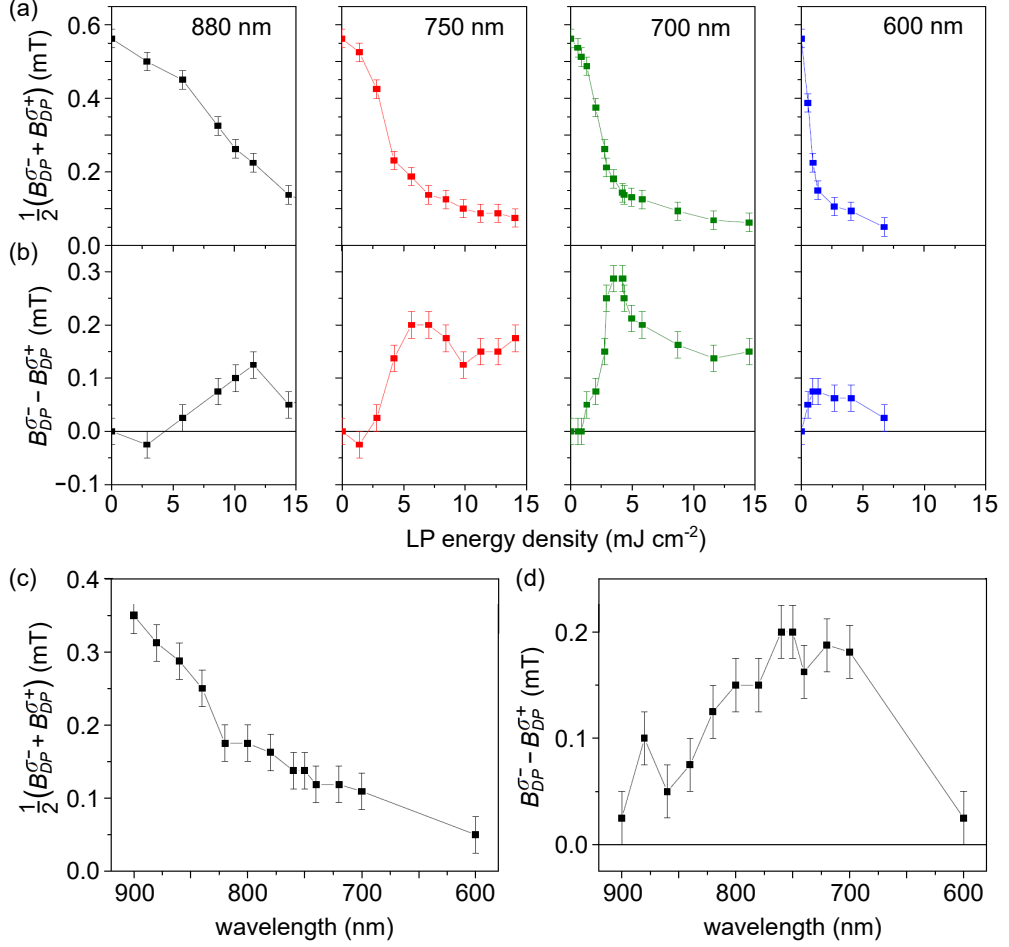


Figure 6.6: Spectral dependence of the DW depinning field. Dependence of the helicity-independent (a) and helicity-dependent (b) components of B_{DP} on the LP energy density obtained for various laser wavelengths as an average and difference of the measurements with σ^- and σ^+ circularly polarized LPs. The experiments were performed in a $4\mu\text{m}$ -wide cross at a base temperature of 75 K. The average B_{DP} indicates the reduction of the geometrical pinning due to the helicity-independent laser heating while the B_{DP} difference scales with the OSTT. The spectral dependence of the average (c) and differential (d) B_{DP} at a fixed LP energy density of 7 mJ cm^{-2} . The former reflects the increasing absorption at shorter wavelengths. The helicity-dependent DW depinning in (d) is consistent with the expected OSTT spectral profile.

resistance R_{sq}^L . The other 26 squares remain in darkness with resistances R_{sq}^D . First, we have to express the relevant resistance variation within the irradiated spot R_{sq} (which can be compared to the known $R(T)$ dependence) using the measurable quantities, i.e., the total resistance of the entire bar R_T with the laser spot on (R_T^L) and off (R_T^D). In the resistor network, one of the nine squares of the central stripe is illuminated with the overall resistance $R_1 = 8R_{sq}^D + R_{sq}^L$ and the two dark side stripes have the resistances $R_0 = 9R_{sq}^D$. The three stripes in parallel have, therefore, total resistance $R_T^D = R_0/3$ in darkness and $R_T^L = (R_0 R_1)/(2R_1 + R_0)$ with the central square irradiated. Combining these relations one can express the resistance ratio $\Delta(T) \equiv R_{sq}^L(T)/R_{sq}^D$ of the irradiated and non-irradiated square by the total bar resistances, $\Delta(T) \approx 27R_T^L/R_T^D - 26$, where the approximation is valid for Δ close to 1. In this range, the measured $R(T)$ dependence of our GaMnAsP film is approximately linear and can be inversely expressed as $T = [\alpha(\Delta - 1) + 90]\text{ K}$, where the slope $\alpha \approx 235$.

In order to avoid any small changes in the laser-spot position and intensity, we

measure the resistance with a fixed LP polarization while simultaneously switching periodically the magnetization between the two opposite saturations $\pm M_z$ at a frequency of 0.2 Hz. We use a sensitive double lock-in technique. The first lock-in amplifier measures the 4-point resistance in response to an alternating probe current ($f = 123$ Hz). After subtracting an offset, the output is multiplied by 100 and fed into the second lock-in amplifier, which extracts the resistance variation due to the alternating magnetization. As a result, we obtain $\delta R_M = R_T^L(+M_z) - R_T^L(-M_z)$. Finally, the MCD-related local temperature difference between the two oppositely magnetized states is $\delta T = T(+M_z) - T(-M_z) = \alpha[\Delta(+M_z) - \Delta(-M_z)] \approx 27\alpha\delta R_M/R_T^D$ with $R_T^D = 1244\Omega$. In Fig. 6.7(b) we show the temperature difference δT within the irradiated spot be-

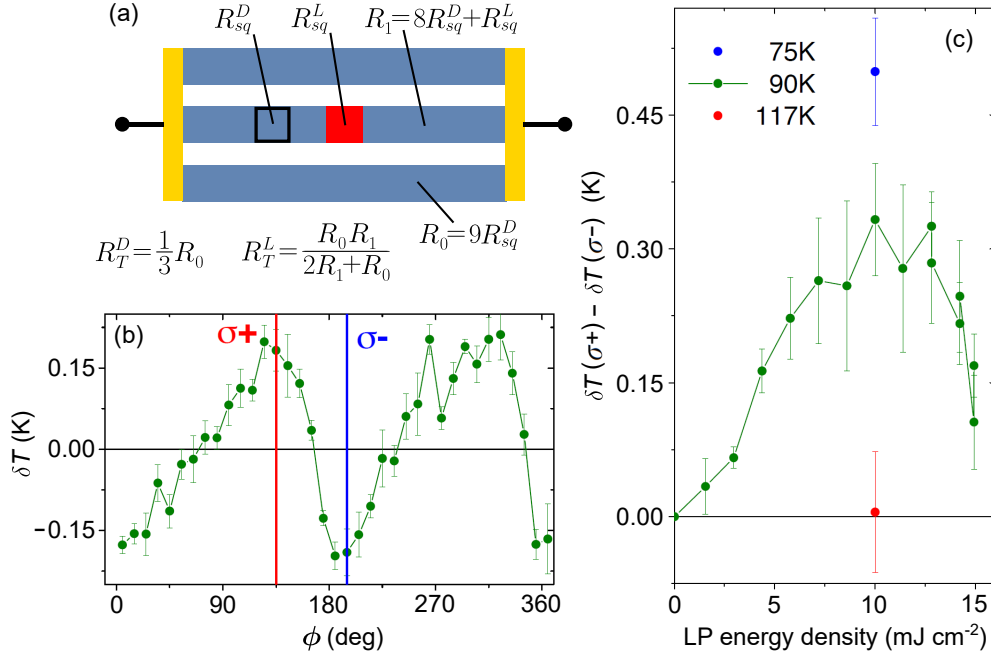


Figure 6.7: MCD-induced temperature variations. (a) Sketch of the resistor network model used to relate the measured variations of the overall bar resistance to the local temperature variations within the LP-irradiated spot. (b) Temperature difference between the oppositely magnetized domains at a base temperature of 90 K and for a LP energy density of 10 mJ cm^{-2} for different LP polarizations. The LP-polarization state is controlled by setting the quarter-wave plate rotation angle ϕ . A constant offset is subtracted from all datapoints. The error bars correspond to the standard deviation of the detected resistance variation. (c) Difference between the temperature variations measured with σ^+ and σ^- circular polarizations as a function of the LP energy density at different base temperatures. The MCD-induced heating effect disappears above the Curie temperature of 115 K.

tween the states with positive and negative magnetization orientations for different LP polarizations and fixed LP energy density of 10 mJ cm^{-2} . The polarization is varied by rotating a quarter-wave plate (angle ϕ).² As expected for MCD-related heating, we find the largest temperature variations for the circular polarizations (σ^\pm). In addition, in Fig. 6.7(c) we show the difference between the δT values obtained for σ^+ and σ^- circular polarizations as a function of the LP energy density. As is obvious from the data measured at different base temperatures, the heating effect is indeed related to the magnetic order, since it disappears above the Curie temperature of the material of

²The discrepancy between the measured and the expected $\cos(2\phi)$ dependence is caused by unintentional polarization changes in the beamsplitters BS1 and BS2 in our setup (see Fig. 5.1). σ^\pm correspond to circular polarizations incident on the sample.

115 K.

From the data of Fig. 6.7(b), we conclude that at the base temperature of 90 K the MCD-induced temperature difference is $\approx +(-)0.2$ K for the circular $\sigma^+(\sigma^-)$ LP polarizations. Hence, the $\sigma^+(\sigma^-)$ -irradiated film with positive (negative) magnetization becomes hotter than the film with negative (positive) magnetization orientation. In the DW depinning experiments presented in Fig. 6.4, we first saturate the sample in a negative magnetic field and then nucleate a domain with positive magnetization orientation. Consequently, the DW pinned at the cross entrance has a positive magnetization on the left (in the input bar) and negative magnetization on the right (inside the cross). When heated with $\sigma^+(\sigma^-)$ -polarized LPs the left (right) domain becomes hotter attracting the DW. In other words, the MCD-induced temperature gradient opposes (assists) the DW depinning for $\sigma^+(\sigma^-)$ -polarized LPs in contradiction to what is observed. We can, therefore, exclude MCD as the effect responsible for the helicity-dependent DW motion in our experiments.

6.4 Conclusion

We have studied the DW motion driven by ultrashort circularly polarized laser pulses in a thin-film crossbar device patterned from a diluted ferromagnetic semiconductor GaMnAsP. We identified two main effects contributing to the DW displacement - the helicity-independent heating from the LPs, which always attracts the DW to the center of the laser spot, and the helicity-dependent driving force from the optical spin transfer torque. The latter effect acts only within the DW where the magnetization has a nonzero in-plane component. The torque from the spin-polarized photo-electrons tilts the wall magnetization out of the sample plane, thus driving the whole DW along the bar with a direction depending on the LP helicity.

The main finding of our experiments is the inertial character of the OSTT-induced DW motion. To prove that, we utilized the special feature of our crossbar devices where a DW propagating along the bar gets pinned at the entrance corners of the cross due to geometrical reasons. In order to propagate further, driven by a magnetic field or laser pulses, the DW has to increase its length, which costs energy. This can be expressed in terms of a virtual restoring field opposing the DW propagation within the entire cross area. If the DW would move only during the ~ 100 fs duration of the LP or during the ~ 10 ps spin lifetime of the photo-electrons it would be driven back to the cross entrance by the restoring field before arrival of the next LP which comes in ~ 10 ns. However, we observed the DW depinning from the cross for one helicity of the circularly polarized LPs. This is only possible, if the DW moves forward during a significant part of the dark period in between the successive LPs. This conclusion was confirmed by micromagnetic simulations performed by our colleagues, which show that during the photo-electron spin lifetime the DW internal structure is severely deformed by the OSTT. After the spin-polarized photo-electrons recombine (~ 10 ps), the DW propagates forward, self-propelled by the processes of return of the DW structure to the unperturbed one, for most of the dark period between the successive LPs (~ 10 ns).

To confirm the OSTT origin of the helicity-dependent DW propagation in our devices, we performed several control experiments. We repeated the DW depinning experiments with the inverted initial domain configuration and, in agreement with the OSTT mechanism, we observed that the direction of the induced DW motion inverts as well. We studied the spectral dependency of the helicity-dependent DW depinning, which agrees with the expected spectral profile of the OSTT strength. Finally, we excluded the MCD-induced temperature gradient as the effect responsible for the helicity-dependent DW response by a direct measurement of the laser-induced temperature variations in

the magnetic film.

7. Ultrafast current pulses in a vertical (anti)ferromagnet-photodiode heterostructure

In the previous chapter we studied the domain wall dynamics induced in a ferromagnet by ultrashort optical pulses. We benefited from the unique properties of the DMS GaMnAs where spin-polarized carriers can be generated by light absorption [64]. The spin transfer torque exerted by the photo-injected spin polarization can manipulate the magnetization on a picosecond timescale [38]. Nevertheless, the subsequent magnetization dynamics is still limited by the GHz-range resonance frequency in ferromagnets, resulting in nanosecond magnetization switching times. Therefore, for a research towards faster electronics it is more promising to apply these ultrashort excitation mechanisms to antiferromagnetic materials, which exhibit the exchange-enhanced magnetic dynamics with resonant frequencies in the THz range [9, 44]. An increasing number of experiments demonstrating an electrical control of the AF order have appeared recently [10, 173, 194, 195]. Néel vector reorientation via the relativistic NSOT mechanism [12] was achieved in a collinear AF CuMnAs using electrical current pulses of lengths ranging from ns down to ~ 0.25 ns [78] and even by picosecond pulses of THz radiation [79]. From a broader perspective, to deliver ultrashort current pulses with a duration $\tau \lesssim 100$ ps, photoconductive switches placed in a close proximity to the investigated device are a standard solution, since the high-frequency components of the current pulse become increasingly attenuated during their propagation from a distant external source.

The photoconductive switches usually use a lateral design of the Auston type [196, 197]. These devices consist of two metallic electrodes separated by a semiconducting gap with a short (~ 1 ps) carrier lifetime. Absorption of an ultrashort laser pulse makes the gap temporarily conductive producing a picosecond current pulse. The non-trivial lateral geometry brings several difficulties and, therefore, for certain purposes it may be beneficial to use a vertical design where the investigated magnetic film is deposited directly on top of a photodiode switch. An example of such a device is a Schottky diode where the built-in electric field associated with the Schottky barrier accelerates the photo-carriers resulting in a short current pulse entering the magnetic metallic electrode of the diode [33, 198, 199]. The advantage of the vertical design is that the whole illuminated area is excited simultaneously and in the same way, i.e., with the same profile of the electrical pulse (except for the effects connected with the Gaussian profile of the laser excitation). An important geometrical property of the layered vertical structure is the direct planar contact of the magnetic film with the current pulse source. This is crucial when applying spin-polarized current pulses since the injected spin polarization typically penetrates only a short distance into the magnetic material. This also makes the effect of the spin-polarized current confined only to the well-defined illuminated area and this excited area can be easily changed by moving the laser spot over the device surface. Furthermore, due to the direct contact, the onset of the current pulse in the entire illuminated area should be almost immediate, comparable to the optical pulse onset. Finally, from an application point of view, the vertical switches are easily scalable, unlike the lateral ones, which require quite a lot of space in the horizontal direction.

In this chapter, we introduce another variant of the vertical photoconductive switch design that is based on a PIN diode. The active part of the structure – the depleted

layer – is much thicker in the PIN diode compared to the Schottky diode, which allows to collect more photo-generated charge and thus produce more powerful current pulses. We first characterized the duration and amplitude of the current pulses generated optically in our devices. Subsequently, we studied the propagation of the current pulses through the structure by observing the effects of the current pulse-induced Oersted magnetic field on the magnetization of an iron layer deposited on top of the diode. Finally, we replaced the iron film by an antiferromagnetic CuMnAs film. This modified device exhibited very similar characteristics of the generated current pulses as the previous one which demonstrated that the PIN diode-based photo-switch design is generally applicable and can be used to deliver picosecond current pulses to a broad variety of conductive magnetic materials that can be grown on a semiconducting substrate. In particular, we show that the estimated current densities achievable with the PIN diode are comparable to those required for manipulation of the antiferromagnetic Néel vector in CuMnAs via NSOT [10, 78, 173, 194, 195].

The results presented in this chapter are currently being prepared for publication.

7.1 The device structure and characterization of the photo-current pulses

In Fig. 7.1(a) we show a sketch of our GaAs PIN diode grown on top of a semi-insulating GaAs substrate. On top of the diode (on the n-layer) a thin (2 nm \approx 14 ML) ferromagnetic iron film is deposited and protected by an aluminum-oxide layer. The GaAs diode consists of a 670 nm thick carbon-doped ($n_C = 2 \times 10^{18} \text{ cm}^{-3}$) p-layer, a 1000 nm thick intrinsic layer, and three silicon-doped n-layers with a dopant concentration gradually increasing towards the diode surface: 150 nm thick layer ($n_{Si} = 1 \times 10^{17} \text{ cm}^{-3}$), 15 nm thick layer (n_{Si} ramping from 1×10^{17} to $5 \times 10^{18} \text{ cm}^{-3}$), and 15 nm thick layer ($n_{Si} = 5 \times 10^{18} \text{ cm}^{-3}$). The micrograph in Fig. 7.1(b) shows the lateral structure of our device. The PIN/FM stack was patterned into a Corbino disc with a diameter of 100 μm . The circular golden contact (yellow) connects the magnetic film (brown), which is separated from the rest of the layer by a trench (black). The contact to the bottom p-layer is outside of the displayed image.

The built-in electric field \mathbf{E} , which is mostly located in the intrinsic layer of the diode, can be tuned by applying an additional external voltage bias between the top and bottom golden contacts. The VI characteristics of our diode measured in darkness [see Fig. 7.1(c)] shows that we can apply a large reverse bias with a negligible leakage current. Unlike in the case of the Schottky diode [33], in our PIN/Fe structure we can apply also a relatively large forward bias. The reason is most probably that in our device there is also a Schottky barrier present between the uppermost n-doped GaAs layer and the metallic Fe film. Polarities of the two junctions are opposite, i.e., when the PIN diode is connected with forward polarity [(-) on Fe and (+) on p-GaAs], the Schottky junction has reverse polarity, which is preventing large currents. The possibility to reverse the current polarity and to apply larger forward biases without destroying the device was important for identification of the effects of the photocurrent pulse on magnetization in the adjacent iron film.

In order to produce ultrashort electrical current pulses, the PIN/Fe structure is illuminated by a focused femtosecond laser beam. Absorption of the laser pulse in the μm -thick intrinsic layer creates electron-hole pairs which are immediately separated by the large internal electric field and accelerated towards the opposite electrodes creating an ultrashort current pulse, as schematically shown in Fig. 7.1(a). The advantage of the vertical photodiode design, compared to the Auston-type lateral switch, is that the photocurrent pulse can excite any place in the disc (selected by the position of

the laser spot) in the same way. Furthermore, thanks to the optical selection rules (i.e., the unequal optical transition probabilities for spin-up and spin-down electrons) in GaAs [64], the current pulses generated in the PIN diode are spin polarized when circularly polarized laser pulses of suitable photon energy are used. The photo-carrier spin is oriented along the laser propagation direction with a polarity given by the light helicity. The maximum theoretical spin polarization of 50% is reached when only the transitions from heavy- and light-hole bands to the conduction band are involved, i.e., for $E_g < \hbar\omega < E_g + \Delta_{SO}$ [see Fig. 2.5(a)]. Here, $E_g \approx 1.52$ eV is the band gap energy and $\Delta_{SO} \approx 0.34$ eV is the separation of the spin-orbit split-off band from the heavy- and light-hole bands in the center of the Brillouin zone (values at $T = 15$ K). In real samples, the spin polarization reaches the maximum of $\approx 40\%$ for photon energies slightly above E_g and quickly drops with increasing energy [65]. All experiments in our Fe/GaAs structures were performed using a laser wavelength of ≈ 800 nm (≈ 1.55 eV) at a temperature of 15 K.

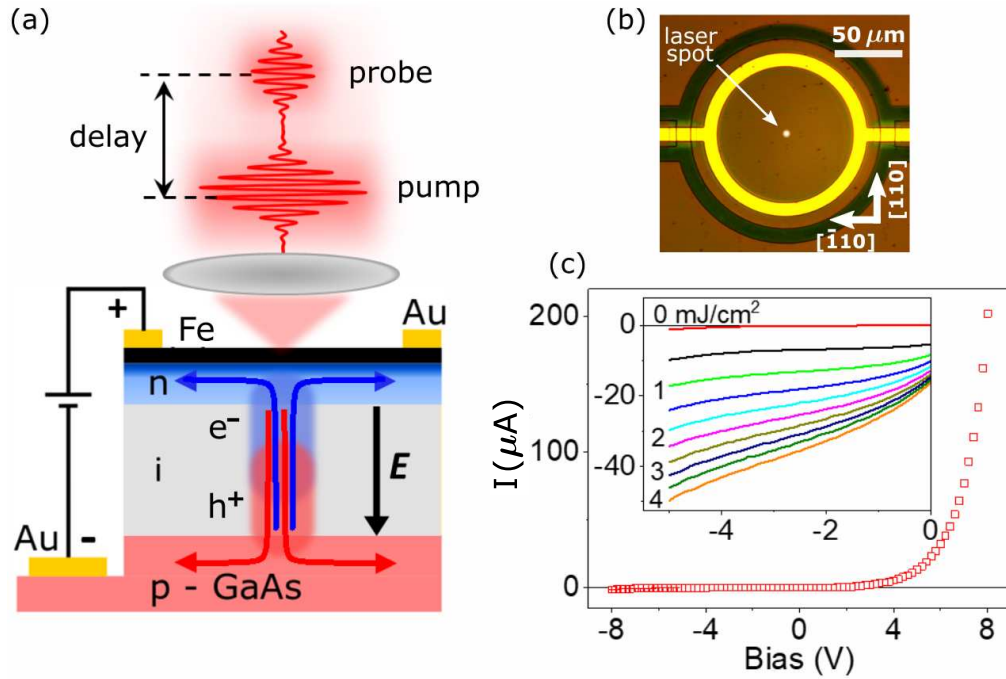


Figure 7.1: Photo-generation of current pulses in Fe/GaAs diode structure. (a) GaAs PIN diode structure with a thin Fe film on top connected in reverse polarity. After an impact of a laser pulse, a cloud of electron-hole pairs is generated. The electrons and holes are separated by the strong electric field E in the intrinsic layer and accelerated towards the opposite electrodes creating a short current pulse. A second laser pulse can probe the excited charge and spin dynamics with a time delay. (b) Lateral structure of the photodiode. Fe/GaAs Corbino disc (brown) is isolated by a trench (black). The Fe film is connected by a golden round contact (yellow), which bridges the trench. The contact to the bottom p-GaAs electrode is outside of the displayed image. (c) VI characteristics of the diode in darkness. Inset: VI curves under illumination by a single femtosecond laser beam. Nonlinear dependence of the photocurrent on the laser fluence is observed.

To study the electron spin and magnetization dynamics excited in the diode we employed a pump-probe MO technique. We used two different pump-probe setups. First, it is a simpler setup with two separate lenses used for focusing of the laser beams incident on the sample and for collimation of the probe beam reflected from the sample. The laser is tuned to a wavelength of 800 nm and the pump and probe beams are focused to a spot size of ≈ 25 μm (FWHM). The average pump power of 60 mW and the pulse repetition rate of 80 MHz result in the laser fluence (pulse

energy density) of $\approx 0.1 \text{ mJ/cm}^2$. The probe power is set to 10% of the pump power. Later, we switched to the pump-probe setup described in chapter 5, which is equipped with a microscope objective providing a high spatial resolution (FWHM $\approx 1.5 \mu\text{m}$). In this case, the laser central wavelength is tuned to 798 nm and we use spectral filters NF808-34 in the pump beam, FB810-10 in the probe beam, and FBH810-10 in the optical bridge (all from Thorlabs) to spectrally separate the pump and probe beams and suppress the noise from the pump photons in the detection system. The resulting central wavelengths of the pump and probe beams are 794 nm and 804 nm, respectively. The pulse repetition frequency is decreased to 8 MHz by a pulse picker and the used pump laser power of $230 \mu\text{W}$ corresponds to a fluence of $\approx 1 \text{ mJ/cm}^2$. The probe power is set to 10–20% of the pump power. The higher probe/pump power ratio was necessary in some measurements to reach a good signal-to-noise ratio with the weak probe beam (the probe beam power was of the order of $\sim 10 \mu\text{W}$). Further in the text, we will always identify the setup used in the individual measurements by mentioning the laser spot size of either 1.5 or 25 μm .

Besides the measurements of spin and magnetization dynamics, we used the same optical setup combined with an electrical measurement also for an evaluation of the basic parameters of the ultrashort electrical current pulses generated in our photodiode by the femtosecond laser pulses. For this purpose, we performed photocurrent correlation measurements [200]. This technique is sensitive to the nonlinear component of the response of the photodiode, i.e., to the mutual interaction between two consecutive photo-generated current pulses. It allows to measure the duration of the temporal overlap of the two current pulses and, since they are identical, the duration of a single current pulse [200–202]. The nonlinear response of the investigated system to the optical stimulus is necessary for the correlation technique to work [202]. The nonlinear behavior of our photodiode is clearly apparent from the VI characteristics shown in the inset of Fig. 7.1(c), which were measured with a single laser beam focused to a 1.5 μm wide spot in the center of the Corbino disc. The individual curves were measured with the laser fluency increasing in constant steps of 0.45 mJ/cm^2 . However, the measured photocurrent increases sub-linearly, which indicates a decreasing charge collection efficiency with an increasing photo-carrier density. This is caused mainly by the interplay between the internal electric field and the photo-generated charge [200, 201], as explained below.

The photocurrent correlation measurement was carried out in the following way. We set the intensity and polarization of the two laser pulses to be equal, i.e., we performed a “pump-pump” experiment. The measured quantity was a time-averaged photocurrent generated in the diode, which was measured by a sensitive ampere-meter as a function of the time delay between the two identical laser pulses. After the impact of the first laser pulse, the photo-generated electron-hole pairs are separated in the strong electric field present in the intrinsic part of the PIN diode and accelerated in the vertical direction towards the opposite electrodes, thus creating a short current pulse [see Fig. 7.1(a)]. The presence of the photo-carriers created by the first laser pulse influences both the material properties (e.g., via saturation of absorption) and the diode properties (e.g., by screening of the electric field) until the photo-carriers are removed from the diode by the electric field. The absorption of the second laser pulse is decreased because of the saturation and the electric field, which is weakened by the screening effect, makes the electrical transport slower, which means that more photo-carriers can recombine before reaching the electrodes. Both these effects decrease the total charge which can be transported out of the diode per one pair of laser pulses and, therefore, the average photocurrent measured in the stroboscopic pump-pump experiment is also decreased. As the influence of the first pulse on the second pulse increases with decreasing time

delay between the pulses, a decrease of the average photocurrent is expected around zero time delay.

The photocurrent correlation curves measured in the Fe/GaAs Corbino device for different external biases applied both in the forward and reverse polarities are shown in Fig. 7.2(a). The photocurrent I_{ph} is plotted relative to its value for zero time delay, $\delta I_{ph} \equiv I_{ph} - I_{ph}(\Delta t = 0)$. In this measurement, the two laser beams were focused to $\approx 1.5 \mu\text{m}$ spot size and overlapped in the middle of the Corbino disc. As expected, the photocurrent is reduced around the zero time delay. Note that in our convention, the current is negative for reverse (negative) bias and positive for forward (positive) bias, i.e., both in the forward and reverse case, the average photocurrent drops in absolute value for small time delays.

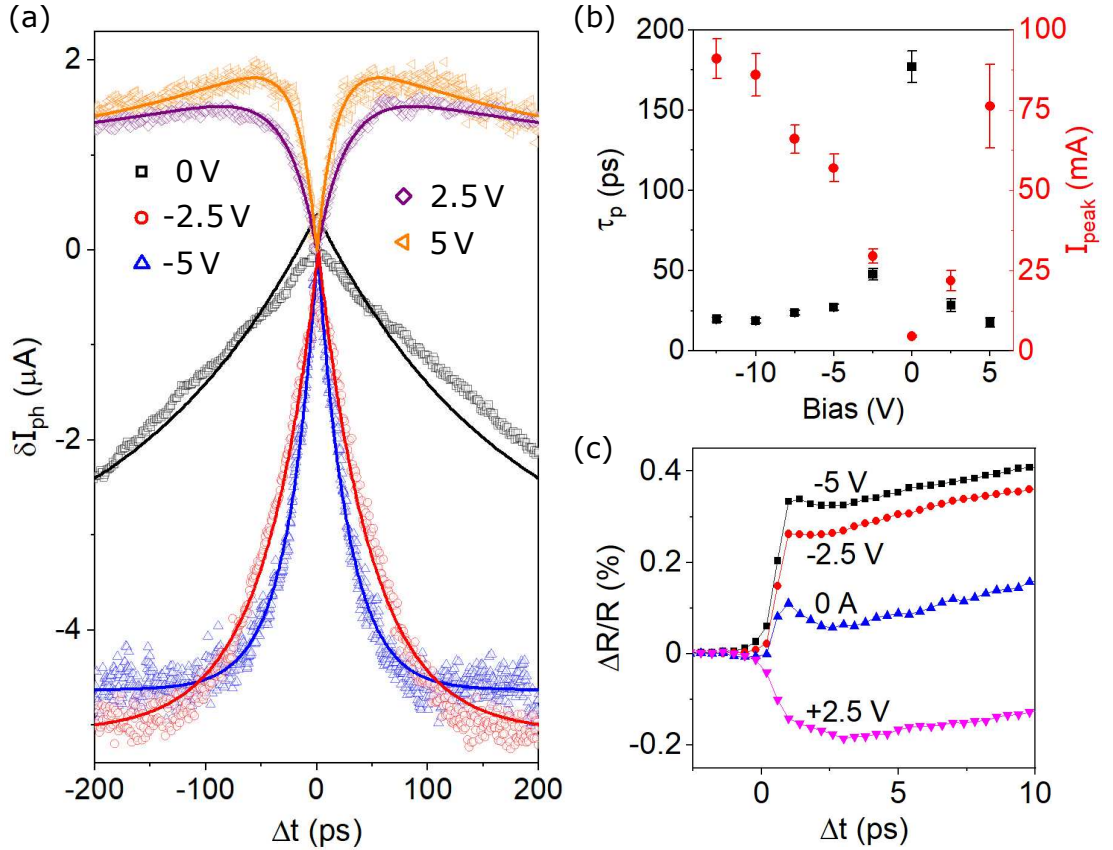


Figure 7.2: Characterization of ultrashort photocurrent pulses. (a) Photocurrent correlation measurement. Time-averaged photocurrent is measured as a function of the mutual delay Δt between two identical laser pulses for different applied biases. The photocurrent is plotted relative to its value for $\Delta t = 0$. The measured data (points) are fitted (lines) by a single- and double-exponential model for reverse and forward biases, respectively. (b) Bias dependence of the decay time τ_p and the peak current I_{peak} of the current pulse extracted by fitting from (a). (c) Transient reflectivity measured in a pump-probe experiment for different applied biases suggesting a ~ 1 ps onset of the current pulse. The laser spot size was $1.5 \mu\text{m}$ in all measurements.

The interpretation of the measured correlation signal is not straightforward. The theoretical analyses performed by Brorson *et al.* [203] and Jacobsen *et al.* [201] link the temporal profile of a single photocurrent pulse to the profile of the time-averaged correlation signal. In their case of a lateral Auston switch, the double-exponential profile of the correlation signal reflects the exponential decay of the photocarriers (and the corresponding photocurrent) via trapping and recombination. In [33], an exponential decay of the photocurrent pulse in a Schottky diode is inferred from time-resolved reflectivity

measurements. As shown in Fig. 7.2(a), the photocurrent correlation data from our PIN diode can be fitted well by a single-exponential model, $I_{ph} = I_0 + I_p \exp(-|\Delta t|/\tau_p)$, for larger reverse biases. Here, I_0 is an offset that corresponds to a dark current plus the photocurrent for well separated pump pulses, I_p is the photocurrent drop by bringing the two pump pulses together in time, i.e., it is a measure of the nonlinearity of the system, and τ_p corresponds to the decay time of the photocurrent pulse. For a low or zero bias, the electric field screening is more pronounced, which might explain the distorted correlation curve. However, based on the aforementioned theoretical analyses, we assume that also in this case the decay time of the photocurrent correlation reflects the duration of the underlying ultrashort photocurrent pulses.

In the case of forward bias, the photocurrent correlation obviously contains an additional component with opposite polarity, i.e., a component which corresponds to an effect increasing the photocurrent with decreasing time delay. We ascribe this contribution to the effect of heating. Each laser pulse absorbed in the diode heats the semiconductor, which temporarily increases its conductivity and, therefore, the forward current supplied by the external electrical source (we apply a constant voltage). Since the conductivity of an intrinsic semiconductor increases super-linearly with temperature, $\sigma \sim \exp(-E_g/2k_B T)$, the closer the two laser pulses are in time, the larger is the temperature increase and correspondingly larger is the average current flowing through the diode. We took into account the heating effect by adding a second exponential term $\sim \exp(-|\Delta t|/\tau_H)$ to the fitting function, where τ_H corresponds to the time-scale at which the pulse-induced heat is dissipated from the illuminated spot.

The decay times τ_p determined by the fitting procedure are shown in Fig. 7.2(b) as a function of the applied bias. The decay time decreases rapidly with increasing reverse bias and saturates at ≈ 25 ps for biases larger than -5 V. This is expected, as the stronger electric field depletes the photo-generated charge faster. In the case of forward bias, similarly short pulses can be created. For the heating-related time constant we obtain from fitting $\tau_H = 210 \pm 30$ ps. Based on the dark current measured in an independent experiment, the repetition rate of the laser pulses, and taking into account the single-exponential decay of the current pulse, we also estimated the peak current I_{peak} flowing during the pulse, as shown in Fig. 7.2(b). We note that the measured decay time is mainly limited by the RC time-constant of the Corbino disc. Therefore, shorter and stronger current pulses are expected in devices of smaller diameter.

In fact, as was pointed out by Jacobsen *et al.* [201], the photocurrent correlation does not necessarily correspond directly to the current pulse decay. It reflects rather generally the time needed to recharge the photoconductive switch. In the case of long carrier lifetime, the photocurrent correlation may not resolve the initial rapid charge dynamics before it is slowed down by the charge separation-induced electric field screening. Taking into account the large electric field in the intrinsic layer of our diode (up to 15 V/ μm), the first portion of the photocarriers should, indeed, enter the electrodes on a subpicosecond timescale. The rapid separation is followed by a rapid deceleration of the charge due to the screening effect. This initial stage is then followed by a slower depletion of the structure and restoration of the internal electric field. This recharging of the switch is visualized by the photocurrent correlation measurement. Therefore, the electrical pulse parameters shown in Fig. 7.2(b) correspond only to an upper (lower) bound of the pulse duration (amplitude). This picture of a rapid initial charge dynamics followed by a slower recharging of the device was confirmed also by a simulation of the charge propagation in our diode. However, as the simulation was not performed by the author of this work, these results are not included in this thesis.

A suitable tool to capture the initial pulse dynamics would be a terahertz spectroscopy, which is sensitive directly to the electric field change in the diode and which

could, therefore, resolve the onset of the screening [201]. However, an indication of the rapid current onset is also given by reflectivity measurements. As already mentioned, in the seminal work utilizing a Schottky diode to generate short current pulses [33], the pulse duration was inferred from a transient reflectivity which is associated with the transient photo-generated charge. In Fig. 7.2(c) we show the reflectivity of our PIN diode measured in the pump-probe experiment with the $1.5\ \mu\text{m}$ laser spots. The ‘0A’ curve corresponds to conditions when the built-in electric field of the diode was exactly compensated by the applied forward bias (zero average photocurrent). In this case, we observed only a relatively slow increase of the transient reflectivity. In contrast, for a reverse bias we observed a rapid ($\Delta t \lesssim 1\ \text{ps}$) increase of the signal followed by a similar slow signal build-up. Moreover, the initial step in the reflectivity was increasing with the applied bias and had opposite sign for opposite bias polarity. A plausible explanation is that this initial signal, which responded to the applied bias, reflected the process of charge separation in the diode, i.e., the onset of the current pulse. The action of the applied bias on such an ultrashort timescale can be explained by the Franz-Keldysh effect (FKE) [204, 205]. Before the impact of the pump laser pulse, the strong electric field present in the intrinsic region of the diode modifies the band energies and, consequently, also the absorption (and reflectivity) spectrum. For photon energies exceeding the band gap (which is our case) FKE causes an oscillatory modulation of the reflectivity spectrum and these oscillations change with the strength of the electric field. The separation of the photo-generated electron-hole pairs causes a rapid decrease of the local electric field and, consequently, a change in the FKE-induced modulation of the reflectivity, which is observed as the ultrafast change in the transient reflectivity.

7.2 Current pulse-induced dynamics of Fe magnetization

After characterizing the photocurrent pulses generated in the PIN diode by femtosecond laser pulses, we performed a set of pump-probe MO experiments studying the magnetization dynamics excited by the current pulses in the iron layer. The static magnetic properties of the iron film were studied by a SQUID magnetometer and magneto-optical methods (see appendix D). The magnetization is confined in the sample plane by a strong demagnetizing field ($\sim 2\ \text{T}$). In the film plane, two magnetic easy axes were identified forming an angle of approximately $\pm 32^\circ$ with the [110] crystal axis.

There are several different mechanisms that could excite the Fe magnetization dynamics in our sample structure. An interesting possibility would be the direct spin transfer from the laser-pulse-induced spin-polarized current pulse to the magnetization. This hybrid photocurrent-induced spin transfer torque would manifest itself as a light helicity-dependent precession of the Fe magnetization. However, no helicity-dependent oscillatory MO signal was detected that would originate from the Fe film. On the other hand, we observed a clear helicity-dependent precession of the photo-electron spins in GaAs, as expected due to the optical orientation. Therefore, we conclude that the spin-polarized carriers generated in the GaAs diode by circularly polarized laser pulses either do not maintain their polarization when crossing the interface to Fe, or their spin-polarization is not sufficient to overcome the large demagnetizing field of the iron film. The magnetization precession, we observed, was helicity-independent and, as we show below, was triggered by the Oersted field of the short photocurrent pulse. We utilized this effect of the current on the magnetization to understand the propagation of the current pulse through the 3D Corbino structure. We found that the initial vertical current flowing in the laser-illuminated column in the diode is followed by a lateral current propagating through the electrode towards the ring contact [see Fig. 7.1(a)].

In Fig. 7.3 we show the results obtained in the case when the pump and probe laser spots were separated by $9\ \mu\text{m}$ (with a spot size of $1.5\ \mu\text{m}$) along $[\bar{1}10]$ direction [see Fig. 7.3(a)]. The linearly polarized pump laser pulses were focused to the middle of the Corbino disc. No external magnetic field was applied during this measurement. In Fig. 7.3(b) we show the pump-probe MO traces measured for different applied biases. The oscillatory signal originates from the precession of magnetization in the iron layer, as confirmed by studying the dependence of the precessional frequency on the external magnetic field strength (see appendix D). The measured MO signal corresponds to the prependicular-to-plane component of the magnetization precession detected, via the polar Kerr effect, as a rotation of the polarization plane of the linearly polarized probe pulses. As one can directly see, the precessional phase is opposite for curves measured with reverse and forward applied bias, respectively. The parameters of the oscillatory signal were determined by a fitting using a damped harmonic function (for the time-delay Δt larger than 100 ps)

$$\text{MO signal} = A \exp(-\Delta t/\tau_D) \sin(2\pi f \Delta t - \delta) + P_4, \quad (7.1)$$

where P_4 is a 4th-order polynomial used to remove the background which is not related to the magnetization precession. The amplitude A and phase δ of the oscillatory signal are shown in Fig. 7.3(c) as a function of the applied bias. The phase change of 180° when changing the bias polarity is a strong indication that the excitation mechanism is closely related to the current pulse generated in the diode. In [33, 198, 199] it was observed that a photocurrent pulse generated in a Schottky diode can excite magnetization precession via the related Oersted magnetic field. The vertical current pulse generates an in-plane magnetic field circulating around the pump laser spot [see Fig. 7.3(a)]. In our PIN diode, the current polarity and, therefore, the polarity of the Oersted field is inverted for forward biases larger than $\approx 0.7\ \text{V}$. This leads to the opposite initial tilt of the magnetization and, consequently, to the opposite phase of the precession. The observed increase of the precessional amplitude with increasing reverse bias is also consistent with the suggested excitation mechanism. As shown in Fig. 7.2(b), the amplitude of the photo-generated current pulse (and the corresponding Oersted-field pulse) increases with increasing reverse bias, which makes the initial magnetization tilt larger.

In [33, 198] it was observed that the precessional amplitude was almost zero when the pump and probe laser spots were overlapped. In such case, the axis of the solenoidal Oersted field is probed and all contributions to the MO signal within the probe laser spot average out. We performed the pump-probe measurements with the overlapped laser spots in the setup with $25\ \mu\text{m}$ spot size under 10 V reverse bias. Thanks to the lithographically defined lateral structure of our device, we were able to observe also the effects of the current pulse propagation in the lateral direction. In Fig. 7.4(a) we show a sketch of the Corbino disc with three measurement spots indicated by the red circles (marked ‘b’, ‘c’, and ‘d’) and in Fig. 7.4(e) we plot the corresponding pump-probe traces measured in these places. When the laser spots are placed in the center of the disc, the precessional amplitude is almost zero. In contrast, when the laser spots are moved by $30\ \mu\text{m}$ away from the center, the precession appears with opposite phase for displacement along $[110]$ and $[\bar{1}\bar{1}0]$ directions. In Fig. 7.4(f) we show the precessional phase and amplitude extracted from the pump-probe curves by fitting with formula (7.1) for several positions along the $[110]$ axis. The amplitude increases with increasing distance from the disc center and the phase changes by 180° within $\pm 15\ \mu\text{m}$ around the disc center and remains constant in larger distances. The range in which the phase changes corresponds to the laser spot size.

These observations can be explained when taking into account the lateral current

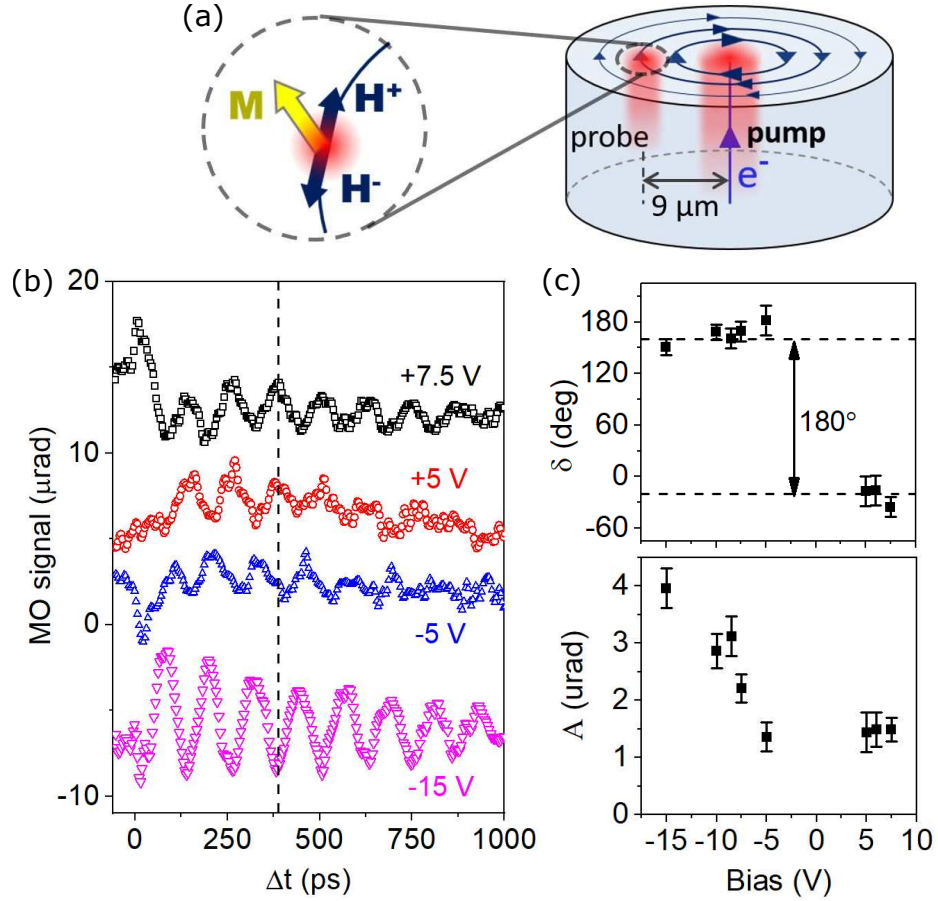


Figure 7.3: Magnetization dynamics induced by the vertical current pulse. (a) Sketch of the horizontally circulating Oersted magnetic field induced by the vertical current pulse which is generated by an absorption of the pump laser pulse in the biased diode. The direction of the photo-electron (e^-) motion is indicated for the case of reverse bias. Switching the bias polarity inverts the direction of the photocurrent and the corresponding Oersted field acting on magnetization within the displaced probe laser spot. (b) Magnetization precession induced by the Oersted field within the probe spot measured via the polar Kerr effect. The curves obtained for different biases are vertically shifted for clarity. (c) Bias dependence of the precessional phase δ and amplitude A extracted from (b) by fitting to formula (7.1). In these measurements we used the laser spot size of $1.5 \mu\text{m}$.

pulse flowing in the Fe/n-GaAs electrode and the circular symmetry of our device. The lateral current distribution for the three investigated places in the disc is indicated by the arrows in Fig. 7.4(a). When the laser spots are placed in the center of the Corbino disc (position ‘b’), the lateral current density is the same in all directions towards the golden ring-contact. The lateral current flowing partially in the n-GaAs layer generates again horizontal Oersted magnetic field in the iron layer which circulates around the center of the laser spots [see Fig. 7.4(b)]. However, thanks to the laser spots position in the center of the circular symmetry, the Oersted field (and consequently also the precessional MO signal) generated within the probe spot averages out. On the other hand, when the laser spots are moved out of the disc center (positions ‘c’ and ‘d’), the lateral current density is largest in the direction of the displacement since the distance to the golden contact is shortest in this direction [see Figs. 7.4(c, d)]. In this case, the Oersted fields (and consequently the precessional MO signal) generated within the probe laser spot do not average out even when the two laser spots are overlapped. When the laser spots are displaced in the opposite direction, the lateral current (and

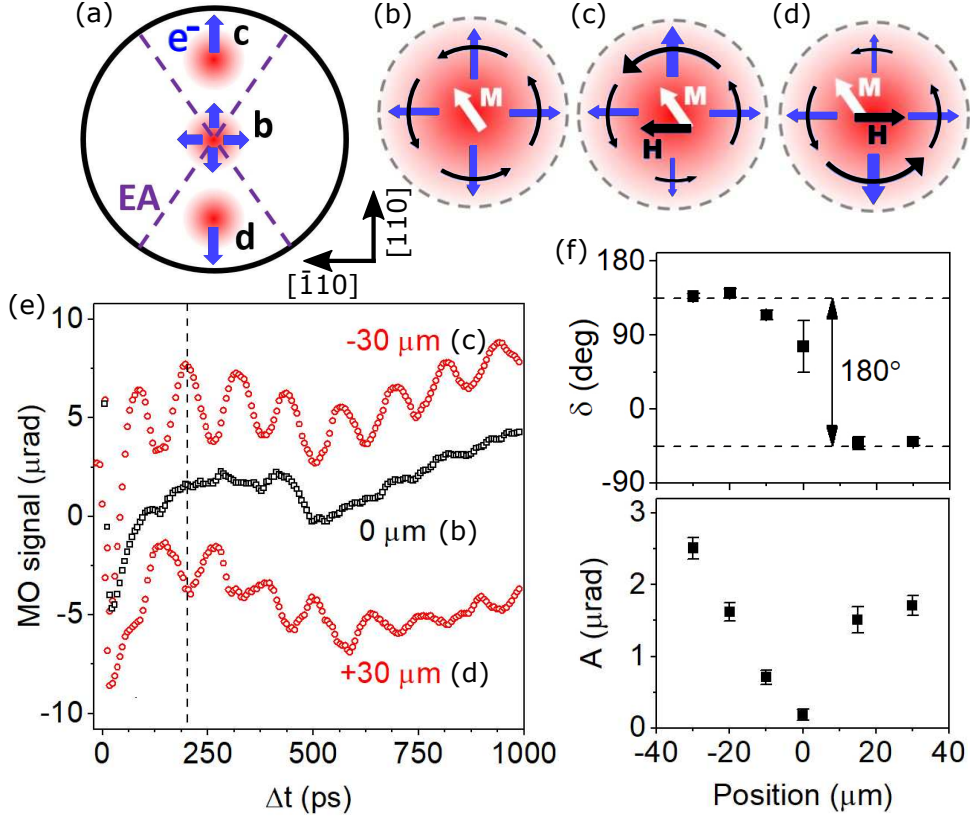


Figure 7.4: Magnetization dynamics induced by the lateral current pulse. (a) Sketch of the Corbino disc with three positions (marked ‘b’-‘d’) investigated by the overlapped pump and probe laser spots. The dominating directions of the lateral photo-electron flow (e^-) in the top electrode are indicated by arrows (-10 V bias applied). The iron magnetization points in one of the easy axes (EAs) indicated by the dashed lines. (b)–(d) Distribution of the lateral photo-electron flow (blue radial arrows) and the corresponding Oersted fields induced in the iron film (black circulating arrows) within the probe laser spot for positions ‘b’-‘d’ in (a). The direction of the average Oersted field \mathbf{H} is shown. (e) Magnetization precession induced by the Oersted fields in positions ‘b’-‘d’ measured via the PKE. The curves are vertically shifted for clarity. (f) The precessional phase δ and amplitude A as a function of the laser spots position in the Corbino disc extracted from (e) by fitting to formula (7.1). In these measurements we used the laser spot size of $25 \mu\text{m}$.

the corresponding Oersted field) switches sign and the magnetization is tilted in the opposite direction, which results in the opposite phase of the precessional MO signal. The increase of the precessional amplitude with increasing displacement of the laser spots from the disc center is caused by the increasing imbalance between the lateral currents flowing in the direction of the displacement and against it. This increasing imbalance means that the average Oersted field within the probe laser spot increases as well and the initial magnetization tilt is larger.

To further confirm our interpretation, we performed experiments in external magnetic field. First, with the overlapped laser spots displaced by $30 \mu\text{m}$ from the disc center along $[110]$ axis [position ‘b’ in Fig. 7.5(a)], we applied an external magnetic field along $[\bar{1}10]$ axis. As shown in Fig. 7.5(d), the magnetization precession amplitude quickly decreases as the magnetic field magnitude exceeds the anisotropy fields. For $\mu_0 H_{ext} \gtrsim 150$ mT, the magnetization points along the $[\bar{1}10]$ axis, i.e., along the Oersted magnetic field generated in position ‘b’ by the lateral current pulse, which then exerts no torque on magnetization [see Fig. 7.5(b)]. When shifting the laser spots along $[\bar{1}10]$ axis (to position ‘c’), we can restore the magnetization precession, as the Oersted field

and magnetization are no more parallel [see Fig. 7.5(c)]. In this position, we recorded the magnetization precession as a function of the external magnetic field applied along $[\bar{1}10]$ axis. The precessional phases extracted by fitting with formula (7.1) are shown in Fig. 7.5(e). We observe a phase change of $\approx 180^\circ$ when switching the magnetization orientation by external field, as the oppositely oriented magnetization is excited in opposite out-of-plane direction. We note that such phase change is not compatible with the magnetization precession induced by a laser heating-related modification of the magnetic anisotropy [199], which is an independent confirmation that the magnetization dynamics is triggered by the ultrashort photocurrent pulse and not directly by the original laser pulse. The precessional phase also changes by $\approx 180^\circ$ when changing the bias polarity, which is caused by the change of the current pulse direction, as in the case of the separated laser spots [cf. Fig. 7.3(c)].

Finally, we note that in the case illustrated in Fig. 7.3, when the pump laser spot was placed in the middle of the disc and the probe spot was displaced by $9\ \mu\text{m}$, both contributions to the Oersted field were present. However, the Oersted field generated by the lateral current points always against the Oersted field generated by the vertical current and, therefore, it only partially compensates its magnitude while not changing its symmetry.

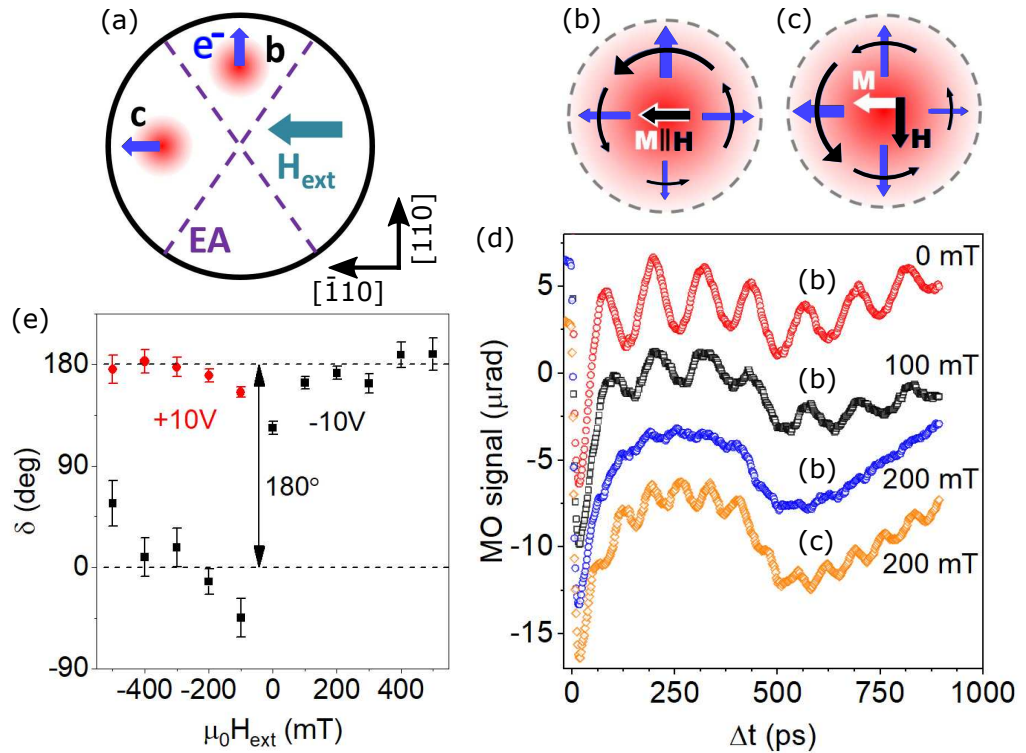


Figure 7.5: The effect of external magnetic field. (a) Sketch of the Corbino disc with two positions (marked ‘b’ and ‘c’) investigated by the pump-probe method with overlapped laser spots. The dominating directions of the pump-induced lateral photoelectron flow (e^-) are indicated by arrows. The magnetic EAs are indicated by dashed lines and the external magnetic field H_{ext} is applied along the $[\bar{1}10]$ crystal axis. (b)–(c) Distribution of the lateral photo-electron flow (blue radial arrows) and the corresponding Oersted fields induced in the iron film (black circulating arrows) within the probe laser spot for positions ‘b’ and ‘c’ in (a). The magnetization points along H_{ext} for $H_{ext} \gtrsim 150\ \text{mT}$. (d) The magnetization precession induced by the Oersted fields in positions ‘b’ and ‘c’ under external magnetic field and 10 V reverse bias. The curves are vertically shifted for clarity. (e) Dependence of the precessional phase δ on H_{ext} in position ‘c’ for opposite bias polarities. Laser spot size of $25\ \mu\text{m}$ was used in these measurements.

7.3 Photocurrent pulses in PIN/CuMnAs structure

In the previous sections we studied the current transients generated in a PIN/Fe photodiode, where we utilized the effect of the current-induced Oersted field on the iron magnetization to trace the current propagation in the 3D structure. The Oersted field-pulses might be used to manipulate non-collinear AFs, such as Mn_3Sn studied in chapter 8, but not for collinear AFs, such as CuMnAs studied in chapter 9, which are insensitive to moderate magnetic fields. The current pulse itself, however, can manipulate the staggered Néel order directly via spin torques [12,47]. The current-induced Néel vector switching was observed in CuMnAs [10, 78, 173, 194] and Mn_2Au [195] using current densities of $\sim 10^{10}\text{--}10^{12}$ A/m². Taking into account the laser spot size of $1.5\ \mu\text{m}$ and the lower bound of the peak current ~ 100 mA generated in our photodiode, we get in the laser-illuminated column a current density of $\sim 4 \times 10^{10}$ A/m². If this current was fed into a CuMnAs bar of 50 nm thickness and $1\ \mu\text{m}$ width, we would even reach a current density of $\sim 2 \times 10^{12}$ A/m², which is enough for the switching experiments in CuMnAs, even if the current pulse gets a bit longer due to dispersion.

To confirm the principal compatibility of our photodiode structure with CuMnAs, we characterized the photocurrent pulses generated in a PIN/CuMnAs Corbino device. In this case, the composition of the n-GaAs multilayer was different, from bottom to top: 10 nm thick layer ($n_{Si} = 5 \times 10^{17}$ cm⁻³), 15 nm thick layer (n_{Si} ramping from 5×10^{17} to 5×10^{18} cm⁻³), and 15 nm thick layer ($n_{Si} = 5 \times 10^{18}$ cm⁻³). The 50 nm thick CuMnAs epilayer grown on top of the n-GaAs electrode was protected by capping with Al. The diameter of the Corbino disc was $50\ \mu\text{m}$. In Fig. 7.6(a) we show the VI characteristics of the PIN/CuMnAs diode at different temperatures. With increasing temperature the diode opens at a lower reverse bias, which is due to the increasing conductivity of the intrinsic GaAs layer. We also see that in forward polarity the current sets on at $\sim 1\text{--}1.5$ V, which is a value typical for GaAs and much lower than what we measured in the PIN/Fe structure [c.f. Figs. 7.6(a) and 7.1(c)]. This indicates that there is a thinner or no Schottky barrier between CuMnAs and n-GaAs.

To characterize the photocurrent pulse length, we used again the correlation technique in the pump-probe setup with $1.5\ \mu\text{m}$ laser spot size. The correlation data measured at 32 K with a laser fluence of $0.9\ \text{mJ}/\text{cm}^2$ for different biases are shown in Fig. 7.6(b) (points) and fitted by a mono-exponential decay model (lines). We observe qualitatively the same behavior as in the PIN/Fe structure, i.e., decreasing photocurrent pulse duration with increasing reverse bias. The pulse decay times obtained by fitting the correlation curves measured at 32 K are shown in Fig. 7.6(c). The values measured with the laser fluence of $1.4\ \text{mJ}/\text{cm}^2$ are very similar to those obtained in the PIN/Fe device for a similar fluence of $1\ \text{mJ}/\text{cm}^2$ [c.f. Figs. 7.6(c) and 7.2(b)]. For the fluence of $1.4\ \text{mJ}/\text{cm}^2$ we also show the peak photocurrent I_{peak} , which was estimated based on the measured time-averaged photocurrent, the pulse repetition frequency, and the expected mono-exponential pulse decay. As expected, I_{peak} increases with increasing reverse bias and its values are comparable with those obtained for the PIN/Fe structure.

Besides the bias dependence of the photocurrent pulse length, we studied in this device also the effect of laser fluence. As is apparent from Fig. 7.6(c), the pulses become shorter (longer) for lower (higher) fluence. This can be explained in terms of screening of the internal electric field in the diode by the photo-injected carriers. Larger laser fluence produces more carriers but the amount of charge consumed to screen the electric field is the same (given by the applied bias). The rest of the photo-induced charge is drained away slowly by the weakened electric field. Therefore, it takes longer to deplete the overall larger number of carriers injected by stronger laser pulses. In Fig. 7.6(d) we plot the photocurrent pulse decay time and the estimated peak photocurrent as a function of the laser fluence for different applied biases. Interestingly, for a low

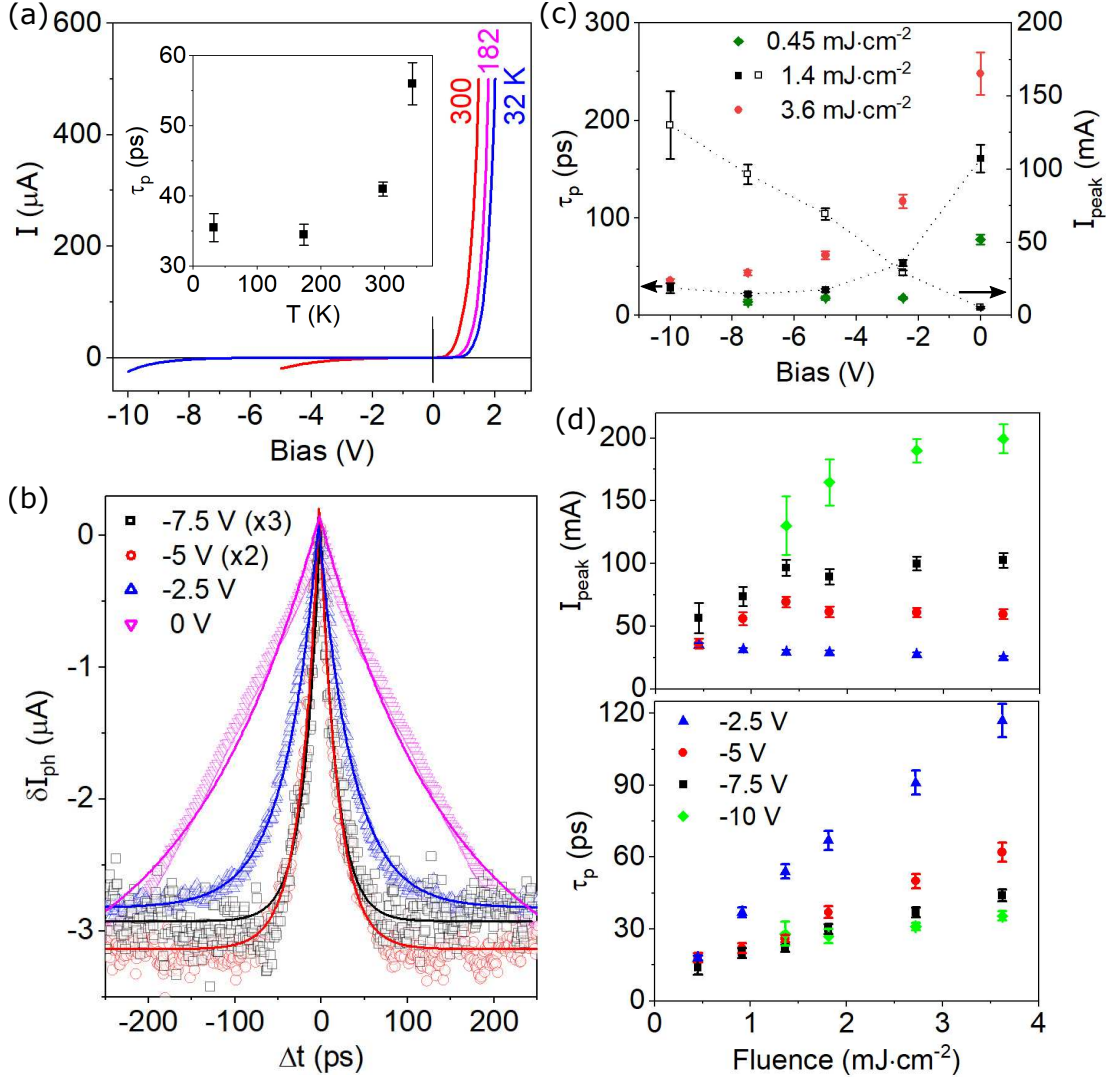


Figure 7.6: Characterization of PIN/CuMnAs photodiode. (a) VI characteristics measured in darkness at different temperatures. Inset: Photocurrent pulse duration as a function of temperature (fluence 3.6 mJ/cm^2 , bias -10 V). (b) Photocurrent correlation curves measured at 32 K for different biases (fluence 0.9 mJ/cm^2). (c) Bias dependence of the photocurrent pulse decay time τ_p for different laser fluences. For the fluence of 1.4 mJ/cm^2 , the estimated peak photocurrent I_{peak} is also shown. For a given fluence, the pulses become shorter and stronger with increasing reverse bias due to the stronger internal electric field in the diode. (d) The photocurrent pulse decay time and the estimated peak photocurrent as a function of laser fluence for different biases. For a low bias of -2.5 V , the pulse length increases with the laser fluence due to the effect of charge screening while the pulse amplitude remains roughly the same. For larger biases, the pulse length tends to saturate while its amplitude increases. The laser spot size was $1.5 \mu\text{m}$ in all measurements.

fluence of 0.45 mJ/cm^2 we generate very short current pulses ($\sim 15 \text{ ps}$) even for a weak bias of -2.5 V and the pulse length does not decrease much with increasing bias. With increasing laser fluence, the pulse length scales linearly for -2.5 V but tends to saturate for larger biases. Consequently, while for -2.5 V the pulse peak current remains roughly the same, for larger biases the peak current increases with the laser fluence. Therefore, we conclude that despite the stronger screening effect, it is better to use larger laser fluences to produce strong current pulses.

Finally, we note that the photocurrent pulse length also increases with temperature,

as shown in the inset of Fig. 7.6(a) for the laser fluence of 3.6 mJ/cm^2 and -10 V bias applied. However, the increase in pulse duration is only from 35 ps at 32 K to 41 ps at room temperature.

7.4 Conclusion

In this chapter, we presented a vertical photo-conductive switch structure in form of a PIN diode patterned into a Corbino disc. A femtosecond laser pulse absorbed in the intrinsic layer of the diode creates electron-hole pairs which are separated by the internal electric field and accelerated towards the opposite electrodes, thus producing a short current pulse. We characterized the photocurrent pulses generated in our PIN diodes in terms of their duration and amplitude and studied the pulse propagation through the 3D diode structure. Our final goal is to use these current pulses to excite, in an ultrafast manner, a magnetic film deposited on top of the n-layer of the diode. In particular, we aim on antiferromagnetic materials, which exhibit a THz-scale spin dynamics and which have been shown to respond to a current pulse excitation. We first investigated the current pulses generated in a GaAs-PIN/Fe(2 nm) Corbino device of $100 \mu\text{m}$ diameter. The photocurrent pulse duration was inferred, using a correlation technique, from a mutual interaction of two consecutive current pulses during their temporal overlap. We observed a rapid decrease of the current pulse decay time with increasing reverse bias and its saturation at $\sim 25 \text{ ps}$ for biases larger than $\sim -5 \text{ V}$. The estimated pulse peak current reaches $\sim 100 \text{ mA}$ for -10 V . The measured decay time is mainly limited by the RC time-constant of the Corbino disc, which would be reduced in devices with a smaller diameter. Moreover, the photocurrent correlation method is primarily sensitive to the recharging time of the photoconductive switch and may not resolve the rapid charge dynamics that is expected to be present before the separated photo-charge starts to screen the internal electric field in the diode. Therefore, the measured pulse duration (amplitude) should be rather understood as an upper (lower) bound value. In fact, an indication of the ultrafast ($\sim 1 \text{ ps}$) onset of the photocurrent pulse was observed experimentally as the bias-dependent transient reflectivity.

After characterizing the photocurrent pulses, we studied their effect on the iron magnetization in a pump-probe experiment. The photo-carriers generated in GaAs by circularly polarized pump laser pulses were spin-polarized, as confirmed by the observed pump-helicity-dependent photo-electron precession in GaAs. The corresponding current pulses should have been also spin-polarized, however, we did not observe any effect of this spin polarization on the dynamics of the iron magnetization. Instead, we found that the iron magnetization precession was pump-helicity-independent and its phase was shifted by 180° when switching the photocurrent polarity or flipping the magnetization. This clearly indicates that the magnetization precession was induced by the Oersted field of the current pulses and it rules out the direct effect of the laser pulses on the magnetization via, e.g., a temperature-dependent magnetic anisotropy. Besides the Oersted field produced by the photocurrent flowing vertically in the illuminated column in the diode, we also observed the magnetization precession for the case of overlapped pump and probe laser spots. This was due to a lateral current flowing in the Fe/n-GaAs electrode after the initial vertical current flow.

The estimated peak current densities of the pulses generated in the PIN diode of $\gtrsim 4 \times 10^{10} \text{ A/m}^2$ for the vertical current injected into the magnetic film (or even of the order of 10^{12} A/m^2 if fed into a thin-film bar device) are comparable with the current densities used to switch the Néel vector in collinear AFs CuMnAs and Mn_2Au . Moreover, the implemented current pulse generation by femtosecond laser pulses is naturally compatible with time-resolved measurements. Therefore, a photocurrent-

pump/optical-probe measurement is an example of a possible future experiment that could elucidate the process of Néel vector switching in CuMnAs. To demonstrate the possible applicability of our PIN diode structure to the investigation of AF materials, we characterized also the current pulses generated in a GaAs-PIN/CuMnAs(50 nm) Corbino device of $50\ \mu\text{m}$ diameter. We observed qualitatively and also quantitatively similar results as in the PIN/Fe device regarding the pulse duration and its dependence on the applied bias. We also observed that the current pulses become longer with increasing laser power which is due to charge screening effects. Applying a sufficiently strong reverse bias can, however, significantly compress the current pulses and these high-power/high-bias conditions lead to the largest current densities.

For envisioned experiments, it is also necessary to have a suitable imaging technique to observe the possible domain changes induced by the current pulses in the AF film. Therefore, in the following two chapters, we focus on developing imaging methods sensitive to antiferromagnets. We begin with a description of the experiments performed in a non-collinear AF, Mn_3Sn , which still shares certain properties with FMs. In particular, it can be controlled by moderate magnetic fields and it also allows for a broad spectrum of readout mechanisms. Finally, we present the results obtained in the collinear compensated AF CuMnAs, whose imaging is much more challenging due to its insensitivity to external magnetic fields and the high material symmetry, which restricts significantly the possible detection mechanisms.

8. Imaging and writing of magnetic domains in a non-collinear antiferromagnet

The non-collinear AFs with a triangular spin arrangement, such as Mn_3Ir , Mn_3Ge , or Mn_3Sn , have gained a lot of attention recently due to their unique properties combining certain characteristics typical for FMs [151, 153] with the advantages of compensated AF state [6–8]. In this chapter, we study a prominent representative of this material class, the Weyl semimetal Mn_3Sn .

In this material, the Mn atoms are arranged in a planar kagome-type lattice with magnetic moments residing in the apices of equilateral triangles. Due to geometrical frustration of the antiferromagnetic interactions in the Mn triangle, the moments adopt a non-collinear arrangement making an angle of 120° with respect to each other within each kagome plane [see Figs. 8.1(a) and (b) and for details section 4.3]. The spins in the triangle are, however, not perfectly compensated. The unsatisfied anisotropy energy in the inverse triangular spin structure causes a slight tilt of the moments from the perfect 120° alignment, which results in a tiny net magnetization of the order of $\sim 0.002 \mu_B/\text{Mn}$ [161, 166]. This uncompensated moment allows for a control of the AF state by moderate magnetic fields $\sim 10 \text{ mT}$ [155]. On the other hand, the net moment is small enough so that it produces negligible stray fields. Moreover, due to the antiferromagnetic coupling, these materials still possess the high-frequency exchange-enhanced spin dynamics [45].

Another important consequence of the non-collinear spin texture is the lowered material symmetry. The ‘traditional’ compensated collinear AFs, such as CuMnAs , typically possess the combined PT symmetry – they are invariant under time reversal combined with another spatial transformation, such as translation or inversion. This symmetry prohibits, in linear response, the effects that are odd under time (spin) reversal [153], i.e., the anomalous Hall effect and its counterparts – the anomalous Nernst effect and MO Kerr and Faraday effects. This significantly reduces the portfolio of available detection methods sensitive to the AF order. The aforementioned effects are generally present in FMs, which all break the PT symmetry. As have been revealed recently, however, the net magnetization is not necessary for these effects to be present; it is enough to break the PT symmetry of the system [151]. This can happen even in an AF material – an example is the class of triangular non-collinear AFs, including Mn_3Sn [152]. These predictions have been confirmed recently by experimental observations of the large AHE [154], ANE [138], and MOKE [155] with magnitudes comparable to FMs despite the vanishingly small magnetization in Mn_3Sn .

The same symmetry considerations that were given above for charge currents (including AHE) can be applied also to spin currents [153]. Many of the key spintronic effects and applications are based on spin polarized currents in FMs – for example, the giant and the tunneling magnetoresistance (GMR, TMR) and the spin transfer torque (STT). In the ‘traditional’ PT-symmetric collinear AFs, the electrical current is not globally spin-polarized due to the same symmetry arguments that exclude AHE. As shown in [153] however, the broken PT-symmetry in the non-collinear AFs allows for spin currents that are odd under time reversal (in analogy to AHE) and, consequently, electrical current in these materials can be spin-polarized.

The broad variety of available spintronic phenomena that can be used for electrical or optical readout (AHE, ANE, MOKE), including the potentially large GMR or

TMR signals in AF spin valves, combined with the multiple ways of control (moderate magnetic fields, STT) and with the vanishingly small stray fields and ultrafast AF spin dynamics make non-collinear AFs, such as Mn_3Sn , an attractive material class for future spintronic research. Imaging and writing of the AF domains is of central importance not only for potential applications but also for investigation of the underlying spintronic phenomena. Preparation of a well-defined domain pattern and imaging of its response to current excitation is required to confirm experimentally the effect of STT on the non-collinear AF domain walls [153]. Imaging of magnetic domains in Mn_3Sn has been realized by MOKE recently [155]. This method has, however, certain limitations which we discuss in more detail at the end of this chapter. In particular, in [155] the domain imaging was realized using the polar Kerr effect upon reflection from the $(2\bar{1}\bar{1}0)$ plane of a bulk single crystal. This is, however, not possible in $[0001]$ -grown thin films, which are of interest for spintronic applications. We developed an imaging technique which utilizes locally generated laser-induced heat currents flowing perpendicular to the film plane to probe the in-plane triangular spin structure via anomalous Nernst effect. In addition to imaging, we demonstrated the ability to write a well-defined domain pattern into the antiferromagnet at room temperature by employing the heat-assisted magnetic recording technique.

The experimental results presented in this chapter were published in [167].

8.1 Scanning thermal gradient microscopy

Experimental devices and measurement setup. The 50 nm thick Mn_3Sn epitaxial film was processed by optical lithography into $5\ \mu\text{m}$ wide Hall bars that were typically oriented along the $[2\bar{1}\bar{1}0]$ crystallographic direction of Mn_3Sn . An example of the experimental device and the measurement geometry are shown in Fig. 8.1(d). We employed the optical setup described in chapter 5 with slight modifications – the wide-field microscope with a green ($\lambda = 525\ \text{nm}$) LED source was used to image the sample (without the MO sensitivity) and to align the device with the focused scanning laser beam that was used for the actual magnetic imaging. For this purpose, we used a CW laser (which was used in chapter 5 as a source for the wide-field MO imaging) which was fed into the ‘pump’ arm of the setup instead of the fs-beam. The laser was tuned to a wavelength of 800 nm with a power of 10 mW and focused to a spotsize of $1.5\ \mu\text{m}$ (FWHM). The sample was placed in an optical cryostat, which allowed us to study the whole temperature range in which Mn_3Sn is antiferromagnetic ($T_N = 420\ \text{K}$), and a magnetic field of up to 0.5 T could be applied along the x -axis (perpendicular to the Hall bar). During the imaging experiment, we scanned the laser spot across the device (by moving the objective lens with the 3D piezo-positioner) in an x - y grid with a stepsize of $0.5\ \mu\text{m}$. For each position of the laser spot on the sample surface, we measured the global thermo-voltage ensuing on the longitudinal voltage contacts of the Hall bar (along the y -axis) due to the perpendicular-to-plane oriented laser-induced thermal gradient, see Fig. 8.1(c). During the measurement, the laser beam was modulated by an optical chopper at a frequency of 1.7 kHz and the laser heating-related thermo-voltage was extracted from the detected and amplified signal by a lock-in amplifier. As shown in Fig. 8.1(e), the spatially resolved thermoelectric response reveals a clear contrast. In the following, we confirm that these spatial maps correspond to the antiferromagnetic domain structure of Mn_3Sn .

Anomalous Hall and Nernst effects in Mn_3Sn . The anomalous Hall effect arises from the antisymmetric dissipationless part of the conductivity (resistivity) tensor $\hat{\sigma}$ ($\hat{\rho}$) (see section 3.2.1). The antisymmetric Hall conductivity tensor $\hat{\sigma}_H$ can be replaced

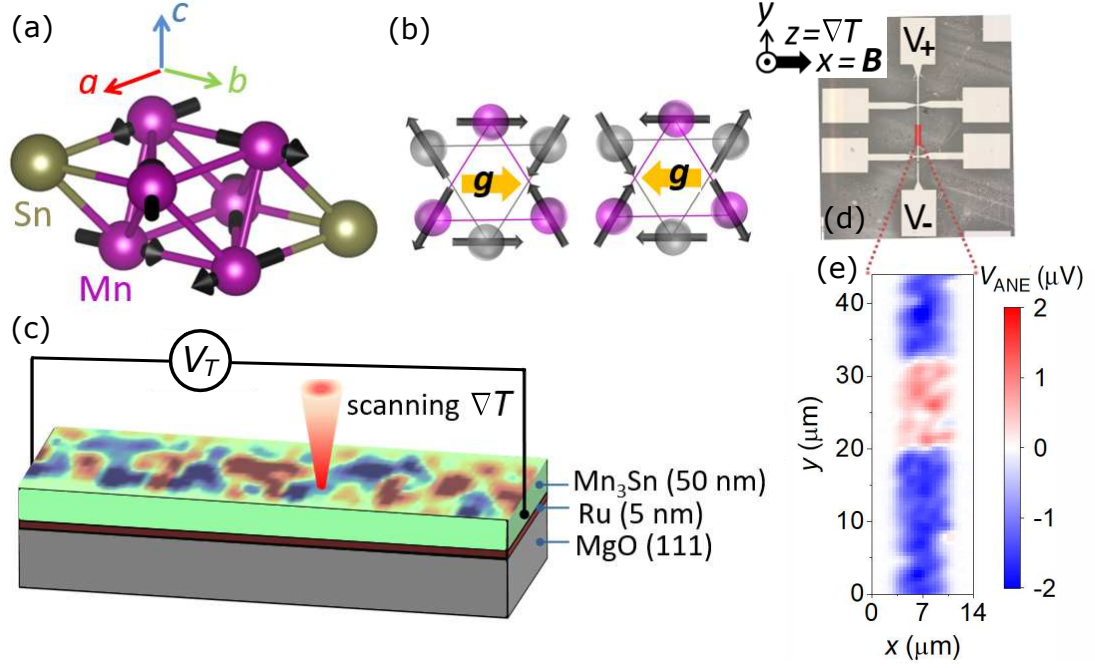


Figure 8.1: Spin order of Mn_3Sn and the imaging technique. (a) Hexagonal crystal structure of Mn_3Sn with Mn atoms forming kagome lattice consisting of equilateral triangles in planes perpendicular to the c -axis. (b) Mn triangles from two adjacent kagome planes (purple and grey) viewed along the c -axis. The antiferromagnetic chiral spin structure is characterized by a pseudovector \mathbf{g} . Two antiparallel configurations are shown that generate opposite ANE response. (c) Schematics of the scanning thermal gradient microscopy. The laser-induced local thermal gradient produces a global thermovoltage V_T that reflects the local magnetic properties in the irradiated spot. By scanning the laser spot over the sample surface an image of the domain structure is obtained. (d) Micrograph of the experimental Hall bar device. Magnetic field \mathbf{B} is applied perpendicular to the bar and longitudinal thermo-voltage $V_T \sim \nabla T \times \mathbf{g}$ is recorded. (e) An example of the spatially resolved thermo-voltage response measured in the highlighted area in (b) at room temperature and in zero magnetic field. The contrast corresponds to the domain structure of Mn_3Sn .

by a corresponding Hall pseudovector \mathbf{g} [206, 207] and the AHE-related part of the Ohm's law, $\mathbf{j}_H = \hat{\sigma}_H \mathbf{E}$, can be rewritten as $\mathbf{j}_H = \mathbf{g} \times \mathbf{E}$. Here \mathbf{j}_H is the Hall current, \mathbf{E} is the applied electric field, $\mathbf{g} \equiv (\sigma_{zy}, \sigma_{xz}, \sigma_{yx})$, and σ_{ij} are the antisymmetric Hall conductivity components. The anomalous magnetotransport plane (the plane in which the electric fields or currents are applied and recorded) is then perpendicular to \mathbf{g} . According to the Mott's relation (3.25), the anomalous Nernst effect has the same symmetry as AHE with the electric field \mathbf{E} replaced by a thermal gradient ∇T , i.e., for the Nernst voltage we obtain

$$V_{ANE} \sim \nabla T \times \mathbf{g}. \quad (8.1)$$

The axial vector \mathbf{g} is odd under time reversal and has also the same spatial symmetry properties as the magnetic dipole moment [207], which gives rise to the net magnetization in FMs. The orientation of the \mathbf{g} -vector is determined by the non-collinear spin structure as shown in Fig. 8.1(b) for two opposite domains. The symmetry properties of the \mathbf{g} -vector also result in a tendency of the material to develop a net magnetic moment along the \mathbf{g} -vector. However, as has been proven by both theory [151, 153] and experiment [138, 150, 154], this tiny uncompensated moment is not the origin of the large anomalous magnetotransport signals observed in Mn_3Sn .

As demonstrated in [138] for a bulk Mn_3Sn crystal, the anomalous Nernst effect is strongly anisotropic in this material. No ANE response was observed when applying the thermal gradient within the kagome plane, while for $\nabla T \parallel [0001]$ a large ANE voltage was measured perpendicular to the applied magnetic field with almost no anisotropy when rotating the moments within the kagome plane. In our experiment, the focused laser heats up the sample surface producing both an in-plane and a perpendicular-to-plane temperature gradient. The former is radially symmetric and averages out (within a domain). Therefore, only the out-of-plane (z -direction) thermal gradient gives a net contribution to the measured signal. From the anomalous Nernst symmetry [see Eq. (8.1)], the largest V_{ANE} is measured along the direction that is perpendicular to the \mathbf{g} -vector of the magnetic texture. Since our bar is oriented along y -axis, we apply the magnetic field along the x -axis [see Fig. 8.1(d)] and the measured thermo-voltage signal is determined by the projection of the \mathbf{g} -vector onto the x -axis. The particular value of V_{ANE} measured for a position (x, y) of the laser spot on the sample thus reflects the corresponding local orientation of the \mathbf{g} -vector in the irradiated area, i.e., the contrast observed in the laser scans corresponds to the AF domain structure of Mn_3Sn .

Spatial resolution. The resolution of our imaging technique is given by the lateral extent of the out-of-plane laser-induced heat gradient. The laser beam has a Gaussian intensity profile with a FWHM of $1.5 \mu\text{m}$ at the sample surface. Consequently, the measured thermo-voltage maps correspond to a convolution of the actual domain distribution with the Gaussian profile of ∇T . In situations when the sample breaks into multiple domains with sizes smaller than the laser spot size, the contributions to V_{ANE} from the differently oriented domains within the laser-generated hotspot partly cancel out resulting in weaker signals. As shown later, this is observed for example during a field-induced magnetic reversal of the film (Fig. 8.3) or when cooling the sample in zero field from above T_N when a random multidomain state establishes [Fig. 8.2(a), (b)]. A significant improvement of the imaging resolution could be achieved by replacing the far-field laser heating, whose confinement is intrinsically limited by the light wavelength, by some kind of near-field approach, such as the scanning near-field optical microscopy [208, 209]. This technique utilizes a metal-coated tip of an atomic force microscope placed in a close proximity to the sample surface to focus the incident laser power into a spot size given by the tip apex diameter, i.e., it would allow to reach a resolution of $\sim 10 \text{ nm}$ [210]. For a given bar width, the highly confined thermal gradient in the near-field approach would generate smaller thermo-voltage, however, considering the large response ($\sim 1 \mu\text{V}$) observed in our experiments, the signal should be still detectable.

8.2 Imaging of the AF domain structure of Mn_3Sn

In this section we confirm by studying the magnetic-field and temperature dependence of the thermo-voltage images that we indeed probe the AF order of Mn_3Sn . The first hint that the images are related to the magnetic order is that the measured V_{ANE} patterns respond to magnetic field. We note that thin Mn_3Sn films have been observed to show a substantially larger coercivity compared to bulk crystals [211, 212]. The highest magnetic field available in our experimental setup is 0.5 T , which is not enough to reverse the spin structure in our Mn_3Sn films at temperatures below $\sim 350 \text{ K}$, as documented in Figs. 8.2(a), (b) by the comparison of V_{ANE} maps with $\pm 0.5 \text{ T}$ applied. At a temperature of 375 K , we notice slight variations in the measured pattern depending on the field polarity, which correspond to switching of the domains with the lowest coercivity [see Figs. 8.2(c), (d)]. Upon heating the sample up by another 25 K , we observe

a complete reversal of the signal polarity with the field polarity in the entire sample, as shown in Figs. 8.2(e), (f). We also notice an increase in the signal magnitude compared to the fragmented domain state at lower temperatures despite we are approaching the Néel temperature. Therefore, at the temperature of 400 K the material becomes soft enough so that the magnetic field of 0.5 T is sufficient to reorient the \mathbf{g} -vector in most of the AF domains. While the magnetic response of the thermo-voltage pattern changes drastically between 350 K and 400 K, the net magnetic moment detected by SQUID magnetometry remains unchanged, which allows us to exclude ferromagnet-like phases appearing at higher temperatures. We note that the actual sample temperature within the 10 mW laser spot may be a bit higher than the base temperature of the cryostat cold finger, however, it remains still safely below $T_N = 420$ K, since the signal remains almost unchanged and strong when the measurement is repeated in zero field.

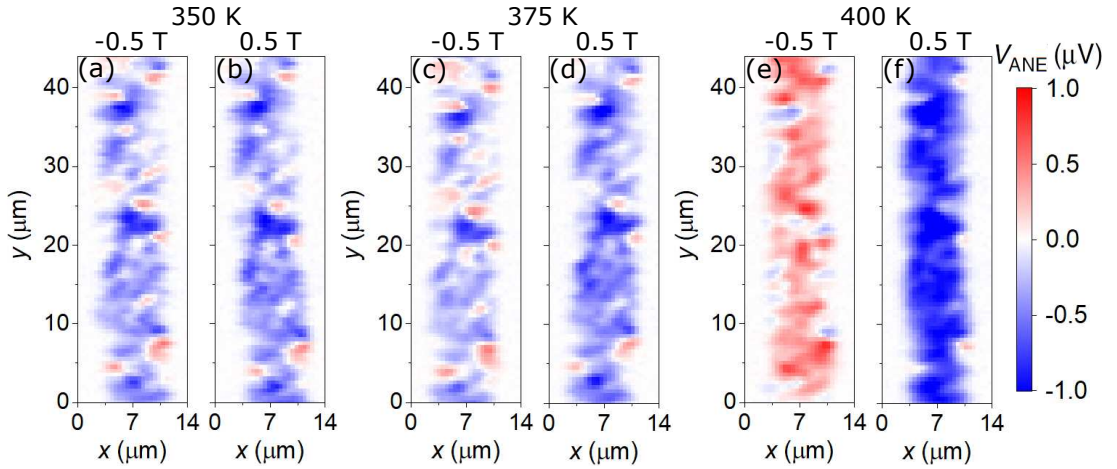


Figure 8.2: Effect of temperature on magnetic switching. Comparison of the thermovoltage maps recorded with an external magnetic field of 0.5 T applied along $-x$ and $+x$ direction at different temperatures: (a) and (b) Up to 350 K no effect of the field on the domain pattern is observed. (c) and (d) At 375 K slight differences appear corresponding to switching of the domains with the lowest coercivity. (e) and (f) At 400 K most of the domains follow the external magnetic field. On the other hand, no change in the net magnetic moment is observed between 350 K and 400 K by SQUID magnetometry.

In order to further explore the effect of magnetic field on the Mn_3Sn domain structure, we performed a complete magnetic field sweep along the x -axis. The field was changed in steps and in each step a thermo-voltage map was recorded in a constant field. The obtained images presented in Fig. 8.3(a) show rather complex reversal process proceeding gradually through a multidomain fragmented state. In Fig. 8.3(b), we plot the thermo-voltage $\langle V_{ANE} \rangle$ averaged over the entire bar segment displayed in Fig. 8.3(a) as a function of the external magnetic field. We obtain a global magnetic hysteresis loop with a clear saturation, coercivity and remanence. The thermo-voltage changes sign upon magnetic field reversal, i.e., the responsible magneto-thermoelectric effect is odd under spin reversal, as is the case of ANE. The measured magneto-thermoelectric response clearly cannot be explained by the ordinary Nernst effect, that is linear in magnetic field and does not exhibit hysteresis. Instead, the detected thermo-voltage maps must be connected to the AF order of Mn_3Sn . In our thin films, we observe larger coercive fields compared to the bulk Mn_3Sn crystals [138, 155]. This can be due to a larger anisotropy, but it could be caused also by stronger pinning at local imperfections, such as grain boundaries, dislocations, local strain variations, etc.

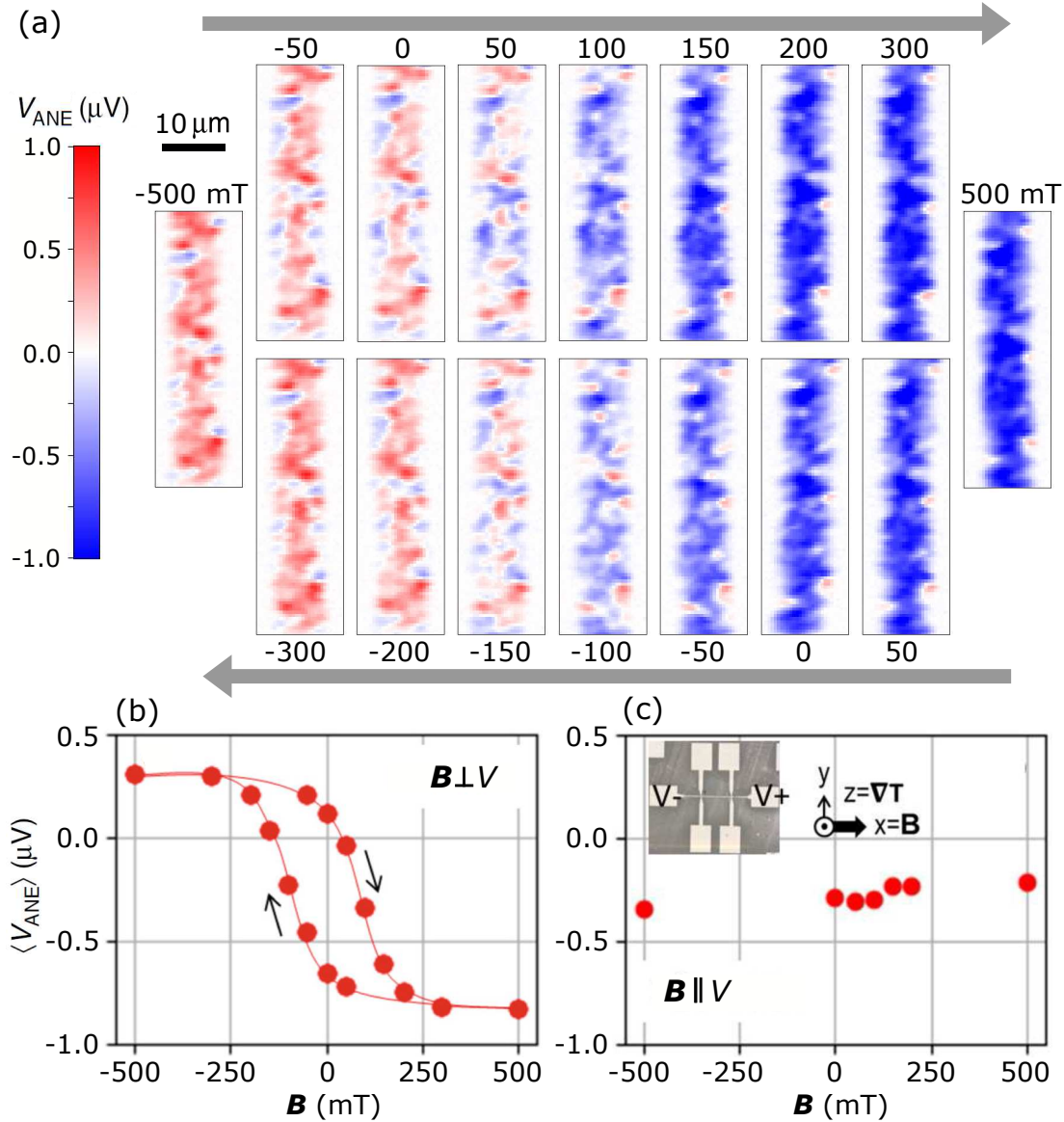


Figure 8.3: Magnetic field-induced reversal of Mn_3Sn domain structure. (a) A series of thermo-voltage scans measured during a magnetic field sweep along the x -axis at 400 K with 10 mW laser power. A complex magnetic reversal proceeding through multidomain states is observed. (b) Net thermo-voltage signal $\langle V_{ANE} \rangle$, obtained by averaging over the entire imaged area, plotted as a function of the applied magnetic field. A clear hysteresis with saturation and remanence is obtained. The red line is a guide for the eye. (c) Analogous measurement performed with the magnetic field swept along the voltage detection direction (the experimental geometry is shown in the inset). No hysteresis is observed as expected for the ANE symmetry.

An additional argument that supports the ANE origin of the measured signal comes from the measurement performed at 400 K but with magnetic field applied along the bar, i.e., along the voltage detection direction. As shown in Fig. 8.3(c), in this geometry we observe no hysteresis, as one would expect from the ANE symmetry (8.1). This supports the notion that the detected thermo-voltage corresponds to the component of the \mathbf{g} -vector that is perpendicular to the voltage detection direction. The uniform constant background, which is observed in both geometries [Figs. 8.3(b) and (c)], is related to the magnetic order of Mn_3Sn as it disappears above T_N [see the inset in Fig. 8.4(f)]. It might originate from the ordinary magneto-Seebeck effect (the thermal

counterpart to ordinary magnetoresistance) or parts of the sample are not possible to be polarized even at 400 K.

An independent confirmation that the spatial contrast in the measured thermovoltage maps corresponds to the AF domain structure of Mn_3Sn is given by the evolution of the measured signal with temperature. We performed the magneto-thermoelectric imaging in a temperature range of 17–430 K with the results summarized in Fig. 8.4. First, the sample was cooled down to 17 K in zero magnetic field, then the temperature was increased in steps and in each step a V_{ANE} map was recorded. The whole experiment was performed in zero magnetic field, which explains the lower magnitude of V_{ANE} at 400 K compared to the polarized state [cf. Figs. 8.3(b) and 8.4(f)]. V_{ANE} scans at several temperatures are shown in Figs. 8.4(a)–(e). Apart from a slight image distortion, which is caused by a sample position drift because of an imperfect temperature equalization, we observe a similar domain patterns with changing intensity. We again extracted the average signal $\langle V_{ANE} \rangle$ at each temperature and plotted its temperature dependence in Fig. 8.4(f) (red points). We observe a smooth variation of the signal magnitude with temperature with maximum in the vicinity of 150 K, in perfect agreement with the temperature dependence of the anomalous Nernst response observed in bulk Mn_3Sn crystals [138], which is reproduced in Fig. 8.4(f) (blue line). Above $T_N = 420$ K, the thermo-voltage signal vanishes completely, as documented by the magnetic field sweep with \mathbf{B} perpendicular to the bar performed at 430 K, which is shown in the inset of Fig. 8.4(f). Note that we did not detect in our thin film samples any sign of presence of a spin glass phase with a large ferromagnetic moment along [0001] direction that was observed in as-grown bulk Mn_3Sn crystals below 50 K [154, 162]. Its absence might be caused by the different magnetic anisotropy of thin films [213].

Estimate of the ANE strength. Our measurements do not give directly a quantitative information about the ANE magnitude. The latter is described by the off-diagonal Seebeck tensor component S_N and the ANE-induced electric field reads $E_y = S_N \nabla T_z$ (see section 3.2.2). The reason is that, unlike in the case of conventional in-plane thermal gradients, which can be calibrated via local temperature measurements, no thermometry below the film can be performed. We can, however, utilize a different magnetic film with known S_N to calibrate the perpendicular-to-plane temperature gradient in our setup and, consequently, use this information to estimate the ANE magnitude in our Mn_3Sn films. We used a 50 nm thick epitaxial film of the ferromagnetic Weyl semimetal Co_2MnGa with $S_N \approx 2 \mu\text{V}/\text{K}$ [214] deposited on the same substrate and having also the same capping layer as our Mn_3Sn films. The Co_2MnGa film was patterned into a $45 \mu\text{m}$ wide Hall bar, which we scanned with the laser spot and recorded the V_{ANE} maps under exactly the same conditions as in the case of the Mn_3Sn films. The FM film can be fully polarized by the 0.5 T field yielding $V_{ANE} \approx \pm 0.09 \mu\text{V}$ for ∓ 0.5 T. Taking into account the $d \approx 1 \mu\text{m}$ extension of the laser-induced hotspot and the bar width w we get the thermally induced electric field of $E_y \approx (w/d)V_{ANE}/d \approx 4 \mu\text{V}/\mu\text{m}$. From this we obtain the temperature gradient of $\nabla T_z = E_y/S_N \approx 2 \text{K}/\mu\text{m}$ at 300 K base temperature and for a laser power of 10 mW, which is in good agreement with laser-induced thermal gradients reported elsewhere [137]. Applying this value to our Mn_3Sn data, we finally obtain an estimate of the ANE magnitude in our AF films, $S_N = E_y/\nabla T_z \approx 2 \mu\text{V}/\text{K}$ at room temperature.¹ This value is a bit higher than those reported in the case of bulk crystals, $0.6 \mu\text{V}/\text{K}$ [138], which could be due to the more localized detection or higher degree of domain polarization in our measurements. Our

¹The different widths of the Co_2MnGa and Mn_3Sn Hall bars were taken into account by considering a simple model of parallel resistances as described, for example, in the Supplementary Information of [137].

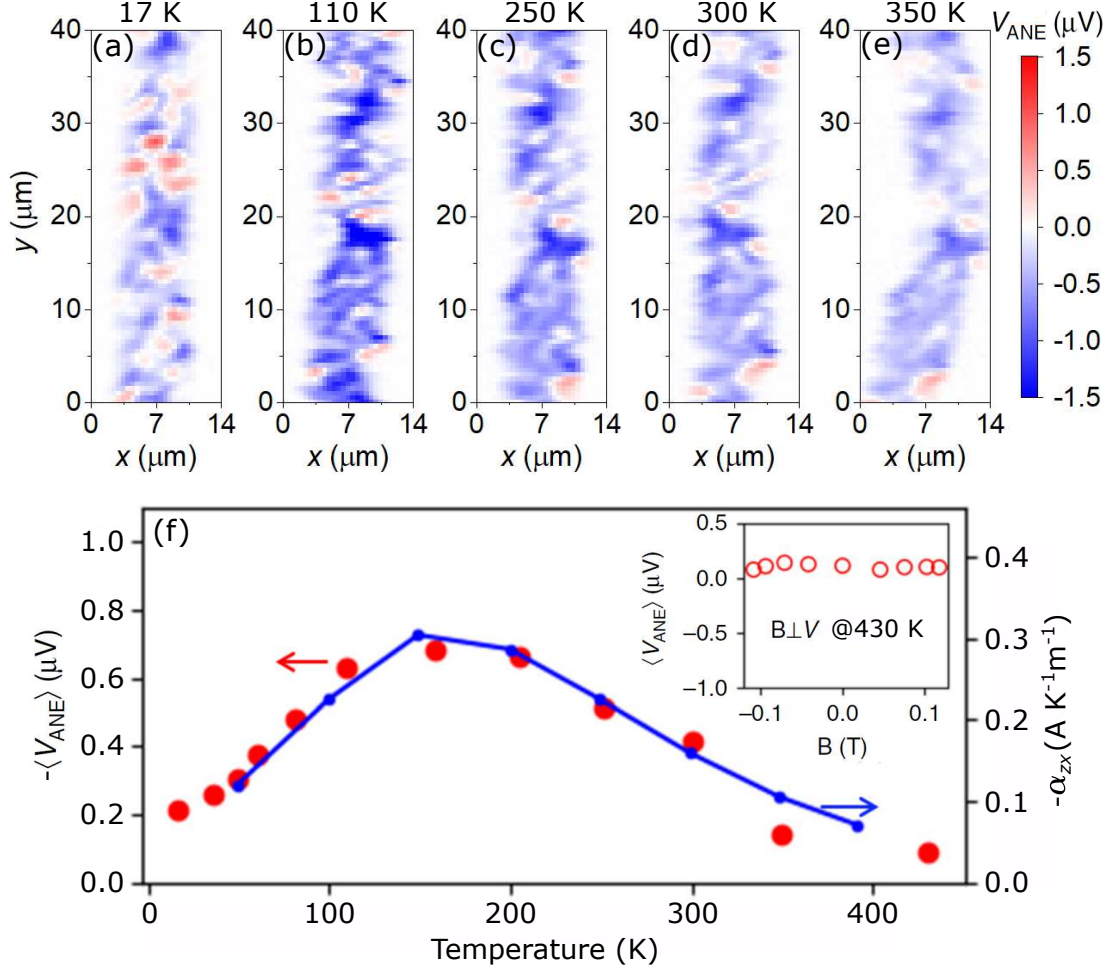


Figure 8.4: Temperature dependence of the ANE response. (a)–(e) Thermo-voltage scans measured with 10 mW laser power at different temperatures showing similar magnetic patterns with changing magnitude of the signal. Slight image distortion is caused by the sample drift due to thermal strains in the setup. (f) Average thermo-voltage signal $\langle V_{ANE} \rangle$ extracted from scans performed in a temperature range of 17–430 K (red points) compared to the temperature dependence of ANE measured in bulk Mn_3Sn crystal (blue line, reproduced from [138]). The excellent agreement confirms the ANE origin of our thermo-voltage signal. Inset: The average ANE signal measured with a magnetic field swept perpendicular to the voltage detection direction [same geometry as in Fig. 8.3(b)] at 430 K (above the Néel temperature of Mn_3Sn).

estimate also depends on the precision of determination of ∇T_z and E_y which both have uncertainties.

8.3 Heat-assisted writing of domains

The ability to intentionally write defined domain patterns in antiferromagnets is crucial not only for practical applications of these materials [13], but also for investigation of effects such as spin transfer torque [153], domain wall motion, or giant magnetoresistance [215]. In Fig. 8.5 we demonstrate that magnetic domains can be intentionally written in our Mn_3Sn thin films at room temperature using a heat-assisted magnetic recording procedure [216, 217] combining a high-power laser heating and external magnetic fields.

We performed a series of write/read experiments at 300 K where writing of a domain

in a selected region in the bar (marked by dashed boxes in Fig. 8.5) by a focused high-power (50 mW) laser beam with ± 0.5 T field applied was followed by mapping of the V_{ANE} response in the entire bar via the same laser beam with low power (10 mW). In the series of measurements, we first initiated the entire bar by scanning it with the 50 mW laser spot and $+0.5$ T magnetic field applied along the x -axis. The subsequent imaging scan with low-power laser spot is displayed in Fig. 8.5(a) showing a uniform magnetic state. In the next step, we exposed to the high-power laser only the area enclosed by the dashed line in Fig. 8.5(b) with -0.5 T applied, which resulted in a corresponding domain pattern with \mathbf{g} -vector reversed only in the exposed area. In Fig. 8.5(c), an area containing parts with both positive and negative V_{ANE} (opposite \mathbf{g} -vector orientations) was exposed again with $+0.5$ T applied resulting in a uniform negative V_{ANE} . From this we can conclude that the resulting state is not affected by the preceeding state (i.e., we do not observe a toggle switching) but it is exclusively defined by the external magnetic field direction applied during the laser exposure. Figures 8.5(d) and (e) show analogous situations like (c) and (b), respectively, with the opposite field polarity.

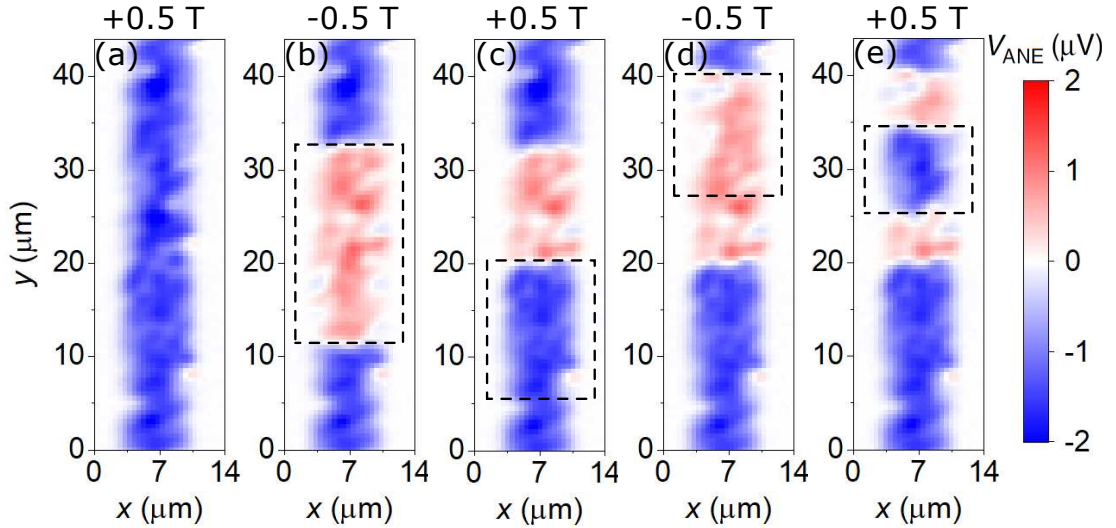


Figure 8.5: Heat-assisted writing of domains. Series of write/read laser scans at room temperature. Domain writing in the area enclosed by the dashed line with 50 mW laser power and $0.25 \mu\text{m}$ step is followed by imaging of the entire bar with 10 mW laser power and $0.5 \mu\text{m}$ step. Magnetic field of ± 0.5 T is applied during writing as indicated on top. (a) First, the whole bar is written with $+0.5$ T applied. (b) Subsequently a reversed domain is written in -0.5 T field. (c) Writing in a sample region that was previously written with the same field polarity causes no change (bottom part of the dashed box). A new domain is only written in region where the field was reversed from last writing (upper part of the box). (d) Analogous situation as in (c) with opposite magnetic configuration and field direction. (e) Analogous to (b) with opposite magnetic configuration and field direction.

We note that to write a homogeneous, fully polarized magnetic state at room temperature it was necessary not only to increase the laser power to 50 mW but we also had to decrease the scanning step-size during the exposure from $0.5 \mu\text{m}$ used for imaging to $0.25 \mu\text{m}$. With the smaller step, each position was exposed to the $1.5 \mu\text{m}$ laser spot for longer time, which allowed to increase the local temperature high enough (~ 400 K) to polarize the AF spin texture with a 0.5 T field. For practical reasons, we kept the magnetic field applied also during the imaging scans since large changes in field magnitude result in sample misalignment in our setup. However, from the previous experiments we know that the ± 0.5 T field has no effect on the domain pattern at temperatures up to ~ 350 K [see Figs. 8.2(a) and (b)] even when combined with the imaging laser power

of 10 mW. The domain structure is only altered in places exposed to the high-power laser heating. To test the stability of the domain pattern written in our scanning-thermal-gradient setup in extreme conditions, we exposed it to a field of 6 T along x -axis in a superconducting magnet. The thermo-voltage maps recorded before and after application of this strong magnetic field are compared in Fig. 8.6 showing no difference. This confirms that our Mn_3Sn films exhibit an interesting combination of an easy room temperature writability and a robustness against large magnetic fields.

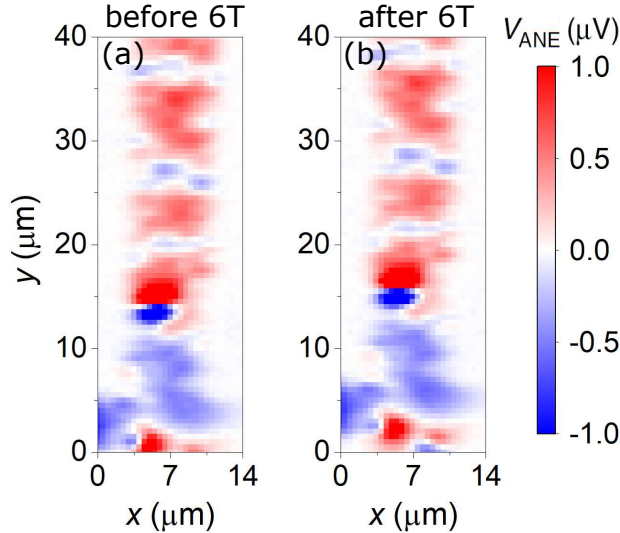


Figure 8.6: Insensitivity of written domains to large magnetic fields. The domain pattern written by the heat-assisted technique was exposed to an in-plane magnetic field of 6 T perpendicular to the bar direction at room temperature. The domain images acquired before (a) and after (b) the field application show no change in the domain structure.

8.4 Comparison to magneto-optical imaging

The three intimately related effects that have been recently observed to have large magnitudes in Mn_3Sn and that are sensitive to its magnetic order – AHE, ANE, and MOKE – differ in their suitability for spatially resolved studies of domain structure in epitaxial thin films. The latter are typically grown with the Mn kagome planes parallel to the film plane [160]. In this geometry, AHE cannot be utilized since one would have to apply the electric current perpendicular to the sample plane. On the other hand, as we demonstrated above, ANE is perfectly suited for this task, since the out-of-plane thermal gradient can be easily applied locally, e.g., via a focused laser beam. Polar MOKE was recently utilized to image the Mn_3Sn magnetic domains on $(2\bar{1}\bar{1}0)$ plane of a bulk crystal [155]. In [218], spatially unresolved measurements utilizing longitudinal MOKE were performed also in reflection from (0001) plane of a bulk Mn_3Sn crystal. Therefore, longitudinal MOKE could be, in principle, used for imaging of the domain structure also in the case of our epitaxial films.

Balk *et al.* in their study [218] performed simultaneously AHE and MOKE measurements on a bulk single crystal and observed substantial differences in coercive fields and phase transition temperatures inferred from the two sets of data. The reason is that MOKE is only surface sensitive, while AHE probes the full thickness of the crystal between the electrical contacts. The MOKE probing depth is limited by the penetration depth of light into the investigated material, which in case of metals is only ~ 20 nm. For example, the light intensity decreases by a factor of $1/e$ in the depth of 16 nm in

Mn, 10 nm in Sn, and 19 nm in Fe [219, 220], neglecting reflections at interfaces and interference effects. In the case of our scanning magneto-thermoelectric imaging, the signal is generated by a nonzero thermal gradient oriented perpendicular to the sample plane. The focused laser beam creates a hotspot at the sample surface and the heat flows into the sample towards the heat sink – the substrate of a thin film or the sample holder in the case of a bulk crystal. The thermal gradient can be still large in a depth of several 100 nm or even several microns, i.e., from the perspective of thin films our imaging method is bulk sensitive. The surface sensitivity of MOKE is particularly limiting in the case of thin films that are often part of a multilayer stack (either with a capping layer or as a functional bilayer with a heavy metal or ferromagnets). Our scanning thermal gradient microscopy also can, unlike MOKE, easily access buried layers below several nanometers of Pt or another heavy metal.

Another difference between magneto-optical and magneto-thermoelectric imaging is a spectral dependency of MO response which differs for different materials. Moreover, MOKE suffers from reflections on surfaces in multilayers and interference effects. The latter also affects the spectral dependence of MO signal and, therefore, it can substantially complicate comparison of results even from different samples of the same material, which differ in thickness or presence of additional layers in the stack. In contrast, the magneto-thermoelectric microscopy is obviously not sensitive to any interferences and allows for direct comparison of the magneto-thermoelectric coefficients of different materials. The necessity to control and precisely measure light polarization at different wavelengths also makes the MO imaging setup more complex. Moreover, in the case of antiferromagnets it is challenging to obtain the MO spectra at all, if there is no means of reliable control of the AF order which would allow to separate the MO signal from nonmagnetic contributions and artifacts.

8.5 Conclusion

In this chapter, we studied thin epitaxial films of Mn_3Sn , a prime representative of non-collinear antiferromagnets with triangular spin structure. These materials are of particular interest for spintronics since they combine the superior characteristics of AFs, such as negligible stray fields and THz-scale spin dynamics, with properties typical rather for FMs, which substantially broadens the spectrum of available control mechanisms (magnetic fields, STT) and detection methods (AHE, ANE, MOKE, etc.). We demonstrated that the AF domain structure of Mn_3Sn can be visualized using a scanning thermal gradient imaging method that combines a localized perpendicular-to-plane temperature gradient induced by a focused laser beam with a global measurement of the ensuing thermo-voltage signal. By studying the magnetic-field and temperature dependences of the recorded spatial maps and by examining the symmetries of the generated signal, we confirmed that the measured spatial contrast corresponds to the AF domain structure of Mn_3Sn that is visualized via anomalous Nernst effect. Furthermore, we demonstrated that domain patterns can be written in the antiferromagnet ‘at will’ using a local laser heating combined with moderate magnetic fields (± 0.5 T). We confirmed that at room temperature and below (and in the absence of laser heating) the written domain pattern remains insensitive to magnetic fields up to 6 T. Such a combination of easy room temperature writability, robustness against large magnetic fields, and absence of perturbing stray fields is particularly interesting for potential high-density non-volatile memory applications. Besides the application potential, the ability to prepare a defined domain configuration and detect its changes is a key prerequisite for studying the intriguing physics of non-collinear AFs with spatial resolution, such as spin transfer torque-induced domain wall motion or domain wall-related mag-

netoresistance.

9. Imaging and manipulation of domain structure in a compensated collinear antiferromagnet

In the previous chapter, we made use of the special symmetry properties of non-collinear triangular AFs, which allow for presence of a strong magnetotransport and magneto-optical response via time reversal-odd effects, such as AHE, ANE, and MOKE. The small net magnetic moment induced by the geometrical frustration in the triangular lattice also allowed for a simple manipulation of the AF order by an external magnetic field. On the other hand, in fully compensated collinear AFs, such as CuMnAs, the net magnetic moment is strictly zero (unless a strong magnetic field is applied), i.e., they cannot be manipulated by moderate magnetic fields. Due to the higher symmetry, electrical currents in collinear AFs are not globally spin-polarized [153], i.e., the spin transfer torque and GMR (TMR) effects, on which the current spintronic memory applications in FMs are based, are not present. Moreover, the PT symmetry excludes the aforementioned time reversal-odd detection mechanisms [153]. All these restrictions make the collinear AF order particularly difficult to detect and control.

CuMnAs is a prime representative of the class of compensated collinear AFs [170]. The breakthrough demonstration in this material [10] of the previously predicted [12] all-electrical control and readout of the AF state via relativistic NSOT and AMR effects represents an important step towards antiferromagnetic spintronic applications. However, as shown in the case of AF-insulator/heavy-metal bilayers [221–223], relying only on the spatially integrating resistive readout may lead to incorrect interpretations, since the electrical switching signal can be strongly affected by non-magnetic contributions. In order to elucidate the physical mechanisms of the magnetic switching and disentangle the possible non-magnetic signals a direct microscopic imaging of the domain states prior and after the electrical- or optical-pulse excitation is needed.

Microscopy techniques sensitive to the compensated collinear AF order are rare. A well experimentally established imaging technique is the photoelectron emission microscopy where the magnetic contrast is generated by X-ray magnetic linear dichroism (XMLD-PEEM) [113]. This method has been used to visualize the electrically induced switching of AF domains in CuMnAs, Mn₂Au, or NiO [10, 86, 173, 194, 195, 224]. In CuMnAs, the NSOT-induced switching of the Néel vector observed via XMLD-PEEM was directly linked to changes in the corresponding electrical readout signal due to AMR [173, 194]. A 90° reorientation of the Néel vector was evidenced by XMLD-PEEM imaging for orthogonal current pulses [10, 194] or, via domain wall motion, when reversing the current polarity [173]. The major drawback of this powerful imaging technique is that it requires a large-scale experimental infrastructure – a synchrotron. For a routine imaging of large sample sets more accessible laboratory techniques are needed. An example of such an approach is the NV-diamond magnetometry [225, 226]. Here a single spin of an NV-center in a diamond nanocrystal attached to a scanning tip is used to detect magnetic stray fields emanating from a magnetic sample. Therefore, this technique is indirect and the domain structure itself is inferred by theoretical modeling. Moreover, in the case of antiferromagnets, the signal is generated only by uncompensated magnetic moments, e.g., at interfaces.

In this chapter, we present a simple table-top microscopy technique that is sensitive

directly to the Néel vector of the compensated collinear antiferromagnet, probes the full thickness of the magnetic film, and can reach a spatial resolution comparable to those of XMLD-PEEM or NV-magnetometry. The method is based on a detection of an anisotropic magneto-Seebeck response generated by a local laser-induced thermal gradient in the vicinity of inhomogeneous magnetic textures, e.g., domain walls. We first confirmed that our imaging technique is indeed sensitive to the collinear AF order by imaging a thin CuMnAs film and comparing the results to images obtained by the established XMLD-PEEM technique. Subsequently, we used our magneto-thermoelectric imaging setup to visualize changes in the domain configuration due to a 90° NSOT-induced switching of the Néel vector in biaxial CuMnAs films. For higher current pulse amplitudes, we observed a distinct switching mechanism which leads to a shattering of the originally μm -sized domains into a metastable fragmented state decaying back into the original domain pattern on macroscopic time-scales. This finding helped to explain the previously observed decay of large resistive switching signals [227] in terms of relaxation of the nano-fragmented domain configuration towards the original domain pattern, in agreement with the independently performed imaging via NV-center magnetometry [226].

All XMLD-PEEM images presented in this chapter were not obtained by the author of this work and serve only for a comparison to the magneto-thermoelectric imaging technique. The following experimental results together with additional near-field measurements (not performed by the author of this thesis) are currently submitted for publication [228].

9.1 The magneto-thermoelectric imaging method and its verification

We first describe the basic working principle of our newly developed microscopy imaging technique and we verify its sensitivity to the compensated collinear AF order by comparing its results to XMLD-PEEM images obtained in a thin CuMnAs film. All experiments were performed at room temperature. The optical setup of our magneto-thermoelectric microscope is the same as that used to image Mn₃Sn domains in the previous chapter. Therefore, we focus here on explaining the differences between the two imaging techniques we used for Mn₃Sn and CuMnAs.

As mentioned above, the time reversal-odd ANE used in the case of Mn₃Sn is not present in CuMnAs. Here, we are left only with time reversal-even effects, such as AMR, MO Voigt effect (or XMLD), and anisotropic magneto-Seebeck effect (AMSE). The latter effect is a thermal counterpart to AMR and XMLD, which have already successfully been used as probes of the AF order in CuMnAs. The geometry of AMSE is fundamentally different from that of ANE. While ANE is sensitive to the magnetization (or \mathbf{g} -vector) component perpendicular to the plane containing the driving heat current and the generated electromotive force [see Eq. (8.1)], AMSE is sensitive to the Néel vector projection onto this plane. Therefore, in a CuMnAs thin film with its staggered magnetic moments oriented parallel to the film plane, the in-plane thermal gradients will contribute to the signal, in contrast to the case of ANE in Mn₃Sn, where the perpendicular-to-plane thermal gradient was relevant. The electromotive forces generated by AMSE in longitudinal (parallel to ∇T) and transverse (perpendicular to ∇T) directions follow harmonic dependencies (3.27) on the angle between the directions of the temperature gradient and the Néel vector (see section 3.2.2).

The temperature gradient is in our case produced locally by a CW laser beam focused onto the sample surface, as shown in Fig. 9.1(a). We use a near-infrared laser with a wavelength of 800 nm and power of 1–5 mW focused into a Gaussian spot with

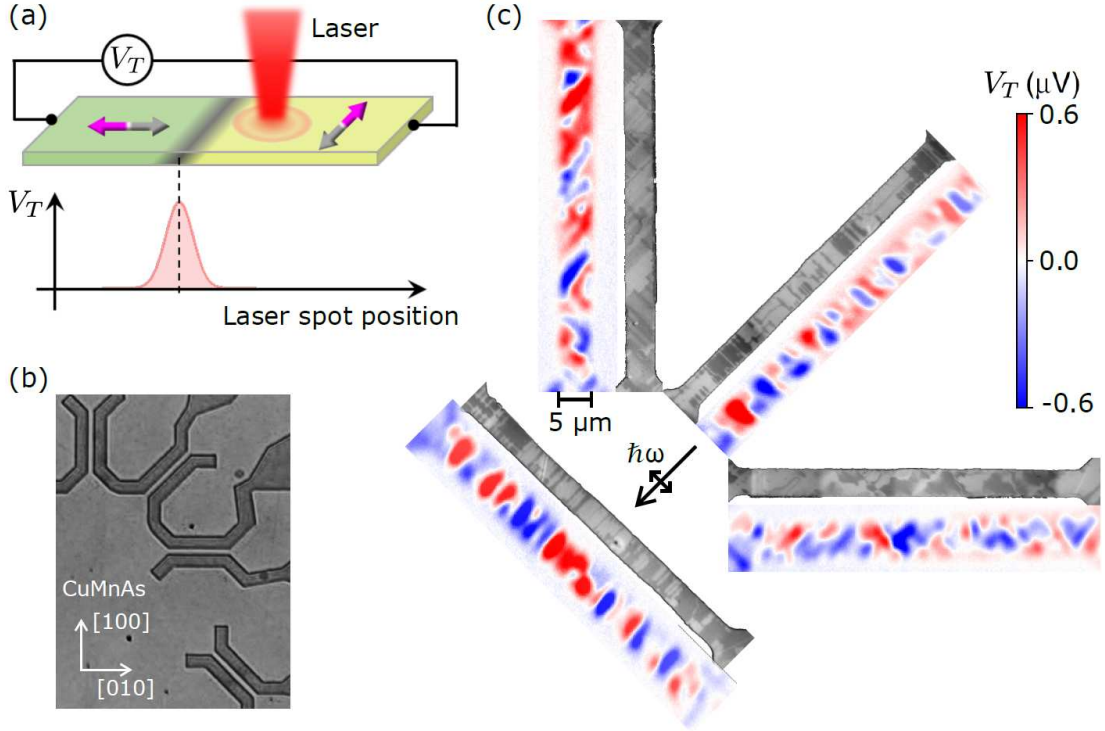


Figure 9.1: Basic working principle and verification of the imaging method.

(a) Schematic illustration of the magneto-thermoelectric imaging of a collinear antiferromagnet. The local laser-induced in-plane thermal gradient generates a global voltage signal via AMSE when an inhomogeneous AF texture is present (here a 90° DW) within the laser-induced hot-spot. The whole image is assembled from the individual local measurements as the laser beam is scanned over the sample. (b) Optical micrograph of four $5\ \mu\text{m}$ wide bars patterned from a $45\ \text{nm}$ thick CuMnAs epilayer along the $[100]$, $[110]$, $[010]$, and $[1\bar{1}0]$ crystal axes and (c) comparison of the AMSE and XMLD-PEEM images obtained in these bars. For the AMSE imaging a laser power of $1\ \text{mW}$ was used.

a FWHM of $1.5\ \mu\text{m}$. Due to the radial symmetry of the laser beam, the in-plane heat gradients are also radially symmetric and within a single magnetic domain the thermo-voltage generated due to ∇T will be always precisely compensated by an opposite voltage contribution due to $-\nabla T$ on the opposite side of the hotspot. Therefore, a net thermo-voltage can be generated only if there is an inhomogeneous magnetic texture present within the extension of the thermal gradient. This can be a domain wall, as depicted in Fig. 9.1(a). Here, a 90° DW separates two domains with different Seebeck coefficients, which is due to their different Néel vector direction with respect to any given ∇T direction. Since we can only detect the thermo-voltage along the CuMnAs bar direction, we can simplify the explanation by taking into account only the thermal gradient components $\pm\nabla T$ along the bar. (Other couples of $\pm\nabla T$ along all other axes will contribute in proportion to their projection on the bar direction.) If there is a DW present within the laser-induced hot-spot, ∇T is predominantly generated in one domain and $-\nabla T$ in the neighboring domain, with the maximum asymmetry for the laser spot center being just on top of the DW. Due to different Seebeck coefficients, the oppositely directed voltage contributions from the two domains do not have equal magnitude and a net thermo-voltage is measured on the device terminals. When the laser spot is scanned across the DW a characteristic unipolar feature with a shape following from the laser intensity profile is measured, as shown in the bottom part of Fig. 9.1(a). For an opposite domain configuration, voltage of opposite polarity would be measured. Spatially resolved images of the domain pattern are again assembled

from the individual thermo-voltage measurements for different positions of the laser spot, as it is scanned over the investigated device. The sensitivity of AMSE microscopy to domain walls represents another fundamental distinction from the ANE microscopy, which is sensitive to the homogeneous magnetic texture within domains.

In Fig. 9.1(b), we show an optical micrograph of four $50\ \mu\text{m}$ long and $5\ \mu\text{m}$ wide bar devices patterned from a $45\ \text{nm}$ thick CuMnAs epitaxial film grown on GaP substrate [173]. The bars are oriented along the main CuMnAs crystal axes – $[100]$, $[110]$, $[010]$, and $[1\bar{1}0]$. Maps of the AMSE-generated thermo-voltage V_T measured in these four bars by our laser-scanning technique are compared in Fig. 9.1(c) to XMLD-PEEM images of the same devices taken with X-ray polarization along $[1\bar{1}0]$ crystal axis. Here, the light (dark) areas correspond to AF domains with the Néel vector pointing parallel (perpendicular) to the X-ray polarization [173]. Two domain populations with orthogonal Néel vectors are observed in agreement with the biaxial in-plane magnetic anisotropy that usually dominates in thicker CuMnAs films. The 90° domain walls separating these orthogonal domains are visualized by the positive (red) or negative (blue) thermo-voltage signals. Both techniques show analogous structures composed of μm -sized domains in all four bars. The domain walls are preferentially oriented along one of the $\langle 110 \rangle$ directions, following the in-plane cubic symmetry of CuMnAs. Therefore, DWs are mostly alligned at 45° (90°) with respect to the voltage detection direction in $[100]$, $[010]$ ($[110]$, $[1\bar{1}0]$)-oriented bars.

The analogous overall structure of the AMSE and XMLD-PEEM images confirms that the thermo-voltage signal originates predominantly from the CuMnAs antiferromagnetic texture and the corresponding anisotropy in the Seebeck response. Quantitative differences between the spatial patterns obtained by the two microscopy techniques can be explained by their different spatial resolution and probing depth. The lateral resolution of the XMLD-PEEM in the metallic CuMnAs is $\sim 50\ \text{nm}$ while the resolution of the AMSE-microscopy is given by the lateral extension of the thermal gradient, which is in our setup generated by a far-field illumination with a $1.5\ \mu\text{m}$ wide Gaussian laser spot. The depth sensitivity of the XMLD-PEEM is limited only to a few-nm thin surface layer of the sample from which the photo-emitted electrons can be detected. On the other hand, the magneto-thermoelectric technique probes the full thickness of our $45\ \text{nm}$ thick CuMnAs film since a large lateral temperature gradient exists throughout the whole film thickness due to a substantial laser penetration depth and the following heat dissipation. Finally, we note that in the described experiment, the AMSE imaging was performed about 10 days after the XMLD-PEEM measurements. Since the domain structure in CuMnAs is not absolutely rigid at room temperature, this could also contribute to the observed differences in the obtained images.

9.2 Imaging of a reversible current-induced switching

In previous studies on biaxial CuMnAs films [173, 194] it has been shown that the current pulse-induced domain pattern variations observed by XMLD-PEEM are accompanied by corresponding resistance variations due to AMR and possibly also DW resistance [227]. In the previous section we correlated the images obtained by our scanning magneto-thermoelectric technique to XMLD-PEEM images. To further evidence that the detected thermoelectric signal is indeed of magnetic origin, we performed simultaneous AMSE imaging and resistance measurements in response to current-pulse excitations.

In these experiments we used devices in form of a symmetric Hall cross, which allow measuring of the thermo-voltage responses along two perpendicular directions. The devices were patterned from nominally the same $45\ \text{nm}$ thick CuMnAs/GaP epilayer as

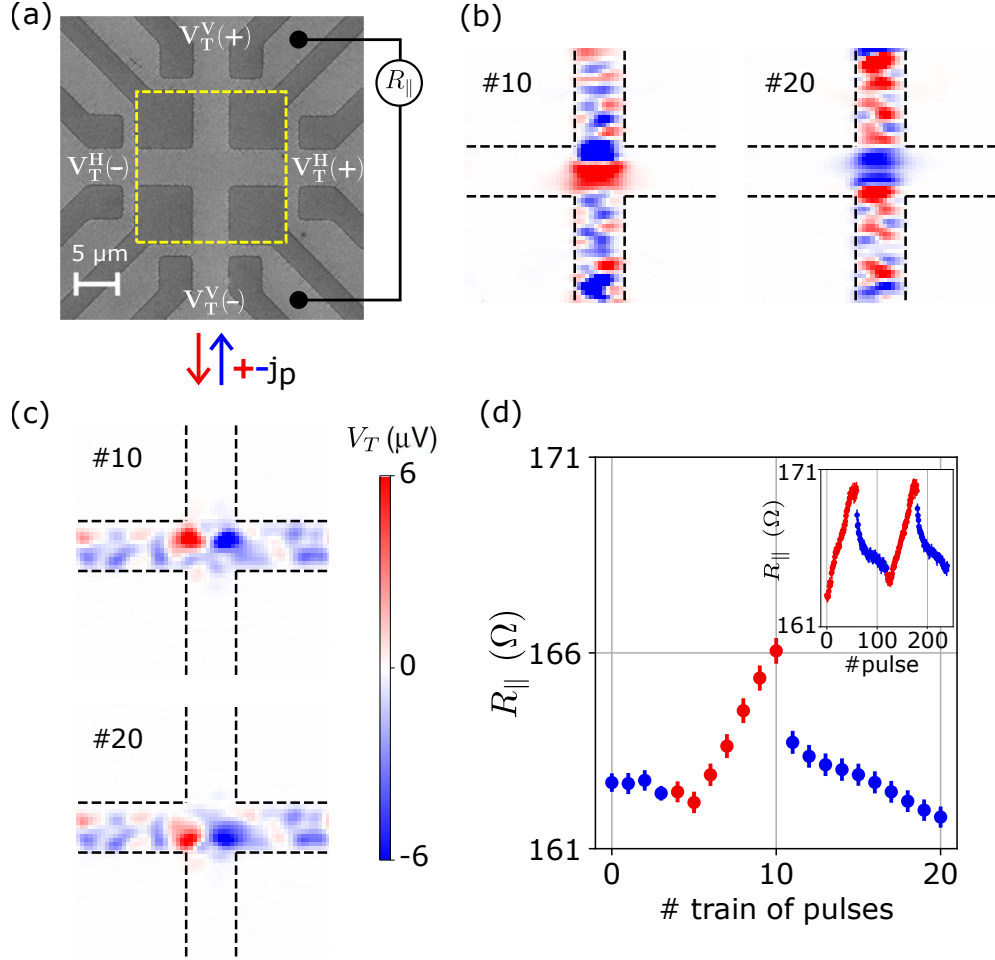


Figure 9.2: Correlation between domain pattern and resistance variations due to current-pulse excitation. (a) Electron microscopy image of a $5\ \mu\text{m}$ wide crossbar structure with the measurement geometry. Trains of 6 current pulses of density $|j_p| = 9.6 \times 10^{10}\ \text{A/m}^2$, 20 ms duration, and either positive or negative polarity are applied along the vertical channel. Subsequently a longitudinal resistance $R_{||}$ is measured in a 4-point geometry and thermoelectric signals along both channels are recorded within the area enclosed by the yellow dashed line. (b) AMSE maps measured via the vertical voltage contacts after 7 trains of positive pulses were applied (#10) followed by 10 trains of negative pulses (#20). (c) AMSE maps obtained by simultaneous detection of the thermovoltage ensuing along the horizontal bar. The laser power used for the AMSE imaging was 5 mW. (d) Corresponding variation of the longitudinal resistance. Red (blue) data points correspond to measurements after positive (negative) pulse trains were applied. Inset: Reversible and reproducible resistance variations. Current polarity is switched after application of 60 individual pulses.

the bars studied in section 9.1. We first show the results obtained in a $5\ \mu\text{m}$ wide cross device. The experimental geometry is depicted in Fig. 9.2(a). The thermovoltages along the vertical $V_T^V = V_T^V(+)-V_T^V(-)$ and horizontal $V_T^H = V_T^H(+)-V_T^H(-)$ channel are simultaneously recorded while the laser spot is scanned over the central crossbar area, which is enclosed by the yellow dashed line. Trains of 6 electrical current pulses of magnitude $|j_p| = 9.6 \times 10^{10}\ \text{A/m}^2$ and duration $\tau_p = 20\ \text{ms}$ were sent through the vertical channel with either positive or negative polarity (red and blue arrows). Figs. 9.2(b) and (c) show the thermovoltage maps recorded at the vertical and horizontal contacts, respectively, after a positive pulse train (#10) and negative pulse train (#20) was applied. The vertical (horizontal) thermoelectric signal is detected only when the

laser spot illuminates the the vertical (horizontal) bar. The measurements reveal a complex microscopic domain structure. Closer look at Figs. 9.2(b) and (c) shows that after the polarity of the current pulses was reversed (cf. #10 and #20), variations in the thermoelectric signal occur along the entire vertical channel (along which the current was applied) whereas the signal in the horizontal channel is modified only in the central cross area where the two channels overlap. This observation is consistent with the current pulse-induced switching of the microscopic domain structure since the thermoelectric signal variations are observed only in areas where the current density of the applied pulse is large enough to induce the switching.

The simultaneously performed electrical resistance measurements are displayed in Fig. 9.2(d). The resistance R_{\parallel} was measured in a 4-point geometry along the vertical channel immediately after a pulse train was applied. The red (blue) points correspond to resistance values measured after application of positive (negative) pulses. We observe that the modifications of the AMSE maps in Figs. 9.2(b) and (c), which are due to the current pulse-induced domain switching in the current carrying bar, are accompanied with variations in R_{\parallel} . The resistance changes reversibly and reproducibly when switching the current pulse polarity, as shown in the inset of Fig. 9.2(d). This is consistent with the NSOT switching mechanism that was identified in the previous studies via XMLD-PEEM [173, 194] using similar current pulse magnitudes. Note, however, that the observed resistance variation of up to 4% is larger than what is expected from AMR due to the 90° Néel vector reorientation in the domains [173, 229]. The resistance signal therefore contains a significant contribution of distinct origin, which will be discussed later.

To further evidence the reversible and reproducible domain switching controlled by the polarity of the current pulse-induced NSOT, we performed additional experiments in a $10\ \mu\text{m}$ wide crossbar device. The experimental geometry remains the same as in Fig. 9.2(a); the only difference is a bit lower current density of the pulses of $|j_p| = 8 \times 10^{10}\ \text{A/m}^2$. We first apply 6 positive current pulses along the vertical bar. The subsequent AMSE imaging reveals the domain pattern shown in Fig. 9.3(a). We continue by applying 6 negative pulses, which results in the substantially modified domain pattern shown in Fig. 9.3(b). Finally, we send 3 positive pulses, which lead to an ‘intermediate’ state [Fig. 9.3(c)], and another 3 positive pulses almost precisely recover the original state [cf. Figs. 9.3(d) and (a)]. The observed arc-shaped features located at the upper or lower entrance of the cross strongly resemble the domain configurations we studied in chapter 6 in ferromagnetic crossbar structures. There, a DW remained pinned at the cross-entrance corners and adopted a bubble-like shape in order to minimize its energy in the geometrically restricted cross structure. We assume now the same domain configuration in the CuMnAs cross and perform a numerical simulation of the resulting thermo-voltage response expected at the vertical and horizontal contacts (the simulation was not performed by the author of this thesis). The simulation results are shown in Fig. 9.3(e) and compared to the measured data. We observe a good qualitative agreement between the simulated and measured AMSE maps. Since the thermo-voltage magnitude scales with the projection of the DW normal on the detection direction, the central part of the DW is sensed by the vertical contacts while the DW parts adjacent to the corners are sensed mostly by the horizontal contacts. Thus, the crossbar geometry provides complementary information via the perpendicular voltage probes and allows for a better reconstruction of the domain pattern. On the other hand, it also suffers from geometrical artifacts in the vicinity of the corners as can be seen both in the experiment and simulation – the red/blue spots near the bottom corners in Figs. 9.3(a) and (e).

In the experiments we have discussed so far, the current-induced NSOT switching

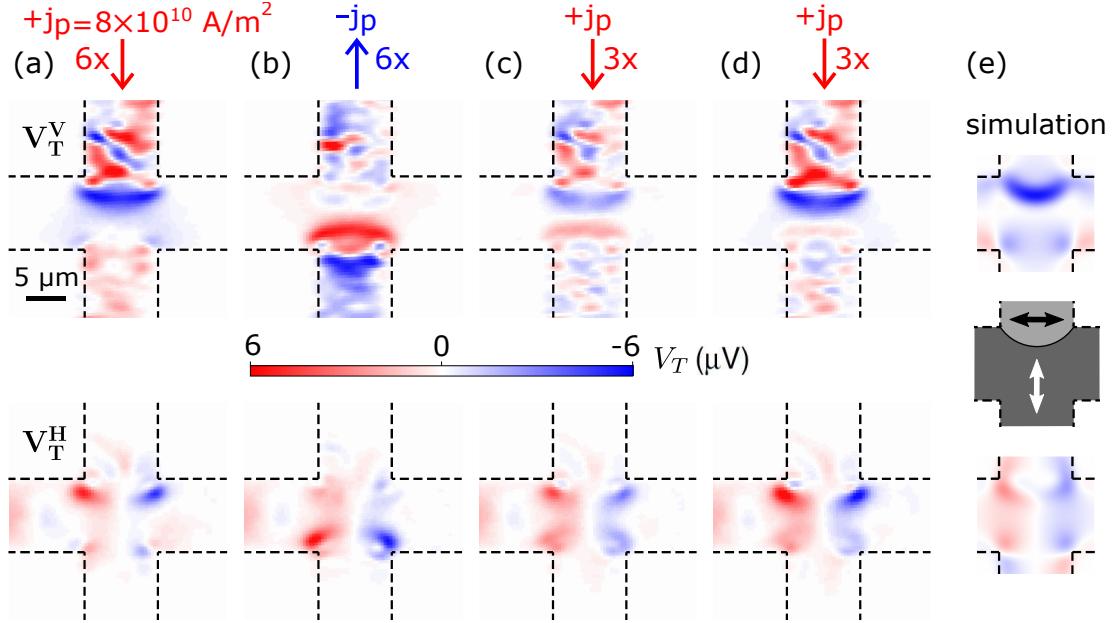


Figure 9.3: Reversible and reproducible current-induced domain switching.

Maps of the AMSE response detected via vertical (V_T^V) and horizontal (V_T^H) voltage contacts of a $10\ \mu\text{m}$ wide symmetrical crossbar device using a laser power of $5\ \text{mW}$. The measurement geometry is identical to that used in Fig. 9.2. (a) AMSE scans obtained after applying 6 positive current pulses of density $|j_p| = 8 \times 10^{10}\ \text{A/m}^2$ and $20\ \text{ms}$ duration along the vertical channel. (b) AMSE maps after applying 6 pulses of the same strength and negative polarity, (c) after another 3 positive pulses, and (d) after additional 3 positive pulses. (e) Numerical simulation of the AMSE response for the depicted domain configuration and taking into account the experimental conditions: laser spot FWHM of $1.5\ \mu\text{m}$, $5\ \text{mW}$ laser power (50% absorbed in CuMnAs film), AMSE amplitude $\Delta S = 4\ \mu\text{V/K}$, and thermal conductivities of 200 (75) W/(K m) for CuMnAs (GaP).

of the Néel vector in μm -sized domains has led to reversible and reproducible changes in the domain pattern controlled by polarity of the electrical current pulses. In this case, when sending more pulses of a constant polarity we usually observe an increase of intensity of the observed features. This might be explained by a growth of the domains preferred by the Néel spin-orbit field of the current pulse and consequently by a smaller effect of signal averaging by our micron-size laser spot. After switching the current polarity, we can reverse the process and finally restore the original domain configuration (see Figs. 9.2 and 9.3). The situation dramatically changes when applying just a bit stronger current pulses. In Figs. 9.4(a) and (b) we compare the AMSE maps measured in a $5\ \mu\text{m}$ wide bar before and after application of a current pulse with a magnitude of $|j_p| = 1.3 \times 10^{11}\ \text{A/m}^2$. The pulse causes a substantial decrease of the image contrast with the main features absent within the bar. We attribute the reduced contrast to shattering of the originally μm -sized domains to a fragmented multidomain state with sub-micron feature sizes. Consequently, the thermoelectric signal generated by the multiple domains present within the extension of the laser-induced thermal gradient mostly averages out resulting in a smeared image. At both ends of the bar, where it widens towards the electrical contacts, the original domain pattern remains unaffected by the current pulse. This is due to the larger cross-section and correspondingly lower current density, which falls below the threshold for domain shattering. In Figs. 9.4(d)–(f) we show for comparison XMLD-PEEM images obtained in a similar CuMnAs film for similar pulse amplitudes. In a virgin state, the crossbar device contains micron-scale domains [Fig. 9.4(d)] which break into number of tiny domains after application

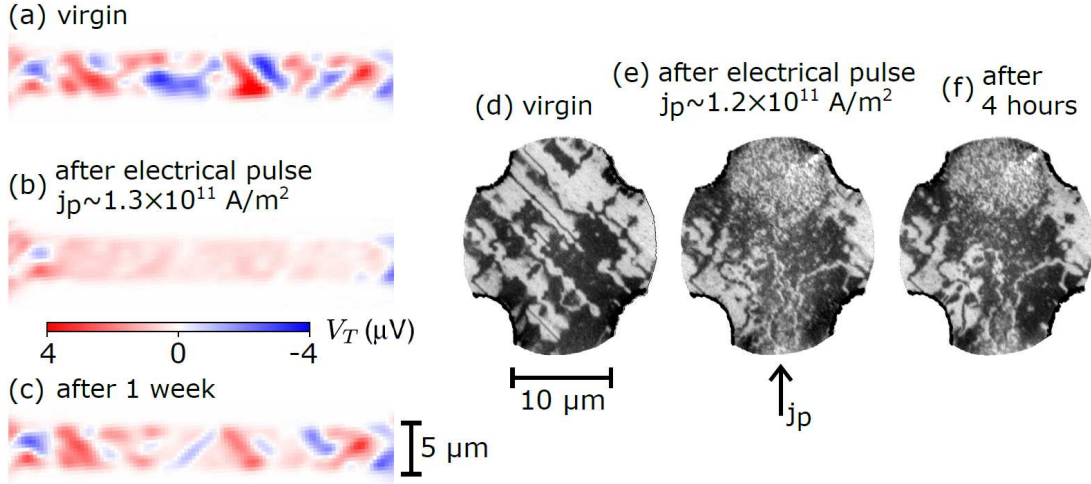


Figure 9.4: Current pulse-induced domain shattering. (a) AMSE map of a $5 \mu\text{m}$ wide bar device obtained prior to any electrical current pulse. (b) After application of a current pulse of density $|j_p| = 1.3 \times 10^{11} \text{ A/m}^2$ and 2 ms duration the thermoelectric image contrast almost disappears. This is attributed to a shattering of the originally μm -sized domains into a nano-fragmented domain state with domains much smaller than the spatial resolution of our far-field imaging technique. (c) Domain pattern closely resembling that of the virgin sample is restored in the image acquired one week after the current pulse application. All measurements were performed with a laser power of 5 mW. (d)–(f) XMLD-PEEM images obtained in a similar CuMnAs film prior to any current pulse (d), just after the pulse of density $|j_p| = 1.2 \times 10^{11} \text{ A/m}^2$ (e), and 4 hours after the pulse (f).

of a current pulse of $|j_p| \sim 1.2 \times 10^{11} \text{ A/m}^2$ along the vertical direction [Fig. 9.4(e)]. This is consistent with the AMSE image in Fig. 9.4(b), together with the observation that the domain fragmentation is most pronounced where the current density is largest, which is for a crossbar structure in the regions where current enters and exits the cross. No changes are observed in the horizontal cross entrances where the current density is low. Formation of the nano-fragmented domain states in CuMnAs has been studied very recently by simultaneous XMLD-PEEM and NV-center imaging [226, 227] and associated with pulse-heating of the system close to the Néel temperature. Simultaneous resistance measurements revealed GMR-level variations of 10–100%, which exceeds by 1–2 orders of magnitude the AMR signals due to the NSOT-induced 90° Néel vector switching in the unshattered micron-size domains [227].

In Fig. 9.4(f) the XMLD-PEEM imaging is repeated after 4 hours from the pulse application. Slight changes of the domain pattern are observed but without any obvious trend. Our easily accessible table-top microscopy technique allows us to explore the relaxation of the metastable fragmented states over long time-scales. Fig. 9.4(c) shows the AMSE map of our bar device after 1 week from the current-induced domain shattering. Remarkably, a domain pattern with micron-size features very similar to the original one present prior the pulsing is restored [cf. Figs. 9.4(a) and (c)]. This observation is in agreement with the recent NV-magnetometry results [226] and points to the presence of nucleation and pinning centers in the CuMnAs film that define the equilibrium state towards which the fragmented domain structure relaxes.

Finally, we note that the vanishing AMSE contrast in Fig. 9.4(b) and its re-appearance in Fig. 9.4(c) gives also an additional confirmation that the thermoelectric signal we measure indeed mostly originates from the AF texture of CuMnAs. Any potential non-magnetic contributions from defects would probably not be affected by the current pulse and, even more importantly, would not re-appear anymore.

9.3 Magnetic anisotropy evaluation via transverse magneto-Seebeck effect

In the previous section we studied thicker (45 nm) CuMnAs epilayers which usually exhibit biaxial magnetic anisotropy. In such case the AMSE signal is mostly generated in the vicinity of 90° domain walls. Due to the imbalance between the electromotive forces generated by the two adjacent domains with different Seebeck coefficients a net voltage is detected at the device terminals. The DW presence is required to break the radial symmetry of the laser-induced thermal gradient, but the net signal is generated within the domains, i.e., within the micron-size area covered by the laser spot. The situation is different in the case of 180° DWs. There is no imbalance between the domains with opposite Néel vectors (AMSE is even under spin reversal) and the net thermoelectric signal is generated only within the thin domain wall, whose Seebeck coefficient differs from that of both adjacent domains. Consequently, the AMSE signal due to a 180° DW should be much weaker than that produced by a 90° DW. Hence, for imaging uniaxial CuMnAs samples, which contain only 180° DWs, using a more tightly focused scanning hot-spot is highly desired. This was achieved by employing a scattering-type scanning near-field optical microscope [208, 209] providing a spatial resolution of the order of ~ 10 nm. These high-resolution measurements were not performed by the author of this thesis and can be found in [228]. Here we show that the low-resolution far-field AMSE imaging can still provide valuable information about the film's magnetic anisotropy even when it cannot resolve the individual domain walls.

We utilize the fact that when the laser spot is positioned on the edge of the magnetic bar, the induced thermal gradient is not radially symmetric anymore; the heat flow into the bar is not balanced by the opposite heat flow and a net thermal gradient perpendicular to the bar direction occurs, as shown in Fig. 9.5(a). In such case a net thermoelectric signal is generated even by a homogeneous magnetic texture, i.e., in a single domain state. Since the voltage detection direction is perpendicular to the induced temperature gradient, it is only the transverse AMSE which can generate a measurable signal by deflecting the thermally induced charge flow. Therefore, only domains whose Néel vector is neither parallel nor perpendicular to the bar edge will generate the thermoelectric signal and the maximum signals of opposite signs are obtained for the angles of $\pm 45^\circ$ between the Néel vector and the bar edge. Moreover, since the direction of the temperature gradient reverses when moving the laser spot to the opposite edge of the bar, signals of opposite sign are expected at the opposite bar edges, as shown by the orange and green curves in Fig. 9.5(a)]. Presence of a 180° DW will appear as a weak feature of opposite sign (due to the 90° rotated Néel vector in the middle of the wall) or only as a local decrease of the signal magnitude due to spatial averaging of the signal.

In thin CuMnAs films, the EAs may be oriented along $[110]$ and $[1\bar{1}0]$ crystal directions (observed in biaxial layers), or along one of the cubic axes $[100]$ or $[010]$ (observed in uniaxial layers) [149, 172–174]. In Fig. 9.5(b) we show all qualitatively different domain configurations that can appear if we restrict the Néel vector orientations to these crystal axes. Configurations (I) and (III) are found in biaxial samples. In (I) the transverse AMSE signal is generated from the domains and switches sign at each 90° DW. The light green and orange curves show the effect of spatial averaging for a denser packing of the DWs – the signal would eventually disappear for domains significantly smaller than the laser spot. In (III) the signal is generated only from the DWs resulting in weak isolated features which would average to zero for high density of DWs. The configurations (II) and (IV) are expected in uniaxial samples. In (II) the transverse AMSE acts within domains and appears as more or less constant signals of

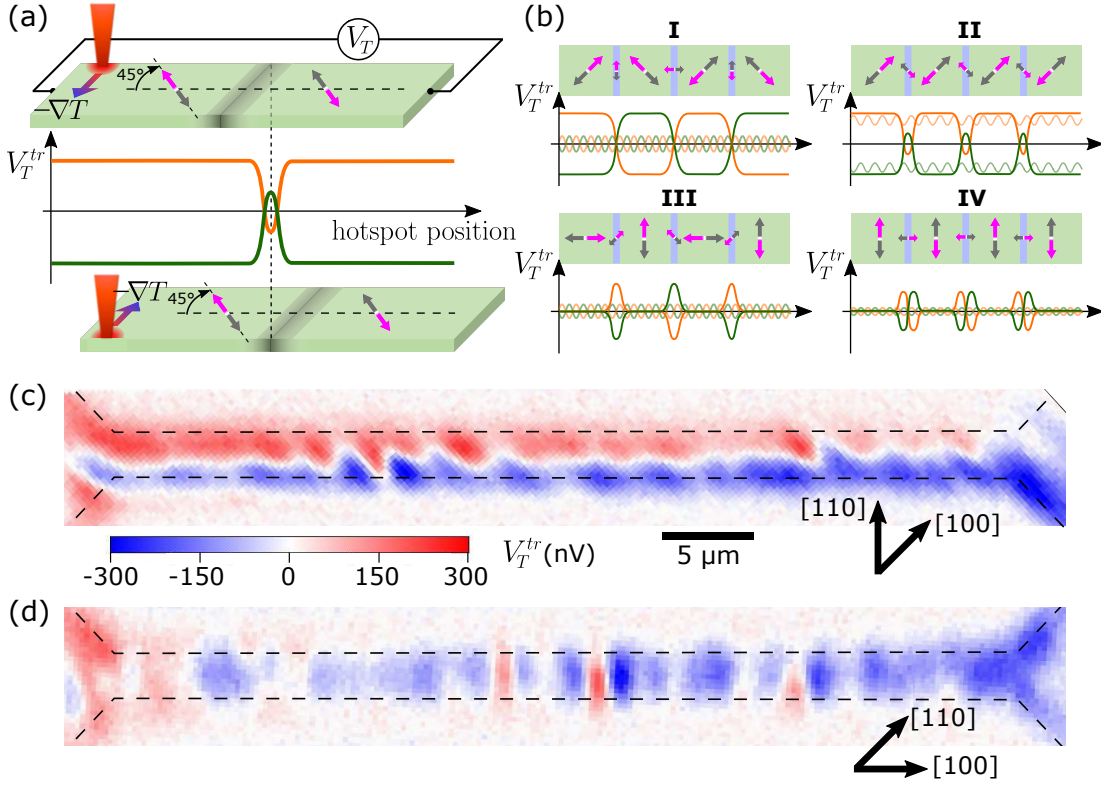


Figure 9.5: Transverse magneto-Seebeck effect in uniaxial CuMnAs films. (a) Schematic illustration of the transverse AMSE that induces opposite thermoelectric signals (V_T^{tr}) at the opposite edges of a CuMnAs bar due to the asymmetric in-plane temperature gradient. The maximum signal is expected for the Néel vector oriented at $\pm 45^\circ$ with respect to the bar edge. (b) Possible magnetic configurations (green domains, blue DWs) in biaxial and uniaxial CuMnAs films and the expected V_T^{tr} signals along the opposite bar edges (green and orange curves). The dark-color curves correspond to the DW spacing in the sketch, the light-color curves show the effect of signal spatial averaging for a denser packing of DWs. (c) AMSE map measured in a $2.5 \mu\text{m}$ wide bar patterned from a 20 nm thin CuMnAs film along the $[1\bar{1}0]$ crystal direction and (d) AMSE map of the bar patterned along the $[100]$ direction. Comparison of (b) with (c) and (d) yields uniaxial magnetic anisotropy with EA either along $[100]$ or $[010]$ direction. The AMSE imaging was performed with a laser power of 1.4 mW.

opposite sign along the two bar edges. High density of 180° DWs would only lead to a slight decrease of the signal magnitude provided that the domain's diameter is still significantly larger than the DW width. Finally, in (IV) the signal is only generated in the DWs leading again only to weak signals, as in (III).

In Fig. 9.5(c) we show the AMSE scan of a $2.5 \mu\text{m}$ wide bar device patterned from a 20 nm thin CuMnAs/GaP epilayer along the $[1\bar{1}0]$ crystal direction. We observe clear monopolar features that follow the two bar edges and have opposite signs on the two sides. The shift of the image colors towards red (blue) close to the left (right) end of the bar is due to an additional thermoelectric signal that arises from the asymmetric heat flow along the bar axis close to the bar widening; more heat flows out of the bar than in, breaking additionally the circular symmetry of temperature gradient. Fig. 9.5(d) shows for comparison the AMSE map obtained in a bar that is 45° rotated with respect to the previous one. Here, no signs of color imbalance between the two bar edges can be seen. Both observations of Figs. 9.5(c) and (d) can only be explained when assuming a uniaxial magnetic anisotropy with EA either along $[100]$ or $[010]$ crystal directions of CuMnAs. This points to configuration (II) for Fig. 9.5(c) and (IV) for

Fig. 9.5(d). Note that configurations with all Néel vectors rotated by 90° would fit equally well. This ambiguity of the actual orientation of magnetic domains could be resolved when the sign of the differential Seebeck coefficient ΔS would be known. The uniaxial anisotropy of the 20 nm thin CuMnAs film from Fig. 9.5 was confirmed by the high-resolution near-field imaging and the 180° DWs were directly observed [228].

Finally, we note that besides the 45 nm thick biaxial CuMnAs film studied in sections 9.1 and 9.2 we performed the AMSE imaging on devices prepared from several other wafers with similar film thicknesses. In one of them we observed the same behavior as in Fig. 9.5, which indicates uniaxial magnetic anisotropy also in this thicker CuMnAs layer. Certain indication that the magnetic anisotropy of CuMnAs may not be governed exclusively by the film thickness was given in a recent comprehensive magneto-optical study performed in a wide range of CuMnAs films [174]. This study, however, used a pump-probe MO technique, which gives reliable results only in case of a very strong magnetic anisotropy, as discussed in [230]. This is usually not the case in CuMnAs and heating from the strong pump pulse (~ 100 K temperature rise) significantly modifies the magnetic anisotropy measured by the delayed probe pulse. Our method, on the other hand, allows to evaluate the magnetic anisotropy of CuMnAs films in equilibrium, since the temperature rise due to the CW laser beam is roughly 1 K/mW [228].

9.4 Conclusion

In this chapter, we studied thin epitaxial films of the compensated collinear antiferromagnet CuMnAs. This material has many appealing properties that make it interesting for applications in spintronics. On the other hand, it is very difficult to study since it produces no magnetic stray fields, it is insensitive to moderate magnetic fields, and, due to its high symmetry, many of the spintronic effects that are routinely used for manipulation and detection of ferromagnetic order are forbidden in CuMnAs. We demonstrated that spin-caloritronics provides a simple means of imaging of the AF domain structure of CuMnAs in a table-top experimental setup. We utilized a CW laser focused onto the surface of a CuMnAs bar device to produce a localized in-plane thermal gradient. If there is a magnetic domain wall present within the laser-induced hot-spot, it produces a net voltage on the device terminals via the anisotropic magneto-Seebeck effect, i.e., due to the varying Seebeck coefficient corresponding to the local Néel vector orientation. By scanning the laser spot across the device and measuring the ensuing thermo-voltage in each position, one obtains an image of the magnetic domain pattern. The AMSE microscopy technique can be applied to any conductive antiferromagnet with sufficiently strong thermoelectric response. It is not limited to either uncompensated AFs, which still produce detectable magnetic stray fields, or to systems with a complex symmetry-breaking spin order, such as non-collinear AFs. Since AMSE is even under spin reversal, it is present also in collinear compensated antiferromagnets.

To confirm that our imaging technique is indeed sensitive to the collinear AF order, we performed the AMSE scanning in a CuMnAs film with a biaxial magnetic anisotropy and compared our results to images obtained by the established synchrotron-based XMLD-PEEM technique. Both measurements have shown similar patterns of micron-size domains with a preferential DW orientation determined by the underlying CuMnAs square lattice. To evidence further the magnetic origin of the measured thermoelectric signal, we performed electrical switching experiments in crossbar devices. We observed reversible and reproducible changes in the AMSE images accompanied by corresponding changes in the device resistance in response to electrical current pulses of $\sim 9 \times 10^{10}$ A/m² magnitude and varying polarity. Analogous correlation between the

variations in the device resistance and in the domain pattern was previously observed for similar current magnitudes via XMLD-PEEM [173, 194]. The observed current-induced magnetic switching is explained in terms of the Néel vector reorientation in micron-scale domains that is induced by the Néel spin-orbit torque [12] acting on the staggered magnetic moments. Apart from this mechanism, we observed also a distinct process. By increasing the current pulse magnitude by $\sim 40\%$ the AMSE image contrast almost completely disappeared. This is ascribed to a shattering of the originally μm -sized domains into a nano-fragmented domain state [226, 227] with domains much smaller than the extension of the laser-induced thermal gradient. We were able to observe also the subsequent relaxation of the fragmented domain state back to micron-scale domains with a spatial distribution closely resembling the original one that was present prior applying the current pulse. This hints to the presence of pinning and nucleation centers in the AF film that determine the equilibrium domain configuration.

Finally, we have shown that the AMSE imaging can be used to evaluate the magnetic anisotropy of thin CuMnAs films. We utilized the asymmetric temperature gradient generated by the laser beam when illuminating the edge of the CuMnAs bar device. Here, the transverse AMSE produces characteristic constant-signal features of opposite sign along the opposite bar edges provided that the sample has a uniaxial magnetic anisotropy with EA making an angle distinct from 0° or 90° with respect to the bar direction. We demonstrated this idea on an example of a 20 nm thin CuMnAs/GaP epilayer where we found a uniaxial anisotropy with EA oriented either along [100] or [010] crystal axis. The uniaxial anisotropy of this particular film was later confirmed by high-resolution near-field thermoelectric measurements [228]. The EA orientation along one of the cubic axes of CuMnAs is in agreement with previous XMLD-PEEM and MO measurements in uniaxial samples [149, 172].

Conclusion

The aim of this work was to develop methods for an ultrafast manipulation of magnetic domains and domain walls and for a detection (imaging) of the resulting magnetic states. Studying properties of these magnetic textures and their response to various excitation mechanisms is of great importance not only because they have, in general, significant influence on the operation of spintronic devices, but also because of the possible direct utilization of magnetic domains and domain walls as information carriers in memory and logic devices. We focused on thin magnetic films, which are of particular interest for spintronic applications, and on excitation and detection techniques which are, apart from ferromagnets, also applicable to antiferromagnets. Due to the strong inter-sublattice exchange coupling and the lack of net magnetization, and the corresponding stray fields, spintronic devices based on AFs promise to reach orders of magnitude faster operation and higher integration densities than their FM counterparts. Practical utilization of these appealing properties of AFs have long time been hindered by the lack of suitable control and detection methods. This is, however, changing now rapidly and this thesis gives its contribution to these efforts.

The starting point was a construction of a versatile experimental setup combining a MO pump-probe scheme, which provides subpicosecond temporal and micrometer spatial resolutions for local measurements, and a wide-field MO microscope, which allows for a real-time imaging of both out-of-plane and in-plane polarized magnetic patterns via the polar Kerr and Voigt effects, respectively. We demonstrated the Voigt effect-based MO imaging on FM GaMnAs samples. The wide-field MO microscope proved to be especially useful for a rapid inspection of spatially inhomogeneous samples, which can be followed by dynamical pump-probe MO measurements in the preselected sample parts. In a test GaMnAs sample attached to a piezoelectric transducer, we were able to visualize the inhomogeneous strain distribution via its effect on the magnetic domain structure and magnetization dynamics. This ability is especially appealing for AF spintronics, where the controlled strain application is considered as one of the possible means of control due to the strong magneto-elastic coupling in AFs and their insensitivity to conventional control mechanisms. Since the Voigt effect is even in magnetization, it should be, in principle, present also in collinear AFs. Separation of the weak MO signals from the non-magnetic background is, however, much more difficult in AFs and our preliminary experiments on MO imaging of the collinear AF CuMnAs have not been successful yet. Nevertheless, the presented optical setup is very flexible and, with only minor modifications, it allowed us to apply distinct excitation and detection techniques and to achieve successful domain imaging in a broad variety of material systems, namely in FMs and both non-collinear and collinear AFs, including CuMnAs.

From the ferromagnetic systems, we studied the DMS GaMnAsP. In this material, we observed a DW motion driven by femtosecond circularly polarized laser pulses with the DW propagation direction controlled by the laser helicity. This effect was attributed to the OSTT from the spin-polarized photo-electrons which tilted the wall magnetization out of the sample plane, thus driving the whole DW along the magnetic bar. The main finding of our experiments is the inertial character of the OSTT-induced DW motion. To prove that, we studied the DW propagation through a cross-shaped structure where the DW motion was opposed by a restoring force induced by the device geometry. Taking into account the limited DW propagation velocity, our observation that the OSTT-driven DW could pass the cross area can only be explained if the DW moved forward during a significant part of the dark period in between the successive

laser pulses, i.e., if the DW motion was driven by its inertia. This picture was confirmed by micromagnetic simulations which revealed the microscopic nature of the inertia being related to deformation of the DW internal structure.

In chapter 7, we continued in the exploration of ultrafast excitation mechanisms with the focus on antiferromagnetic materials. Among the control mechanisms applicable to AFs, electrical currents represent the best choice from the application point of view due to the simplicity and scalability of this approach. For the exploration of the THz-scale spin dynamics of AFs, the current pulses have to be correspondingly short. We developed a photoconductive switch based on a vertical GaAs PIN-diode structure patterned into a Corbino disc, which is capable of generating picosecond current pulses. Here, a femtosecond laser pulse absorbed in the intrinsic region of the diode is converted into an ultrashort photocurrent pulse, which excites a magnetic film deposited directly on the n-GaAs electrode. We used a 2 nm thin iron film and, to demonstrate the applicability of the design to the relevant AF materials, also a 50 nm thick CuMnAs film. The photocurrent pulses were characterized using a double-pulse correlation technique. Both devices have shown very similar characteristics – a rapid decrease of the current pulse decay time with an increasing reverse bias and its saturation at ~ 20 ps for biases larger than ~ -5 V. The effect of the current pulse-induced Oersted field on the iron magnetization was utilized to trace the current propagation in the Corbino device. The current initially flowing vertically in the illuminated region of the diode enters the Fe/n-GaAs electrode and continues in lateral direction towards the external contact. The estimated peak current density of $\sim 4 \times 10^{10}$ A/m² entering the magnetic film, or even $\gtrsim 10^{12}$ A/m² if the pulse was fed into a typical lateral microbar device, should be sufficient to induce the Néel vector switching in CuMnAs. Moreover, as indicated by transient reflectivity data and confirmed by numerical simulations, the initial rapid ($\lesssim 1$ ps) onset of the current terminated by the charge screening effects is associated with even shorter photocurrent pulse and larger current densities. This initial rapid charge dynamics is, however, not resolved by the correlation measurement due to a long carrier lifetime in our GaAs diode.

The last two chapters were devoted to the development of easily accessible table-top imaging techniques applicable to thin AF films. For this purpose we modified the experimental setup described in chapter 5. The fs-laser beam was replaced by a CW-laser beam that was used to generate a localized temperature gradient in a magnetic bar device. The presence of AF domains or domain walls manifests itself via magneto-thermoelectric effects as a voltage that can be detected on the device terminals. The domain image was assembled from the individual local thermoelectric measurements by scanning the focused laser beam over the sample surface. We first presented the results obtained in the simpler case of a non-collinear AF, Mn₃Sn, which still shares certain properties with FMs. In particular, it can be controlled by moderate magnetic fields and its symmetry-breaking structure also allows for a broad spectrum of readout mechanisms. By studying the magnetic-field and temperature dependence of the recorded thermovoltage maps and by examining the symmetries of the detected signal, we confirmed that the measured spatial contrast corresponds to the AF domain structure of Mn₃Sn that is visualized via anomalous Nernst effect induced by a perpendicular-to-plane component of the laser-induced temperature gradient. Furthermore, we demonstrated that the same experimental scheme can be used also to write magnetic domains in the antiferromagnet at room temperature. Increasing the imaging laser power by a factor of ~ 5 combined with moderate magnetic fields (± 0.5 T) allowed us to write magnetic patterns ‘at will’, which remained insensitive to magnetic fields up to 6 T at room temperature and below. Such a combination of easy room temperature writability, robustness against large magnetic fields, and absence of perturbing

stray fields is particularly interesting for potential high-density non-volatile memory applications.

Finally, we described our experiments performed in the collinear AF CuMnAs, whose investigation is much more challenging due to the high material symmetry which restricts significantly the possible control and detection mechanisms. In particular, CuMnAs does not respond to moderate magnetic fields and the odd-in-M effects, such as ANE, are zero by symmetry. To image the CuMnAs domain structure, we employed the anisotropic magneto-Seebeck effect, which is the thermoelectric counterpart to AMR and XMLD that were used to study CuMnAs previously. In this case, an in-plane thermal gradient is needed. However, since the laser-induced temperature gradient is radially symmetric, an inhomogeneous magnetic texture is required within the laser-induced hotspot to break the symmetry and generate nonzero thermovoltage. Therefore, in CuMnAs we imaged magnetic domain walls instead of domains. To confirm that our imaging technique is indeed sensitive to the collinear AF order, we compared our results obtained in biaxial CuMnAs samples to XMLD-PEEM images with a good qualitative agreement between both techniques. The magnetic origin of our thermoelectric signal was further evidenced by electrical switching experiments. We observed reversible and reproducible changes in the AMSE images accompanied by corresponding changes in the device resistance in response to current pulses of $\sim 9 \times 10^{10}$ A/m² magnitude and alternating polarity. These variations were explained in terms of 90° Néel vector reorientation via NSOT in micron-size domains. A slight increase in the current density resulted in a complete loss of the AMSE image contrast. This was attributed to a shattering of the macroscopic domain pattern into a fragmented state with nano-scale domains, which cannot be resolved by our $\sim 1 \mu\text{m}$ laser spot. Interestingly, at a time-scale of days, the domain pattern relaxed back towards the original distribution of the micron-size domains present prior application of the current pulse. This hints to the presence of pinning and nucleation centers in the AF film that determine the equilibrium domain configuration. Finally, we also demonstrated that the AMSE imaging can be used for a simple evaluation of the magnetic anisotropy of CuMnAs films. Uniaxial anisotropy manifests itself via transverse AMSE as characteristic unipolar signals along the edges of the magnetic bar.

The next step in a future research is, naturally, to combine the developed excitation and imaging techniques in one experiment and try to image the domain changes induced in CuMnAs by the ultrashort photocurrent pulses generated in the PIN-diode switch. Moreover, the current pulse generation by femtosecond laser pulses is naturally compatible with time-resolved measurements. A photocurrent-pump/optical-probe measurement is, therefore, an example of a possible future experiment that could shed light on the time-scales of Néel vector switching process in CuMnAs.

Bibliography

- [1] Baibich, M. N. *et al.* Giant Magnetoresistance of (001)Fe/(001)Cr Magnetic Superlattices. *Physical Review Letters* **61**, 2472 (1988).
- [2] Wolf, S. A. *et al.* Spintronics: A Spin-Based Electronics Vision for the Future. *Science* **294**, 1488–1495 (2001).
- [3] Chappert, C., Fert, A. & Dau, F. N. V. The emergence of spin electronics in data storage. *Nature Materials* **6**, 813–823 (2007).
- [4] Waldrop, M. M. The chips are down for Moore’s law. *Nature News* **530**, 144 (2016).
- [5] Bhatti, S. *et al.* Spintronics based random access memory: a review. *Materials Today* **20**, 530–548 (2017).
- [6] Jungwirth, T., Marti, X., Wadley, P. & Wunderlich, J. Antiferromagnetic spintronics. *Nature Nanotechnology* **11**, 231–241 (2016).
- [7] Jungwirth, T. *et al.* The multiple directions of antiferromagnetic spintronics. *Nature Physics* **14**, 200–203 (2018).
- [8] Baltz, V. *et al.* Antiferromagnetic spintronics. *Reviews of Modern Physics* **90**, 015005 (2018).
- [9] Gomonay, O., Baltz, V., Brataas, A. & Tserkovnyak, Y. Antiferromagnetic spin textures and dynamics. *Nature Physics* **14**, 213–216 (2018).
- [10] Wadley, P. *et al.* Electrical switching of an antiferromagnet. *Science* **351**, 587–590 (2016).
- [11] Bodnar, S. *et al.* Writing and reading antiferromagnetic Mn₂Au by Néel spin-orbit torques and large anisotropic magnetoresistance. *Nature Communications* **9**, 348 (2018).
- [12] Železný, J. *et al.* Relativistic Néel-Order Fields Induced by Electrical Current in Antiferromagnets. *Physical Review Letters* **113**, 157201 (2014).
- [13] Parkin, S. S. P., Hayashi, M. & Thomas, L. Magnetic Domain-Wall Racetrack Memory. *Science* **320**, 190–194 (2008).
- [14] Allwood, D. A. *et al.* Magnetic Domain-Wall Logic. *Science* **309**, 1688–1692 (2005).
- [15] Gerlach, W. & Stern, O. Der experimentelle Nachweis der Richtungsquantelung im Magnetfeld. *Zeitschrift für Physik* **9**, 349–352 (1922).
- [16] Phipps, T. E. & Taylor, J. B. The Magnetic Moment of the Hydrogen Atom. *Phys. Rev.* **29**, 309–321 (1927).
- [17] Dirac, P. A. M. The Quantum Theory of the Electron. *Proceedings of the Royal Society A* **117**, 610–624 (1928).
- [18] Skála, L. *Úvod do kvantové mechaniky* (Academia, Prague, 2005).

- [19] Coey, J. M. D. *Magnetism and Magnetic Materials* (Cambridge University Press, New York, 2010).
- [20] Winkler, R. *Spin-orbit Coupling Effects in Two-Dimensional Electron and Hole Systems* (Springer, Berlin, 2003).
- [21] Thomas, L. H. The Motion of the Spinning Electron. *Nature* **117**, 514 (1926).
- [22] Fabian, J., Matos-Abiague, A., Ertler, C., Stano, P. & Žutić, I. Semiconductor spintronics. *Acta Physica Slovaca* **57**, 565–907 (2007).
- [23] Blundell, S. *Magnetism in Condensed Matter* (Oxford University Press, New York, 2001).
- [24] Jungwirth, T., Sinova, J., Mašek, J., Kučera, J. & MacDonald, A. H. Theory of ferromagnetic (III,Mn)V semiconductors. *Reviews of Modern Physics* **78**, 809–864 (2006).
- [25] Tesařová, N. *et al.* Experimental observation of the optical spin–orbit torque. *Nature Photonics* **7**, 492–498 (2013).
- [26] Hubert, A. & Schäfer, R. *Magnetic Domains* (Springer, Berlin, 2009).
- [27] Zemen, J., Kučera, J., Olejník, K. & Jungwirth, T. Magnetocrystalline anisotropies in (Ga,Mn)As: Systematic theoretical study and comparison with experiment. *Physical Review B* **80**, 155203 (2009).
- [28] Wastlbauer, G. & Bland, J. A. C. Structural and magnetic properties of ultrathin epitaxial Fe films on GaAs(001) and related semiconductor substrates. *Advances in Physics* **54**, 137–219 (2005).
- [29] Rushforth, A. W. *et al.* Voltage control of magnetocrystalline anisotropy in ferromagnetic-semiconductor-piezoelectric hybrid structures. *Physical Review B* **78**, 085314 (2008).
- [30] Li, Y. Y. Domain Walls in Antiferromagnets and the Weak Ferromagnetism of α -Fe₂O₃. *Phys. Rev.* **101**, 1450–1454 (1956).
- [31] Farztdinov, M. M. Structure of Antiferromagnets. *Soviet Physics Uspekhi* **7**, 855–876 (1965).
- [32] Gomonay, H. & Loktev, V. M. Magnetostriction and magnetoelastic domains in antiferromagnets. *J. Phys.: Condens. Matter* **14**, 3959–3971 (2002).
- [33] Acremann, Y. *et al.* Ultrafast generation of magnetic fields in a Schottky diode. *Nature* **414**, 51–54 (2001).
- [34] Rozkotová, E. *et al.* Light-induced magnetization precession in GaMnAs. *Applied Physics Letters* **92**, 122507 (2008).
- [35] Slonczewski, J. C. Current-driven excitation of magnetic multilayers. *Journal of Magnetism and Magnetic Materials* **159**, L1–L7 (1996).
- [36] Myers, E. B., Ralph, D. C., Katine, J. A., Louie, R. N. & Buhrman, R. A. Current-Induced Switching of Domains in Magnetic Multilayer Devices. *Science* **285**, 867–870 (1999).

- [37] Fernández-Rossier, J., Núñez, A. S., Abolfath, M. & MacDonald, A. H. Optical spin transfer in ferromagnetic semiconductors. *arXiv e-prints* cond-mat/0304492 (2003). URL <https://arxiv.org/abs/cond-mat/0304492>.
- [38] Němec, P. *et al.* Experimental observation of the optical spin transfer torque. *Nature Physics* **8**, 411–415 (2012).
- [39] Manchon, A. & Zhang, S. Theory of nonequilibrium intrinsic spin torque in a single nanomagnet. *Physical Review B* **78**, 212405 (2008).
- [40] Chernyshov, A. *et al.* Evidence for reversible control of magnetization in a ferromagnetic material by means of spin-orbit magnetic field. *Nature Physics* **5**, 656–659 (2009).
- [41] Němec, P. *et al.* The essential role of carefully optimized synthesis for elucidating intrinsic material properties of (Ga,Mn)As. *Nature Communications* **4**, 1422 (2013).
- [42] Tesařová, N. *et al.* Comparison of micromagnetic parameters of the ferromagnetic semiconductors (Ga,Mn)(As,P) and (Ga,Mn)As. *Physical Review B* **90**, 155203 (2014).
- [43] Schmoranzarová, E. *et al.* Probing of Spin Wave Resonances in (Ga,Mn)As by Time-Resolved Magneto-Optical Technique. *IEEE Transactions on Magnetics* **50**, 2401604 (2014).
- [44] Kittel, C. Theory of Antiferromagnetic Resonance. *Physical Review* **82**, 565 (1951).
- [45] Gomony, O. V. & Loktev, V. M. Using generalized Landau-Lifshitz equations to describe the dynamics of multi-sublattice antiferromagnets induced by spin-polarized current. *Low Temperature Physics* **41**, 698–704 (2015).
- [46] Železný, J., Wadley, P., Olejník, K., Hoffmann, A. & Ohno, H. Spin transport and spin torque in antiferromagnetic devices. *Nature Physics* **14**, 220–228 (2018).
- [47] Gomony, H. V. & Loktev, V. M. Spin transfer and current-induced switching in antiferromagnets. *Physical Review B* **81**, 144427 (2010).
- [48] Reichlová, H. *et al.* Current-induced torques in structures with ultrathin IrMn antiferromagnets. *Physical Review B* **92**, 165424 (2015).
- [49] Němec, P., Fiebig, M., Kampfrath, T. & Kimel, A. V. Antiferromagnetic optospintronics. *Nature Physics* **14**, 229–241 (2018).
- [50] Scholl, A., Liberati, M., Arenholz, E., Ohldag, H. & Stöhr, J. Creation of an Antiferromagnetic Exchange Spring. *Physical Review Letters* **92**, 247201 (2004).
- [51] Krzysteczko, P. *et al.* Nanoscale thermoelectrical detection of magnetic domain wall propagation. *Physical Review B* **95**, 220410(R) (2017).
- [52] Berger, L. Low-field magnetoresistance and domain drag in ferromagnets. *Journal of Applied Physics* **49**, 2156 (1978).
- [53] Freitas, P. P. & Berger, L. Observation of *s-d* exchange force between domain walls and electric current in very thin Permalloy films. *Journal of Applied Physics* **57**, 1266 (1985).

- [54] Grünberg, P., Schreiber, R., Pang, Y., Brodsky, M. B. & Sowers, H. Layered Magnetic Structures: Evidence for Antiferromagnetic Coupling of Fe Layers across Cr Interlayers. *Physical Review Letters* **57**, 2442 (1986).
- [55] Binasch, G., Grünberg, P., Saurenbach, F. & Zinn, W. Enhanced magnetoresistance in layered magnetic structures with antiferromagnetic interlayer exchange. *Physical Review B* **39**, 4828(R) (1989).
- [56] Berger, L. Emission of spin waves by a magnetic multilayer traversed by a current. *Physical Review B* **54**, 9353 (1996).
- [57] Katine, J. A., Albert, F. J., Buhrman, R. A., Myers, E. B. & Ralph, D. C. Current-Driven Magnetization Reversal and Spin-Wave Excitations in Co /Cu /Co Pillars. *Physical Review Letters* **84**, 3149 (2000).
- [58] Miyazaki, T. & Tezuka, N. Giant magnetic tunneling effect in Fe/Al₂O₃/Fe junction. *Journal of Magnetism and Magnetic Materials* **139**, L231–L234 (1995).
- [59] Huai, Y., Albert, F., Nguyen, P., Pakala, M. & Valet, T. Observation of spin-transfer switching in deep submicron-sized and low-resistance magnetic tunnel junctions. *Applied Physics Letters* **84**, 3118 (2004).
- [60] Haney, P. M., Duine, R. A., Núñez, A. S. & MacDonald, A. H. Current-induced torques in magnetic metals: Beyond spin-transfer. *Journal of Magnetism and Magnetic Materials* **320**, 1300–1311 (2008).
- [61] Stiles, M. D. & Zangwill, A. Anatomy of spin-transfer torque. *Physical Review B* **66**, 014407 (2002).
- [62] Ralph, D. C. & Stiles, M. D. Spin transfer torques. *Journal of Magnetism and Magnetic Materials* **320**, 1190–1216 (2008).
- [63] Cheng, R., Daniels, M. W., Zhu, J.-G. & Xiao, D. Ultrafast switching of antiferromagnets via spin-transfer torque. *Physical Review B* **91**, 064423 (2015).
- [64] Optical Orientation, edited by F. Meier & B. P. Zakharchenya, in *Modern Problems in Condensed Matter Sciences*, vol. 8, general editors: V. M. Agranovich & A. A. Maradudin (Elsevier Science, Amsterdam, 1984).
- [65] Pierce, D. T. & Meier, F. Photoemission of spin-polarized electrons from GaAs. *Physical Review B* **13**, 5484–5500 (1976).
- [66] Matos-Abiague, A. & Rodríguez-Suárez, R. L. Spin-orbit coupling mediated spin torque in a single ferromagnetic layer. *Physical Review B* **80**, 094424 (2009).
- [67] Miron, I. M. *et al.* Current-driven spin torque induced by the Rashba effect in a ferromagnetic metal layer. *Nature Materials* **9**, 230–234 (2010).
- [68] Miron, I. M. *et al.* Perpendicular switching of a single ferromagnetic layer induced by in-plane current injection. *Nature* **476**, 189–193 (2011).
- [69] Gambardella, P. & Miron, I. M. Current-induced spin-orbit torques. *Phil. Trans. R. Soc. A* **369**, 3175–3197 (2011).
- [70] Silsbee, R. H. Spin-orbit induced coupling of charge current and spin polarization. *Journal of Physics: Condensed Matter* **16**, R179–R207 (2004).

- [71] Dresselhaus, G. Spin-Orbit Coupling Effects in Zinc Blende Structures. *Physical Review* **100**, 580–586 (1955).
- [72] Bychkov, Y. A. & Rashba, E. I. Oscillatory effects and the magnetic susceptibility of carriers in inversion layers. *Journal of Physics C: Solid State Physics* **17**, 6039–6045 (1984).
- [73] Adagideli, I., Bauer, G. E. W. & Halperin, B. I. Detection of Current-Induced Spins by Ferromagnetic Contacts. *Physical Review Letters* **97**, 256601 (2006).
- [74] Yang, W., Chang, K., Wu, X. G., Zheng, H. Z. & Peeters, F. M. Interplay between s - d exchange interaction and Rashba effect: Spin-polarized transport. *Applied Physics Letters* **89**, 132112 (2006).
- [75] Kurebayashi, H. *et al.* An antidamping spin-orbit torque originating from the Berry curvature. *Nature Nanotechnology* **9**, 211–217 (2014).
- [76] Sinova, J. *et al.* Universal Intrinsic Spin Hall Effect. *Physical Review Letters* **92**, 126603 (2004).
- [77] Zhang, X., Liu, Q., Luo, J.-W., Freeman, A. J. & Zunger, A. Hidden spin polarization in inversion-symmetric bulk crystals. *Nature Physics* **10**, 387–393 (2014).
- [78] Olejník, K. *et al.* Antiferromagnetic CuMnAs multi-level memory cell with microelectronic compatibility. *Nature Communications* **8**, 15434 (2017).
- [79] Olejník, K. *et al.* Terahertz electrical writing speed in an antiferromagnetic memory. *Science Advances* **4**, 3566 (2018).
- [80] Hirsch, J. E. Spin hall effect. *Physical Review Letters* **83**, 1834–1837 (1999).
- [81] Sinova, J., Valenzuela, S. O., Wunderlich, J., Back, C. & Jungwirth, T. Spin hall effects. *Reviews of Modern Physics* **87**, 1213–1260 (2015).
- [82] Kato, Y. K., Myers, R. C., Gossard, A. C. & Awschalom, D. D. Observation of the Spin Hall Effect in Semiconductors. *Science* **306**, 1910–1913 (2004).
- [83] Wunderlich, J., Kaestner, B., Sinova, J. & Jungwirth, T. Experimental Observation of the Spin-Hall Effect in a Two-Dimensional Spin-Orbit Coupled Semiconductor System. *Physical Review Letters* **94**, 047204 (2005).
- [84] Takahashi, S. & Maekawa, S. Spin current, spin accumulation and spin Hall effect. *Science and Technology of Advanced Materials* **9**, 014105 (2008).
- [85] Liu, L. *et al.* Spin-Torque Switching with the Giant Spin Hall Effect of Tantalum. *Science* **336**, 555–558 (2012).
- [86] Moriyama, T., Oda, K., Ohkochi, T., Kimata, M. & Ono, T. Spin torque control of antiferromagnetic moments in NiO. *Scientific Reports* **8**, 14167 (2018).
- [87] Murakami, S., Nagaosa, N. & Zhang, S.-C. Dissipationless Quantum Spin Current at Room Temperature. *Science* **301**, 1348–1351 (2003).
- [88] Haney, P. M., Lee, H.-W., Lee, K.-J., Manchon, A. & Stiles, M. D. Current induced torques and interfacial spin-orbit coupling: Semiclassical modeling. *Physical Review B* **87**, 174411 (2013).

- [89] Mougín, A., Cormier, M., Adam, J. P., Metaxas, P. J. & Ferré, J. Domain wall mobility, stability and Walker breakdown in magnetic nanowires. *Europhysics Letters* **78**, 57007 (2007).
- [90] Thiaville, A., Nakatani, Y., Miltat, J. & Suzuki, Y. Micromagnetic understanding of current-driven domain wall motion in patterned nanowires. *Europhysics Letters* **69**, 990–996 (2005).
- [91] Miltat, J., Albuquerque, G. & Thiaville, A. , in *Spin Dynamics in Confined Magnetic Structures I*, edited by B. Hillebrands & K. Ounadjela (Springer, Berlin, 2002), Chap. 1.
- [92] Walker, L. R.: unpublished, reported in J. F. Dillon Jr., Domains and Domain Walls, in *Magnetism*, Vol. III, edited by G. T. Rado & H. Suhl (Academic Press, New York, 1963), p. 450–454.
- [93] Beach, G. S. D., Tsoi, M. & Erskine, J. L. Current-induced domain wall motion. *Journal of Magnetism and Magnetic Materials* **320**, 1272–1281 (2008).
- [94] Lemerle, S. *et al.* Domain Wall Creep in an Ising Ultrathin Magnetic Film. *Physical Review Letters* **80**, 849–852 (1998).
- [95] Metaxas, P. J. *et al.* Creep and Flow Regimes of Magnetic Domain-Wall Motion in Ultrathin Pt/Co/Pt Films with Perpendicular Anisotropy. *Physical Review Letters* **99**, 217208 (2007).
- [96] Döring, W. Über die Trägheit der Wände zwischen Weißschen Bezirken. *Zeitschrift für Naturforschung* **3a**, 373–379 (1948).
- [97] Rhensius, J. *et al.* Imaging of Domain Wall Inertia in Permalloy Half-Ring Nanowires by Time-Resolved Photoemission Electron Microscopy. *Physical Review Letters* **104**, 067201 (2010).
- [98] Thomas, L., Moriya, R., Rettner, C. & Parkin, S. S. P. Dynamics of Magnetic Domain Walls Under Their Own Inertia. *Science* **330**, 1810–1813 (2010).
- [99] Saitoh, E., Miyajima, H., Yamaoka, T. & Tatara, G. Current-induced resonance and mass determination of a single magnetic domain wall. *Nature* **432**, 203–206 (2004).
- [100] Chauleau, J.-Y., Weil, R., Thiaville, A. & Miltat, J. Magnetic domain walls displacement: Automotion versus spin-transfer torque. *Physical Review B* **82**, 214414 (2010).
- [101] Thiaville, A., Nakatani, Y., Piéchon, F., Miltat, J. & Ono, T. Transient domain wall displacement under spin-polarized current pulses. *The European Physical Journal B* **60**, 15–27 (2007).
- [102] Li, Z. & Zhang, S. Domain-wall dynamics driven by adiabatic spin-transfer torques. *Physical Review B* **70**, 024417 (2004).
- [103] Zhang, S. & Li, Z. Roles of Nonequilibrium Conduction Electrons on the Magnetization Dynamics of Ferromagnets. *Physical Review Letters* **93**, 127204 (2004).
- [104] Tatara, G. & Kohno, H. Theory of current-driven domain wall motion: Spin transfer versus momentum transfer. *Physical Review Letters* **92**, 086601 (2004).

- [105] Vanhaverbeke, A. & Viret, M. Simple model of current-induced spin torque in domain walls. *Physical Review B* **75**, 024411 (2007).
- [106] Ranieri, E. D. *et al.* Piezoelectric control of the mobility of a domain wall driven by adiabatic and non-adiabatic torques. *Nature Materials* **12**, 808–814 (2013).
- [107] Hartmann, U., Göddenhenrich, T. & Heiden, C. Magnetic force microscopy: Current status and future trends. *Journal of Magnetism and Magnetic Materials* **101**, 263–270 (1991).
- [108] Gross, I. *et al.* Real-space imaging of non-collinear antiferromagnetic order with a single-spin magnetometer. *Nature* **549**, 252–256 (2017).
- [109] Appel, P. *et al.* Nanomagnetism of Magnetoelectric Granular Thin-Film Antiferromagnets. *Nano Letters* **19**, 1682–1687 (2019).
- [110] Scheinfein, M. R., Unguris, J., Kelley, M. H., Pierce, D. T. & Celotta, R. J. Scanning electron microscopy with polarization analysis (SEMPA). *Review of Scientific Instruments* **61**, 2501 (1990).
- [111] McCord, J. Progress in magnetic domain observation by advanced magneto-optical microscopy. *Journal of Physics D: Applied Physics* **48**, 333001 (2015).
- [112] Mertins, H.-C. *et al.* Magneto-optical polarization spectroscopy with soft X-rays. *Applied Physics A* **80**, 1011–1020 (2005).
- [113] Scholl, A. *et al.* Observation of Antiferromagnetic Domains in Epitaxial Thin Films. *Science* **287**, 1014–1016 (2000).
- [114] Fiebig, M., Pavlov, V. V. & Pisarev, R. V. Second-harmonic generation as a tool for studying electronic and magnetic structures of crystals: review. *Journal of the Optical Society of America B* **22**, 96–118 (2005).
- [115] Bode, M. Spin-polarized scanning tunnelling microscopy. *Reports on Progress in Physics* **66**, 523–582 (2003).
- [116] Yang, R., Yang, H., Smith, A. R., Dick, A. & Neugebauer, J. Energy-dependent contrast in atomic-scale spin-polarized scanning tunneling microscopy of Mn_3N_2 (010): Experiment and first-principles theory. *Physical Review B* **74**, 115409 (2006).
- [117] Argyres, P. N. Theory of the Faraday and Kerr Effects in Ferromagnetics. *Physical Review* **97**, 334 (1955).
- [118] Zvezdin, A. K. & Kotov, V. A., *Modern magneto-optics and magneto-optical materials*. Studies in condensed matter physics (Institute of Physics Publishing, Bristol, 1997).
- [119] Tesařová, N. *et al.* Systematic study of magnetic linear dichroism and birefringence in (Ga,Mn)As. *Physical Review B* **89**, 085203 (2014).
- [120] Azzam, R. M. A. & Bashara, N. M. *Ellipsometry and polarized light* (North-Holland Publishing Company, Amsterdam, 1977).
- [121] Schäfer, R., Investigation of Domains and Dynamics of Domain Walls by the Magneto-optical Kerr-effect, in *Handbook of Magnetism and Advanced Magnetic Materials*, edited by H. Kronmüller & S. Parkin (John Wiley & Sons, 2007), Vol. 3.

- [122] Inoué, S. & Hyde, W. L. Studies on depolarization of light at microscope lens surfaces: II. The simultaneous realization of high resolution and high sensitivity with the polarizing microscope. *The Journal of Biophysical and Biochemical Cytology* **3**, 831–838 (1957).
- [123] Kirilyuk, A., Kimel, A. V. & Rasing, T. Ultrafast optical manipulation of magnetic order. *Reviews of Modern Physics* **82**, 2731 (2010).
- [124] *Semiconductor Spintronics and Quantum Computation*, Series NanoScience and Technology, edited by D. D. Awschalom, D. Loss, and N. Samarth (Springer, Berlin, 2002).
- [125] Ruzicka, B. A., Werake, L. K., Samassekou, H. & Zhao, H. Ambipolar diffusion of photoexcited carriers in bulk GaAs. *Applied Physics Letters* **97**, 262119 (2010).
- [126] Kumar, N. *et al.* Spatially resolved femtosecond pump-probe study of topological insulator Bi₂Se₃. *Physical Review B* **83**, 235306 (2011).
- [127] Li, J. *et al.* Magnetic imaging with femtosecond temporal resolution. *Review of Scientific Instruments* **80**, 073703 (2009).
- [128] Henn, T. *et al.* Ultrafast supercontinuum fiber-laser based pump-probe scanning magneto-optical Kerr effect microscope for the investigation of electron spin dynamics in semiconductors at cryogenic temperatures with picosecond time and micrometer spatial resolution. *Review of Scientific Instruments* **84**, 123903 (2013).
- [129] Tesařová, N. *et al.* Direct measurement of the three-dimensional magnetization vector trajectory in GaMnAs by a magneto-optical pump-and-probe method. *Applied Physics Letters* **100**, 102403 (2012).
- [130] Bauer, G. E. W., Saitoh, E. & van Wees, B. J. Spin caloritronics. *Nature Materials* **11**, 391–399 (2012).
- [131] Nagaosa, N., Sinova, J., Onoda, S., MacDonald, A. H. & Ong, N. P. Anomalous Hall effect. *Reviews of Modern Physics* **82**, 1539–1592 (2010).
- [132] Wunderlich, J. *Extraordinary Hall effect in multi-layered magnetic films: Application to the study of magnetization reversal dynamics*. Ph.D. thesis, Université Paris-Sud, Paris (2001).
- [133] Godinho, J. *et al.* Electrically induced and detected Néel vector reversal in a collinear antiferromagnet. *Nature Communications* **9**, 4686 (2018).
- [134] Krzysteczko, P., Hu, X., Liebing, N., Sievers, S. & Schumacher, H. W. Domain wall magneto-Seebeck effect. *Physical Review B* **92**, 140405(R) (2015).
- [135] Mizuguchi, M., Ohata, S., Uchida, K., Saitoh, E. & Takanashi, K. Anomalous Nernst Effect in an L1₀-Ordered Epitaxial FePt Thin Film. *Applied Physics Express* **5**, 093002 (2012).
- [136] Baumgaertl, K. *et al.* Magnetization reversal in individual Py and CoFeB nanotubes locally probed via anisotropic magnetoresistance and anomalous Nernst effect. *Applied Physics Letters* **108**, 132408 (2016).
- [137] Weiler, M. *et al.* Local Charge and Spin Currents in Magnetothermal Landscapes. *Physical Review Letters* **108**, 106602 (2012).

- [138] Ikhlas, M. *et al.* Large anomalous Nernst effect at room temperature in a chiral antiferromagnet. *Nature Physics* **13**, 1085–1090 (2017).
- [139] Böhnert, T., Vega, V., Michel, A.-K., Prida, V. M. & Nielsch, K. Magneto-thermopower and magnetoresistance of single Co-Ni alloy nanowires. *Applied Physics Letters* **103**, 092407 (2013).
- [140] Avery, A. D., Pufall, M. R. & Zink, B. L. Observation of the Planar Nernst Effect in Permalloy and Nickel Thin Films with In-Plane Thermal Gradients. *Physical Review Letters* **109**, 196602 (2012).
- [141] Ohno, H. *et al.* Electric-field control of ferromagnetism. *Nature* **408**, 944–946 (2000).
- [142] Koshihara, S. *et al.* Ferromagnetic Order Induced by Photogenerated Carriers in Magnetic III-V Semiconductor Heterostructures of (In,Mn)As/GaSb. *Physical Review Letters* **78**, 4617 (1997).
- [143] Ohno, H. *et al.* (Ga,Mn)As: A new diluted magnetic semiconductor based on GaAs. *Applied Physics Letters* **69**, 363–365 (1996).
- [144] MacDonald, A. H., Schiffer, P. & Samarth, N. Ferromagnetic semiconductors: moving beyond (Ga,Mn)As. *Nature Materials* **4**, 195–202 (2005).
- [145] Jungwirth, T. *et al.* Spin-dependent phenomena and device concepts explored in (Ga,Mn)As. *Reviews of Modern Physics* **86**, 855–896 (2014).
- [146] Kimel, A. V. *et al.* Observation of Giant Magnetic Linear Dichroism in (Ga, Mn)As. *Physical Review Letters* **94**, 227203 (2005).
- [147] Rushforth, A. W. *et al.* Molecular beam epitaxy grown (Ga,Mn)(As,P) with perpendicular to plane magnetic easy axis. *Journal of Applied Physics* **104**, 073908 (2008).
- [148] Jungwirth, T. *et al.* Systematic Study of Mn-Doping Trends in Optical Properties of (Ga,Mn)As. *Physical Review Letters* **105**, 227201 (2010).
- [149] Saidl, V. *et al.* Optical determination of the Néel vector in a CuMnAs thin-film antiferromagnet. *Nature Photonics* **11**, 91–96 (2017).
- [150] Nayak, A. K. *et al.* Large anomalous Hall effect driven by a nonvanishing Berry curvature in the noncollinear antiferromagnet Mn₃Ge. *Science Advances* **2**, e1501870 (2016).
- [151] Chen, H., Niu, Q. & MacDonald, A. H. Anomalous Hall Effect Arising from Noncollinear Antiferromagnetism. *Physical Review Letters* **112**, 017205 (2014).
- [152] Kübler, J. & Felser, C. Non-collinear antiferromagnets and the anomalous Hall effect. *Europhysics Letters* **108**, 67001 (2014).
- [153] Železný, J., Zhang, Y., Felser, C. & Yan, B. Spin-Polarized Current in Non-collinear Antiferromagnets. *Physical Review Letters* **119**, 187204 (2017).
- [154] Nakatsuji, S., Kiyohara, N. & Higo, T. Large anomalous Hall effect in a non-collinear antiferromagnet at room temperature. *Nature* **527**, 212–215 (2015).

- [155] Higo, T. *et al.* Large magneto-optical Kerr effect and imaging of magnetic octupole domains in an antiferromagnetic metal. *Nature Photonics* **12**, 73–78 (2018).
- [156] Liu, J. & Balents, L. Anomalous Hall Effect and Topological Defects in Antiferromagnetic Weyl Semimetals: $\text{Mn}_3\text{Sn}/\text{Ge}$. *Physical Review Letters* **119**, 087202 (2017).
- [157] Yang, H. *et al.* Topological Weyl semimetals in the chiral antiferromagnetic materials Mn_3Ge and Mn_3Sn . *New Journal of Physics* **19**, 015008 (2017).
- [158] Kuroda, K. *et al.* Evidence for magnetic Weyl fermions in a correlated metal. *Nature Materials* **16**, 1090–1095 (2017).
- [159] Manna, K., Sun, Y., Muechler, L., Kübler, J. & Felser, C. Heusler, Weyl and Berry. *Nature Reviews Materials* **3**, 244–256 (2018).
- [160] Markou, A. *et al.* Noncollinear antiferromagnetic Mn_3Sn films. *Physical Review Materials* **2**, 051001(R) (2018).
- [161] Tomiyoshi, S. & Yamaguchi, Y. Magnetic structure and weak ferromagnetism of Mn_3Sn studied by polarized neutron diffraction. *Journal of the Physical Society of Japan* **51**, 2478–2486 (1982).
- [162] Brown, P. J., Nunez, V., Tasset, F., Forsyth, J. B. & Radhakrishna, P. Determination of the magnetic structure of Mn_3Sn using generalized neutron polarization analysis. *Journal of Physics: Condensed Matter* **2**, 9409–9422 (1990).
- [163] Sticht, J., Höck, K.-H. & Kübler, J. Non-collinear itinerant magnetism: the case of Mn_3Sn . *Journal of Physics: Condensed Matter* **1**, 8155–8170 (1989).
- [164] Zhang, D. *et al.* First-principles study of the structural stability of cubic, tetragonal and hexagonal phases in Mn_3Z ($\text{Z} = \text{Ga}, \text{Sn}$ and Ge) Heusler compounds. *Journal of Physics: Condensed Matter* **25**, 206006 (2013).
- [165] Sung, N. H., Ronning, F., Thompson, J. D. & Bauer, E. D. Magnetic phase dependence of the anomalous Hall effect in Mn_3Sn single crystals. *Applied Physics Letters* **112**, 132406 (2018).
- [166] Nagamiya, T., Tomiyoshi, S. & Yamaguchi, Y. Triangular spin configuration and weak ferromagnetism of Mn_3Sn and Mn_3Ge . *Solid State Communications* **42**, 385–388 (1982).
- [167] Reichlova, H. *et al.* Imaging and writing magnetic domains in the non-collinear antiferromagnet Mn_3Sn . *Nature Communications* **10**, 5459 (2019).
- [168] Mündelein, J. & Schuster, H. U. Darstellung und Kristallstruktur der Verbindungen MnCuX ($\text{X} = \text{P}, \text{As}, \text{P}_x\text{As}_{1-x}$). *Zeitschrift für Naturforschung B* **47**, 925–928 (1992).
- [169] Máca, F. *et al.* Room-temperature antiferromagnetism in CuMnAs . *Journal of Magnetism and Magnetic Materials* **324**, 1606–1612 (2012).
- [170] Wadley, P. *et al.* Tetragonal phase of epitaxial room-temperature antiferromagnet CuMnAs . *Nature Communications* **4**, 2322 (2013).
- [171] Máca, F. *et al.* Physical properties of the tetragonal CuMnAs : A first-principles study. *Physical Review B* **96**, 094406 (2017).

- [172] Wadley, P. *et al.* Antiferromagnetic structure in tetragonal CuMnAs thin films. *Scientific Reports* **5**, 17079 (2015).
- [173] Wadley, P. *et al.* Current polarity-dependent manipulation of antiferromagnetic domains. *Nature Nanotechnology* **13**, 362–365 (2018).
- [174] Saidl, V. *Ultrarychlá laserová spektroskopie antiferomagnetů*. Ph.D. thesis, Charles University, Prague (2018).
- [175] Wadley, P. *et al.* Control of antiferromagnetic spin axis orientation in bilayer Fe/CuMnAs films. *Scientific Reports* **7**, 11147 (2017).
- [176] Mozooni, B., von Hofe, T. & McCord, J. Picosecond wide-field magneto-optical imaging of magnetization dynamics of amorphous film elements. *Physical Review B* **90**, 054410 (2014).
- [177] Butkovičová, D. *et al.* Critical role of the sample preparation in experiments using piezoelectric actuators inducing uniaxial or biaxial strains. *Review of Scientific Instruments* **84**, 103902 (2013).
- [178] Janda, T. *et al.* Voigt effect-based wide-field magneto-optical microscope integrated in a pump-probe experimental setup. *Review of Scientific Instruments* **89**, 073703 (2018).
- [179] Nádvořník, L. *et al.* Long-range and high-speed electronic spin-transport at a GaAs/AlGaAs semiconductor interface. *Scientific Reports* **6**, 22901 (2016).
- [180] Surynek, M., Nadvornik, L., Schmoranzero, E. & Nemeč, P. Quasi-nondegenerate pump-probe magneto-optical experiment in GaAs/AlGaAs heterostructure based on spectral filtration. *arXiv e-prints* 2004.03311 (2020). URL <https://arxiv.org/abs/2004.03311>.
- [181] Wang, J. *et al.* Ultrafast magneto-optics in ferromagnetic III–V semiconductors. *Journal of Physics: Condensed Matter* **18**, R501–R530 (2006).
- [182] Tesařová, N. *et al.* High precision magnetic linear dichroism measurements in (Ga,Mn)As. *Review of Scientific Instruments* **83**, 123108 (2012).
- [183] Astakhov, G. V. *et al.* Magnetization manipulation in (Ga,Mn)As by subpicosecond optical excitation. *Applied Physics Letters* **86**, 152506 (2005).
- [184] Sapozhnik, A. A. *et al.* Manipulation of antiferromagnetic domain distribution in Mn₂Au by ultrahigh magnetic fields and by strain. *Physica Status Solidi RRL* **11**, 1600438 (2017).
- [185] Crooker, S. A. & Smith, D. L. Imaging Spin Flows in Semiconductors Subject to Electric, Magnetic, and Strain Fields. *Physical Review Letters* **94**, 236601 (2005).
- [186] Kato, Y., Myers, R. C., Gossard, A. C. & Awschalom, D. D. Coherent spin manipulation without magnetic fields in strained semiconductors. *Nature* **427**, 50–53 (2004).
- [187] Shayegan, M., Karrai, K., Shkolnikov, Y. P., Vakili, K. & Poortere, E. P. D. Low-temperature, in situ tunable, uniaxial stress measurements in semiconductors using a piezoelectric actuator. *Applied Physics Letters* **83**, 5235 (2003).
- [188] Gomonay, H. V. & Loktev, V. M. Shape-induced phenomena in finite-size antiferromagnets. *Physical Review B* **75**, 174439 (2007).

- [189] Vogel, J. *et al.* Direct Observation of Massless Domain Wall Dynamics in Nanostripes with Perpendicular Magnetic Anisotropy. *Physical Review Letters* **108**, 247202 (2012).
- [190] Ramsay, A. J. *et al.* Optical Spin-Transfer-Torque-Driven Domain-Wall Motion in a Ferromagnetic Semiconductor. *Physical Review Letters* **114**, 067202 (2015).
- [191] Janda, T. *et al.* Inertial displacement of a domain wall excited by ultra-short circularly polarized laser pulses. *Nature Communications* **8**, 15226 (2017).
- [192] Adam, J.-P. *et al.* Nonadiabatic spin-transfer torque in (Ga,Mn)As with perpendicular anisotropy. *Physical Review B* **80**, 193204 (2009).
- [193] Yamanouchi, M., Chiba, D., Matsukura, F. & Ohno, H. Current-induced domain-wall switching in a ferromagnetic semiconductor structure. *Nature* **428**, 539–542 (2004).
- [194] Grzybowski, M. J. *et al.* Imaging Current-Induced Switching of Antiferromagnetic Domains in CuMnAs. *Physical Review Letters* **118**, 057701 (2017).
- [195] Bodnar, S. Y. *et al.* Imaging of current induced Néel vector switching in antiferromagnetic Mn₂Au. *Physical Review B* **99**, 140409(R) (2019).
- [196] Auston, D. H. Picosecond optoelectronic switching and gating in silicon. *Applied Physics Letters* **26**, 101 (1975).
- [197] Auston, D. H., in *Picosecond Optoelectronic Devices*, edited by C. H. Lee (Academic, London, 1984), p. 73.
- [198] Buess, M., Knowles, T. P. J., Ramsperger, U., Pescia, D. & Back, C. H. Phase-resolved pulsed precessional motion at a Schottky barrier. *Physical Review B* **69**, 174422 (2004).
- [199] Yuan, H. *et al.* Photoinduced Spin Precession in Fe/GaAs(001) Heterostructure with Low Power Excitation. *Applied Physics Express* **6**, 073008 (2013).
- [200] Carruthers, T. F. & Weller, J. F. Picosecond optical mixing in fast photodetectors. *Applied Physics Letters* **48**, 460 (1986).
- [201] Jacobsen, R. H., Birkelund, K., Holst, T., Jepsen, P. U. & Keiding, S. R. Interpretation of photocurrent correlation measurements used for ultrafast photoconductive switch characterization. *Journal of Applied Physics* **79**, 2649 (1996).
- [202] Wang, Z. *et al.* Spin dynamics triggered by subterahertz magnetic field pulses. *Journal of Applied Physics* **103**, 123905 (2008).
- [203] Brorson, S. D., Zhang, J. & Keiding, S. R. Ultrafast carrier trapping and slow recombination in ion-bombarded silicon on sapphire measured via THz spectroscopy. *Applied Physics Letters* **64**, 2385 (1994).
- [204] Hoof, C. V., Deneffe, K., Boeck, J. D., Arent, D. J. & Borghs, G. Franz-Keldysh oscillations originating from a well-controlled electric field in the GaAs depletion region. *Applied Physics Letters* **54**, 608 (1989).
- [205] Airaksinen, V. M. & Lipsanen, H. K. Photorefectance study of photovoltage effects in GaAs diode structures. *Applied Physics Letters* **60**, 2110 (1992).

- [206] Kleiner, W. H. Space-Time Symmetry of Transport Coefficients. *Physical Review* **142**, 318–326 (1966).
- [207] Šmejkal, L., González-Hernández, R., Jungwirth, T. & Sinova, J. Crystal Hall effect in collinear antiferromagnets. *arXiv e-prints* 1901.00445 (2019). URL <https://arxiv.org/abs/1901.00445>.
- [208] Pfitzner, E. *et al.* Near-field magneto-caloritronic nanoscopy on ferromagnetic nanostructures. *AIP Advances* **8**, 125329 (2018).
- [209] Woessner, A. *et al.* Near-field photocurrent nanoscopy on bare and encapsulated graphene. *Nature Communications* **7**, 10783 (2016).
- [210] Mastel, S. *et al.* Understanding the Image Contrast of Material Boundaries in IR Nanoscopy Reaching 5 nm Spatial Resolution. *ACS Photonics* **5**, 3372–3378 (2018).
- [211] Higo, T. *et al.* Anomalous Hall effect in thin films of the Weyl antiferromagnet Mn_3Sn . *Applied Physics Letters* **113**, 202402 (2018).
- [212] You, Y. *et al.* Anomalous Hall Effect-Like Behavior with In-Plane Magnetic Field in Noncollinear Antiferromagnetic Mn_3Sn Films. *Advanced Electronic Materials* **5**, 1800818 (2019).
- [213] Bisson, W. G. & Wills, A. S. Anisotropy-driven spin glass transition in the kagome antiferromagnet hydronium jarosite, $(\text{H}_3\text{O})\text{Fe}_3(\text{SO}_4)_2(\text{OH})_6$. *Journal of Physics: Condensed Matter* **20**, 452204 (2008).
- [214] Reichlova, H. *et al.* Large anomalous Nernst effect in thin films of the Weyl semimetal Co_2MnGa . *Applied Physics Letters* **113**, 212405 (2018).
- [215] Gregg, J. F. *et al.* Giant Magnetoresistive Effects in a Single Element Magnetic Thin Film. *Physical Review Letters* **77**, 1580–1583 (1996).
- [216] Mei, A. B. *et al.* Local Photothermal Control of Phase Transitions for On-demand Room-temperature Rewritable Magnetic Patterning. *arXiv e-prints* 1906.07239 (2019). URL <https://arxiv.org/abs/1906.07239>.
- [217] Singh, U., Echtenkamp, W., Street, M., Binek, C. & Adenwalla, S. Local Writing of Exchange Biased Domains in a Heterostructure of Co/Pd Pinned by Magneto-electric Chromia. *Advanced Functional Materials* **26**, 7470–7478 (2016).
- [218] Balk, A. L. *et al.* Comparing the anomalous Hall effect and the magneto-optical Kerr effect through antiferromagnetic phase transitions in Mn_3Sn . *Applied Physics Letters* **114**, 032401 (2019).
- [219] Golovashkin, A. I. & Motulevich, G. P. Optical and electrical properties of tin. *Journal of Experimental and Theoretical Physics* **19**, 310–317 (1964).
- [220] Johnson, P. B. & Christy, R. W. Optical constants of transition metals: Ti, V, Cr, Mn, Fe, Co, Ni, and Pd. *Physical Review B* **9**, 5056–5070 (1974).
- [221] Chiang, C., Huang, S., Qu, D., Wu, P. & Chien, C. Absence of Evidence of Electrical Switching of the Antiferromagnetic Néel Vector. *Physical Review Letters* **123**, 227203 (2019).

- [222] Zhang, P., Finley, J., Safi, T. & Liu, L. Quantitative Study on Current-Induced Effect in an Antiferromagnet Insulator/Pt Bilayer Film. *Physical Review Letters* **123**, 247206 (2019).
- [223] Churikova, A. *et al.* Non-magnetic origin of spin Hall magnetoresistance-like signals in Pt films and epitaxial NiO/Pt bilayers. *Applied Physics Letters* **116**, 022410 (2020).
- [224] Baldrati, L. *et al.* Mechanism of Néel Order Switching in Antiferromagnetic Thin Films Revealed by Magnetotransport and Direct Imaging. *Physical Review Letters* **123**, 177201 (2019).
- [225] Degen, C. L. Scanning magnetic field microscope with a diamond single-spin sensor. *Applied Physics Letters* **92**, 243111 (2008).
- [226] Wörnle, M. S. *et al.* Current-induced fragmentation of antiferromagnetic domains. *arXiv e-prints* 1912.05287 (2019). URL <https://arxiv.org/abs/1912.05287>.
- [227] Kašpar, Z. *et al.* High electrical and optical resistive switching in a thin-film antiferromagnet. *arXiv e-prints* 1909.09071 (2019). URL <https://arxiv.org/abs/1909.09071>.
- [228] Janda, T. *et al.* Magneto-Seebeck microscopy of domain switching in collinear antiferromagnet CuMnAs. *arXiv e-prints* 2004.05460 (2020). URL <https://arxiv.org/abs/2004.05460>.
- [229] Wang, M. *et al.* Spin flop and crystalline anisotropic magnetoresistance in CuMnAs. *Physical Review B* **101**, 094429 (2020).
- [230] Surýnek, M. *et al.* Investigation of magnetic anisotropy and heat dissipation in thin films of compensated antiferromagnet CuMnAs by pump–probe experiment. *Journal of Applied Physics* **127**, 233904 (2020).
- [231] Tserkovnyak, Y., Brataas, A. & Bauer, G. E. Theory of current-driven magnetization dynamics in inhomogeneous ferromagnets. *Journal of Magnetism and Magnetic Materials* **320**, 1282–1292 (2008).
- [232] Wang, K.-Y. *et al.* Spin Reorientation Transition in Single-Domain (Ga, Mn)As. *Physical Review Letters* **95**, 217204 (2005).
- [233] McPhail, S. *et al.* Interface bonding versus strain-induced magnetic anisotropy in epitaxial Fe/semiconductor structures. *Physical Review B* **67**, 024409 (2003).
- [234] Thiaville, A., Belliard, L., Majer, D., Zeldov, E. & Miltat, J. Measurement of the stray field emanating from magnetic force microscope tips by Hall effect microsensors. *Journal of Applied Physics* **82**, 3182 (1997).

List of Figures

1.1	Temperature dependence of spontaneous magnetization	12
1.2	Magnetic susceptibilities of different magnetic materials	13
1.3	Relations between magnetization and magnetic fields	17
1.4	Formation of magnetic domain structure	21
1.5	Internal structure of magnetic domain walls	22
2.1	Stoner-Wolfarth model of magnetization switching	29
2.2	Effect of defects on magnetization switching	30
2.3	Physics of the spin transfer torque	32
2.4	Staggered and non-staggered fields in AFs	33
2.5	Optical orientation and OSTT in GaMnAs	35
2.6	Effective SO-fields and current-induced spin polarization	37
2.7	Spin-orbit torques in antiferromagnets	40
2.8	Field-induced DW motion	43
2.9	Current-induced DW motion	47
3.1	Magneto-optical effects in reflection geometry	52
3.2	Wide-field MO microscope	55
3.3	The Hall effects and anisotropic magnetoresistance	59
4.1	Crystal structure and ferromagnetism of (Ga,Mn)As and (Ga,Mn)(As,P)	64
4.2	Crystal and magnetic structures of Mn ₃ Sn	66
4.3	Crystal structure and electrical switching of CuMnAs	68
5.1	Pump-probe experimental setup with a high spatial resolution combined with a wide-field MO microscope	71
5.2	Magneto-optical properties of the test (Ga,Mn)As sample	75
5.3	Imaging of the sample around surface imperfections	77
5.4	Visualization of magnetic inhomogeneity of the (Ga,Mn)As sample at- tached to a piezoelectric transducer	78
5.5	Comparison of the magnetization switching and dynamics observed in regions A and B depicted in Fig. 5.4(a)	79
6.1	OSTT-driven domain wall motion - basic idea and device geometry . . .	84
6.2	Soap-bubble-like domain wall expansion	86
6.3	Elastic response of a geometrically pinned DW	87
6.4	Laser-induced helicity-dependent DW depinning	89
6.5	Helicity-dependent DW depinning at inverted domain configuration . . .	91
6.6	Spectral dependence of the DW depinning field	93
6.7	MCD-induced temperature variations	94
7.1	Photo-generation of current pulses in Fe/GaAs diode structure	99
7.2	Characterization of ultrashort photocurrent pulses	101
7.3	Magnetization dynamics induced by the vertical current pulse	105
7.4	Magnetization dynamics induced by the lateral current pulse	106
7.5	The effect of external magnetic field	107
7.6	Characterization of PIN/CuMnAs photodiode	109
8.1	Spin order of Mn ₃ Sn and the imaging technique	115
8.2	Effect of temperature on magnetic switching	117

8.3	Magnetic field-induced reversal of Mn_3Sn domain structure	118
8.4	Temperature dependence of the ANE response	120
8.5	Heat-assisted writing of domains	121
8.6	Insensitivity of written domains to large magnetic fields	122
9.1	Basic working principle and verification of the imaging method	127
9.2	Correlation between domain pattern and resistance variations due to current-pulse excitation	129
9.3	Reversible and reproducible current-induced domain switching	131
9.4	Current pulse-induced domain shattering	132
9.5	Transverse magneto-Seebeck effect in uniaxial CuMnAs films	134
D.1	Magnetic characterization of the Fe/GaAs epilayer	169
E.1	Magnetic energy density in unstrained and strained $(\text{Ga},\text{Mn})\text{As}$ sample	171
F.1	Bubble-like DW propagation in crossbar structure	173
F.2	Sensitivity distribution function and AHE response to a DW propagating through a Hall cross	174

List of Abbreviations

Eq(s).	equation(s)
Fig(s).	figure(s)
Ref(s).	reference(s)
1D, 2D, 3D	one/two/three dimensional
AF, AF(s)	antiferromagnetic, antiferromagnet(s)
AFMR	antiferromagnetic resonance
AHE	anomalous Hall effect
AMR	anisotropic magnetoresistance
AMSE	anisotropic magneto-Seebeck effect
ANE	anomalous Nernst effect
bcc	body-centered cubic
BIA	bulk inversion asymmetry
CB	conduction band
CCD	charge-coupled device
CMOS	complementary metal-oxide-semiconductor
CW	continuous-wave (laser)
DMS	diluted magnetic semiconductor
DW	domain wall
EA	easy axis
FKE	Franz-Keldysh effect
FM, FM(s)	ferromagnetic, ferromagnet(s)
FMR	ferromagnetic resonance
FWHM	full width at half maximum
GMR	giant magnetoresistance
HH	heavy hole
HM	heavy metal
HWP	half-wave plate
I	insulator (in heterostructures)
ISGE	inverse spin galvanic effect
LED	light-emitting diode
LH	light hole
LLG	Landau-Lifshitz-Gilbert (equation)
LP(s)	laser pulse(s)
LSR	laser speckle reducer
MA	magnetic anisotropy
MCD	magnetic circular dichroism
ML	monolayer
MLD	magnetic linear dichroism
MO	magneto-optical
MOKE	magneto-optical Kerr effect
NIR	near infrared
NM	nonmagnetic (normal) metal
NSOT	Néel spin-orbit torque
NV	nitrogen vacancy
OHE	ordinary Hall effect
ONE	ordinary Nernst effect
OSOT	optical spin-orbit torque

OSTT	optical spin transfer torque
(P)BS	(polarizing) beamsplitter
PEEM	photoemission electron microscopy
PIN	p-doped/intrinsic/n-doped (semiconductor heterostructure)
PKE	polar Kerr effect
PM	paramagnet, paramagnetic
PT	parity-time (symmetry)
PZT	piezoelectric transducer
QWP	quarter-wave plate
RC	resistance-capacity (time-constant)
RKKY	Ruderman-Kittel-Kasuya-Yosida (interaction)
SHE	spin Hall effect
SIA	structural inversion asymmetry
SO	spin-orbit, spin-orbit split-off (band)
SOC	spin-orbit coupling
SOT	spin-orbit torque
SQUID	superconducting quantum interference device
STT	spin transfer torque
TMR	tunneling magnetoresistance
VE	Voigt effect
VI	voltage-current (characteristics)
WB	Walker breakdown
XMLD	X-ray magnetic linear dichroism

List of Symbols

Constants

c	speed of light
e	absolute value of electron charge
ε_0	electrical permittivity of vacuum
h, \hbar	Planck constant, reduced Planck constant
i	complex unit
k_B	Boltzman constant
m_e	electron mass
μ_0	magnetic permeability of vacuum
μ_B	Bohr magneton
σ	vector of Pauli matrices

Selected quantities

\mathbf{A}	vector potential
A	exchange stiffness constant
a_0	lattice constant
α	Gilbert damping constant
α_R	Rashba spin-orbit coupling constant
α_{SH}	spin-Hall angle
\mathbf{B}	magnetic field (magnetic flux density)
B_A, B_R	applied magnetic field, virtual restoring field
B_{PR}, B_{DP}	DW propagation and depinning fields
$\mathbf{B}_{SO}, (\mathbf{B}_R, \mathbf{B}_D)$	effective spin-orbit field, (Rashba, Dresselhaus)
\mathcal{B}_J	Brillouin function
b_j	adiabatic STT amplitude
β	relative strength of non-adiabatic STT
β_D	Dresselhaus spin-orbit coupling constant
C	Curie constant
C_{MO}	magneto-optical contrast
c_j	non-adiabatic STT amplitude
D	dipole operator
\mathcal{D}	density of states
δ_{DW}	domain wall width
Δ_{SO}	spin-orbit split-off energy
\mathbf{e}	unit vector
ϵ	volume energy density
ε	electric permittivity
ε_{eff}	effective permittivity
$E, (E_F, E_g)$	energy, (Fermi energy, bandgap energy)
\mathbf{E}	electric field
f	frequency
F	free energy
ϕ	scalar electric potential or azimuthal angle
φ_{CF}	crystal-field potential
$g, (g_L)$	magnetic g-factor, (Landé g-factor)
\mathbf{g}	Hall pseudovector

γ	gyromagnetic ratio
\mathbf{H}	auxiliary magnetic field (magnetic field strength)
H_a, H_a^{eff}	anisotropy field, effective anisotropy field
H_c, H_u, H_S	cubic, uniaxial, and strain-induced anisotropy field
H_{out}	out-of-plane anisotropy field
$\mathbf{H}_d, \mathbf{H}_{ext}$	demagnetizing field, external magnetic field
$\mathbf{H}_{ex}, \mathbf{H}_{eff}$	exchange field, effective magnetic field
H_c	coercive field
\hat{H}	Hamiltonian operator
χ	magnetic susceptibility
I	light intensity
I, I_{ph}	electrical current, photocurrent
\mathcal{I}	Stoner exchange parameter
\mathbf{j}, \mathbf{j}_c	charge current density
\mathbf{j}_H	Hall current density
\mathbf{j}_s	spin current density
\mathbf{j}_Q	heat current density
\mathcal{J}	exchange integral
$\hat{\mathbf{j}}, \hat{\mathbf{J}}$	total angular momentum operator
J, j, m_J, m_j	quantum numbers of total angular momentum and its projection
\mathbf{k}	wavevector
k_F	Fermi wavevector
$K_a, (K_c, K_u)$	anisotropy constant, (cubic, uniaxial)
K_d	demagnetizing (shape anisotropy) constant
ξ	angular separation of easy axes
$\hat{\mathbf{l}}, \hat{\mathbf{L}}$	orbital angular momentum operator
L, l, m_L, m_l	quantum numbers of orbital angular momentum and its projection
\mathbf{L}	Néel (antiferromagnetic) vector
λ	light wavelength
\mathbf{m}	magnetic moment
$\mathbf{M}, (M_s, M_0)$	magnetization, (spontaneous magnetization, saturation magnetization)
m_0	saturated magnetic moment
m^*	effective domain wall mass
m_e^*	effective electron mass
μ	magnetic permeability
n	spatial density of magnetic moments
n	index of refraction
\mathbf{n}	sample normal
$n_{\uparrow, \downarrow}$	spin-resolved electron density
\mathcal{N}	demagnetizing tensor
$N_{x,y,z}$	demagnetizing factors
n_W, n_S	Weiss and Stoner factors (molecular field theory)
ω	angular frequency
Ω	Larmor (precession) frequency
$\hat{\mathbf{p}}$	momentum operator
P	spin current polarization
P_s	spin polarization
P^{VE}	Voigt effect magnitude
\mathcal{P}	optical injection rate
Π	Peltier coefficient
Ψ, ψ, Φ, ϕ	wavefunctions
ψ_K, ψ_V	Kerr and Voigt polarization ellipticity

q	electric charge
\mathbf{Q}	spin current density
\mathbf{r}, r	position vector, radial coordinate
r	complex optical reflection amplitude
r_{SN}	signal-to-noise ratio
R	electrical resistance or optical reflectivity
$R_{\uparrow,\downarrow}$	spin-resolved reflection amplitude of electron wavefunction
R_0, R_A	ordinary and anomalous Hall coefficients
ρ, ρ_m	charge density, magnetic charge density
ρ	electrical resistivity
ρ_H	Hall resistivity
$\sigma, (\sigma_{DW})$	surface energy density, (domain wall energy density)
σ, σ_H	electrical conductivity, Hall conductivity
$\sigma^+, \sigma^-, \sigma^0$	circular left, right, and linear light polarization
$\hat{\mathbf{s}}, \hat{\mathbf{S}}$	spin operator
S, s, m_S, m_s	quantum numbers of spin and its projection
S	Seebeck coefficient
\mathbf{s}	spin density
$\delta\mathbf{s}$	non-equilibrium spin density
θ	polar angle
θ_K, θ_V	Kerr and Voigt polarization rotation
t	time
Δt	time delay in a pump-probe experiment
\mathbf{T}	torque
$T, (T_C, T_N)$	temperature, (Curie temperature, Néel temperature)
τ	carrier spin lifetime
τ_{ex}	precession time in exchange field
τ_p	electrical pulse decay time
τ_{sf}	spin-flip relaxation time
\mathbf{v}	velocity
V	volume or voltage
w	width of a bar device
Y_l^m	spherical harmonic function
$ \uparrow\rangle, \downarrow\rangle$	spin-up and spin-down eigenstates
∇	gradient operator
Δ	Laplace operator or difference

List of publications

Publications related to the results presented in this thesis

1. T. Janda, J. Godinho, T. Ostatnický, E. Pfitzner, G. Ulrich, A. Hoehl, S. Reimers, Z. Šobáň, T. Metzger, H. Reichlová, V. Novák, R. P. Campion, J. Heberle, P. Wadley, K. W. Edmonds, O. J. Amin, J. S. Chauhan, S. S. Dhesi, F. Maccherozzi, R. M. Otxoa, P. E. Roy, K. Olejník, P. Němec, T. Jungwirth, B. Kaestner, and J. Wunderlich. Magneto-Seebeck microscopy of domain switching in collinear antiferromagnet CuMnAs. *accepted in Physical Review Materials*.
2. H. Reichlova, T. Janda, J. Godinho, A. Markou, D. Kriegner, R. Schlitz, J. Zelezny, Z. Soban, M. Bejarano, H. Schultheiss, P. Nemeč, T. Jungwirth, C. Felser, J. Wunderlich, and S. T. B. Goennenwein. Imaging and writing magnetic domains in the non-collinear antiferromagnet Mn₃Sn. *Nature Communications* **10**, 5459 (2019).
3. T. Janda, L. Nádvorník, J. Kuchařík, D. Butkovičová, E. Schmoranzarová, F. Trojánek, and P. Němec. Voigt effect-based wide-field magneto-optical microscope integrated in a pump-probe experimental setup. *Review of Scientific Instruments* **89**, 073703 (2018).
4. T. Janda, P. E. Roy, R. M. Otxoa, Z. Šobáň, A. Ramsay, A. C. Irvine, F. Trojánek, M. Surýnek, R. P. Campion, B. L. Gallagher, P. Němec, T. Jungwirth, and J. Wunderlich. Inertial displacement of a domain wall excited by ultra-short circularly polarized laser pulses. *Nature Communications* **8**, 15226 (2017).
5. A. J. Ramsay, P. E. Roy, J. A. Haigh, R. M. Otxoa, A. C. Irvine, T. Janda, R. P. Campion, B. L. Gallagher, and J. Wunderlich. Optical Spin-Transfer-Torque-Driven Domain-Wall Motion in a Ferromagnetic Semiconductor. *Physical Review Letters* **114**, 067202 (2015).

Other publications

6. P. Krzysteczko, J. Wells, A. F. Scarioni, Z. Soban, T. Janda, X. Hu, V. Saidl, R. P. Campion, R. Mansell, J.-H. Lee, R. P. Cowburn, P. Nemeč, O. Kazakova, J. Wunderlich, and H. W. Schumacher. Nanoscale thermoelectrical detection of magnetic domain wall propagation. *Physical Review B* **95**, 220410(R) (2017).
7. L. Nádvorník, P. Němec, T. Janda, K. Olejník, V. Novák, V. Skoromets, H. Němec, P. Kužel, F. Trojánek, T. Jungwirth, and J. Wunderlich. Long-range and high-speed electronic spin-transport at a GaAs/AlGaAs semiconductor interface. *Scientific Reports* **6**, 22901 (2016).
8. L. Nádvorník, K. Olejník, P. Němec, V. Novák, T. Janda, J. Wunderlich, F. Trojánek, and T. Jungwirth. Enhancement of the spin Hall voltage in a reverse-biased planar p-n junction. *Physical Review B* **94**, 075306 (2016).
9. V. Saidl, M. Brajer, L. Horák, H. Reichlová, K. Výborný, M. Veis, T. Janda, F. Trojánek, M. Maryško, I. Fina, X. Marti, T. Jungwirth, and P. Němec. Investigation of magneto-structural phase transition in FeRh by reflectivity and transmittance measurements in visible and near-infrared spectral region. *New Journal of Physics* **18**, 083017 (2016).

10. I. Matulková, H. Solařová, P. Štěpnička, I. Císařová, T. Janda, P. Němec, and I. Němec. (2-Azoniaethyl)guanidinium dichloride – A promising phase-matchable NLO material employing a simple hydrogen bond acceptor in its structure. *Optical Materials* **42**, 39–46 (2015).
11. P. Němec, E. Rozkotová, N. Tesařová, T. Janda, D. Butkovičová, F. Trojánek, P. Malý, V. Novák, J. Zemen, K. Olejník, and T. Jungwirth. Experimental observations of optical spin transfer and spin-orbit torques in magnetic semiconductors. *Ultrafast Magnetism I*, Springer Proceedings in Physics **159**, J.-Y. Bigot et al. (eds.), pages 16–18 (Springer, Cham, 2014).
12. E. Schmoranzarová, N. Tesařová, T. Janda, D. Butkovičová, F. Trojánek, P. Malý, V. Novák, K. Olejník, T. Jungwirth, and P. Němec. Probing of Spin Wave Resonances in (Ga,Mn)As by Time-Resolved Magneto-Optical Technique. *IEEE Transactions on Magnetism* **50**, 2401604 (2014).
13. N. Tesařová, P. Němec, E. Rozkotová, J. Zemen, T. Janda, D. Butkovičová, F. Trojánek, K. Olejník, V. Novák, P. Malý, and T. Jungwirth. Experimental observation of the optical spin-orbit torque. *Nature Photonics* **7**, 492-498 (2013).

Appendices

A From single electron to solid

The starting point is the hydrogen-like atom [18], i.e., a configuration where a single electron moves in the central-symmetric electrical potential of a nucleus having Z protons and a charge of $q = Ze$. The stationary electron states are the eigenstates of Hamiltonian $\hat{H}_H = -\frac{\hbar^2}{2m_e}\Delta - \frac{1}{4\pi\epsilon_0}\frac{Ze^2}{r}$ having in spherical coordinates the form $\psi_{nlm} = R_{nl}(r)Y_{lm}(\theta, \varphi)$, where R_{nl} are central-symmetric functions and Y_{lm} are spherical harmonics specified by the quantum numbers n , l , and m . In central-symmetric potential \hat{L} is a constant of motion and \hat{H} , \hat{L}^2 , and \hat{L}_z all commute. Consequently, Y_{lm} are also eigenfunctions of \hat{L}^2 and \hat{L}_z and we can ascribe each electron state ψ_{nlm} a specific value of the orbital angular momentum: $\hat{L}^2 = \hbar^2 l(l+1)$ with $l = 0, 1, \dots, n-1$, and $\hat{L}_z = \hbar m$ with $m = 0, \pm 1, \dots, \pm l$. Here we have chosen z -axis as the quantization direction. The principal quantum number $n \in \mathbb{N}$ specifies the energy $E_n = -1\text{Ry}\frac{Z^2}{n^2}$, where $1\text{Ry} \approx 13.6\text{eV}$. Each state ψ_{nlm} has a specific spatial distribution of electronic charge $\rho(\mathbf{r}) = e|\psi_{nlm}(\mathbf{r})|^2$, known as an orbital. The orbitals are named as nx_m , where $x = s, p, d, f$ stands for $l = 0, 1, 2, 3$. At the energy level n there are n^2 orbitals and each orbital can accommodate two electrons with opposite spin. This additional degree of freedom is described by fourth quantum number $m_s = \pm 1/2$.

The situation in real atoms with many electrons is considerably more complicated. Despite the large number of electrons the total atomic magnetic moments are of similar size as that of a single electron. This can be roughly understood in terms of energy minimization when filling the single-electron states described above. Filling only the states with one particular spin orientation would require occupying higher energy levels to accommodate all electrons.

The single-electron states are no longer the eigenstates of many-electron atom. We have to take into account the additional Coulomb repulsion between the electrons [19]. The Hamiltonian becomes $\hat{H}_0 = \sum_i \hat{H}_{Hi} + \sum_{i < j} e^2/4\pi\epsilon_0|r_i - r_j|$, where the first sum represents the kinetic and potential energy of each individual electron in the central potential of the nucleus and the second sum accounts for all the electron-electron Coulomb interactions. Such system is too complex to solve analytically. Instead, an approximation is used in which each electron is assumed to move in a central potential created by the nucleus and the other electrons. The total wavefunction of the system is constructed from the single-electron functions which are varied in an iterative process in order to minimize the energy of the system. This is known as the Hartree-Fock method. The potentials experienced by electrons are not simple Coulomb wells anymore and, consequently, the degeneracy of energy of the states with the same principal quantum number n but different orbital number l is lifted.

The central-symmetric potential considered above is only an approximation. The residual angular part of the Coulomb interaction between the electrons leads to the coupling of all individual orbital and spin angular momenta giving rise to the total orbital and spin angular momenta $\hat{\mathbf{L}} = \sum \hat{\mathbf{L}}_i$ and $\hat{\mathbf{S}} = \sum \hat{\mathbf{S}}_i$ where only the partially filled electron shells contribute [19]. Consequently, the states available for given n and l group to several terms X_J ($X = S, P, D, F$ for $L = 0, 1, 2, 3$) described by the new quantum numbers L and S ($m_L = \sum m_{L_i} = -L, -L+1, \dots, L$ and $m_S = \sum m_{S_i} = -S, -S+1, \dots, S$). The energy splitting between the terms is of the order of 1 eV.

Adding the spin-orbit coupling $\hat{H}_{SO} \sim \hat{\mathbf{L}} \cdot \hat{\mathbf{S}}$ between the total spin and orbital angular momenta then splits the terms into multiplets $^{2S+1}X_J$ [19] described also by the additional quantum number J of total angular momentum $\hat{\mathbf{J}} = \hat{\mathbf{L}} + \hat{\mathbf{S}}$, where

$|L - S| \leq J \leq L + S$. The SOC-induced energy splitting $\Delta E_{SO} \lesssim 0.1$ eV for most of the $3d$ ions. The lowest-energy multiplet is determined by Hund's rules. For example, for manganese, which is present in several materials studied in this thesis, the ground state of Mn^{2+} ion is ${}^6S_{5/2}$ with the corresponding magnetic moment of $5\mu_B$.

The final step is to bring the atoms together to create a solid where the atomic states are influenced by the electrostatic interaction with the neighboring atoms. The effect of the surrounding charge is described by the *crystal-field* potential $\varphi_{CF}(\mathbf{r})$ acting on the electronic charge distribution $\rho_0(\mathbf{r})$ of the magnetic atom with the interaction Hamiltonian $\hat{H}_{CF} = \int \rho_0(\mathbf{r})\varphi_{CF}(\mathbf{r})d^3r$ [19]. Obviously, the crystal field has the largest effect on the surface electron shells which are directly exposed to the surrounding charge. If these outer electrons are responsible for the atomic magnetic moments, as it is in the case of $3d$ transition-metal elements, the character of magnetism can be very different depending on the crystal environment. In this case the crystal-field effect is stronger than the spin-orbit coupling and has to be taken into account first. The description of magnetism then depends on whether the electrons responsible for magnetic moments are localized or delocalized. The former is the case for the insulating ionic compounds such as Fe_2O_3 whereas the latter applies for metals.

In conclusion, the additional interactions lead to an intraatomic coupling of electronic angular momenta and the total atomic magnetic moments are described by quantum numbers J, m_J . In magnetic metals the magnetic moments are carried by delocalized electrons. In magnetism we are concerned with the energy scales comparable to the thermal energy. At ambient temperature ($k_B T \approx 25$ meV) electrons usually occupy only the ground state of $\hat{H}_0 + \hat{H}_{CF}$ and its sublevels resulting from the interactions with electric (\hat{H}_{SO}) and magnetic (\hat{H}_Z) fields, which produce a splitting $\Delta E \lesssim 0.1$ eV.

B STT at a normal-metal/ferromagnet interface [35, 61, 62]

The conduction electron incident on the NM/FM interface has the Fermi kinetic energy $E_F = \hbar^2 k_F^2 / 2m_e$ where the wavevector consists of a longitudinal and a perpendicular component, $\mathbf{k} = (k_x, \mathbf{q})$. At the interface there is a spin-dependent potential energy step [see Fig. 2.3(a)] given by the exchange splitting ΔE_x in the FM where the wavevectors (kinetic energies) become also spin-dependent, $k_F^\uparrow > k_F^\downarrow$. The quantization axis is given by the direction of \mathbf{M} , here chosen along z . The free-electron wavefunction for the incident, reflected, and transmitted electron can be expressed as a linear combination of the FM eigenstates of (1.10) form

$$\begin{aligned}\psi_i &= (\cos \frac{\theta}{2} e^{-i\phi/2} |\uparrow\rangle + \sin \frac{\theta}{2} e^{i\phi/2} |\downarrow\rangle) e^{ik_x x} e^{i\mathbf{q} \cdot \mathbf{R}}, \\ \psi_r &= (\cos \frac{\theta}{2} e^{-i\phi/2} R_\uparrow |\uparrow\rangle + \sin \frac{\theta}{2} e^{i\phi/2} R_\downarrow |\downarrow\rangle) e^{-ik_x x} e^{i\mathbf{q} \cdot \mathbf{R}}, \\ \psi_t &= (\cos \frac{\theta}{2} e^{-i\phi/2} T_\uparrow e^{ik_x^\uparrow x} |\uparrow\rangle + \sin \frac{\theta}{2} e^{i\phi/2} T_\downarrow e^{ik_x^\downarrow x} |\downarrow\rangle) e^{i\mathbf{q} \cdot \mathbf{R}},\end{aligned}\tag{B.1}$$

where θ and ϕ are the polar and azimuthal angles defining the incident spin orientation and \mathbf{R} is the perpendicular position vector, $\mathbf{r} = (x, \mathbf{R})$. R_\uparrow (T_\uparrow) and R_\downarrow (T_\downarrow) are the reflection (transmission) amplitudes for the majority and minority electrons, respectively. These coefficients are given by the matching conditions for the wavefunctions and their derivatives at the interface ($x = 0$)

$$T_\sigma(q) = \frac{2k_x(q)}{k_x(q) + k_x^\sigma(q)} \quad R_\sigma(q) = \frac{k_x(q) - k_x^\sigma(q)}{k_x(q) + k_x^\sigma(q)},\tag{B.2}$$

where σ is \uparrow or \downarrow , $k_x(q) = \sqrt{k_F^2 - q^2}$ is real, and $k_x^\sigma(q) = \sqrt{(k_F^\sigma)^2 - q^2}$ becomes imaginary for $q^2 > (k_F^\sigma)^2$. The reflection and transmission probabilities

$$T^\sigma(q) = \frac{k_x^\sigma(q)}{k_x(q)} |T_\sigma(q)|^2 \quad R^\sigma(q) = |R_\sigma(q)|^2 \quad (\text{B.3})$$

satisfy $T^\sigma(q) + R^\sigma(q) = 1$. Finally, inserting (B.1) into (2.8) yields the incident, reflected, and transmitted spin current densities

$$\begin{aligned} \mathbf{Q}_x^i &= \frac{\hbar^2 k_x}{2m_e} \begin{pmatrix} \sin \theta \cos \phi \\ \sin \theta \sin \phi \\ \cos \theta \end{pmatrix} \quad \mathbf{Q}_x^r = -\frac{\hbar^2 |k_x|}{2m_e} \begin{pmatrix} \frac{1}{2} \sin \theta \operatorname{Re}(R_\uparrow^* R_\downarrow e^{i\phi}) \\ \frac{1}{2} \sin \theta \operatorname{Im}(R_\uparrow^* R_\downarrow e^{i\phi}) \\ \cos^2 \frac{\theta}{2} |R_\uparrow|^2 - \sin^2 \frac{\theta}{2} |R_\downarrow|^2 \end{pmatrix} \\ \mathbf{Q}_x^t &= \frac{\hbar^2}{2m_e} \begin{pmatrix} \frac{k_x^\uparrow + k_x^\downarrow}{4} \sin \theta \operatorname{Re}(T_\uparrow^* T_\downarrow e^{i\phi} e^{i\Delta k x}) \\ \frac{k_x^\uparrow + k_x^\downarrow}{4} \sin \theta \operatorname{Im}(T_\uparrow^* T_\downarrow e^{i\phi} e^{i\Delta k x}) \\ k_x^\uparrow \cos^2 \frac{\theta}{2} |T_\uparrow|^2 - k_x^\downarrow \sin^2 \frac{\theta}{2} |T_\downarrow|^2 \end{pmatrix}, \end{aligned} \quad (\text{B.4})$$

where $\Delta k = k_x^\downarrow - k_x^\uparrow$. The spin currents flow perpendicular to the NM/FM interface and represent the directions of the itinerant electron spin before and after the interaction with magnetization. Using (B.3) one can easily show that $Q_{zx}^i + Q_{zx}^r - Q_{zx}^t = 0$, i.e., there is no torque associated with the spin-component parallel to \mathbf{M} . The torque from the transverse ($\mathbf{Q}_x \perp \mathbf{M}$) spin-component is generally nonzero.

C Derivation of current-induced STTs on magnetization

The starting point is the spin continuity equation for the itinerant electron spin density \mathbf{s} [61, 103]

$$\frac{\partial \mathbf{s}}{\partial t} + \nabla \cdot \mathbf{Q} = -\frac{1}{\tau_{ex} M_s} \mathbf{s} \times \mathbf{M} - \frac{\delta \mathbf{s}}{\tau_{sf}}, \quad (\text{C.1})$$

where $\tau_{ex} = \hbar/SJ_{ex}$, S being the dimensionless spin of the d -electrons and J_{ex} the exchange constant. \mathbf{s} , \mathbf{M} , \mathbf{Q} , and $\delta \mathbf{s}$ are in general spatially and time-dependent. The left-hand side of the equation resembles the well-known particle (charge) continuity equation which is in the case of spin augmented by the two terms on the right-hand side. These correspond to the exchange torque from the inhomogeneous magnetization and to the spin decay which is described in the relaxation time approximation with τ_{sf} being the spin-flip relaxation time [103].

The itinerant spin density can be separated into two terms [103]

$$\mathbf{s}(\mathbf{r}, t) = \mathbf{s}_0(\mathbf{r}, t) + \delta \mathbf{s}(\mathbf{r}, t) = n_0 \frac{\mathbf{M}(\mathbf{r}, t)}{M_s} + \delta \mathbf{s}(\mathbf{r}, t), \quad (\text{C.2})$$

where n_0 is the local equilibrium spin density which points parallel to the magnetization. The first term represents the adiabatic spin density which instantaneously follows the local magnetization. It is reasonable to assume that this contribution describes approximately the itinerant spin dynamics. Since the magnetization dynamics is slow compared to that of the conduction electron spins, these can adiabatically adjust to the magnetization. The second term represents the deviation from the adiabatic spin dynamics.

In similar sense one can separate also the spin current density [103]

$$\mathbf{Q}(\mathbf{r}, t) = \mathbf{Q}_0(\mathbf{r}, t) + \delta \mathbf{Q}(\mathbf{r}, t) = -\frac{\mu_B P}{e} \mathbf{j} \otimes \frac{\mathbf{M}(\mathbf{r}, t)}{M_s} + \delta \mathbf{Q}(\mathbf{r}, t), \quad (\text{C.3})$$

where the dimensionless $P = (\sigma_{\uparrow} - \sigma_{\downarrow}) / (\sigma_{\uparrow} + \sigma_{\downarrow})$ describes the degree of the spin current polarization [231] ($\sigma_{\uparrow, \downarrow}$ being the spin-dependent conductivity) and \mathbf{j} is the charge current density. The first term corresponds to the current spin-polarized along the local magnetization. The nonequilibrium contribution is, within the semiclassical transport theory, generated by a diffusion of the nonequilibrium spin density, $\delta\mathbf{Q} = -D_0\nabla\delta\mathbf{s}$, where D_0 is the diffusion constant [103]. For smoothly varying magnetization textures (wide enough DWs) this term can be neglected. Since we only consider the linear response of $\delta\mathbf{s}$ to \mathbf{j} and $\partial\mathbf{M}/\partial t$ we also neglect $\partial\delta\mathbf{s}/\partial t$ which is already of higher order [103].

Inserting (C.2) and (C.3) into (C.1) allows, after a straightforward algebra, to express the nonequilibrium spin density induced by the electrical current \mathbf{j} and the magnetization change $\partial\mathbf{M}/\partial t$

$$\delta\mathbf{s} = \frac{\tau_{ex}}{1 + \beta^2} \left[-\frac{\beta n_0}{M_s} \frac{\partial\mathbf{M}}{\partial t} - \frac{n_0}{M_s^2} \mathbf{M} \times \frac{\partial\mathbf{M}}{\partial t} + \frac{\mu_B P \beta}{e M_s} (\mathbf{j} \cdot \nabla) \mathbf{M} + \frac{\mu_B P}{e M_s^2} \mathbf{M} \times (\mathbf{j} \cdot \nabla) \mathbf{M} \right], \quad (\text{C.4})$$

where $\beta = \tau_{ex}/\tau_{sf}$. As is obvious, the nonequilibrium spin density is generated by both the spatial and temporal variation of the magnetization. The nonequilibrium spin density $\delta\mathbf{s}$, which is misaligned with the magnetization, in turn exerts an exchange torque on \mathbf{M} , $\mathbf{T} = -(1/\tau_{ex} M_s) \mathbf{M} \times \delta\mathbf{s}$. Using the expression (C.4) this yields the torque which has to be added on the right-hand side of the LLG equation (2.4).¹ The two terms proportional to $\partial\mathbf{M}/\partial t$ can be merged with the damping term in the LLG equation and with the term on the left-hand side of the LLG equation. This leads to a renormalization of the gyromagnetic ratio $\gamma = g_L \mu_B / \hbar$ and the Gilbert damping constant α in (2.4). We can finally write the LLG equation including the current-induced torques as [90, 103]

$$\frac{\partial\mathbf{M}}{\partial t} = -\gamma^* \mu_0 \mathbf{M} \times \mathbf{H}_{eff} + \frac{\alpha^*}{M_s} \mathbf{M} \times \frac{\partial\mathbf{M}}{\partial t} + b_j (\mathbf{e}_j \cdot \nabla) \mathbf{M} - \frac{c_j}{M_s} \mathbf{M} \times (\mathbf{e}_j \cdot \nabla) \mathbf{M}, \quad (\text{C.5})$$

where $\mathbf{e}_j \equiv \mathbf{j}/|\mathbf{j}|$ and the renormalized parameters are $\gamma^* = \gamma/(1 + \eta)$ and $\alpha^* = (\alpha + \beta\eta)/(1 + \eta)$ with $\eta = n_0/[M_s(1 + \beta^2)]$. The amplitudes of the current-induced torques, $b_j = g_L P j \mu_B / [2e M_s (1 + \beta^2)(1 + \eta)]$ and $c_j = \beta b_j$, have the units of velocity.

D Magnetic anisotropy of the studied Fe/GaAs epilayer

Magnetization in our thin (2 nm \approx 14 ML) iron film grown on GaAs(001) lies in the sample plane because of the strong (\approx 2 T) demagnetizing field. The in-plane magnetic anisotropy of the film was characterized by a SQUID magnetometer. The $M(H)$ dependencies measured along three different crystallographic directions are shown in Fig. D.1(a). By fitting the data to the theoretical expressions given in [232] we identified an uniaxial anisotropy component with easy axis (EA) along [110] direction and anisotropy field of $\mu_0 H_u = -13 \pm 3$ mT and a cubic component with EAs along [100] and [010] directions and anisotropy field of $\mu_0 H_c = 30 \pm 6$ mT. This is quite unusual as in very thin films (\lesssim 25 ML) usually the uniaxial anisotropy dominates [28]. A possible explanation is the influence of interfaces. It is known that the cubic anisotropy has both surface and volume contributions while the uniaxial one originates purely from the interfaces (both Fe/GaAs and Fe/cap). The surface anisotropies are very sensitive to the surface

¹In the two terms which are not proportional to β we utilize the fact that the magnetization has a constant magnitude and, therefore, any change of \mathbf{M} is perpendicular to \mathbf{M} , which implies $\mathbf{M} \times (\mathbf{M} \times d\mathbf{M}/dt) = -M_s^2 d\mathbf{M}/dt$ and $\mathbf{M} \times [\mathbf{M} \times (\mathbf{e}_j \cdot \nabla) \mathbf{M}] = -M_s^2 (\mathbf{e}_j \cdot \nabla) \mathbf{M}$.

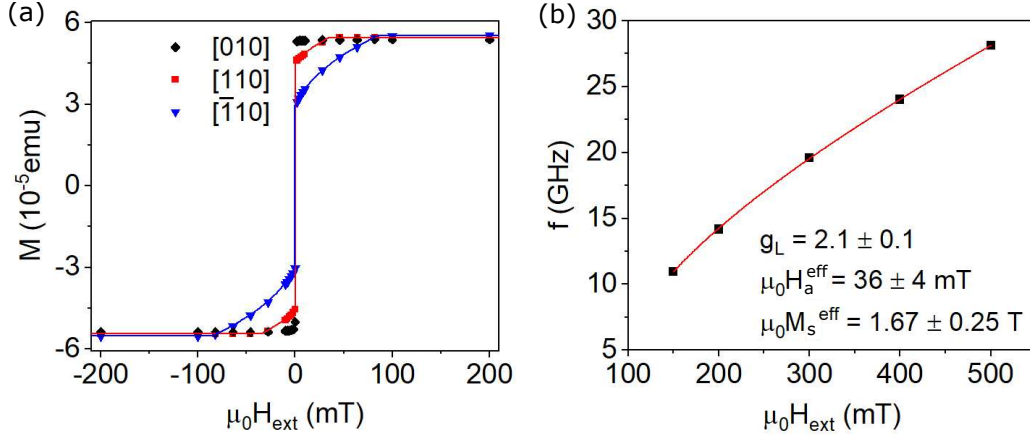


Figure D.1: Magnetic characterization of the Fe/GaAs epilayer. (a) Magnetization components along different crystallographic directions measured by SQUID magnetometry. EA position close to [010] axis indicates a strong cubic contribution to the magnetic anisotropy. (b) Magnetization precession frequency measured as a function of the magnetic field strength in a pump-probe MO experiment (points). Fit (curve) by formula (D.2) yields magnetic parameter values typical for iron.

quality, termination of the substrate, material of the capping layer or possible mixing of iron with these materials at the interfaces. These surface effects become increasingly important with decreasing thickness of the iron layer and can significantly modify the overall magnetic anisotropy in very thin films.

In an independent magneto-optical pump-probe experiment we measured the magnetization precession frequency as a function of the external magnetic field applied along $[\bar{1}10]$ direction. For fields larger than ≈ 150 mT, the magnetization points in the field direction and the precessional frequency follows the Kittel formula [42]

$$f = \frac{gL\mu_B\mu_0}{h} \sqrt{(H_{ext} + M_s^{eff} + H_c + 2H_u)(H_{ext} - 2H_c + 2H_u)}, \quad (\text{D.1})$$

where H_{ext} is the magnitude of the external magnetic field and H_c and H_u are the anisotropy fields corresponding to the in-plane cubic and uniaxial contributions, respectively. $M_s^{eff} = M_s - 2H_{out}$ contains the contributions from the shape anisotropy (demagnetizing field) and the out-of-plane uniaxial anisotropy. While in the first bracket the material anisotropy fields do not play an important role (it is dominated by the demagnetizing field $\mu_0 M_s \approx 2$ T), in the second bracket H_c and H_u have a significant influence. Therefore, we define the effective anisotropy field $H_a^{eff} = H_c - H_u$ and the fitting formula reduces to

$$f = \frac{gL\mu_B\mu_0}{h} \sqrt{(H_{ext} + M_s^{eff} + H_a^{eff} + 3H_u)(H_{ext} - 2H_a^{eff})}. \quad (\text{D.2})$$

Because the fitting procedure is almost insensitive to the precise value of H_u in the first bracket we set $\mu_0 H_u = -13$ mT, as measured by SQUID. The fitted MO data are shown in Fig. D.1(b) together with the determined parameters. The g-factor of 2.1 exactly fits the values reported in literature for iron [233] confirming that the oscillatory MO signal, we measure, corresponds to the precession of iron magnetization. The effective anisotropy field $\mu_0 H_a^{eff} = 36 \pm 4$ mT also corresponds very well to the value obtained by SQUID ($\mu_0 H_c - \mu_0 H_u = 43 \pm 9$ mT). Finally, the value of the effective magnetization $M_s^{eff} = M_s - 2H_{out} = 1.67 \pm 0.25$ T for the typical value of $H_{out} = 235$ mT [28] gives $\mu_0 M_s = 2.14$ T which exactly fits the saturation magnetization of bulk iron [28].

E The effect of strain on the magnetic energy density of (Ga,Mn)As

As mentioned in section 4.1, the in-plane magnetic anisotropy of a bare (Ga,Mn)As epilayer grown on a GaAs substrate consists of two contributions - cubic and uniaxial - whose competition results in two EAs inclining towards the $[\bar{1}10]$ crystallographic direction with increasing Mn content and temperature [25, 41]. In the presence of an externally applied uniaxial strain, the sample magnetic anisotropy is modified by an additional uniaxial contribution [27]. Within the single-domain Stoner-Wolfarth model (see section 2.2.1) the magnetization switching takes place when the energy barrier between two neighboring energy minima disappears due to the applied magnetic field. The total magnetic energy density has the following dependence [27, 29] on the in-plane magnetization direction ϕ :

$$\epsilon_{tot} = \frac{\mu_0 M_s}{2} \left[\frac{H_c}{4} \sin^2 2\phi - \frac{H_u}{2} (1 - \sin 2\phi) - H_S \cos^2(\phi - \delta) - H_{EXT} \cos(\phi - \phi_H) \right]. \quad (\text{E.1})$$

Here M_s is the saturation magnetization, H_c , H_u , and H_S are the effective anisotropy fields arising from the cubic, uniaxial, and strain-induced contributions to the total magnetic anisotropy, respectively, and H_{EXT} is the external magnetic field magnitude. Angle ϕ_H denotes the magnetic field direction, and δ is the angle at which the strain-induced energy minimum is located (all angles are measured with respect to the $[100]$ in-plane crystallographic direction). In the case of strain applied along one of the main crystal axes ($[100]$, $[010]$, $[110]$, and $[\bar{1}10]$), the respective easy direction δ coincides with the strain direction. However, this does not have to be the case for a strain applied in a general direction [27] and, therefore, we treat δ as an unknown parameter.

Our test $\text{Ga}_{1-x}\text{Mn}_x\text{As}/\text{GaAs}/\text{PZT}$ stack contains a 20 nm thick epilayer with $x \approx 0.038$, where $\mu_0 H_c = 47$ mT and $\mu_0 H_u = 28$ mT [41]. Fig. E.1(a) shows the angular dependence of the resulting magnetic anisotropy that can be characterized by four easy directions: “3” ($\phi = 108^\circ$), “2” ($\phi = 161^\circ$), “1” ($\phi = 288^\circ$), and “4” ($\phi = 341^\circ$). If the external magnetic field H_{EXT} is applied close to one of the easy directions (in our case, $\phi_H = 112^\circ$ is close to the direction “3” located at 108°), the magnetic anisotropy will change with H_{EXT} , as depicted in Fig. E.1(b). In particular, if the magnetization is rotated to the easy direction “3” by an application of large positive H_{EXT} , it will remain in this state until sufficiently strong H_{EXT} of *opposite polarity* is applied, when the magnetization switching to the opposite magnetic state “1” occurs. We note that the simple Stoner-Wolfarth model of magnetization switching does not take into account the presence of defects which can serve as low-energy nucleation centers for the magnetization reversal process (see section 2.2.2). Once the reversed domain is nucleated, the switching process can continue via a DW motion that will decrease the value of H_{EXT} required to achieve the magnetization switching.

In the presence of a mechanical strain - induced, e.g., by a piezo-electric transducer - the magnetic field-induced magnetization switching can be considerably different. In Fig. E.1(c), we show how the energy density profile of the magnetic anisotropy around the easy direction “3” changes with the direction δ of the strain-induced uniaxial anisotropy (with a magnitude $\mu_0 H_S = 8$ mT). In Fig. E.1(d), we demonstrate that for $\delta = 180^\circ$, for example, the switching from state “3” can occur even *before* the polarity of H_{EXT} is changed, which is consistent with the experimental data shown in Fig. 5.5(a). However, as there exist several possible combinations of H_S and δ that predict a rather similar behavior with H_{EXT} , Fig. E.1(d) should be regarded solely as a qualitative explanation of the data in Fig. 5.5(a).

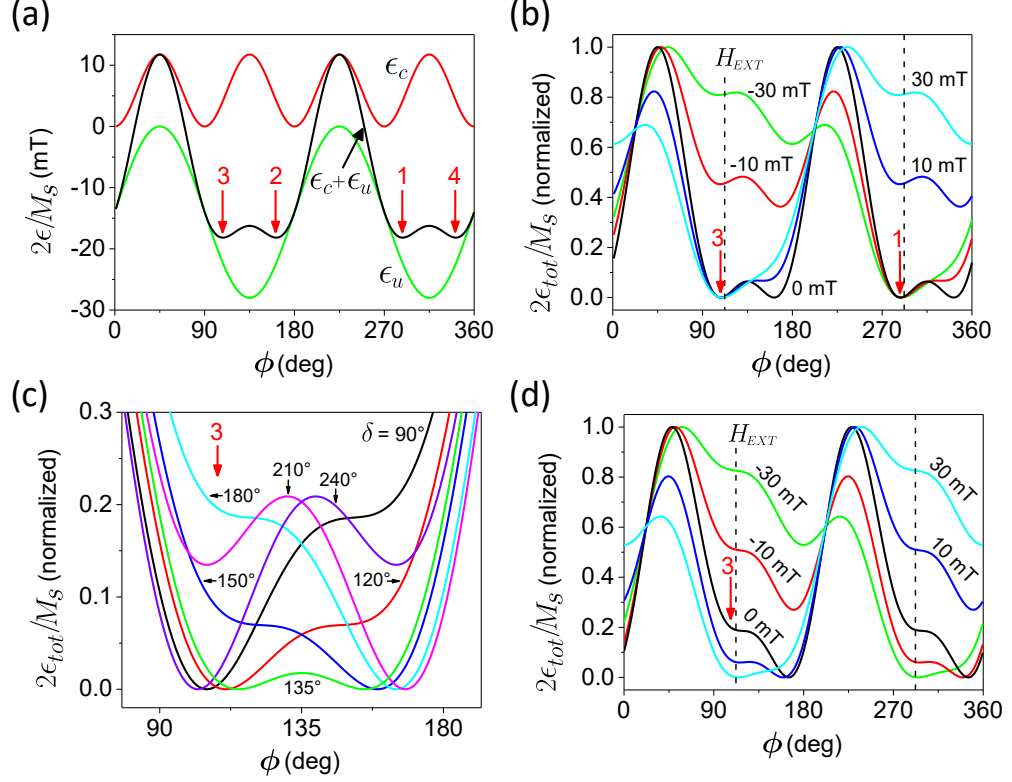


Figure E.1: Magnetic energy density in unstrained and strained (Ga,Mn)As sample. (a) Angular dependence of cubic (ϵ_c), uniaxial (ϵ_u), and total ($\epsilon_c + \epsilon_u$) magnetic anisotropy energy density in a bare (unstrained) $\text{Ga}_{1-x}\text{Mn}_x\text{As}$ epilayer with $x \approx 0.038$, where $\mu_0 H_c = 47$ mT and $\mu_0 H_u = 28$ mT. The positions of the easy directions 1–4 shown in Fig. 5.4(a) are depicted by vertical arrows. (b) Change of the magnetic anisotropy shown in (a) by H_{EXT} applied in the direction depicted by a vertical dashed line both for positive ($\phi_H = 112^\circ$) and negative ($\phi_H = 292^\circ$) fields. (c) Modification of the magnetic anisotropy around easy direction “3” by the strain-induced uniaxial anisotropy of $\mu_0 H_S = 8$ mT pointing in different directions δ . (d) Same as (b) for the case when the strain-induced anisotropy with $\mu_0 H_S = 8$ mT and $\delta = 180^\circ$ is also included.

F Elastic DW expansion, geometrical pinning, and Hall detection of a DW position

Bubble model of DW propagation. In the following we introduce a simplified model of DW propagation in geometrically restricted structures fabricated from perpendicular-to-plane magnetized FM thin films. This model, described in [132], contains several approximations. First, we neglect the magnetic charges resulting from the curvature of the domain wall, which is well justified if the radius r of the DW curvature is much larger than the DW width δ_{DW} . This is safely fulfilled in our case since $r \gtrsim 1 \mu\text{m}$ and $\delta_{DW} \sim 10$ nm. Second, we do not take into account inhomogeneities of the demagnetizing field. These appear inside the DW and in close proximity of the structure edges (at distances of the order of the film thickness). As shown in [132] the effects on DW structure and total magnetic energy density are small and should not influence significantly the DW pinning at the cross-entrance corners. Third, we neglect the DW ‘friction’ due to the edge roughness of the patterned structure. Finally, we assume uniform distribution of structural defects, inhomogeneities, etc. in the magnetic film, whose effect on the DW propagation can be described by a coercive intrinsic propagation field H_{PR} which is considered to be everywhere the same.

Under the above assumptions, the DW shape and propagation is given only by competition of the DW energy $E_{DW} = \sigma_{DW}tl$ and the Zeeman energy of the reversed domain in the applied magnetic field H_A , $E_Z = -\mu_0 M_s H_A t S$. Here, $\sigma_{DW} = \pi\sqrt{AK_u}$ is the DW energy per unit area (see section 1.4.1) with A being the exchange stiffness and K_u the effective out-of-plane anisotropy constant, t is the magnetic layer thickness, l is the DW length, and S is the area of the reversed domain. This DW propagation model is also known as the *bubble* model since it represents an exact analogy, in 2D, to a 3D soap bubble, where it is the internal air pressure (analog of the magnetic field strength) competing with the surface tension of the bubble (analog of the DW areal energy density). This competition results in spherical shape of the bubble and, in the 2D case, in circular shape of the magnetic domain. In other words, for a given air volume (domain area), i.e., for a given pressure (Zeeman energy) a boundary of spherical (circular) shape has the minimum area (length) and, consequently, the minimum energy.

Let's first consider an infinite magnetic film where a circular domain of radius r expands due to the applied magnetic field. If the DW moves by dq (here $q = r$) the Zeeman energy decreases by $-dE_Z = \mu_0 M_s H_A t (\partial S / \partial q) dq$ and the wall energy increases by $dE_{DW} = \sigma_{DW} t (\partial l / \partial q) dq$. In equilibrium

$$\frac{dE_{tot}}{dq} = \sigma_{DW} t \frac{dl}{dq} - \mu_0 M_s H_A t \frac{dS}{dq} = 2\pi r t \mu_0 M_s (H_R - H_A) = 0, \quad (\text{F.1})$$

which gives a relation between the applied field and the corresponding stable domain size. The applied field is opposed by a *virtual* restoring field H_R originating from the 'bubble' surface tension, $H_R = \sigma_{DW} / (r \mu_0 M_s)$.

Now we take into account the geometrical restrictions in our symmetrical crossbar device of width w . DW nucleated in a straight bar is straight and perpendicular to the bar edges [position A in Fig. F.1(a)]. When an out-of-plane magnetic field H_A is applied in a direction that favours the left domain, the DW will move to right for $H_A > H_{PR}$ until it reaches the cross entrance (position B). In order to propagate further the DW has to increase its length which is accompanied by energy increase. As H_A is increased, the DW stays pinned at the cross-entrance corners and bends into the cross keeping a shape of a circle arc with decreasing radius. The Zeeman energy gain by enlarging the left domain is smaller than the energy cost of the stretched DW, which results in a virtual restoring field H_R opposing the DW expansion.

Due to the simple circular shape of the DW, its position in the structure can be described by a single coordinate q - position of the DW center (intersection of the DW and the bar axis). Propagation of the real arc-shaped DW in the 2D structure in the field H_A is thus effectively reduced to a 1D problem of a virtual straight DW with a position corresponding to the center of the real wall and propagating in the total field $H_A - H_R$. Between the positions B and C in Fig. F.1(a) the DW length is expressed as $l = 2r \arcsin(w/2r)$. The area of the reversed magnetization left from the DW (hatched) is given as $S = r^2 [\arcsin(w/2r) - (w/2r) \sqrt{1 - (w/2r)^2}]$. The radius r decreases from ∞ to $w/2$ as the DW moves from $q = -w/2$ (position B) to $q = 0$ (C), where q is measured from the cross center and its relation to r is given by

$$q = r - w/2 - \sqrt{r^2 - (w/2)^2}. \quad (\text{F.2})$$

The equilibrium position of the wall for a given applied field is again given by the condition $dE_{tot}/dq = 0$ which yields

$$(\sigma_{DW} - \mu_0 M_s H_A^{eq} r) t \frac{2\sqrt{r^2 - (w/2)^2} \arcsin(w/2r) - w}{\sqrt{r^2 - (w/2)^2} - r} = 0. \quad (\text{F.3})$$

In equilibrium the external magnetic field H_A^{eq} is exactly balanced by the restoring field H_R , i.e., from the first bracket of Eq. (F.3) we get

$$H_R = H_A^{eq} = \frac{\sigma_{DW}}{\mu_0 M_s r}. \quad (\text{F.4})$$

This together with the relation (F.2) gives the dependence of the restoring field on the DW position q in the cross between the points B and C which is plot in Fig. F.1(b). The restoring field reaches its maximum $H_R^{\max} = \sigma_{DW}/M_s w$ in position C, when the DW center reaches center of the cross with the curvature diameter equal to the bar width. Beyond this point the cross-entrance corners do not influence the DW propagation any more and the domain expands further as in an infinite film (keeping a semi-circular shape) until it reaches the output corners of the cross (position D). In this region H_R follows the same dependence as that deduced from Eq. (F.1) which expressed by the coordinate q of the cross reads

$$H_R = \frac{\sigma_{DW}}{\mu_0 M_s (q + w/2)}. \quad (\text{F.5})$$

When reaching the output corners the DW can minimize its energy by splitting to three DWs in the individual output arms of the cross with each DW straight and perpendicular to the local bar axis. Further propagation of the DWs is again free in the output arms opposed only by the propagation field H_{PR} .

AHE detection of magnetic configurations. The anomalous Hall effect is sensitive to the perpendicular-to-plane component of magnetization in the cross area. For the opposite saturated magnetic states it gives a voltage of the same magnitude and opposite sign. When a DW is present in the cross, the measured Hall voltage lies between these two extreme values. From the bubble model we know how the DW propagates through the cross structure, i.e., for each position q we know the corresponding magnetization distribution $\mathbf{M}(x, y)$ within the cross area and we can calculate the Hall voltage generated by such configuration at the transverse contacts. The resulting dependence $V_H(q)$ can be used, in the opposite way, to deduce the magnetization configuration (DW position) in the cross from the measured Hall voltage.

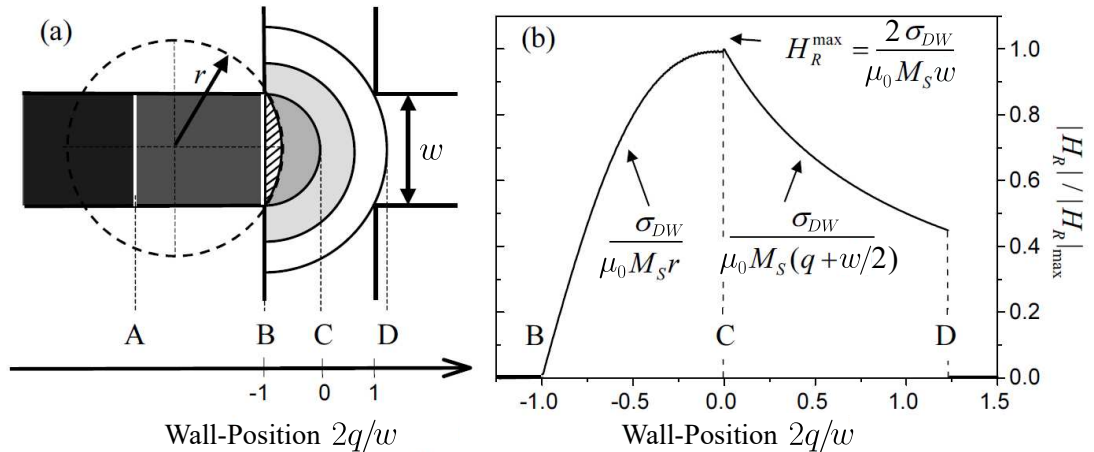


Figure F.1: Bubble-like DW propagation in crossbar structure. (a) Several consecutive positions of a DW during its propagation through a symmetric Hall cross and (b) the corresponding virtual restoring field H_R originating from the DW surface energy opposing the DW propagation. The wall remains pinned at the cross-entrance corners until its center reaches the cross center. At this point H_R reaches its maximum and the DW is released. The figure is reproduced from [132].

In a simplified model where the current density is uniform and restricted only to one of the bars, the device would be sensitive only to the magnetization in the central cross area with each point of the central square contributing equally to the overall Hall voltage. This is not the case in reality, since the current density is nonuniform and is not restricted only to the current-carrying bar but it enters also the transverse arms of the cross. Consequently, not only the central square but also the arms contribute to the Hall voltage and the contributions from different places in the cross structure to the overall Hall signal are not equal. One can find a sensitivity distribution function [132, 234] which relates the magnetization in a given point (x, y) to the Hall signal. This function is plot in Fig. F.2(a) for a symmetrical cross. The maximum sensitivity is obtained in the central area of the cross and is quite uniform.

Combining the sensitivity distribution function with the magnetization distribution $M(x, y)$ and integrating over the whole cross structure gives the Hall voltage [132].

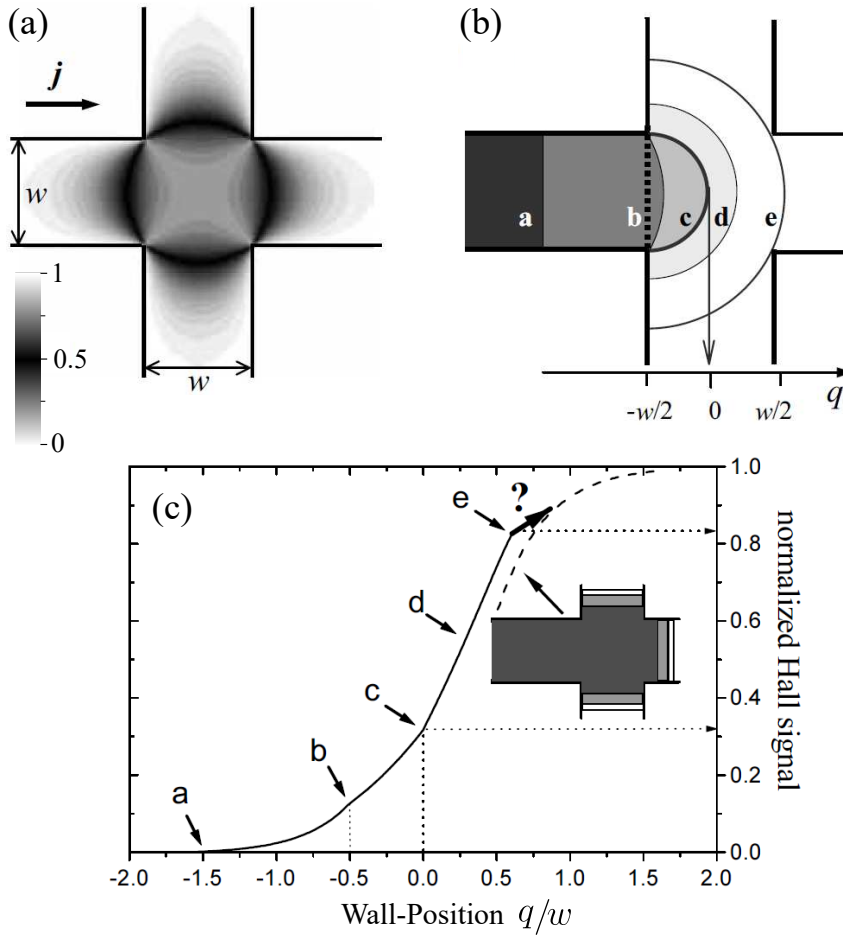


Figure F.2: Sensitivity distribution function and AHE response to a DW propagating through a Hall cross. (a) Sensitivity distribution function of a symmetrical Hall cross. In order to emphasize the structure of the sensitivity function the gray scale is chosen such that both the maximum and minimum values are white and the middle value of 0.5 corresponds to black. The maximum value is obtained in the cross center. (b) Several consecutive positions of a DW during its propagation through the cross structure and (c) the corresponding normalized Hall signal obtained as an integral of the sensitivity distribution from (a) combined with the magnetization distribution from (b). The bubble model is able to describe the DW propagation up to the stage ‘e’. Beyond this point the DW splits into three individual straight DWs in the output arms (see the inset) with the Hall signal given by the dashed line. The figure is reproduced from [132].

Figs. F.2(b) and (c) show several consecutive positions of a DW propagating through a crossbar device and the corresponding normalized Hall signal. The onset of the Hall signal (0–0.15) corresponds to the DW propagation in the input arm of the cross. The largest sensitivity to the DW displacement is obtained in the central square of the cross (between configurations ‘b’ and ‘e’). The bubble model is unable to describe the DW transformation between the stage ‘e’ and the final configuration with the three individual straight DWs in the output arms (see the inset sketch) which corresponds to the final part of the signal (0.85–1, dashed line).

